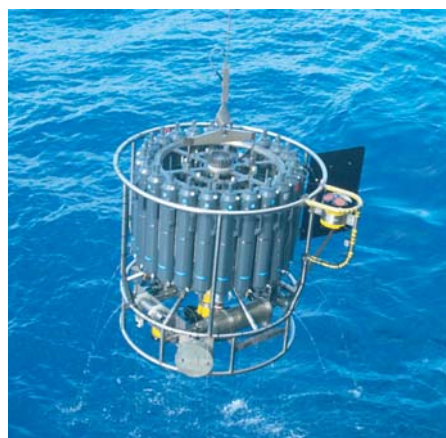




Weather Research and Forecasting Model with Chemistry (WRF-CHEM) over South Asia

Rajesh Kumar



Hinweis

Die Berichte zur Erdsystemforschung werden vom Max-Planck-Institut für Meteorologie in Hamburg in unregelmäßiger Abfolge herausgegeben.

Sie enthalten wissenschaftliche und technische Beiträge, inklusive Dissertationen.

Die Beiträge geben nicht notwendigerweise die Auffassung des Instituts wieder.

Die "Berichte zur Erdsystemforschung" führen die vorherigen Reihen "Reports" und "Examensarbeiten" weiter.



Notice

The Reports on Earth System Science are published by the Max Planck Institute for Meteorology in Hamburg. They appear in irregular intervals.

They contain scientific and technical contributions, including Ph. D. theses.

The Reports do not necessarily reflect the opinion of the Institute.

The "Reports on Earth System Science" continue the former "Reports" and "Examensarbeiten" of the Max Planck Institute.

Anschrift / Address

Max-Planck-Institut für Meteorologie
Bundesstrasse 53
20146 Hamburg
Deutschland

Tel.: +49-(0)40-4 11 73-0
Fax: +49-(0)40-4 11 73-298
Web: www.mpimet.mpg.de

Layout:

Bettina Diallo, PR & Grafik

Titelfotos:

vorne:

Christian Klepp - Jochem Marotzke - Christian Klepp

hinten:

Clotilde Dubois - Christian Klepp - Katsumasa Tanaka

Weather Research and
Forecasting Model with
Chemistry (WRF-CHEM) over South Asia

Rajesh Kumar

aus Indien

Hamburg 2012

Rajesh Kumar

Max Planck Institute for Meteorology, Bundestrasse, 53, 20146 Hamburg, Germany

Climate Service Center, Helmholtz Zentrum Geesthacht, 20146 Hamburg, Germany

Aryabhata Research Institute of Observational Sciences, 263129 Nainital, India

Als Dissertation angenommen

vom Department Geowissenschaften der Universität Hamburg

auf Grund der Gutachten von

Prof. Dr. Martin Claussen

und

Prof. Dr. Guy P. Brasseur

Hamburg, den 7. Juni 2012

Prof. Dr. Jürgen Oßenbrügge

Leiter des Departments für Geowissenschaften

Thesis Committee

Prof. Dr. Martin Claußen

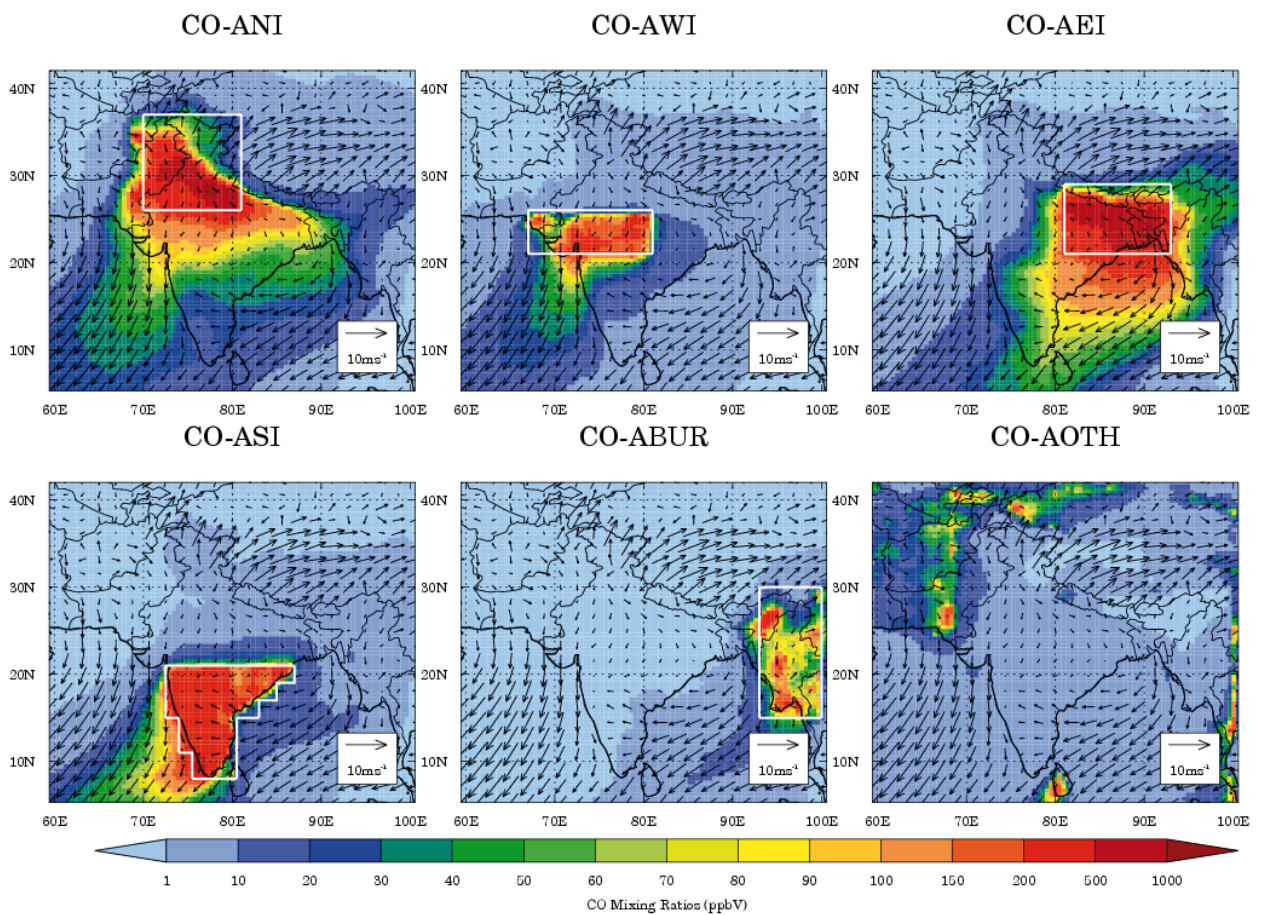
Prof. Dr. Guy P. Brasseur

Prof. Dr. K. Heinke Schluenzen

Dr. Thomas Pohlmann

Manish Naja, PhD

Weather Research and Forecasting Model with Chemistry (WRF-CHEM) over South Asia



Rajesh Kumar

Hamburg 2012

ACKNOWLEDGMENTS

I take this opportunity to express my deep respect and gratitude to my thesis supervisors Prof. Martin Claussen and Prof. Guy P. Brasseur for their help, support, supervision, commitment, constant encouragement and fruitful discussions. I consider myself extremely lucky to get an opportunity to work with Manish Naja, Aryabhata Research Institute of Observational Sciences (ARIES), Nainital, India. I have been greatly benefited and learned very much from his exemplary scientific and personal integrity, generosity, never ending enthusiasm and positive approach to understand research problems. He always provided me the independence to pursue my own scientific ideas and encouraged me to work according to my own ideas from the moment I started working with him. The constructive criticism and suggestions from my supervisors have improved my writing and scientific thinking substantially. It gives me immense pleasure to express my sincere thanks to them for all the help and support during the entire period of this work without which the composition of this dissertation in its current form would have been impossible.

I am also deeply indebted to Prof. Shyam Lal, Physical Research Laboratory, Ahmedabad, India for his valuable help in learning the fundamentals of atmospheric trace species, wholehearted support and useful interactions. I would also like to thank Prof. Ram Sagar, Director, ARIES, Nainital for his help and support in all the academic and administrative perspectives and in establishing observational and modeling facilities at ARIES. I am deeply grateful to him for consistent encouragement, positive outlook and personal interest in the progress of my work. I am highly grateful to Prof. W. J. Randel for providing me an opportunity to visit National Center for Atmospheric Research (NCAR), Boulder, USA for learning the WRF-Chem model. I am deeply indebted to Drs. Mary Barth and Gabriele Pfister for introducing me to the fundamentals of WRF-Chem model. I am also thankful to Drs. L. K. Emmons, C. Wiedinmyer, A. Hodzic and H. M. Worden for their timely help in setting-up WRF-Chem model and various fruitful discussions. I greatly acknowledge the administrative help and support from S. Montoya and J. Martin, and from Elke Lord and Christina Rieckers in organization of my trips to USA and Germany respectively. I also acknowledge Cornelia Kampmann for her wholehearted support and kindness in all the administrative matters related to this dissertation. The help from Claudia Wunram, Björn Weber and Hinnerk Ries is greatly acknowledged.

I gratefully acknowledge Drs. Narendra Singh, U. C. Dumka, Amitava Guharay, Pankaj Kumar and Fahad Saeed for their wonderful company, help and support throughout the tenure of this work. I would like to thank the valuable technical help and support provided by the engineering, technical and library staff of ARIES. Thanks are extended to all the faculty members and staff of ARIES, MPI, CSC and NCAR who directly or indirectly helped me during the course of this work. I would like to thank all my seniors and juniors at ARIES for their company, timely help and suggestions. I was very fortunate to have Narendra Ojha, Aparna Mishra, Tapaswini Sarangi, Kalpana Pandey., Bindu Rani, Sanjit Sahu and Akashpirya as my friends. Their pleasant company, constant encouragement and selfless support in all kinds of academic and personal matters have made my journey to Ph.D. an incredible fun and a gratifying experience. The critical efforts of MOPITT, AIRS, TES, OMI, TRMM and GOME-2 science team members for designing retrieval algorithms and providing the satellite data products are greatly acknowledged.

Above all, I express my deep respect and gratitude to my parents who poured everything they had into me from the moment I was born. Truly speaking, I could not have wished for better parents and would have never been able to pursue study for Ph.D. without the loving, stable and encouraging family environment provided by them. I will always be highly grateful to my elder brother Bijender who believed and trusted in my abilities much more than I did and always encouraged me to progress even when I used to get out of energy. Special thanks are due to my elder sister Babita, my younger brother Sandeep and my sister-in-law Sarita who made my periodic visits to home a delight every time. I pay my thankfulness to my fiancé Pinki Sharma for her care and support. Last but not the least, I express my gratefulness towards my entire family members who always encouraged me during my thesis period. I personally believe that my thesis is purely an outcome of my parents' and teachers' blessings and prayers, and that is why I dedicate this dissertation to them.

Rajesh Kumar

List of Abbreviations

AIRS	Atmospheric Infrared Sounder
AK	Averaging Kernel
AMSU	Advanced Microwave Sounding Unit
AOD	Aerosol Optical Depth
PEM	Pacific Exploratory Mission
TRACE-P	Transport and Chemical Evolution over the Pacific
CARE	Campaign of Air Quality Research
REMO	Regional Model
WRF	Weather Research and Forecasting Model
PNNL	Pacific Northwest National Laboratory
CTM	Chemical Transport Model
DFS	Degrees of Freedom for Signal
DOE	Department of Energy
NMM	Nonhydrostatic Mesoscale Model
ARW	Advanced Research WRF
EDGAR	Emission Database for Global Atmospheric Research
PM	Particulate Matter
EOS	Earth Observing System
FDDA	Four Dimensional Data Analysis
FINN	Fire Inventory from NCAR
FNL	Final Analysis Datasets
BC	Black Carbon
OC	Organic Carbon
GEIA	Global Emission Inventory Activity
CE	Combustion Efficiency
GFS	Global Forecasting System
GLC	Global Land Cover
CFL	Courant-Friedrichs-Levy
GMT	Greenwich Mean Time
GOME	Global Ozone Monitoring Experiment
GRIB	Gridded Binary
RAOB	Radiosonde Observations
FAR	False Alarm Rate
HSB	Humidity Sounder for Brazil
FBI	Frequency Bias Index
ICARB	Integrated Campaign for Aerosols, Gases and Radiation Budget
IGP	Indo-Gangetic Plain
POD	Probability of Detection
IMD	Indian Meteorological Department
INDOEX	Indian Ocean Experiment
INTEX-B	Intercontinental Chemical Transport Experiment - Phase B
HKS	Hansen Kuipers Score
IPCC	Intergovernmental Panel on Climate Change
ORT	Odd Ratios
IST	Indian Standard Time
MAE	Mean Absolute Error
KNMI	Royal Netherlands Meteorological Institute
MADE	Modal Aerosol Dynamics Model for Europe
MATCH	Multiple Scale Atmospheric Transport and Chemistry
MB	Mean Bias
JOSIE	Jülich Ozone Sonde Intercomparison Experiment
MEGAN	Model of Emissions of Gases and Aerosols from Nature

GOME	Global Ozone Monitoring Experiment
AMF	Air Mass Factor
ONP	Ozone Net Production
MM5	Meteorological Model – Version 5
MNB	Mean Normalized Bias
MNGE	Mean Normalized Gross Error
MODIS	Moderate Resolution Imaging Spectroradiometer
MOPITT	Measurements of Pollution in the Troposphere
FT	Free Troposphere
MOZART	Model of Ozone and Related Tracers
MPIC	Max Planck Institute for Chemistry
MYJ	Mellor-Yamada-Janjic Scheme
NASA	National Aeronautics and Space Administration
NCAR	National Center for Atmospheric Research
NCEP	National Centers for Environmental Prediction
MAP	Maximum a Posteriori
NMHC	Non-Methane Hydrocarbons
NMVOC	Non-Methane Volatile Organic Compounds
NOAA	National Oceanic and Atmospheric Administration
OMI	Ozone Monitoring Instrument
PBL	Planetary Boundary Layer
POET	Precursors of Ozone and their Effects in the Troposphere
PPFD	Photosynthetic Photon Flux Density
RACM	Regional Atmospheric Chemical Mechanism
RADM	Regional Acid Deposition Model
REAS	Regional Emission Inventory for Asia
RETRO	Reanalysis of Tropospheric Chemical composition
RMSE	Root Mean Square Error
RRTM	Rapid Radiative Transfer Model
SCIAMACHY	Scanning Imaging Absorption Spectrometer for Atmospheric Cartography
SOA	Secondary Organic Aerosol
SORGAM	Secondary Organic Aerosol Model
TES	Tropospheric Emission Spectrometer
TKE	Turbulent Kinetic Energy
TRMM	Tropical Rainfall Measuring Mission
USGS	United States Geological Survey
VOC	Volatile Organic Compounds
WMO	World Meteorological Organization
WPS	WRF Preprocessing System
WRF-Chem	Weather Research and Forecasting-Chemistry Model

Abstract

The Weather Research and Forecasting model with Chemistry (WRF-Chem) has been set-up and used for the first time to simulate the meteorology and air quality of South Asia during the year 2008. The model performance is thoroughly evaluated by comparing model results with ground-, balloon- and satellite-based observations of meteorological and chemical fields. The spatial and temporal variability of meteorological parameters is reproduced well by the model with index of agreement greater than 0.6. The mean bias (MB) and root mean square error (RMSE) values are within ± 2 K and 1-4 K for temperature, 30% and 20-65% for water vapor, 1.6 ms^{-1} and 5.1 ms^{-1} for wind components and within 25 hPa for tropopause pressure. The model overestimates precipitation in summer and underestimates during other seasons. The modeled meteorology is found to be of sufficient quality for use in chemistry simulations with meteorological biases affecting chemistry simulations within \pm (10-25%). The model shows good ability in simulating ozone and CO variability but shows differences for NO_x . The model underestimates TES ozone, OMI tropospheric column NO_2 and MOPITT total column CO retrievals during all the months except MOPITT retrievals during August-January and OMI retrievals during winter. The evaluation results indicate large uncertainties in anthropogenic and biomass burning emission estimates, especially for NO_x . The model results indicate clear regional differences in surface ozone seasonality over South Asia with estimated daytime (1130-1530 hours) net ozone production of 0-5 ppbv hr^{-1} over inland regions and 0-2 ppbv hr^{-1} over marine regions during outflow periods. The model results indicate that ozone production in this region is mostly NO_x -limited. Eleven CO tracers are included in the model to study wintertime CO budget over South Asia. CO mixing ratios at the surface (318 ± 290 ppbv) and in the planetary boundary layer (277 ± 207 ppbV) are mainly due to pollution inflow (surface: $60 \pm 30\%$; PBL: $63 \pm 29\%$) and regional anthropogenic emissions (surface: $34 \pm 27\%$, PBL: $30 \pm 25\%$), while those in free troposphere (124 ± 27 ppbV) are mainly due to pollution inflow ($89 \pm 13\%$). Biogenic, biomass burning and photochemical sources contribute less than 10%. Regional emissions are generally constrained within lowest 3 km of the atmosphere but biomass burning emissions reach up to altitudes as high as 5 km over Burma. Intra-regional transport is estimated to enhance surface CO by 20-100 ppbV. Anthropogenic surface CO over the Arabian Sea mainly comes from northern (36%), western (27%) and southern India (22%), while eastern (62%) and northern India (14%) are the main contributors to that over the Bay of Bengal. This study shows that WRF-Chem model captures many important features of the observations over South Asia and gives confidence to using the model for future studies in this region.

Abstrakt

Das Wettervorhersagemodell “Weather Research and Forecasting-Modell with Chemistry” (WRF-Chem) wurde zum ersten Mal für Südasien aufgesetzt und dazu genutzt, die Meteorologie und Luftqualität im Jahr 2008 zu simulieren. Die Güte des Modells wurde durch den Vergleich der Modellergebnisse mit Boden-, Ballon- und Satellitengestützten Beobachtungen der meteorologischen und chemischen Parameter gründlich überprüft. Die räumliche und zeitliche Variabilität der meteorologischen Parameter wird durch das Modell mit einem “Index of agreement von größer” als 0,6 gut wiedergegeben. Der mittlere Bias (MB) und die Standardabweichung (RMSE) liegen innerhalb von ± 2 K und 4.1 K für die Temperatur, 30% und 20-65% für den Wasserdampf, $1,6 \text{ ms}^{-1}$ und $5,1 \text{ ms}^{-1}$ für die Wind-Komponenten und bei 25 hPa für den Druck auf Tropopausenniveau. Das Modell überschätzt den Niederschlag im Sommer und unterschätzt ihn während der anderen Jahreszeiten. Die Modell-Meteorologie zeigt eine ausreichende Qualität für den Einsatz in Chemie-Simulationen. Abweichungen in den meteorologischen Größen beeinflussen die Chemie-Simulationen um $\pm (10-25\%)$. Das Modell simuliert die Variabilität von Ozon und CO gut, zeigt aber Abweichungen für NO_x . Die aus Satellitenmessungen abgeleiteten Werte des Ozons (TES Satellit), der troposphärischen NO_2 -Säule (OMI Satellit) und des CO-Gesamtsäulengehalts (MOPITT Satellit) werden vom Modell ganzjährig unterschätzt. Während der Monate August-Januar werden die MOPITT-Retrievals und während des Winters die OMI-Retrievals jedoch leicht überschätzt. Große Bandbreiten werden bei den Abschätzungen anthropogenen Emissionen und aus der Verbrennung von Biomasse, insbesondere für NO_x , gefunden. Die Modellergebnisse zeigen deutliche regionale und saisonale Unterschiede im bodennahen Ozongehalt über Südasien im Vergleich zur geschätzten Netto-Ozon-Produktion (11:30-15:30 Uhr) von $0-5 \text{ ppbv hr}^{-1}$ über dem Landesinneren und $0-2 \text{ ppbv hr}^{-1}$ über Meeresregionen in Abfluss-Perioden. Es zeigt sich, dass die Ozon-Produktion in dieser Region vor allem durch NO_x begrenzt wird. Im Modell sind elf CO-Tracer enthalten, die das winterliche CO-Budget über Südasien untersuchen. CO- Mischungsverhältnisse am Boden ($318 \pm 290 \text{ ppbv}$) und in der planetaren Grenzschicht ($277 \pm 207 \text{ ppbV}$) beruhen vor allem auf dem CO-Eintrag in die Modellregion (bodennah: $60 \pm 30\%$; PBL: $63 \pm 29\%$) und auf regionalen anthropogenen Emissionen (bodennah: $34 \pm 27\%$, PBL: $30 \pm 25\%$). In der freien Troposphäre hingegen spielt vor allem der Eintrag in die Modellregion eine Rolle ($89 \pm 13\%$) für das CO-Mischungsverhältnis ($124 \pm 27 \text{ ppbV}$). Biogene Quellen, Verbrennung von Biomasse und photochemische Quellen tragen weniger als 10% bei. Regionale Emissionen werden in der Regel in den untersten 3 km der Atmosphäre gehalten. Die Emissionen durch Verbrennung von Biomasse hingegen können über Birma bis in 5 km Höhe gelangen. Durch den Luftmassentransport zwischen den einzelnen Regionen wird der CO-Gehalt in Bodennähe um etwa 20-100 ppbV erhöht. Der anthropogene, bodennahe CO-Gehalt über dem Arabischen Meer wird hauptsächlich aus Einträgen aus Nord-(36%), West- (27%) und Süd-Indien (22%) bestimmt. Demgegenüber tragen Ost-(62%) und Nord-Indien (14%) hauptsächlich über dem Golf von Bengalen zum CO-Gehalt bei. Diese Studie zeigt, dass das WRF-Chem Modell viele wichtige Charakteristika der Beobachtungen über Südasien erfasst und somit vertrauenswürdig ist für zukünftige Modell-Studien in dieser Region.

Table of Contents

1. INTRODUCTION.....	1
2. WRF-CHEM MODEL SET-UP	5
2.1 The WRF-Chem Model Description	5
2.2 The WRF Preprocessing System (WPS).....	6
2.3 Real Data Initialization - Meteorology.....	8
2.4 Real Data Initialization – Emissions	9
2.5 Model Physics	16
2.6 Model Chemistry	19
3. WRF-CHEM: METEOROLOGY EVALUATION	23
3.1 Datasets and Evaluation Methodology	24
3.1.1 Radiosonde Observations	24
3.1.2 Satellite-borne Observations	26
3.1.3 Reanalysis Dataset.....	27
3.1.4 Evaluation Methodology.....	27
3.1.5 Statistical Metrics.....	28
3.2 General Features of WRF-Chem Meteorology	30
3.3 Results of Model Evaluation.....	33
3.3.1 AIRS Temperature and Water Vapor.....	33
3.3.2 NCEP Zonal and Meridional Winds	41
3.3.3 TRMM Precipitation	46
3.3.4 Radiosonde Observations – Temperature and Dew Point Temperature	49
3.3.5 Tropopause Pressure (AIRS and Radiosonde)	52
3.4 Sensitivity Simulations	54
3.5 Summary	57
4. WRF-CHEM: CHEMISTRY EVALUATION AND INITIAL RESULTS.....	59
4.1 Datasets and Evaluation Methodology	59
4.1.1 Ground-based and Balloon-borne Observations.....	59
4.1.2 Satellite-borne Observations	61
4.2 Evaluation Methodology	63
4.2.1 Data Filtering and Model-Satellite Co-location.....	64
4.2.2 Averaging Kernels and a Priori Profiles	64
4.2.3 Statistical Metrics.....	65

4.3	Comparison with Ground-based and Ozone-sonde Observations.....	66
4.4	Comparison with Space-borne Observations.....	72
4.4.1	Comparison with TES Ozone Retrievals.....	73
4.4.2	Comparison with MOPITT CO Retrievals.....	78
4.4.3	Comparison with OMI NO ₂ Retrievals.....	84
4.5	Analysis of Modeled Surface Ozone.....	92
4.6	Summary	97
5.	TRACER-BASED ANALYSIS OF WINTERTIME CO.....	99
5.1	The Model description	101
5.2	Model Evaluation.....	103
5.3	Spatial Distribution of CO	106
5.4	Vertical Distribution of CO	109
5.5	CO Budget Analysis	112
5.6	Regional Meteorology and surface CO distribution.....	114
5.7	Summary	117
6.	CONCLUSIONS AND FUTURE SCOPE.....	119
6.1	Conclusions	120
6.2	Future Scope	123
	REFERENCES.....	125

1. Introduction

The climate change is one of the most important problems of the global environmental concern which are being faced by the human civilization today. The fingerprints of the climate change have become visible in the form of global scale warming, aggravation of sea-ice and glacier melting, rise in global mean sea level and increase in the frequency and intensity of extreme weather events such as the floods, droughts, wildfires and cyclonic storms. The Intergovernmental Panel on Climate Change (IPCC) in its latest Assessment Report-4 stated that although both natural processes and human activities can affect the climate of our planet but human impacts are estimated to be much larger than the natural influences [Forster *et al.*, 2007]. The major anthropogenic activities through which mankind have contributed to climate change are the combustion of fossil fuels and deforestation. These activities have led to a substantial increase in the concentrations of several key trace gases and aerosols in the atmosphere since the commencement of industrial era.

In view of the above, numerous efforts have been made to understand and predict the impact of human activities on atmospheric composition and global climate by integrating multi-platform (ground-based, balloon-borne, air-borne, ship-borne and satellite-borne) observations with mathematical models. However, such efforts have been limited over the Asian region where anthropogenic emissions have been increasing dramatically over the last decade while they are either decreasing or nearly stable over North America and Europe [e.g. Akimoto, 2003; Richter *et al.*, 2005]. The rise in Asian emissions potentially has serious consequences on air quality and climate not only affecting the large population on this continent but also on other continents, particularly through the intercontinental transport of pollution [e.g. Pfister *et al.*, 2010]. In this perspective, some efforts have been made to understand the impact of Asian emissions on the regional and global atmospheric composition and on climate by conducting intensive field campaigns (e.g. PEM West-A,

PEM-West B, TRACE-P and CARE-Beijing etc.) along with modeling studies. However, such efforts focused mainly on the East Asian region and are limited (INDOEX) over South Asia where increasing pollution is suggested to have important implications for crop/vegetation growth [Agrawal, 2003] and the freshwater resources through impacts on the Himalayan glaciers [Yasunari *et al.*, 2010] and summer monsoonal rainfall [Lau *et al.*, 2010].

South Asia is a region of immense diversity both in terms of the natural landscape and the anthropogenic emissions. The region is composed of widely-varying landscape including the elevated Himalayan terrain, semi-arid and desert land masses, tropical rainforests, sea-shores and the vast plains. South Asia accommodates over a quarter of the world's population and is therefore also characterized by large anthropogenic emissions. However, the characteristics of anthropogenic emissions in this region are very different as compared to other parts of the world due to the use of bio-fuels in domestic cooking and the crop residue burning [Lelieveld *et al.*, 2001; Reiner *et al.*, 2001; Lawrence and Lelieveld, 2010]. The rapid growth in the industries, transportation, urbanization, agricultural activities and thus the economy has led to significant increase in the anthropogenic emissions over this region [e.g. Akimoto, 2003; Ohara *et al.*, 2007; Ghude *et al.*, 2008; Tanimoto *et al.*, 2009]. In addition, South Asia is also a region of high photochemical activity due to strong solar insolation and high amounts of water vapor.

The rising emissions and high photochemical activity can potentially enhance the concentrations of several secondary pollutants such as ozone and secondary organic aerosols, which along with primary pollutants have a wide range of potential consequences for health, vegetation, ecosystems, visibility, radiation budget and atmospheric chemistry. The pollutants from the South Asian region have been seen to influence the atmospheric composition and radiation budget over the cleaner Indian Ocean [e.g. Lal *et al.*, 1998; Lelieveld *et al.*, 2001; Ramanathan *et al.*, 2001; Lawrence and Lelieveld, 2010] and pristine Himalayas [Hegde *et al.*, 2007; Kumar *et al.*, 2010; Marcq *et al.*, 2010; Decesari *et al.*, 2010]. Further, strong convection during summer/monsoon is also seen to transport South Asian pollutants to the Mediterranean Sea [e.g. Lawrence *et al.*, 2003; Park *et al.*, 2007]. Explicitly, South Asia is emerging as a significant source region for several key trace species but the implications of South Asian pollution on air quality and climate are not well understood.

Numerous efforts have been made since the early 1990s to conduct in situ measurements of both trace gases [e.g. *Lal et al.*, 2000; *Naja et al.*, 2004; *Beig et al.*, 2007; *Reddy et al.*, 2008] and aerosols [e.g. *Sagar et al.*, 2004; *Moorthy et al.*, 2005; *Niranjana et al.*, 2006; *Ramachandran and Rajesh*, 2007; *Satheesh et al.*, 2009] over the Indian region. Additionally, an international intensive field campaign called Indian Ocean Experiment (INDOEX) [*Ramanathan et al.*, 2001; *Lelieveld et al.*, 2001] was conducted to study the export of pollutants from South Asia to the surrounding pristine oceanic environments. Another field campaign called Integrated Campaign for Aerosols, gases and Radiation Budget (ICARB) [*Moorthy et al.*, 2008] was conducted to characterize the physico-chemical properties and radiative effects of trace gases and aerosols over the Indian subcontinent. However, these efforts focused largely on the measurements of basic trace gases (ozone, CO, NO_x, lighter non-methane hydrocarbons (NMHCs)) and measurements of other gases and radicals like hydroxyl radicals and peroxy radicals, other oxides of nitrogen and heavier NMHCs are nearly non-existent. Further, poor spatial coverage and lack of continuous measurements hinders sufficient understanding of spatio-temporal distribution of these species over India. The scarcity of measurements makes the application of chemical transport models and satellite observations essential for understanding the distribution of trace species and ozone photochemistry over this region.

Few studies have employed global and regional scale models over the South Asian region to simulate the spatio-temporal variabilities in ozone, CO, NO_x and aerosols over the Indian region. *Saraf et al.* [2003] employed Model of Ozone and Related Tracers-2 (MOZART-2) to analyze the observations of ozone and precursors made over the Indian Ocean during INDOEX in 1999. The MOZART-2 model has also been applied to study the distributions of boundary layer ozone and precursors over the Indo-Gangetic Plain region [*Beig and Ali*, 2006] and to assess the changes in tropospheric ozone and precursors over the Indian region due to changes in anthropogenic emissions between 1991 and 2001 [*Beig and Brasseur*, 2006]. The regional models used to simulate the spatial distributions of ozone and precursors over the Indian region include the HANK model [*Mittal et al.*, 2007], Multiple scale Atmospheric Transport and Chemistry modeling system (MATCH) [*Engardt*, 2008] and REMO-CTM [*Roy et al.*, 2008]. The MATCH model has also been used to examine the regional NO_x emission strength and influences of external emissions on ozone-related chemistry [*Kunhikrishnan et al.*, 2004, 2006]. All the regional models qualitatively reproduced the patterns of surface ozone with higher levels over the Indo-Gangetic Plain

region. In addition to simulations of trace gases, several studies have also simulated the spatial distribution of various aerosol components such as sulfate, organic matter, black carbon, dust, sea-salt and fly ash [Rasch *et al.*, 2001; Collins *et al.*, 2001, 2002; Reddy *et al.*, 2004; Minvielle *et al.*, 2004a, 2004b]. The regional distribution of different aerosol components and their contribution to the total concentration and AOD is similar. These models have also been validated against aerosol measurements from INDOEX and are seen to exhibit a tendency to underestimate the high-pollution episode [e.g. Reddy *et al.*, 2004]. However, all these studies offline models which may miss important information about short-term atmospheric processes due to inherent decoupling of meteorology and chemistry.

In light of above conditions, the present thesis is aimed at establishing the credibility of a newly developed next generation fully coupled “online” Weather Research and Forecasting Model with Chemistry (WRF-Chem) over the South Asian region and use the model to understand regional distribution and variability of wintertime tropospheric CO. The winter season is chosen because CO loading over this region is highest in this season and low level circulation is favourable for transport of pollutants from inland to the oceanic regions. The thesis is composed of six chapters including this introductory chapter. The configuration of the WRF-Chem model specific to this study is presented in **Chapter 2**. The physical and chemical parameterization, different emission inventories, initial and lateral boundary conditions used by the model are discussed in this chapter. The performance of the model is assessed using different statistical metrics. The meteorological fields predicted by the WRF-Chem model are evaluated against ground-based observations, satellite retrievals and the reanalysis fields in **Chapter 3**. The calculated statistical parameters are also compared with a set of benchmarks proposed by earlier studies to assess the adequacy of model simulated meteorology for the chemistry simulations. The chemical fields predicted by the WRF-Chem model are evaluated against ground-based observations, balloon-borne and satellite observations in **Chapter 4**. The initial results of surface ozone simulations are also presented. The budget of wintertime tropospheric CO is analyzed in **Chapter 5** by including eleven CO tracers into the WRF-Chem model. The budget analysis is presented for CO at the surface, in the planetary boundary layer, in the free troposphere, and different geographical regions of South Asia. The important findings from the work presented in this thesis are summarized in **Chapter 6** along with the future research plans in this area.

2. WRF-Chem Model Set-up

The “Weather Research and Forecasting model with Chemistry” (WRF-Chem) [Grell *et al.*, 2005] is a newly developed chemistry transport model capable of simulating the spatial and temporal distribution of trace gases and aerosols simultaneously with meteorology. The chemistry and meteorological components of the WRF-Chem model are fully consistent with each other as they use same transport scheme, same horizontal and vertical grids, same time steps and the same physics schemes for subgrid-scale transport [Grell *et al.*, 2005]. The online nature of the WRF-Chem model also allows for feedbacks between chemistry and meteorology. The meteorological component of this model, i.e. WRF has been used extensively to simulate the meteorological conditions associated with the extreme weather events over the Indian region [e.g. Deb *et al.*, 2008; Govindankutty *et al.*, 2008; Chang *et al.*, 2009; Routray *et al.*, 2010; Rajeevan *et al.*, 2010; Dutta and Prasad, 2010] but has not been used until now to simulate the atmospheric chemistry in the Indian region. Here, we have set-up the WRF-Chem model for the first time over the South Asian region and this chapter describes the configuration of the model specific to the present study.

2.1 The WRF-Chem Model Description

This study uses the version 3.1.1 of the fully compressible and non-hydrostatic Advanced Research WRF model (<http://www.mmm.ucar.edu/wrf/users/>) coupled with Chemistry (WRF-Chem; <http://ruc.fsl.noaa.gov/wrf/WG11>) developed jointly by NOAA, NCAR, DOE/PNNL and other research institutes. The model contains several dynamical cores and allows the user to select among a number of different physical parameterizations to represent the processes that cannot be resolved by the model. The dynamical cores include a fully mass- and scalar-conserving flux form mass coordinate system and availability of different physical parameterization allows the model to be applicable at different scales. The WRF model [Skamarock *et al.*, 2008] uses the terrain-following hydrostatic pressure as the vertical

coordinate and Arakawa-C grid for grid staggering. The model uses the Runge-Kutta second and third order time integration schemes and second to sixth order advection schemes in both the horizontal and vertical directions. A time-split small step scheme is used for an acoustic and gravity-wave model. The WRF-Chem model is composed mainly of three components as portrayed in Figure 2-1. These components are the (1) WRF Preprocessing System, (2) real data initialization and (3) the WRF solver (ARW or NMM) including the chemistry. These components are described in detail in the following subsections along with external datasets used as input.

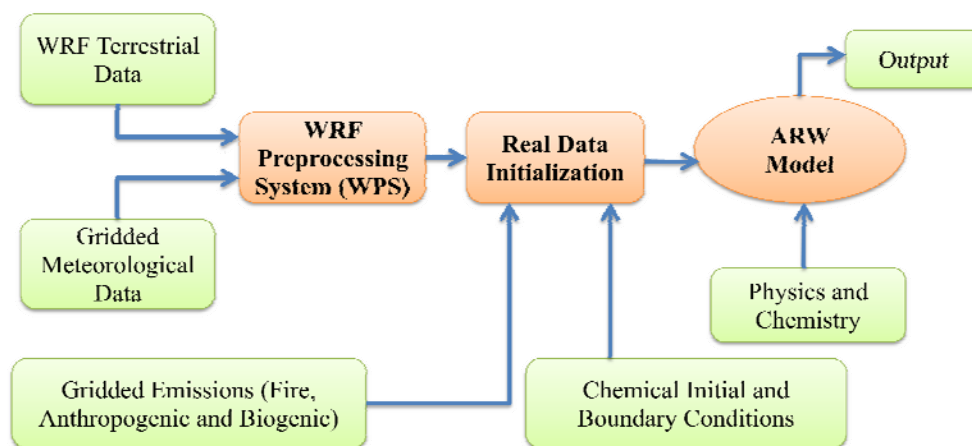


Figure 2-1: Major components and flow chart of the WRF-Chem Modeling System specific to this study. The light green boxes represent the external data to the model system while the light orange boxes represent the major components of the modeling system.

2.2 The WRF Preprocessing System (WPS)

The main objective of the WRF Preprocessing System (WPS) is to prepare input meteorological data for next step, i.e. for real data initialization program. WPS is composed of a set of three programs known as (1) geogrid, (2) ungrib and (3) metgrid. The geogrid program defines the model domain and interpolates the static terrestrial data to the model domain while the ungrib program extracts the meteorological data from the gridded binary (GRIB) format and writes the data into an intermediate format. The metgrid program combines the outputs from geogrid and ungrib programs, and horizontally interpolates intermediate format meteorological data onto the simulation domain. The data flow among three components of WPS is shown in Figure 2-2.

All WPS programs read parameters from a common “namelist.wps” file, which is composed of three separate sections specific to each of the WPS programs and a shared section

containing the parameters to be used by more than one WPS program. The information about the WRF model solver (ARW or NMM), total number of domains to be used in the simulation, the start and end time of the simulation for each domain, time resolution of input meteorological data and the input/output formats is declared under the shared section of namelist.wps. The parameters required for defining the simulation domain such as number of grid points in the west-east and north-south direction, spatial resolution, map projection, reference latitude and longitude for the domain and the location of static terrestrial data are defined under the geogrid section. In this study, the simulation domain is defined on a Mercator projection with center at 25° N, 80° E.

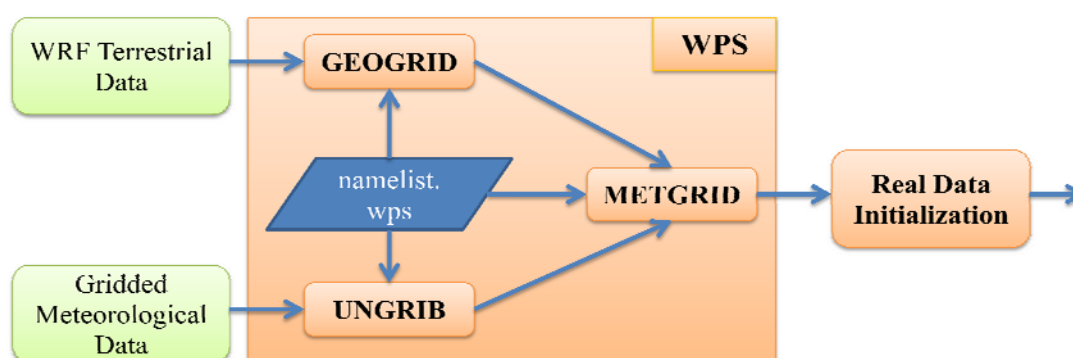


Figure 2-2: Major Components of the WPS are shown along with the data flow among these components.

The model domain and the interpolated terrain height used by the model are shown in Figure 2-3a. The domain covers nearly the entire South Asian region at 45 km spatial resolution with 90 grid points in both the west-east and north-south directions. The terrain height, land-use/vegetation, soil properties, vegetation fraction and albedo are interpolated from 10 min (approximately 19 km) USGS datasets to the model domain. After defining the simulation domain, the next step is to extract the meteorological fields embedded into gridded binary (GRIB) files using the ungrib program. The GRIB files generally represent the output of other regional/global models and contain more fields than required to initialize the WRF-Chem model. The ungrib program uses a predefined variables table called “Vtable” to extract the required variables from the GRIB files. For this study, the NCEP Final Analysis (FNL) data from Global Forecasting System (GFS) available at spatial resolution of 1° and temporal resolution of 6 hours (<http://dss.ucar.edu/datasets/ds083.2/data/>) has been used for initializing the meteorological fields in the model. The Vtable corresponding to this dataset has been

defined as Vtable.GFS, using which the ungrib program extracts temperature, winds, relative humidity, sea-level and surface pressure, soil properties and landscape features from the GRIB format FNL files.

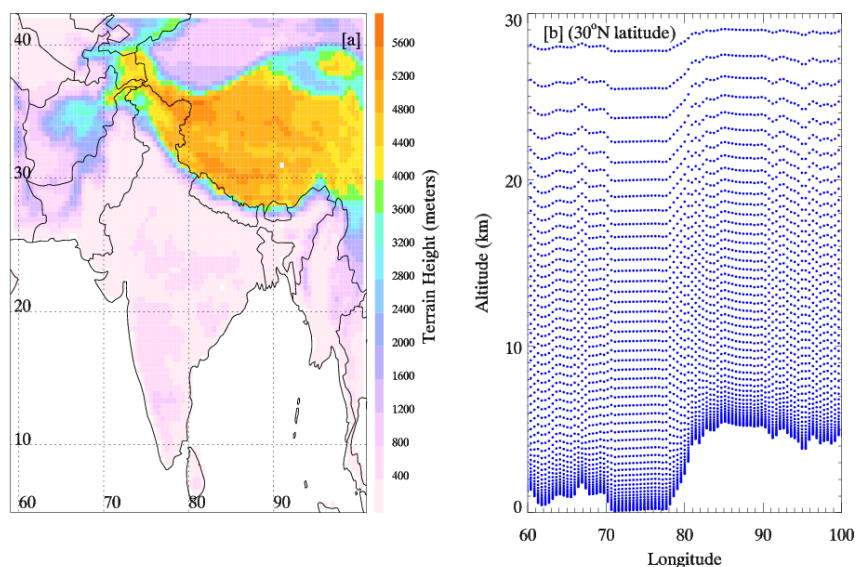


Figure 2-3: [a] Simulation domain and the topography used by the model. [b] Vertical grid structure of the model at 30° N latitude.

The final step of WPS is to combine the outputs from geogrid and ungrib programs through the metgrid program. The metgrid program horizontally interpolates the meteorological fields (extracted by ungrib) onto the simulation domain (defined by geogrid). The interpolated metgrid output is now ready for use by the real data initialization program. The real data initialization program of the WRF-Chem model can also be segregated into two parts. The first part deals with the initialization of the model with the meteorological fields and static terrestrial data available in the WPS output, while the second part deals with the preparation of emissions and initialization of models with the chemical fields.

2.3 Real Data Initialization - Meteorology

The real data initialization program reads meteorological and static terrestrial data from WPS output. During the initialization process, the real program computes a base state or reference profile for the geopotential and column pressure. The program calculates the perturbations from base state for geopotential and column pressure in the next step and initializes the meteorological variables u , v , potential temperature and water vapor mixing ratios. It should be noted that horizontal interpolation of meteorological fields is performed by WPS while vertical interpolation is performed by the real program. The real program defines a vertical

coordinate for the model to which the meteorological data is interpolated. The present model configuration uses a terrain-following hydrostatic pressure coordinate defined as

$$\eta = \frac{P_h - P_{ht}}{P_{hs} - P_{ht}} \quad (2-1)$$

where P_h is the hydrostatic component of the pressure at any given level in the atmosphere while P_{hs} and P_{ht} are the pressure values corresponding to the model surface and top boundaries respectively. The definition of this coordinate was proposed by *Laprise* [1992] and this coordinate has been used in many hydrostatic models. The η values vary from 1 at the surface to 0 at the upper boundary of the model domain. Here, the atmosphere has been divided into 51 vertical levels between the surface and 10 mb (approximately 30 km). The η values corresponding to these levels are 1.00000, 0.99381, 0.98643, 0.97786, 0.96815, 0.95731, 0.94538, 0.93122, 0.91490, 0.89653, 0.87621, 0.85405, 0.82911, 0.80160, 0.77175, 0.73981, 0.70509, 0.66798, 0.62889, 0.58823, 0.54957, 0.51281, 0.47788, 0.44471, 0.41323, 0.38336, 0.35503, 0.32819, 0.30276, 0.27869, 0.25592, 0.23439, 0.21405, 0.19484, 0.17672, 0.15963, 0.14352, 0.12836, 0.11410, 0.10070, 0.08811, 0.07630, 0.06523, 0.05487, 0.04517, 0.03611, 0.02765, 0.01977, 0.01243, 0.00560 and 0.00000 respectively. The vertical grid used by the model at 30° N latitude is shown in Figure 2-3b. The levels are designed in such a way that the model has 10 levels within the lowest 1 km layer. It is clear from Figure 2-3b that the vertical coordinate follows the terrain used by the model.

The real program also prepares soil fields for use in the model by vertically interpolating the soil properties to the levels required by the specified land-surface scheme and checking the consistency of soil categories with land use, land mask, soil temperature and sea surface temperature. Apart from generating the initial conditions, the real program also processes multiple time periods present in the WPS output to generate the lateral boundary conditions file. The lateral boundary condition file encompass the total column pressure along with three dimensional boundary data for u, v, potential temperature, water vapor mixing ratios and total geopotential.

2.4 Real Data Initialization – Emissions

After completion of the meteorological processing, the next step in the real data initialization program is to include the anthropogenic, biogenic and biomass burning emissions of chemical species into the model. The anthropogenic emissions of trace gases and aerosols for the Indian region are available from a number of global (e.g. RETRO, EDGAR3.2FT2000,

IIASA, GEIA and POET) and regional emission inventories (e.g. REAS, Indian Inventory and INTEX-B). However, the emissions from regional inventories are representative of more recent times [(REAS and Indian Inventory (year 2003); INTEX-B (year 2006))] as compared to global inventories (year 2000). Since anthropogenic emissions are increasing rapidly over this region [e.g. Ohara *et al.*, 2007; Zhang *et al.*, 2009], therefore latest anthropogenic emission estimates from INTEX-B emission inventory [Zhang *et al.*, 2009], which was developed to support the modeling activities for Intercontinental Chemical Transformation Experiment – Phase B (INTEX-B), are used here. The anthropogenic emission of four major species namely CO, NO_x, NMVOC and SO₂ from INTEX-B inventory are compared with those from two other regional inventories namely REAS [Ohara *et al.*, 2007] and Indian inventory [Dalvi *et al.*, 2006] in Table 2-1.

Table 2-1: Anthropogenic emissions (Gg per year) of CO, NO_x, NMVOC and SO₂ from REAS, INTEX-B and Indian emission inventories are shown. The emission estimates for NMVOC and SO₂ are not been available from Indian Inventory.

Species	REAS	INTEX-B	Indian Inventory
CO	84400	61106	71420
NO _x	4970	4861	4412
NMVOC	9680	10767	-
SO ₂	7020	5596	-

The CO emissions from INTEX-B are lower by about 20% and 14% as compared to REAS and Indian emission inventory respectively. NO_x and SO₂ emissions in INTEX-B inventory are also lower than REAS emissions by about 2% and 15% respectively. However, INTEX-B NO_x emissions are higher than Indian Inventory by about 11% and INTEX-B NMVOC emissions are higher than REAS inventory by about 11%.

Anthropogenic Emissions: Anthropogenic emissions of CO, NO_x, SO₂, NMVOC, PM10, PM2.5, BC and OC available from INTEX-B emission inventory does not cover the regions west of Pakistan in our simulation domain and the emissions for these regions are thus taken from Reanalysis of Tropospheric Chemical Composition (RETRO) (<http://retro.enes.org/>) database. At present, there is no single tool available in WRF-Chem model that can convert these emissions into a format compatible with the model framework if the model domain is

located outside North America. Since the present model domain is located over South Asia (Figure 2-3a), a new algorithm is developed to prepare the emissions for this domain. Further, a seasonal variation is applied to INTEX-B emissions because seasonality in anthropogenic emissions over Asian region has been shown to play an important role in air quality simulations [e.g. *Han et al.*, 2009].

Table 2-2: Seasonal variations of total anthropogenic emissions (Gg) of different gaseous and aerosol species over the simulation domain are shown.

	CO	NO _x	SO ₂	NH ₃	NM- VOC	PM 2.5	PM 10	SO ₄	NO ₃	OC	EC
Jan	9935	670	791	600	1692	390	491	16	8	132	48
Feb	8678	548	740	561	1183	365	459	15	8	123	45
Mar	8186	557	791	600	1160	390	491	16	8	132	48
Apr	6317	507	766	580	950	377	475	15	8	127	46
May	4850	478	791	600	817	390	491	16	8	132	48
Jun	3064	425	766	580	631	377	475	15	8	127	46
Jul	2013	406	791	600	540	390	491	16	8	132	48
Aug	3142	441	791	600	649	390	491	16	8	132	48
Sep	4700	474	766	580	793	377	475	15	8	127	46
Oct	6824	532	791	600	1025	390	491	16	8	132	48
Nov	8489	556	766	580	1177	377	475	15	8	127	46
Dec	10127	602	791	600	1345	390	491	16	8	132	48
Total	76326	6196	9343	7082	11962	4601	5794	185	95	1554	562

The seasonal variation in anthropogenic emissions is extracted from the RETRO inventory and is applied to the annual fluxes from INTEX-B emissions. The seasonal variations of the total emissions over the simulation domain are shown in Table 2-2. The anthropogenic emissions of CO, NO_x and NMVOC show a distinct seasonal cycle with highest values in winter and lowest values in summer/monsoon while those of other species do not show any significant seasonal variability. The spatial distributions of seasonal average anthropogenic CO emissions during winter (DJF), spring (MAM), summer (MAM) and autumn (SON) over model domain are shown in Figure 2-4.

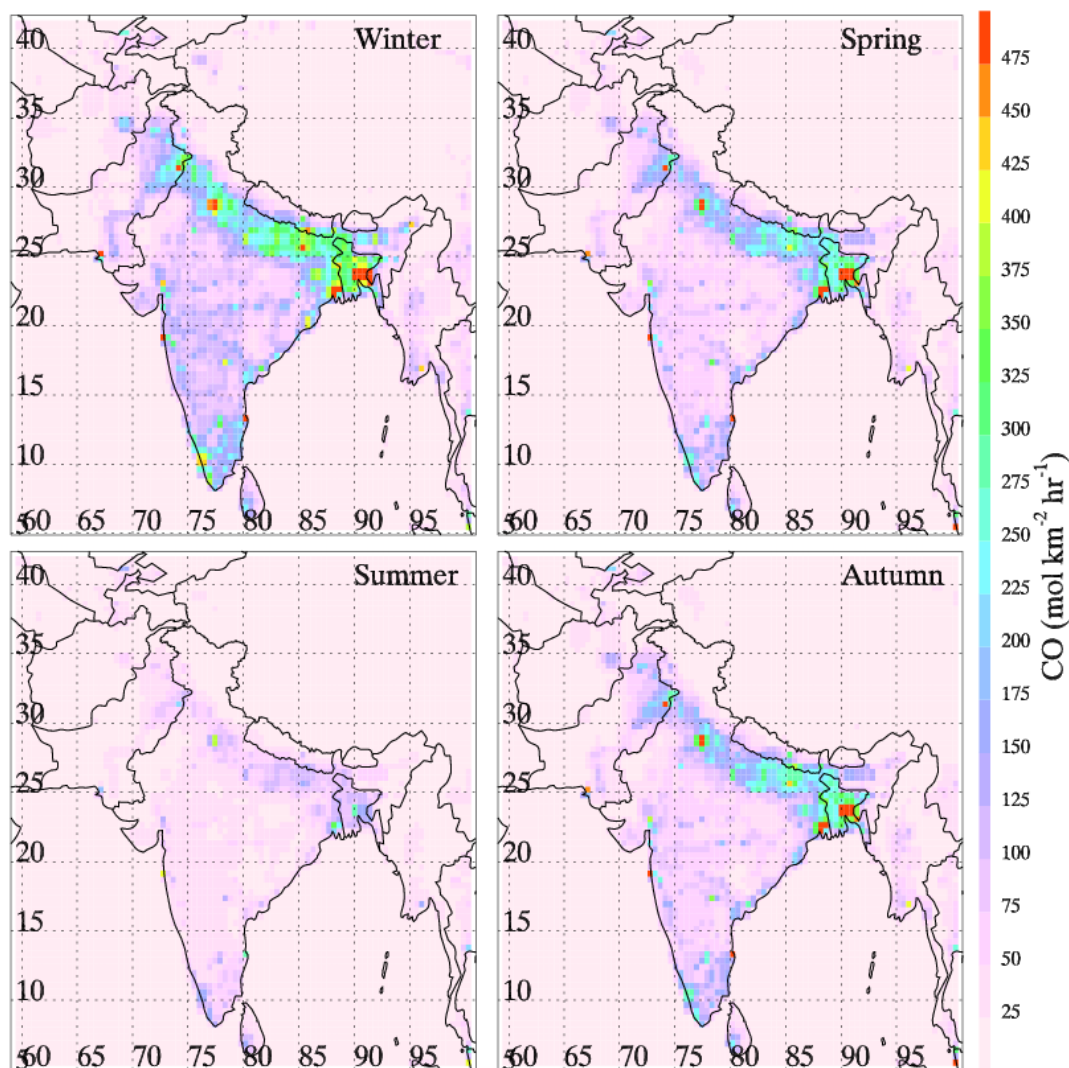


Figure 2-4: Anthropogenic CO emissions over the simulation domain during winter (DJF), spring (MAM), summer (JJA) and autumn (SON) seasons of the year 2008. The emissions are representative of the year 2006.

The spatial distribution of anthropogenic CO emissions is more or less similar to the spatial distribution of population density shown in Figure 2-5. This is expected because inventories generally distribute the emissions primarily by population. Both the population density and the anthropogenic CO emissions are higher, particularly over the Indo-Gangetic Plain (IGP) region in northern India, southern parts of India and Bangladesh. However, it is seen that NO_x emission distribution exhibits less spread as compared to the distributions of CO and NMVOC emissions. The total anthropogenic emission for each species are segregated into four sectors namely the domestic, industry, power and transport to understand the reasons for less spread in NO_x emissions. The percentage contribution of each sector to the total anthropogenic emissions is shown in Table 2-3. The domestic sources (mainly biofuel

burning in cooking stoves) are identified as the largest contributors to the CO (41%) and NMVOC (38%) emissions while NO_x emissions are dominated by the power (36%) and transport (34%) sectors. Larger contribution from domestic sources indicates that CO and NMVOC emission sources are distributed more evenly, particularly in the rural areas, as compared to NO_x emissions sources. The emissions of particulate matter over the simulation domain are also dominated by the domestic sources.

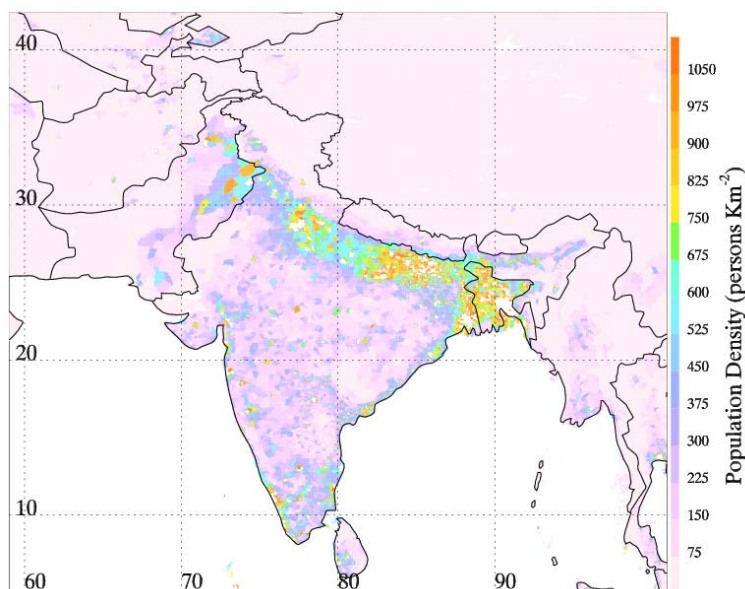


Figure 2-5: Spatial distribution of population density over the simulation domain.

Table 2-3: Annual total anthropogenic CO, NO_x, SO₂, NMVOC, BC, OC, PM_{2.5} and PM₁₀ emissions used by the model. The relative contributions from different source categories to the total emissions over the simulation domain are also shown. All the contributions are reported in percentage values rounded to the nearest integer.

Species	Total Annual Emissions (Gg)	Percentage Contribution from the Sector			
		Domestic	Industry	Power	Transport
CO	76326	41	30	1	28
NO _x	6196	6	24	36	34
SO ₂	9343	9	39	49	3
NMVOC	11962	38	27	2	33
BC	562	59	24	2	15
OC	1554	85	10	1	4
PM _{2.5}	4601	46	36	13	5
PM ₁₀	5794	38	42	16	4

Biogenic Emissions: The biogenic emissions of trace species are calculated online within the WRF-Chem model using the Model of Emissions of Gases and Aerosols from Nature (MEGAN) [Guenther *et al.*, 2006]. The biogenic emission of any trace species in MEGAN is calculated using the formula given as:

$$EM = \varepsilon * \gamma_{CE} * \gamma_{age} * \gamma_{SM} * \rho \quad (2-2)$$

where EM is the emission ($\mu\text{g m}^{-2} \text{hr}^{-1}$), ε is the emission factor ($\mu\text{g m}^{-2} \text{hr}^{-1}$), γ_{CE} is the canopy factor, γ_{age} is the leaf age factor, γ_{SM} is the soil moisture factor and ρ is the production and loss within the plant canopy. At present, the algorithm and data for γ_{SM} and ρ are not available for inclusion in the model and hence their values are taken as 1. The canopy factor is further calculated as:

$$\gamma_{CE} = \gamma_{LAI} * \gamma_P * \gamma_T \quad (2-3)$$

where γ_{LAI} is the leaf area index, γ_P is the light-dependent photosynthetic photon flux density (PPFD) emission activity factor and γ_T is the temperature response factor. The light-dependent PPFD factor is only applied to the fractions of emission factors based on biological function of plants. The isoprene emissions are calculated using spatial maps of isoprene emission factors while emission factors for other species are assigned according to the plant function types. The information about the spatial distributions of isoprene emission factors, plant function type leaf area index, surface temperature and solar flux needs to be preprocessed before the simulation and this preprocessing is performed through the preprocessor available from <http://www.acd.ucar.edu/wrf-chem/>.

Biomass Burning Emissions: The emissions of trace gases and aerosols from biomass burning are calculated daily using the Fire Inventory from NCAR (FINN version 1) [Wiedinmyer *et al.*, 2006, 2011]. In this methodology, the emission of any trace species is calculated using a simple bottom-up approach with the following equation:

$$E_i = A * B * CE * e_i \quad (2-4)$$

where A is the area burned, B is the fuel loading (total biomass per unit area), CE is the combustion efficiency and e_i is the emission factor for species i . The values of B and e_i are dependent on land cover classification while those of CE depend upon the tree cover. Fire locations over the simulation domain are identified using MODIS Terra and Aqua derived Fire and Thermal Anomalies Product [Giglio *et al.*, 2006]. The fuel loadings for the pixels showing fire activity are determined from Global land cover Dataset for 2000 [Latifovic *et al.*, 2003] that describe the land use, vegetation types and percentage vegetative covers. The

MODIS Vegetation Continuous Fields product [*Hansen et al.*, 2003], which provides information about the distribution of surface vegetation and identifies tree, herbaceous and bare cover at the spatial resolution of 500 m, is overlaid on GLC2000 land cover characterization map to better define the fuel loadings and vegetation distribution assigned to the identified fire pixels. The combustion efficiency for the herbaceous and woody fuels for each pixel is estimated using the methodology described by *Ito and Penner* [2004].

Table 2-4: Seasonal variations of total biomass burning emissions (Gg/month) of different gaseous and aerosol species over the simulation domain are shown.

Month	CO	NO _x	SO ₂	NH ₃	NMVOC	PM2.5	OC	EC
January	490	15	4	8	22	10	7	4
February	1753	45	13	26	83	36	27	13
March	8364	188	57	115	410	170	129	65
April	13079	269	81	175	664	269	205	104
May	1223	33	8	20	63	25	19	9
June	57	2	0	1	3	2	1	0
July	37	1	0	1	2	2	1	0
August	60	2	1	1	3	2	1	0
September	69	2	1	1	3	2	1	1
October	515	18	3	11	30	11	7	4
November	562	19	4	11	33	12	8	4
December	228	7	2	4	11	5	3	2
Annual Total	26438	600	174	373	1326	546	409	207

The emission factors for different land cover classifications are taken from the published literature [see *Wiedinmyer et al.*, 2006 for more details]. The seasonal variations of total biomass burning emissions estimated using this approach over the simulation domain is shown in Table 2-4. Biomass burning contributes very little to the emissions of PM₁₀, SO₄ and NO₃ and hence these species are not shown in the Table 2-4. Unlike anthropogenic emissions, the biomass burning emissions over the simulation domain show highest values in spring. However, fire emissions are also lowest during summer.

The initial and boundary conditions for chemical fields in WRF-Chem are obtained from the

Model of Ozone and Related Tracers-version 4 (MOZART-4) results [Emmons *et al.*, 2010]. The MOZART-4 results are interpolated in space using the “mozbc” program available from <http://www.acd.ucar.edu/wrf-chem/>. The mozbc program does not perform any time interpolation and since MOZART-4 results are available at a time resolution of 6 hours, therefore chemical boundary conditions in WRF-Chem are also updated every 6 hours.

2.5 Model Physics

This section describes different physics options used here for parameterization of microphysical, convection, planetary boundary layer, land-surface and radiative processes. The four dimensional data assimilation (FDDA) method, which applies extra forcing to the model equations and is internally treated similar to physics, is also described in this section.

Microphysics: The WRF-Chem model encompasses a variety of single and double moment schemes to explicitly resolve water vapor, clouds and precipitation processes. The single moment schemes predict only the number concentrations of prognostic species of water (e.g. cloud, ice, rain, snow, graupel and hail) while double moment schemes also predict mixing ratios of these variables along with the number concentrations. The prediction of both number concentrations and mixing ratios allows for a more robust treatment of the particle size distributions, which are very important for calculating the microphysical process rates and cloud/precipitation evolution. Therefore, the double moment microphysical parameterization described by *Thompson et al.* [2004] has been used here. As compared to single-moment schemes available in WRF-Chem, this microphysical scheme incorporates a large number of improvements to physical processes. The assumed snow size distribution in this scheme depends upon both ice water content and temperature and is represented as a sum of exponential and gamma distributions. Further, this scheme assumes a non-spherical shape for snow in contrast to other schemes which assume spherical snow with constant density. More details of the scheme and its advantages over other schemes can be found elsewhere [Skamarock *et al.*, 2008].

Cumulus Parameterization: The spatial resolution of 45 km constrains the model to use parameterization for subgrid scale effects of convective and/or shallow clouds. The cumulus parameterization schemes are intended to represent the vertical fluxes due to unresolved updrafts and downdrafts and compensating motion outside the clouds. These schemes operate only on the individual columns where the scheme is triggered and provide vertical heating

and moistening profiles. The Kain-Fritsch cumulus parameterization scheme [Kain, 2004] that utilizes a simple cloud model with moist updrafts and downdrafts including the effects of detrainment, entrainment and relatively simple microphysics has been used here. This scheme is seen to perform better as compared to another scheme (Grell-Devenyi scheme) available in WRF-Chem for the present model domain.

Atmospheric Radiation: The radiation scheme provide atmospheric heating due to radiative flux divergence and surface downward longwave and shortwave radiation for the ground heat budget. Longwave radiation includes infrared or thermal radiation absorbed and emitted by gases and surfaces. Upward longwave radiative flux from the ground is determined by surface emissivity that in turn depends upon land-use types as well as the ground (skin) temperature. Shortwave radiation includes visible and surrounding wavelengths that make up the solar spectrum. The main physical processes included in this scheme are the absorption, reflection and scattering in the atmosphere and at the surface. For shortwave radiation, the upward flux is the reflection due to surface albedo. Within the atmosphere, the radiation responds to model-predicted cloud and water vapor distributions, as well as specified carbon dioxide, ozone and optionally the trace gas concentrations. The long wave radiation in the present model set-up is simulated using the rapid radiative transfer model (RRTM) [Mlawer *et al.*, 1997]. RRTM is a spectral-band scheme that uses correlated-k method and pre-set tables to accurately represent longwave processes due to water vapor, ozone, CO₂ and trace gases and also accounts for the cloud optical depth. The RRTM scheme is well tested and has also been used in the MM5 model. The shortwave radiation processes are simulated using the Goddard shortwave scheme [Chou and Suarez, 1994]. The Goddard shortwave scheme has a total of 11 spectral bands and considers diffuse and direct solar radiation components in two-stream approach that accounts for the scattered and reflected components. Ozone is considered with several climatological profiles available.

The Surface Layer Scheme: The surface layer schemes provides friction velocities and exchange coefficients that enable the calculation of surface heat and moisture fluxes in the land-surface models and surface stress in the planetary boundary layer scheme. The surface fluxes and the surface diagnostic fields over the water surfaces are computed in the surface layer scheme itself. The Eta surface layer scheme [Janjic, 1996, 2002], which is based on similarity theory [Monin and Obukhov, 1954] and includes parameterization of viscous sub-layer following Janjic [1994], has been used here. The effects of the viscous sub-layer over

land are taken into account through the variable roughness height for temperature and humidity as proposed by *Zilitinkevich* [1995]. Further, the correction proposed by *Beljaars* [1994] is applied to avoid the singularities in the case of an unstable surface layer and vanishing wind speed. The surface fluxes are computed by an iterative method. In the present WRF-Chem model configuration, every surface layer scheme is tied to a specific PBL scheme. The scheme used here is tied to Eta Mellor-Yamada-Janjic (MYJ) PBL scheme and is therefore referred to as MYJ surface scheme.

Land-Surface Model: The land-surface models use the atmospheric information from the surface layer scheme, radiative forcing from the radiation scheme and precipitation forcing from the microphysics and convective schemes, together with internal information on the land's state variables and land-surface properties to provide the heat and moisture fluxes over land points and sea-points. These fluxes provide a lower boundary condition for the vertical transport done in the PBL schemes. The Noah land-surface model, developed jointly by NCAR and NCEP, has been used in the model set-up for this study. This model has the benefit of being consistent with the time-dependent soil fields provided in the analysis datasets. This is a 4-layer soil temperature and moisture model with canopy moisture and snow cover prediction. The layer thicknesses are 10, 30, 60 and 100 cm (adding to 2 meters) from the top down. It includes root zone, evapo-transpiration, soil drainage and runoff, taking into account the vegetation categories, monthly vegetation categories and soil texture. The scheme provides sensible and latent heat fluxes to the boundary-layer scheme described below.

Planetary Boundary Layer Scheme: The planetary boundary layer (PBL) scheme is responsible for the vertical subgrid scale fluxes due to eddy transport in the whole atmospheric column and not just the boundary layer. Therefore, the explicit vertical diffusion process in the model is deactivated immediately after the activation of PBL scheme and the PBL scheme is assumed to handle this process. The surface fluxes are provided by the surface layer and land-surface schemes discussed above. The PBL schemes determine the flux profiles within the well-mixed boundary layer and the stable layer and thus provide the atmospheric tendencies of temperature, moisture (including clouds) and horizontal momentum in the entire atmospheric column. Here, the Mellor-Yamada-Janjic (MYJ) scheme is used for the parameterization of the turbulence in the PBL and free atmosphere [*Janjic, 2002*]. The parameterization represents a nonsingular implementation of the Mellor-Yamada

Level 2.5 turbulence closure model [Mellor and Yamada, 1982] through the full range of atmospheric turbulent regimes. In this implementation, an upper limit is imposed on the master length scale. This upper limit depends on the turbulent kinetic energy (TKE) as well as the buoyancy and shear of the driving flow. In the unstable range, the upper limit is derived from the requirement that the TKE production be nonsingular in case of growing turbulence. In the stable range, the upper limit is derived from the requirement that the ratio of variance of the vertical velocity deviation and TKE cannot be smaller than that corresponding to the regime of vanishing turbulence. The TKE production/dissipation differential equation is solved iteratively.

Four Dimensional Data Assimilation (FDDA): The four dimensional data assimilation (FDDA), also known as nudging, is a method of keeping the simulations close to the analyses and/or the observations over the course of integration. The WRF-Chem model offers two types of FDDA namely the analysis nudging and the observation nudging. The analysis nudging (also called grid nudging) forces the model simulations towards a series of analyses grid-point by grid-point while the observation nudging (also called station nudging) locally forces the simulation towards the observational data. In the present study, analysis nudging has been applied to the model simulations. In analysis nudging, the model is nudged towards spatially and temporally interpolated analyses using a point by point relaxation terms. The analysis nudging was developed originally by *Stauffer and Seaman* [1999] and has several major advantages. Firstly, the model can be run with grid-nudging for long periods (e.g. for months) to provide a four dimensional meteorologically self-consistent dataset that also stays on track with the driving analyses. Such datasets are very much useful for atmospheric chemistry simulations where the errors in the wind fields can lead to erroneous transport of chemical species. Secondly, a nested simulation run with the outer domain nudged towards analysis and the nest running un-nudged provides better temporal details at the nest boundary than driving it directly from linearly interpolated analysis. Thirdly, analysis nudging can be used for dynamic initialization of the model and can reduce the spin-up period of the model. In this study, the temperature, moisture and winds are nudged with a nudging coefficient of $6 \times 10^{-4} \text{ s}^{-1}$ and nudging has been kept active throughout the duration of simulation. The nudging coefficient has been selected on the basis of a set of sensitivity runs.

2.6 Model Chemistry

Gas-Phase Chemistry: The Regional Atmospheric Chemical Mechanism (RACM)

developed by *Stockwell et al.* [1997] has been used here to simulate the gas-phase chemistry. This mechanism is designed to represent the tropospheric chemistry of different chemical environments ranging from remote to polluted regions. The mechanism includes 17 stable inorganic species, 4 inorganic intermediates, 32 stable organic species with 4 of them being of biogenic origin and 24 organic intermediates participating in 237 reactions. Reactive organic species in RACM are grouped according to *Middleton et al.* [1990] and *Stockwell et al.* [1990]. The isoprene mechanism in RACM includes a good representation of methacrolein, isoprene ozonolysis, hydroperoxide production and production of carbonitrates from the reaction of isoprene with NO_3 . The RACM mechanism also includes a mechanism for the oxidation of α -pinene and d-limonene.

Dry Deposition: The spatially and temporally varying deposition velocities for trace gases and aerosols in WRF-Chem are estimated using surface resistance parameterization developed by *Wesley* [1989]. In this parameterization, the surface resistance is proportional to sum of three characteristic resistances including the aerodynamic, sub-layer and surface resistances and is determined from the resistances of soil and plant surfaces in the model. The properties of the plants are determined using land-use data and the season. In addition to land-use types, the surface resistance also depends on the diffusion coefficient, the reactivity and water solubility of the trace gases. The deposition velocities calculated in this way are then multiplied with the concentrations of the trace gases in the lowest model layer to estimate the flux of trace species from the atmosphere to the surface. In the simulations which do not calculate aerosols explicitly, the sulfate is assumed to be present in the form of aerosol particles and its deposition is described according to *Erisman et al.* [1994]. In the simulations employing the aerosol parameterizations, the deposition velocity (\hat{v}_{dk}) for the k^{th} moment of a polydisperse aerosol is given by:

$$\hat{v}_{dk} = (r_a + \hat{r}_{dk} + r_a \hat{r}_{dk} \hat{v}_{Gk})^{-1} + \hat{v}_{Gk} \quad (2-5)$$

where r_a is the surface resistance, \hat{v}_{Gk} is the polydisperse settling velocity and \hat{r}_{dk} is the Brownian diffusivity [*Slinn and Slinn*, 1980; *Pleim et al.*, 1984].

Aerosol Parameterization: The aerosol module is based on the Modal Aerosol Dynamics for Europe (MADE) [*Ackermann et al.*, 1998] derived from the Regional Particulate Model [*Binkowski and Shankar*, 1995]. The secondary organic aerosols (SOA) have been incorporated into MADE by *Schell et al.* [2001] by means of Secondary Organic Aerosol

Model (SORGAM). The size distribution of the submicron-meter aerosols is represented by two overlapping modes, both of which assume a log-normal distribution given by:

$$n(\ln d_p) = \frac{N}{\sqrt{2\pi} \ln \sigma_g} \exp \left[-\frac{1}{2} \frac{(\ln d_p - \ln d_{pg})^2}{\ln^2 \sigma_g} \right] \quad (2-6)$$

Where N is the number concentration (m^{-3}), d_p is the particle diameter, d_{pg} is the median diameter and σ_g is the standard deviation of the distribution. The k^{th} moment of the distribution is defined as:

$$M_k = \int_{-\infty}^{\infty} d_p^k n(\ln d_p) d(\ln d_p) \quad (2-7)$$

The solution of the above integral is:

$$M_k = N d_{pg}^k \exp \left[\frac{k^2}{2} \ln^2 \sigma_g \right] \quad (2-8)$$

M_0 is the total number of aerosol particles within the mode suspended in a unit volume of air. M_2 and M_3 are proportional to the total particulate surface area and total particulate volume within the mode suspended in a unit volume of air, respectively.

Aerosol Growth Process: The aerosol growth and secondary organic aerosol formation in the WRF-Chem model are described by the processes of nucleation, condensation and coagulation. The homogeneous nucleation in the sulfuric acid-water system is calculated by the method given by *Kulmala et al.* [1998]. The growth of aerosols by condensation occurs through the production of condensable material by the reaction of chemical precursors and the condensation/evaporation of ambient volatile species on aerosols. The Kelvin effect is neglected in MADE and allows the calculation of time rate of change of a moment M_k for the continuum and free-molecular regime. The mathematical expressions of the rates and their derivation can be seen in *Binkowski and Shankar* [1995]. The coagulation process in the model considers only the effects caused by Brownian motion and the aerosol distribution remains log-normal. The mathematical formulation of the coagulation process can be seen in *Whitby et al.* [1991] and *Binkowski and Shankar* [1995]. The changes in moments due to coagulation are modified according to *Whitby et al.* [1991]. *Whitby et al.* [1991] suggested that the collision of particles within a mode result in the formation of a particle within that mode while MADE allows a particle resulting from two particles colliding within the Aitken mode to be assigned to the accumulation mode. In the MADE, the diameter (d_{eq}) at which the

two modes have equal number concentrations are calculated. If one of the colliding particles has a diameter greater than d_{eq} , the resulting particle is assigned to the accumulation mode.

Aerosol Chemistry: The WRF-Chem model uses inorganic chemistry to calculate the chemical composition of a sulphate-nitrate-ammonium-water aerosol according to the equilibrium thermodynamics. The inorganic chemistry is based on MARS [Saxena *et al.*, 1986] and its modifications by Binkowski and Shankar [1995]. The model considers two regimes depending upon the molar ratio of ammonium and sulphate. The model solves a cubic polynomial for hydrogen ion molality for molar ratios less than 2 and calculates the dissolved nitrate if ammonium and liquid water are present in sufficient amount. Nitrate is not assumed to be present for modal ionic strengths greater than 50. All the sulphate is assumed to be ammonium sulphate and a calculation is made for the presence of water for molar ratios greater than or equal to 2. The organic aerosol chemistry is based on SORGAM [Schell *et al.*, 2001], which assumes that SOA compounds interact and forms a quasi-ideal solution. The partitioning of SOA compounds between the gas and particle phases is parameterized according to Odum *et al.* [1996]. All the activity coefficients are assumed to be unity due to lack of information. The anthropogenic and biogenic emissions in SORGAM are treated separately, which makes it usable with the gas-phase chemical mechanism RACM that provides biogenic precursors.

Photolysis Frequencies: The gas-phase chemical mechanism (RACM) used here encompass 23 photolysis reactions and photolysis frequencies for these reactions are calculated at each grid point using the Fast-J photolysis scheme [Wild *et al.*, 2000]. This scheme has an online treatment of molecular and aerosol absorption and scattering. The online computation of photolysis frequencies in WRF-Chem model has several advantages over the offline techniques. The absorption cross sections of ozone are temperature dependent and thus can be updated at each time step during the simulation. The hygroscopic growth of the aerosols can be taken into account using the simultaneous simulations of water vapor mixing ratios. This is important because aerosols have a strong effect on the photolysis frequency of NO_2 [Ruggaber *et al.*, 1994]. Further, the parameterization of cloud droplets as a function of sulfate content [Jones *et al.*, 1994] can be included in the model.

3. WRF-Chem: Meteorology Evaluation

The previous chapter described the set-up of the Weather Research and Forecasting model with Chemistry (WRF-Chem) including the description of the simulation domain, meteorological and emission datasets, meteorological and chemical initial and boundary conditions datasets, and the parameterization of physical and chemical processes. Twelve 1-month simulations are conducted for January to December 2008 and the model is reinitialized at 00 UTC on the first date of every month. The time-step of the model simulation is taken as 180 seconds (4 x grid spacing) to ensure that the model does not violate the Courant-Friedrichs-Levy (CFL) stability criterion [*Courant et al.*, 1928]. The radiation physics modules are called every 540 seconds while the modules for boundary layer and cumulus physics are called every time step. The instantaneous model results are output every hour. This chapter presents the evaluation and quantification of errors and biases in WRF-Chem simulated meteorological fields over the course of all seasons and impact of meteorological errors on chemistry simulations with focus on tropospheric ozone. The meteorological fields simulated by the WRF-Chem model are evaluated against a set of balloon-borne and space-borne observations and reanalysis datasets.

Ground-based observations are amongst the most accurate and reliable dataset for evaluating the model performance in regard to atmospheric chemistry but these measurements have limited geographical and altitude coverage over the Indian region and are highly sparse over the remote oceanic and mountainous regions. This spatial heterogeneity in the availability of in situ observations might lead to a sampling bias in the model evaluation. The gap in spatial heterogeneity can be minimized to a large extent by the use of satellite observations and reanalysis datasets. The satellites provide daily global three dimensional observations of the atmospheric state while the reanalysis datasets are generated by the quality controlled assimilation of observations from different platforms such as from land, ship, aircraft,

radiosonde and pibal (pilot balloon) etc. This study uses temperature and dew point temperature from radiosonde observations, temperature, water vapor and tropopause pressure retrieved by the Atmospheric Infrared Sounder (AIRS), daily total precipitation amounts from the Tropical Rainfall Measuring Mission (TRMM), as well as NCEP/NCAR reanalysis zonal and meridional wind components for the evaluation of WRF-Chem meteorological fields. The chapter begins with a description of different observational datasets, the reanalysis fields and the evaluation methodology used in this study. The evaluation and sensitivity results are described thereafter.

3.1 Datasets and Evaluation Methodology

3.1.1 Radiosonde Observations

The radiosonde observations (RAOB) of temperature and dew point temperature at 12 mandatory pressure levels (1000 hPa, 925 hPa, 850 hPa, 700 hPa, 600 hPa, 500 hPa, 400 hPa, 300 hPa, 250 hPa, 200 hPa, 150 hPa and 100 hPa) for 34 stations located in the Indian region are used for the evaluation. Table 3-1 provides the details of all the RAOB stations used in this study and the geographical locations of these stations are shown in Figure 3-1.

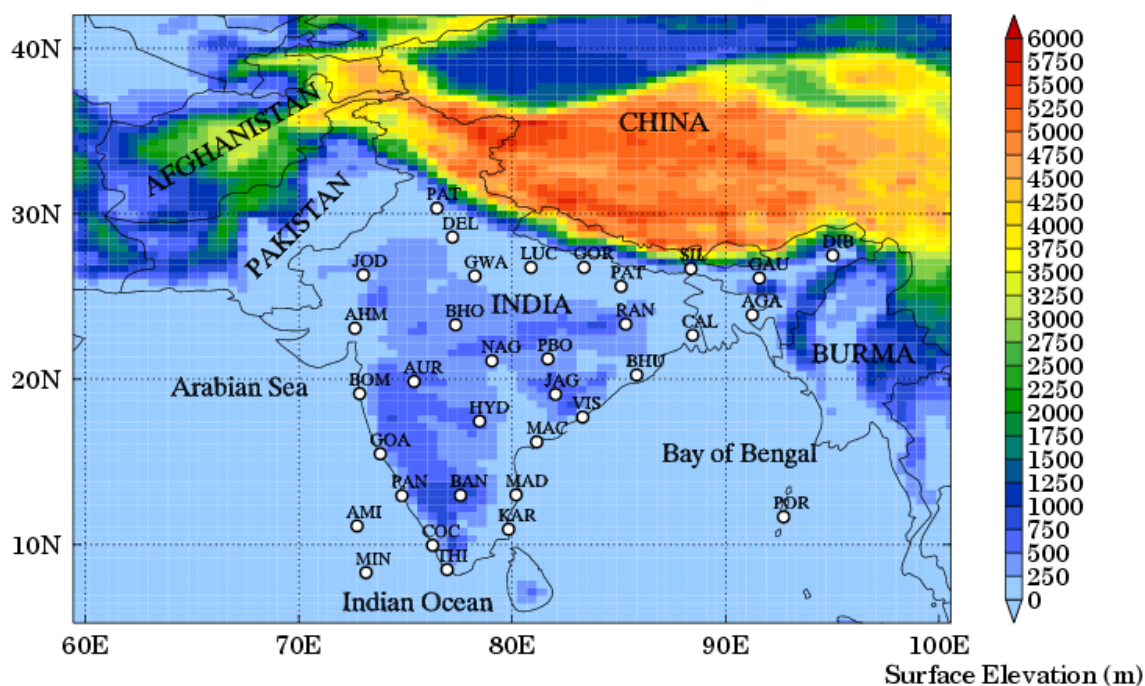


Figure 3-1: The simulation domain and the topography used by the model. The geographic locations of RAOB sites used in this study are also shown. The description of station codes is provided in Table 3-1.

These observations are generally carried out around 00 and 12 GMT each day and are quality checked for the climatological limits as described by *Schwartz and Govett* [1992] prior to their archival. Several studies have used the RAOB datasets for validating satellite retrievals [e.g. *Remsberg et al.*, 1992; *Divakarla et al.*, 2006].

Table 3-1: Details and the categorization of the RAOB sites used in this study.

Station Name	Station Code	Longitude (°E)	Latitude (°N)	Actual Altitude ^a	Model Altitude ^a	Category
Bhubaneswar	BHU	85.83	20.25	46	47	
Bombay	BOM	72.85	19.12	14	42	
Machilipatnam	MAC	81.15	16.20	3	3	
Goa/Panjim	GOA	73.82	15.48	60	120	
Madras	MAD	80.18	13.00	16	22	Coastal Sites
Panambur	PAN	74.83	12.95	31	45	
Vishakhapatnam	VIS	83.30	17.70	66	54	
Thiruvananthapuram	THI	76.95	8.48	64	100	
Karaikal	KAR	79.83	10.92	7	3	
Cochin	COC	76.27	9.95	3	15	
Port-Blair	POR	92.72	11.67	79	8	
Minicoy-Island	MIN	73.15	8.30	2	0	Island Sites
Amini-Divi	AMI	72.73	11.12	4	0	
Patiala	PAT	76.47	30.33	251	245	
Delhi	DEL	77.20	28.58	216	213	
Dibrugarh	DIB	95.02	27.48	111	57	
Jodhpur	JOD	73.02	26.30	224	225	
Gwalior	GWA	78.25	26.23	207	191	
Lucknow	LUC	80.88	26.75	128	123	
Gorakhpur	GOR	83.37	26.75	77	64	Low Altitude Sites
Siliguri	SIL	88.37	26.67	123	224	
Gauhati	GAU	91.58	26.10	54	298	
Patna	PAT	85.10	25.60	60	45	
Ahmedabad	AHM	72.63	23.07	55	54	
Raipur	RAI	81.67	21.22	298	283	
Nagpur	NAG	79.05	21.10	310	322	
Agartala	AGA	91.25	23.88	16	25	
Calcutta	CAL	88.45	22.65	6	6	
Aurangabad	AUR	75.40	19.85	579	559	
Bhopal	BHO	77.35	23.28	523	467	Moderately High
Ranchi	RAN	85.32	23.32	652	502	
Jagdapur	JAG	82.03	19.08	553	564	Altitude Sites
Hyderabad	HYD	78.47	17.45	545	537	
Bangalore	BAN	77.58	12.97	921	853	

^aThe altitude values are in meters above mean sea level (amsl)

Here, the RAOB sites over the Indian region are classified into four categories namely coastal, island, low altitude and moderately high altitude sites depending upon the surrounding landscape and the altitude. The sites located along the eastern and western coasts of India are classified as “coastal sites” while those located on the islands are termed as “island sites”. All other sites having altitudes between 0-500 m and 500-1000 m are classified as “low altitude” and “moderately high altitude” sites, respectively.

3.1.2 Satellite-borne Observations

We use data products from the Atmospheric Infrared Sounder (AIRS) aboard the Aqua satellite and Tropical Rainfall Measuring Mission (TRMM) for model evaluation. AIRS is a high resolution infrared spectrometer accompanied by the Advanced Microwave Sounding Unit (AMSU) and Humidity Sounder for Brazil (HSB) [Aumann *et al.*, 2003]. AIRS has a field of view of 1.1° and measures the Earth’s radiance in 3.74-15.4 μm wavelength range. The horizontal resolution is ~ 45 km and the vertical resolution in the troposphere is ~ 1 km for temperature and ~ 2 km for water vapor. The AIRS temperature and water vapor retrievals have been successfully validated against a variety of in situ and aircraft observations [e.g. Gettelman *et al.*, 2004; Divakarla *et al.*, 2006]. These validation studies show that the accuracy of AIRS retrievals is about 1 K in 1 km layers for temperature and is better than 15% in 2 km layers for water vapor. All the AIRS datasets used in this study are version-5 Level-2 standard products.

The Tropical Rainfall Monitoring Mission (TRMM) is a multi-sensor instrument, which uses the space-borne observations to adjust the geosynchronous infrared satellite data and provide the gridded precipitation amounts at a range of spatial and temporal resolutions [Adler *et al.*, 2000]. We use daily total precipitation amount at spatial resolution of $0.25^\circ \times 0.25^\circ$ corresponding to 3B42 algorithm of the TRMM. The 3B42 algorithm produces the infrared calibration parameters from the measured radiances, which are then used to adjust the merged-infrared precipitation data (<http://trmm.jpl.nasa.gov>). The TRMM 3B42 precipitation data products are shown to accurately reproduce the climatology and rainfall variability over the Indian region [Nair *et al.*, 2009] and have been used previously for the evaluation of WRF simulated rainfall over this region [e.g. Rakesh *et al.*, 2009].

3.1.3 Reanalysis Dataset

The NCEP/NCAR reanalysis datasets generated by the assimilation of quality controlled ground-based, ship-based, air-borne and space-borne meteorological observations into a state-of-the-art global data assimilation system [Kalnay *et al.*, 1996; Kistler *et al.*, 2001] are also used here for the model evaluation. These datasets have been widely used by the atmospheric research community for providing input to several regional and global models, transport models and for understanding various research problems of scientific interest [e.g. Rao *et al.*, 1998; Hashiguchi *et al.*, 2006]. In this study, we have used the NCEP/NCAR reanalysis U and V wind components for evaluating the WRF simulated wind components. These NCEP/NCAR wind components are available 4 times (00, 06, 12 and 18 GMT) daily at the spatial resolution of 2.5° and at 17 pressure levels between 1000 and 10 hPa.

3.1.4 Evaluation Methodology

The model predicted value is matched with the observed fields (RAOB/satellite retrieval/reanalysis data location) in space and time and paired values are stored for further analysis. The spatial matching between the model and observations is achieved in two steps. First, the grid index (i, j) corresponding to the geographical location of the observation site is determined. In the second step, the model value at the estimated grid index (i, j) is calculated from the surrounding four model grid points by bi-linear interpolation. The temporal matching is obtained by averaging the WRF-Chem output over the hours enclosing the time of observation. To assure the quality of RAOB datasets, all the observations in the monthly datasets outside the range of $2 \cdot \sigma$ (standard deviation) around the mean are excluded from the further analysis.

The best quality AIRS retrievals are obtained for the model evaluation by selecting clear sky AIRS temperature and water vapor retrievals corresponding to highest quality assurance flags as suggested by AIRS science team. The quality assurance flags also allow discrimination of erroneous retrievals above a certain height and thus total number of samples accepted at different pressure levels is not the same. We select for clear sky retrievals only, and hence the total number of samples accepted at any pressure level in summer is even smaller (30-90%) than those in any other season because of the frequent occurrence of cloudy conditions in summer over the South Asian region. The water vapor profiles for which the estimated error in the retrieved value is either negative or greater than 50% of the retrieved value are also rejected. Complete description of these quality assurance flags are provided in Olsen *et al.*

[2007]. The temperature and water vapor profiles in AIRS retrievals are reported as layer average quantities. Hence, layer average WRF-Chem profiles are also calculated by averaging all the model data lying between any two consecutive AIRS pressure levels.

3.1.5 Statistical Metrics

This section defines different statistical metrics used for evaluating the model performance and quantifying the errors in model simulated meteorological variables. These include the mean bias (MB), coefficient of determination (r^2), root mean square error (RMSE), the systematic and unsystematic root mean square errors (RMSE_s and RMSE_u) and the index of agreement (d) [Willmott, 1981]. The mean bias provides the information on the overestimation/underestimation of any variable by the model and is defined as:

$$MB = \frac{1}{N} \sum_{i=0}^N (O_i - M_i) \quad (3-1)$$

In equation (3-1), the summations are performed over the total number of model-observations pair values (N) while O_i and M_i represent the i^{th} observed and modeled values respectively. The coefficient of determination (r^2) tells about the strength of linear relationship between model and observations and is represented simply by the square of Person's product moment correlation coefficient (r), which is calculated as:

$$r = \left[\frac{\sum_{i=1}^N (O_i - \bar{O})(M_i - \bar{M})}{\sqrt{\sum_{i=1}^N (O_i - \bar{O})^2 \sum_{i=1}^N (M_i - \bar{M})^2}} \right] \quad (3-2)$$

In equation (3-2), the over bars over O and M indicate the average values in the observation and model. The index of agreement (d), which determines the model skill in predicting the variations about the observed mean, is calculated as:

$$d = 1 - \frac{N \cdot RMSE^2}{\sum_{i=1}^N (|O_i - \bar{O}| + |M_i - \bar{O}|)^2} \quad (3-3)$$

Both d and r^2 are dimensionless statistical quantities and vary between 0 (no agreement between model and observations) and 1 (perfect agreement). The RMSE considers error compensation due to opposite sign differences and is calculated as

$$RMSE = \sqrt{\frac{\sum_{i=1}^N (O_i - M_i)^2}{N}} \quad (3-4)$$

Although RMSE encapsulates the average error produced by the model but it does not illuminate the sources or the types of errors. Thus, it is helpful to define a systematic

($RMSE_s$) and unsystematic ($RMSE_u$) component of RMSE. Both of these components are related to the RMSE through the relation:

$$RMSE^2 = RMSE_s^2 + RMSE_u^2 \quad (3-5)$$

The unsystematic component ($RMSE_u$) is calculated as:

$$RMSE_u = \sqrt{(1 - r^2)\sigma_m^2} \quad (3-6)$$

In equation (3-6), r^2 and σ_m^2 represent the coefficient of determination and the variance of modeled values respectively. Once $RMSE_u$ is estimated, $RMSE_s$ is estimated through equation (3-5).

In addition, five hit rate statistical parameters, the Probability of Detection (POD), False Alarm Rate (FAR), Frequency Bias (FBI), Hansen-Kuipers score (HKS) and Odds Ratios (ORT) are calculated [Stephenson, 2000] to evaluate model simulated precipitation. Hit rate statistics is calculated using the symbolic representation shown in Table 3-2. The symbols 'A', 'B', 'C' and 'D' represents the correct hits, false hits, false rejections and correct rejections respectively.

Table 3-2: Different symbols used in calculation of the hit rate statistics.

		Precipitation Observed by TRMM	
		Yes	No
Precipitation Simulated by WRF-Chem	Yes	A	B
	No	C	D

The probability of detection (POD), which is a measure of the model skill in simulating the observed precipitation, is estimated as:

$$POD = \frac{A}{A + C} \quad (3-7)$$

The relative number of times when the model simulated the precipitation but it did not occur is given by the False Alarm Rate (FAR) defined below:

$$FAR = \frac{B}{B + D} \quad (3-8)$$

To identify whether the model overestimates or underestimates the observed precipitation, frequency bias (FBI) is calculated as follows:

$$FBI = \frac{A + C}{A + B} \quad (3-9)$$

The value of FBI should be unity for a perfect forecasting system but generally differs from unity due to presence of systematic biases in the model or the observations. FBI values less (greater) than 1 indicate the overestimation (underestimation) of precipitation by the WRF. The ability of the model to correctly simulate the observed precipitation while avoiding the false alarm rates is assessed using Hansen-Kuipers score (HKS), which is estimated as:

$$HKS = \frac{AD - BC}{(A + C)(B + D)} \quad (3-10)$$

The odd ratios (ORT) provide another measure of evaluating the model skills by weighting the probability of occurrence of the event with the probability of non-occurrence of the event.

$$ORT = \frac{AD}{BC} \quad (3-11)$$

The ORT values greater than 1 indicates that $POD > FAR$ and vice-versa.

3.2 General Features of WRF-Chem Meteorology

The spatial distributions of the model simulated average surface pressure, 2 m temperature, 2 m water vapor and the total precipitation over the model domain during the four seasons winter (DJF), spring (MAM), summer (JJA) and autumn (SON) of the year 2008 are depicted in Figure 3-2. The surface pressure does not show significant seasonal variability except over some regions in Central and Northern India. In contrast, other parameters i.e. temperature, water vapor and precipitation show a distinct seasonal cycle with the highest values in summer and the lowest values in winter. Highest temperatures are seen in summer over Western India encompassing the desert land masses. Temperature and water vapor do not show significant changes from spring to autumn over the oceanic region of Bay of Bengal. The magnitude of seasonal variations in temperature and water vapor is higher for the regions located north of the 20°N latitude belt as compared to the regions located south of this belt. The temperature changes by 25-30 K during a seasonal cycle in the regions northward of 20°N while only by 10-15 K in the regions southward of 20°N. The north-south gradient in 2 m temperature is most prominent during winter. The gradient is also seen during autumn but it is smaller and is within 5 K. Similarly, average water vapor changes by 10-15 g kg⁻¹ and 5-10 g kg⁻¹ in the northern and southern regions, respectively. This spatial and temporal variability in both temperature and water vapor can be attributed to the differential heating and natural landscape diversity (e.g. southern parts of the domain are covered largely by the

oceans) across the model domain along with the seasonal changes in the regional meteorology.

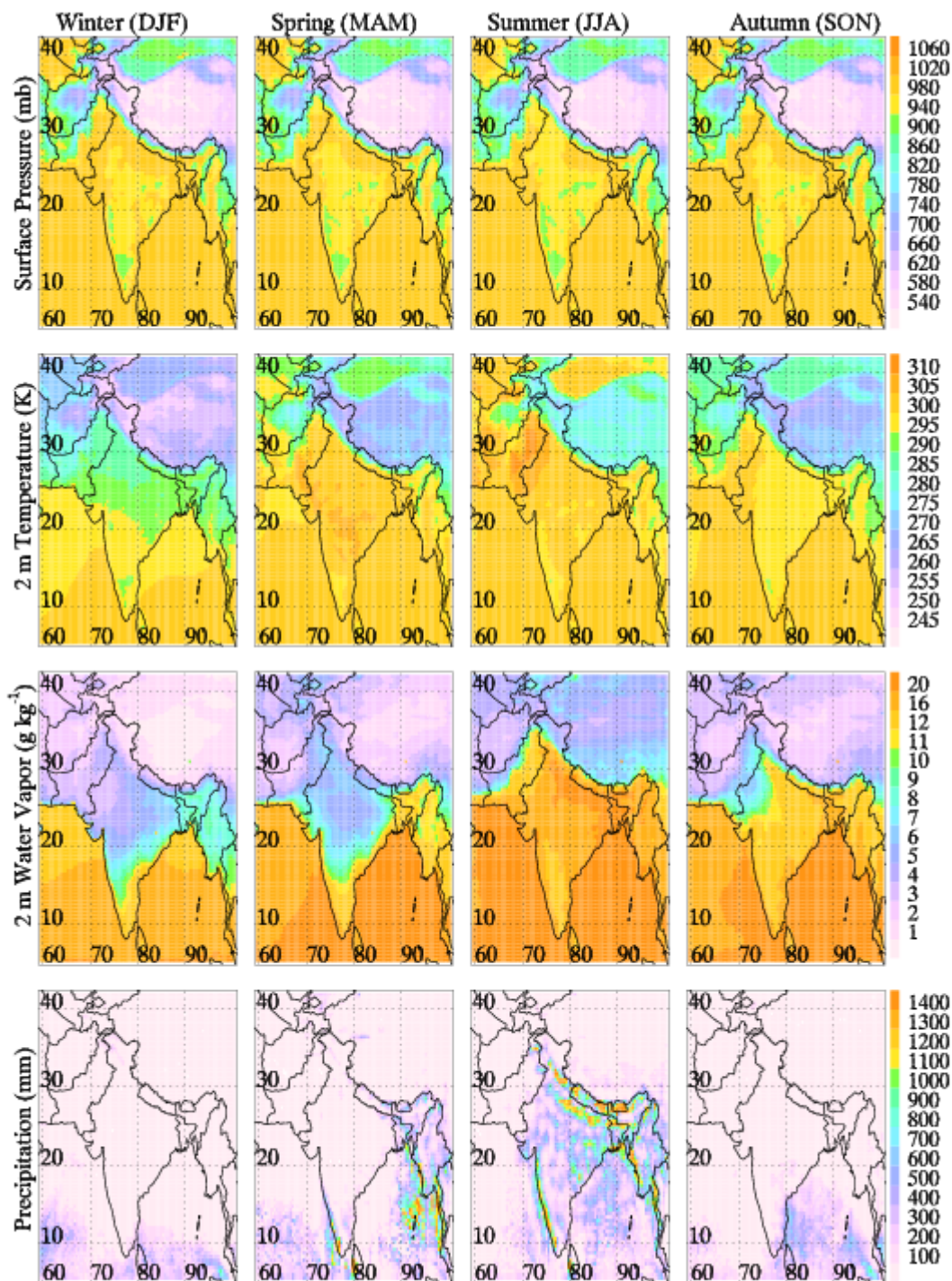


Figure 3-2: Spatial distributions of the model simulated average near surface pressure, 2m temperature, 2m water vapor and total precipitation during winter, spring, summer and autumn seasons of the year 2008. For precipitation the color scale is limited to 1400 mm, but actual rainfall amounts can exceed this limit.

Analysis of modeled solar radiation at the surface show a stronger seasonal cycle over regions north of 20°N with seasonal amplitude of 300-400 W m⁻² as compared to 200-250 W m⁻² over regions south of 20°N. Maximum precipitation is simulated during summer when rainfall is abundant over the Indian landmass region. Model simulated rainfall exceeds 1400 mm over the IGP region, Himalayan foothills and the Western Indian coast in summer. The seasonal total rainfall in spring also exceeds 1400 mm over the parts of the Bay of Bengal and southern tip of India.

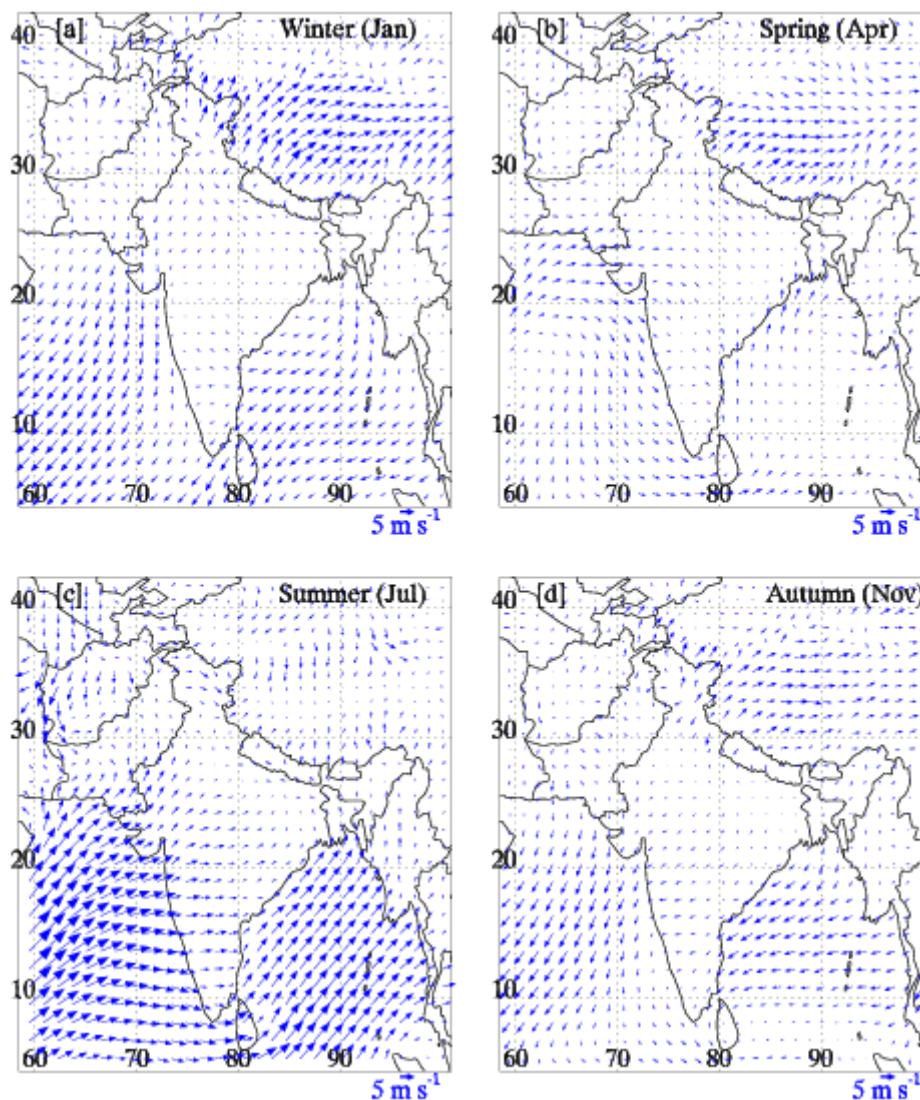


Figure 3-3: Simulated average wind vectors over the model domain during (a) January, (b) April, (c) July and (d) November. The wind vectors are shown at every third grid point (135 km) for the clarity.

Model simulated average 10 m wind patterns for January, April, July and November (representing the winter, spring, summer and autumn seasons, respectively) are shown in

Figure 3-3. Average surface winds are weaker over the land regions than over the oceanic regions during all the seasons because of the low surface roughness over the oceans compared to the land. During winter, surface temperatures over South Asian land-masses are lower than over the oceanic regions. This leads to the development of a high pressure area over land and a low pressure area over the ocean, causing a low level north-easterly air flow near the surface over most of the model domain. Over the Himalayan region, including the Tibetan Plateau, the wintertime wind patterns are generally south-westerly. During the transition from winter to spring, land regions warm up rapidly leading to the formation of heat lows over the subcontinent and cold highs over the oceanic regions. Thus, springtime near-surface winds are nearly zonal over the regions north of 20°N while winds are northerly over the Arabian Sea and southerly over the Bay of Bengal.

The continuous heating of land mass during spring leads to the development of the South Asian monsoon during early summer and south-westerly near-surface winds prevail during summer. Surface temperature again decreases over land from summer to autumn and consequently the winds again change to a north-easterly direction. Clearly, the summertime winds are stronger as compared to any other seasons. The southwesterly winds transport moist air masses from the oceans to inland regions during summer and thus lead to highest water vapor mixing ratios and precipitation over the domain in this season when the South Asian monsoon occurs. Such seasonal changes in temperature, water vapor, precipitation and the wind patterns are typical feature of the South Asian meteorology [e.g. *Asnani, 2005*], which appears to be very well replicated by the model. The errors in the simulated meteorological fields are quantified in the subsequent sections by comparison to satellite retrievals, reanalysis fields and radiosonde observations.

3.3 Results of Model Evaluation

3.3.1 AIRS Temperature and Water Vapor

The spatial distributions of AIRS retrieved and WRF-Chem simulated temperature and water vapor values at 700 hPa during winter (DJF), spring (MAM), summer (JJA) and autumn (SON) of the year 2008 are depicted in Figure 3-4. The model data have been co-located in both space and time with the quality controlled AIRS retrievals (Section 3.1.4). The model simulated spatial and temporal variations in temperature and water vapor distribution at 700 hPa are similar to those seen near the surface (Figure 3-2).

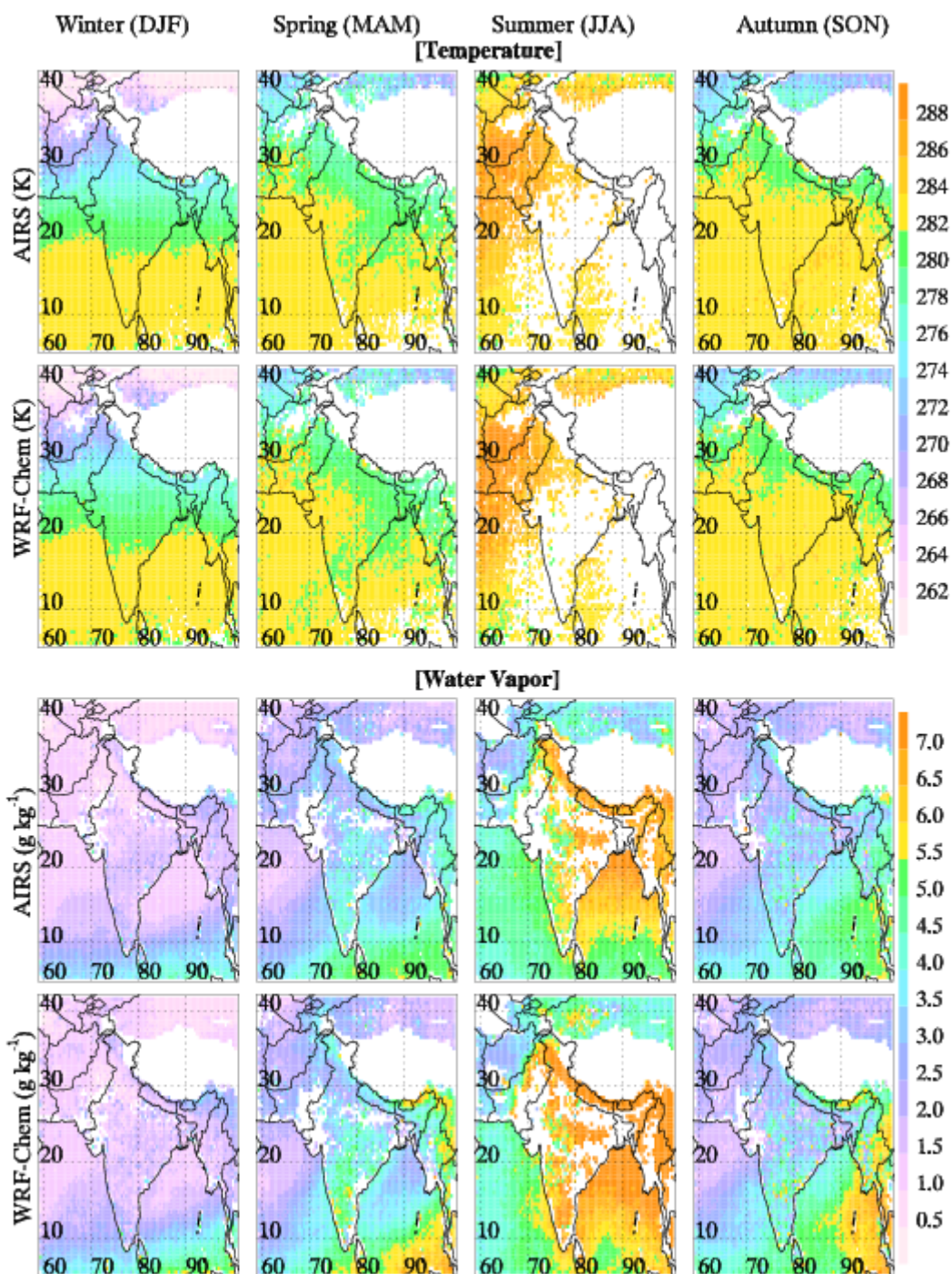


Figure 3-4: Spatial distributions of co-located AIRS retrieved and simulated average temperature (first and second rows) and water vapor (third and fourth rows) at 700 hPa during the winter (DJF), spring (MAM), summer (JJA) and autumn (SON) seasons of the year 2008. The white space indicates missing data.

Both the model and AIRS retrieval at 700 hPa show that temperature and water vapor at this level generally increase from winter to summer and decrease during autumn. However, some

differences between the AIRS retrieved and model simulated spatial distributions of water vapor are discernible in each season. The differences are most prominent during summer and can be noted over both the inland and oceanic regions. These differences are quantified using different statistical metrics and are discussed below. The relationship between the AIRS and simulated temperature values at 700 hPa for each season are shown as scatter plots and frequency analyses (Figure 3-5). The scatter plots indicate a very strong correlation (both r^2 and index of agreement are greater than 0.85) between the AIRS and simulated values during all the seasons.

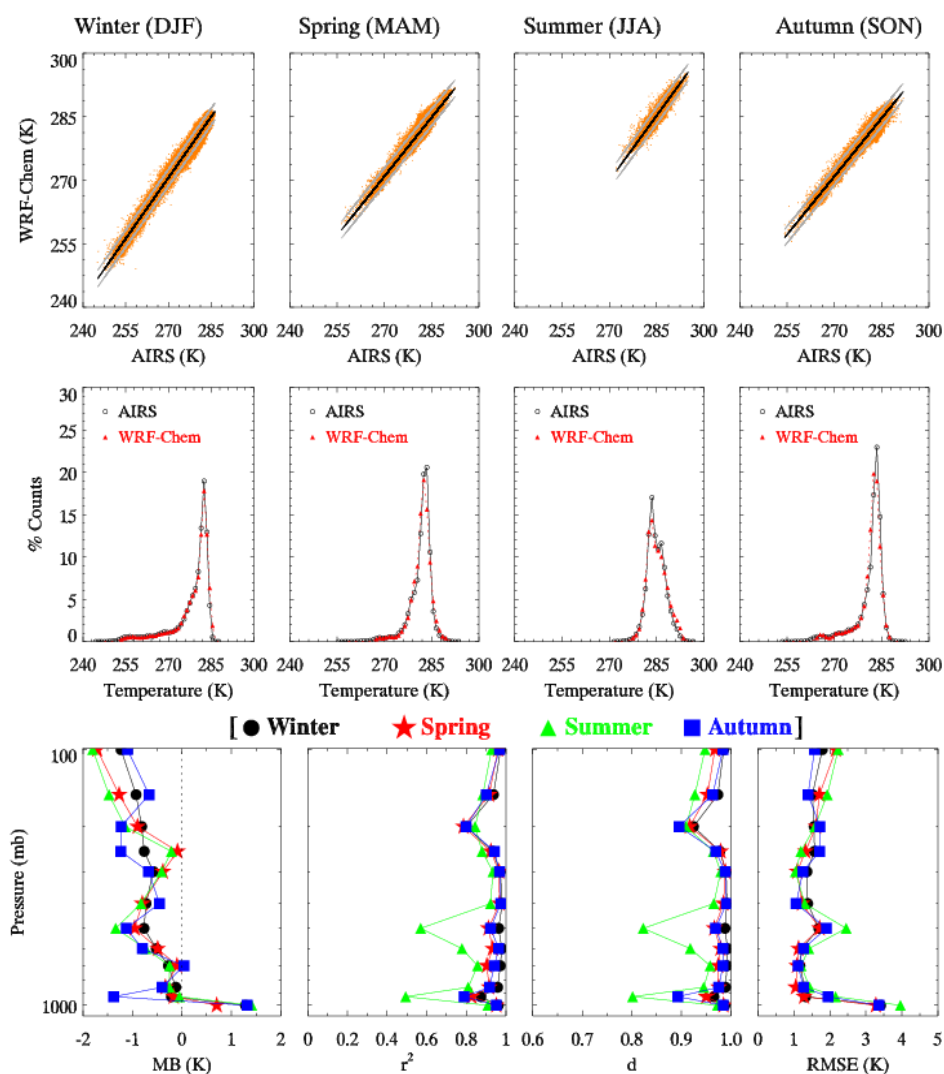


Figure 3-5: The scatter plots (top panel) and the frequency analyses (middle panel) of AIRS and simulated temperature at 2 K interval for 700 hPa during the four seasons of the year 2008. The black lines in the scatter plots represent the linear fit to the data while the grey lines are the 95% confidence interval estimates in the fitted values. The vertical profiles (bottom panel) of mean bias (MB), coefficient of determination (r^2), index of agreement (d) and root mean square error (RMSE) for each season are also shown.

Frequency analyses indicate similar distributions for the domain-wide AIRS and model temperature values among 2 K intervals and both distributions peak around 282-284 K temperature values during all seasons. Due to the distinct seasonal cycle, the temperature distributions are skewed towards lower values during winter and autumn as compared to spring and summer. To quantify the differences in model and observations, the vertical profiles of MB, r^2 , index of agreement (d) and RMSE in temperature for each season are shown in Figure 3-5.

Table 3-3: Domain-wide average and standard deviation of AIRS and WRF-Chem temperature values (K) at the surface and at different pressure levels between 925 and 100 hPa during the winter, spring, summer and autumn seasons of the year 2008.

Pressure (hPa)	Winter		Spring		Summer		Autumn	
	AIRS ^a	WRF ^a						
Surface	285.1±15.4	283.8±16	293.3±13	292.6±14	293.1±12.2	291.7±12.1	291.3±13.2	290.0±14
925	292.7±3.6	292.9±3.7	296.9±3.1	297.1±2.8	295.8±3.0	295.8±2.1	294.6±2.9	295.9±2.9
850	287.2±6.2	287.4±6.3	292.3±3.4	292.7±3.5	293.1±3.2	293.3±3.0	290.3±4.0	290.7±4.2
700	278.3±6.8	278.6±6.6	281.6±3.5	281.7±3.4	284.9±2.9	285.1±3.1	281.3±4.6	281.2±4.3
600	270.9±7.6	271.4±7.4	273.2±4.0	273.7±3.9	276.1±2.5	276.8±2.5	273.2±5.1	273.9±4.9
500	261.1±7.9	261.9±7.7	263.4±4.8	264.4±4.6	266.5±3.0	267.8±2.9	263.4±5.5	264.5±5.4
400	249.7±7.5	250.4±8.0	251.7±4.9	252.5±5.2	256.3±3.4	257.1±3.6	252.1±5.5	252.6±5.8
300	235.6±6.8	236.2±7.2	237.3±5.1	237.8±5.4	243.5±3.6	243.9±3.8	237.2±5.8	237.9±5.8
250	227.5±5.2	228.3±5.3	229.1±4.5	229.3±4.8	235.4±3.4	235.6±3.1	228.2±5.0	229.4±4.9
200	219.0±2.3	219.8±2.7	219.2±2.8	220.1±2.9	224.0±2.8	225.1±2.4	218.9±2.6	220.2±2.7
150	209.0±4.8	209.9±4.6	208.2±3.9	209.4±3.9	210.9±3.6	212.4±3.4	209.1±3.9	209.7±3.5
100	198.6±7.7	199.8±7.2	196.7±6.2	198.3±5.7	199.5±4.9	201.2±4.8	199.4±6.3	200.5±6.1

^aMean ± 1 Sigma

The mean bias (MB) in the model simulated and AIRS retrieved temperature is estimated to be within ±2 K at all pressure levels in all seasons. The model is generally biased cold at the surface and warm aloft with respect to the AIRS temperature. The cold bias at the surface might be due to the local closure model employed in the MYJ PBL scheme as this model allows the entrainment to develop only through local mixing, which partially leads to lower temperatures near the surface [Hu et al., 2010]. Both r^2 and index of agreement show similar vertical profiles and higher values at all the pressure levels except at 925 hPa and 500 hPa

during summer. This lower correlation in summer can partially be attributed to the fewer number of samples in this season.

The estimated RMSE in temperature is largest at the surface (3.3-3.9 K) and is about 1-2 K at all other pressure levels. Larger differences at the surface can be caused by the uncertainty in the representation of the surface forcing physics, topography and land surface characteristics in the model due to its coarser resolution (45 km). Further, large errors in the AIRS surface temperature retrievals, due to heterogeneity of the land surface and the associated spectral emissivity variations [Divakarla *et al.*, 2006] can also contribute to these differences. Like RMSE, both $RMSE_s$ and $RMSE_u$ are also estimated to be higher at the surface and lower aloft (not shown here). However, the RMSE in the model predicted temperature are estimated to be largely unsystematic except at 100 hPa. The simulated temperature values at all other pressure levels between 1000 hPa/surface pressure (whichever is lower) and 100 hPa are also found to be in good agreement with the AIRS retrievals (Table 3-3). The model simulated average temperature values at individual pressure levels are within $\pm 1\%$ of the AIRS retrieved value respectively.

The errors in simulated temperature can affect the atmospheric chemistry simulations by influencing biogenic emissions, gas phase chemistry, gas/particle partitioning of the semi volatile organic compounds, dry deposition of pollutants through the surface exchange scheme. In the absence of other errors, the cold model bias estimated here at the surface will tend to underestimate photochemical ozone production in the surface layer by lowering the emissions and slowing down the reaction rates while the warm bias aloft will tend to overestimate photochemical ozone production by enhancing reaction rates. The cold bias at the surface will also tend to underestimate the dry deposition of trace species by reducing the strength of mixing within the boundary layer. The adequacy of the model's meteorological performance is assessed by comparing estimated statistical metrics with a set of benchmarks proposed by Emery [2001] who suggested that errors in model simulated temperature will have little impact on atmospheric chemistry simulations if the index of agreement (d) is greater than 0.8, the mean bias (MB) is less than ± 0.5 K and the mean absolute error (MAE) is less than 2 K.

The index of agreement is estimated to be greater than 0.8 at all the pressure levels during all the seasons fulfilling the proposed criterion. MAE values (less than 1.5 K) are also much

smaller than the proposed criteria value (2 K) at all pressure levels except at the surface (2-2.5 K). Some part of the higher MAE values at the surface might be related to uncertainties involved in AIRS temperature retrievals as previously mentioned. The MB values (within ± 2 K) in model simulated temperature are slightly higher than the proposed criteria value but they are not expected to induce large errors in the atmospheric chemistry simulations because temperature variations of ± 5 K are shown to induce errors of typically less than ± 10 ppbv in simulating ozone concentrations [Vieno *et al.*, 2010].

The model simulated water vapor values at all pressure levels between 1000 hPa/surface pressure (whichever is lower) and 300 hPa are also found to be in good agreement with the AIRS retrievals (Table 3-4). The model simulated average water vapor values at individual pressure levels are within $\pm 17\%$ of the AIRS retrieved average value respectively.

Table 3-4: Same as Table 3-3 but for AIRS water vapor ($g\ kg^{-1}$).

Pressure (hPa)	Winter		Spring		Summer		Autumn	
	AIRS ^a	WRF ^a						
1000	12.8 \pm 3.2	12.5 \pm 3.5	14.4 \pm 3.0	14.1 \pm 3.8	16.1 \pm 1.7	17.2 \pm 1.2	14.8 \pm 2.7	14.9 \pm 2.9
925	8.9 \pm 3.7	7.9 \pm 3.6	10.6 \pm 3.9	9.1 \pm 4.0	13.1 \pm 2.7	13.6 \pm 2.3	11.3 \pm 3.7	10.5 \pm 3.6
850	4.0 \pm 2.6	4.7 \pm 2.9	5.8 \pm 2.9	6.3 \pm 3.0	8.0 \pm 2.3	9.2 \pm 2.8	6.1 \pm 3.0	7.1 \pm 3.2
700	1.8 \pm 1.6	2.1 \pm 1.9	3.0 \pm 1.8	3.4 \pm 2.1	4.9 \pm 1.6	5.3 \pm 2.1	3.2 \pm 2.0	3.6 \pm 2.5
600	1.0 \pm 1.0	1.0 \pm 1.1	1.6 \pm 1.3	1.7 \pm 1.4	3.5 \pm 1.5	3.8 \pm 1.6	2.0 \pm 1.5	2.1 \pm 1.7
500	0.5 \pm 0.5	0.5 \pm 0.5	0.7 \pm 0.7	0.8 \pm 0.7	1.8 \pm 0.9	2.1 \pm 1.1	1.0 \pm 0.9	1.1 \pm 0.9
400	0.2 \pm 0.2	0.2 \pm 0.2	0.3 \pm 0.3	0.3 \pm 0.3	0.7 \pm 0.5	0.9 \pm 0.5	0.4 \pm 0.4	0.4 \pm 0.4
300	0.1 \pm 0.1	0.1 \pm 0.1	0.1 \pm 0.1	0.1 \pm 0.1	0.2 \pm 0.2	0.3 \pm 0.2	0.1 \pm 0.1	0.2 \pm 0.2

^aMean \pm 1 Sigma

The scatter plot between AIRS retrieved and model simulated water vapor values at 700 hPa also show positive correlation (Figure 3-6) but there is a larger scatter and weaker correlation compared to the comparison of temperature. Largest scatter is seen during summer and is likely due to large spatial variability of water vapor associated with spatially varying influence of South Asian monsoon in this region and simulations of Indian summer monsoon are difficult due to its anomalous characteristics in the tropical circulation.

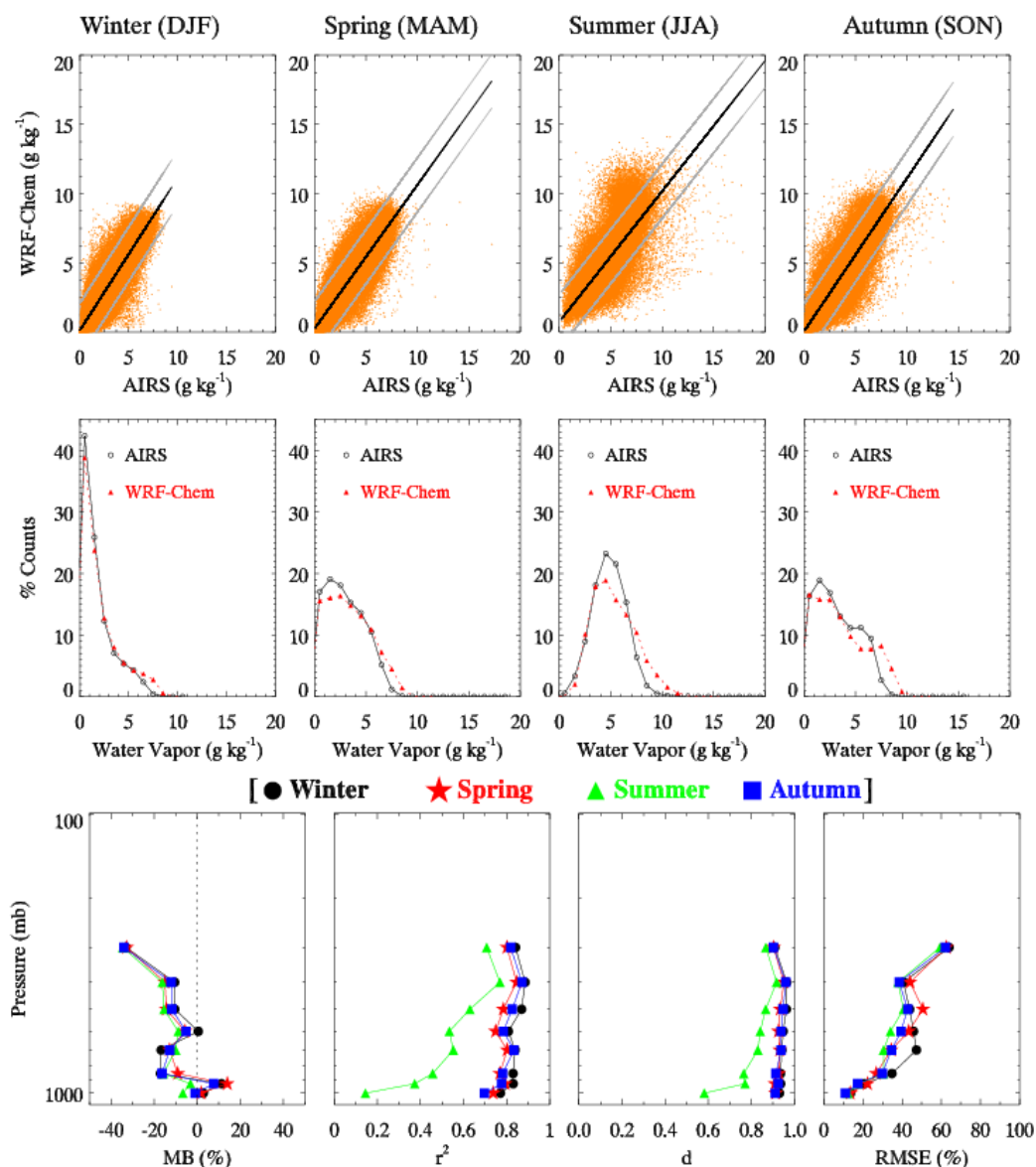


Figure 3-6: The scatter plots (top panel) and the frequency analyses (middle panel) of AIRS and model water vapor at 1 g kg^{-1} interval for 700 hPa during the four seasons of the year 2008. The black lines in the scatter plots represent the linear fit to the data while the grey lines are the 95% confidence interval estimates in the fitted values. The vertical profiles (bottom panel) of MB, r^2 , d and RMSE for each season are also shown.

The frequency analyses of AIRS and the model water vapor values exhibit similar distributions. However, the model distribution gets slightly more contribution from higher water vapor mixing ratio as compared to the AIRS distribution in all the seasons. These higher model simulated water vapor values arise mainly due to an overestimation over much of the Bay of Bengal, along the western coasts of India and the Himalayan foothills in summer and over the southern Bay of Bengal, eastern Burma and northeast India during

spring and autumn. These discrepancies could arise due to uncertainty in the representation of topography, insufficient mixing in the boundary layer, errors in moisture transport and simulation of surface moisture availability, soil temperature and an excessive water vapor flux from the ocean. However, it is difficult to diagnose the relative contributions of these processes due to the lack of in situ observations.

As before, Figure 3-6 also shows the vertical profiles of MB, r^2 , index of agreement and RMSE. Here, these statistical metrics are calculated only up to 300 hPa because AIRS has limited sensitivity to water vapor in the upper troposphere [Gettelman *et al.*, 2004; Divakarla *et al.*, 2006]. Further, the MB and RMSE for water vapor are reported in percentage and are computed by weighting these metrics with the average AIRS water mixing ratio. The values of both r^2 and index of agreement in summer (r^2 : 0.14-0.77; d: 0.58-0.92) are significantly lower than those in any other season (r^2 : 0.7-0.9; d: 0.91-0.97), which can partially be attributed to the relatively small number of data samples in this season. The model results are biased wet with respect to AIRS retrievals at all levels in summer and above 900 hPa in other seasons. The model is biased dry below 900 hPa in all other seasons except at 1000 hPa in autumn. The mean bias remains less than 20% at all the pressure levels between 1000 and 400 hPa and exceeds 30% at 300 hPa. The increase in RMSE at higher levels could be related to the errors in the simulated temperature and the reduction in the sensitivity of AIRS associated with the decrease in water vapor mixing ratios with altitude [Gettelman *et al.*, 2004]. The RMSE between AIRS and WRF water vapor profiles is less than 20% at 1000 hPa and increase gradually to 60-65% at 300 hPa. Like temperature, RMSE in water vapor is also estimated to be largely unsystematic.

The errors in water vapor mixing ratios can also affect the concentrations of certain types of pollutants simulated by the model. For instance, a wet bias in the model can enhance the conversion of nitrogen species into aerosol nitrates at night. In fact, aerosol nitrate has been observed to increase significantly at night when relative humidity rises above 80% [Nenes *et al.*, 1998]. The wet bias of the model would also tend to overestimate the concentrations of hydroxyl radicals, which in turn would tend to underestimate the concentrations of several volatile organic compounds and would affect ozone. The set of benchmarks proposed for water vapor mixing ratio [Emery, 2001] suggest that index of agreement (d) should be greater than 0.6, mean bias (MB) should be less than $\pm 1 \text{ g kg}^{-1}$ and mean absolute error (MAE) should be less than 2 g kg^{-1} . The model evaluation shows that these metrics are well within

the proposed benchmarks. Therefore, errors in simulation of water vapor are also expected to have little impact on atmospheric chemistry simulations in absence of other errors. The impact of biases in temperature and water vapor on the simulations of tropospheric ozone, CO and NO_x will be assessed later in Section 3.4.

3.3.2 NCEP Zonal and Meridional Winds

The spatial distributions of the NCEP reanalysis and the model simulated zonal and meridional wind components (2.5° resolution) at 700 hPa during the four seasons of the year 2008 are shown in Figure 3-7. The spatial distributions simulated by the model are fairly similar to the NCEP distributions. The model slightly overestimates both the zonal and meridional wind components during all the seasons except during summer over central/northern India, the Arabian Sea and the Bay of Bengal. In contrast, it slightly underestimates the zonal wind over the Arabian Sea and the Bay of Bengal during summer.

The major factors limiting the accuracy of model simulated winds are likely linked to uncertainties in the simulation of the large scale pressure gradient, improper representation of topography and land surface characteristics due to coarser grid resolution (45 km in this case) and errors in the initial and lateral boundary conditions [Bao *et al.*, 2005]. However, the initial conditions should play a minor role for long-term simulations. The model simulated domain-wide average values of both the wind components at all the pressure levels between 1000 and 100 hPa are found to be in good agreement with the corresponding NCEP values (Tables 3-5 and 3-6). The average zonal and meridional wind component values simulated at different pressure levels by the model are within $\pm 15\%$ of the corresponding NCEP values below 300 hPa.

Despite the above mentioned differences, the scatter plots indicate a reasonable positive correlation between NCEP fields and the model for both wind components (Figure 3-8 and 3-9). The agreement is better in winter and autumn ($r^2 = 0.6-0.8$) than in spring and summer ($r^2 = 0.4-0.7$). The frequency analyses indicate very similar distributions for both NCEP and model wind components. The vertical profiles of MB, r^2 , d and RMSE during all four seasons are also shown in Figures 3-8 and 3-9 respectively. The mean bias in the zonal wind component is small (0.6 m s^{-1}) below 300 hPa while the model underestimates the zonal flow above 300 hPa by $0.6-1.6 \text{ m s}^{-1}$ during all the seasons. The mean bias in the meridional wind component is lower than the zonal wind component with the meridional wind component

being overestimated by the model in the lower to middle troposphere (850 - 500 hPa) by 0.1-0.7 m s^{-1} and underestimated in the upper troposphere (300-100 hPa) by 0.1-0.5 m s^{-1} .

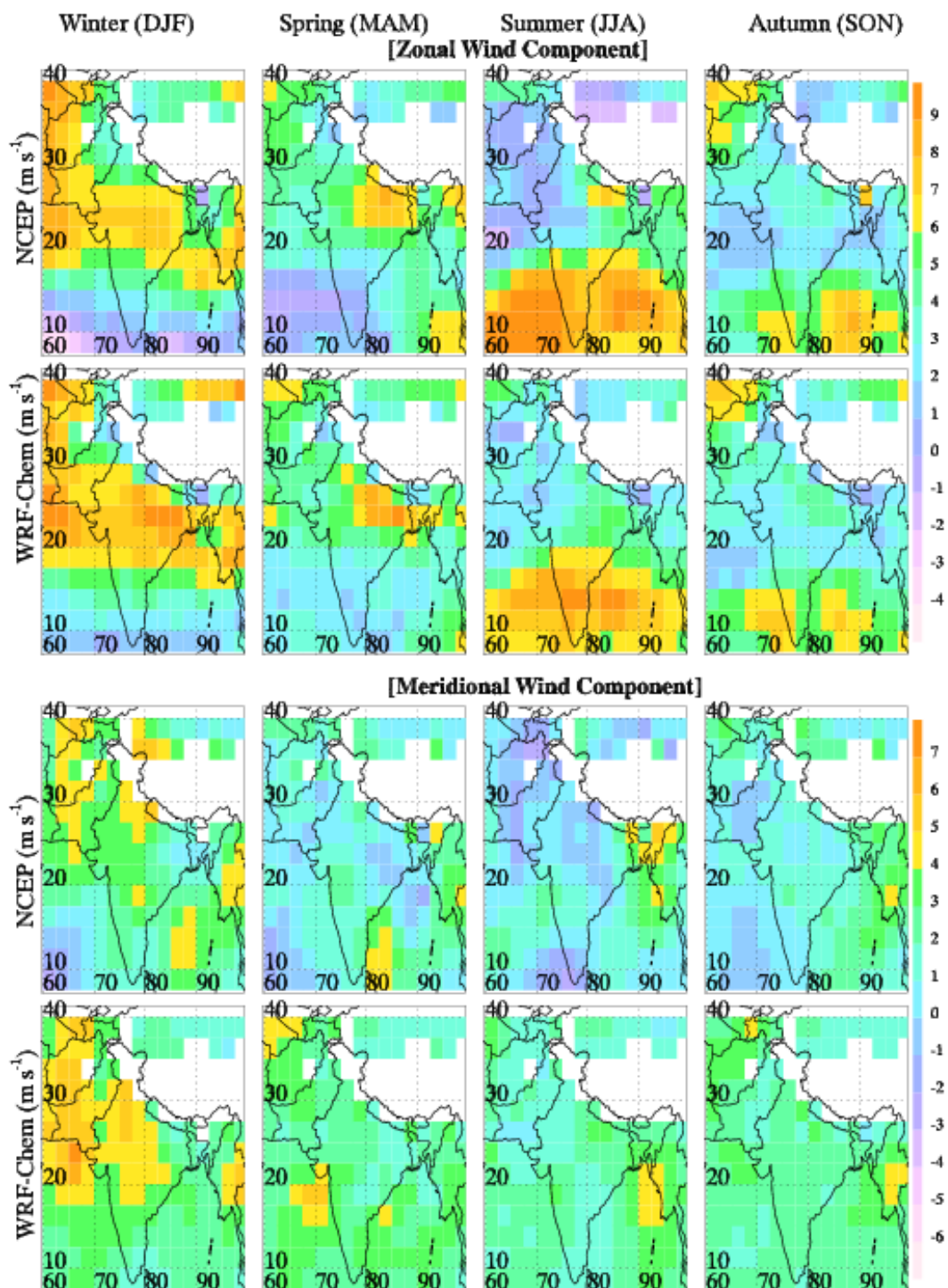


Figure 3-7: Spatial distribution of co-located NCEP and the model simulated average zonal (first and second rows) and meridional (third and fourth rows) wind components at 700 hPa during the winter, spring, summer and autumn seasons of the year 2008. The white space indicates missing data in NCEP as well as in the model.

Table 3-5: Domain-wide average and standard deviation of zonal component of NCEP and WRF winds at different pressure levels between 1000 hPa and 100 hPa during winter, spring, summer and autumn of 2008.

Pressure (hPa)	Winter		Spring		Summer		Autumn	
	NCEP ^a	WRF ^a						
1000	3.0±2.0	3.4±2.2	3.1±2.2	3.5±2.4	6.2±3.2	6.8±3.0	3.2±2.4	3.7±2.7
925	3.2±2.4	3.5±2.5	3.7±3.0	4.0±3.1	7.1±4.8	7.4±4.8	3.7±3.1	4.0±3.2
850	3.3±2.5	3.4±2.6	3.6±2.9	3.7±2.9	7.3±5.4	7.2±5.3	3.8±3.3	3.9±3.3
700	5.5±3.8	5.6±4.0	4.4±3.1	4.5±3.3	5.2±4.3	4.8±3.8	4.2±3.3	4.1±3.2
600	8.6±5.9	8.3±6.0	5.6±3.9	5.5±4.0	4.4±3.5	4.2±3.3	5.0±3.6	4.9±3.6
500	12.7±8.5	12.0±8.4	7.6±5.3	7.2±5.2	4.4±3.5	4.2±3.3	6.6±5.0	6.5±5.0
400	17.8±12.3	17.4±11.9	10.3±7.7	9.9±7.4	5.7±4.6	5.6±4.5	9.4±7.5	9.3±7.5
300	24.1±17.0	23.8±16.7	14.6±11.2	14.2±10.9	10.1±7.3	10.1±7.2	14.3±11.1	14.2±11.1
250	27.2±19.2	26.9±19.0	17.3±12.9	17.0±12.8	13.3±8.7	13.3±8.6	17.4±13.0	17.3±13.0
200	29.0±20.3	28.8±19.8	19.7±14.0	19.3±13.7	16.5±9.7	16.5±9.5	20.1±14.3	20.0±14.1
150	27.9±18.5	27.7±17.7	19.3±13.0	18.7±12.3	19.2±10.3	19.2±10.4	20.2±13.5	20.2±13.1
100	20.7±13.5	21.0±13.0	13.9±9.0	13.9±8.6	19.0±10.9	19.6±10.4	14.2±9.8	14.7±9.3

Table 3-6: Same as the Table 3-5 but for the meridional wind component.

Pressure (hPa)	Winter		Spring		Summer		Autumn	
	NCEP ^a	WRF ^a						
1000	3.4±2.3	3.7±2.5	2.8±2.1	3.0±2.2	4.5±2.9	4.7±2.7	2.7±2.0	3.0±2.1
925	2.9±2.2	3.1±2.4	2.6±2.0	3.0±2.4	4.1±3.1	4.5±3.3	2.6±2.1	2.8±2.2
850	2.8±2.2	2.7±2.2	2.4±1.9	2.5±2.1	3.4±2.6	3.4±2.6	2.6±2.0	2.5±2.2
700	3.7±3.0	3.4±2.9	3.1±2.4	3.2±2.7	3.0±2.3	2.9±2.4	2.9±2.3	2.8±2.4
600	4.1±3.4	4.3±3.4	3.3±2.6	3.3±2.8	3.0±2.5	2.9±2.5	3.1±2.5	2.9±2.5
500	5.1±4.3	5.5±4.4	3.7±3.0	3.6±3.0	3.0±2.6	2.9±2.5	3.4±2.9	3.3±3.0
400	6.4±5.5	7.3±5.6	4.4±3.8	4.4±3.8	3.0±2.5	2.9±2.5	4.0±3.7	4.0±3.8
300	8.1±7.3	8.2±7.4	5.8±5.1	5.8±5.2	3.4±3.2	3.6±3.4	5.0±5.0	5.1±5.2
250	9.1±8.2	8.4±8.3	6.6±5.8	6.6±5.8	3.9±3.8	4.2±4.0	5.7±5.7	5.7±5.7
200	9.7±8.4	6.9±8.4	6.9±5.8	7.0±5.8	4.8±4.4	5.0±4.4	6.3±5.9	6.4±5.9
150	8.7±6.9	4.6±6.8	6.2±4.8	6.3±4.8	5.5±4.5	5.8±4.5	6.1±5.2	6.2±5.2
100	5.9±4.6	3.2±4.7	4.4±3.4	4.0±3.1	5.0±3.8	4.7±3.5	4.2±3.4	3.8±3.2

^aMean ± sigma

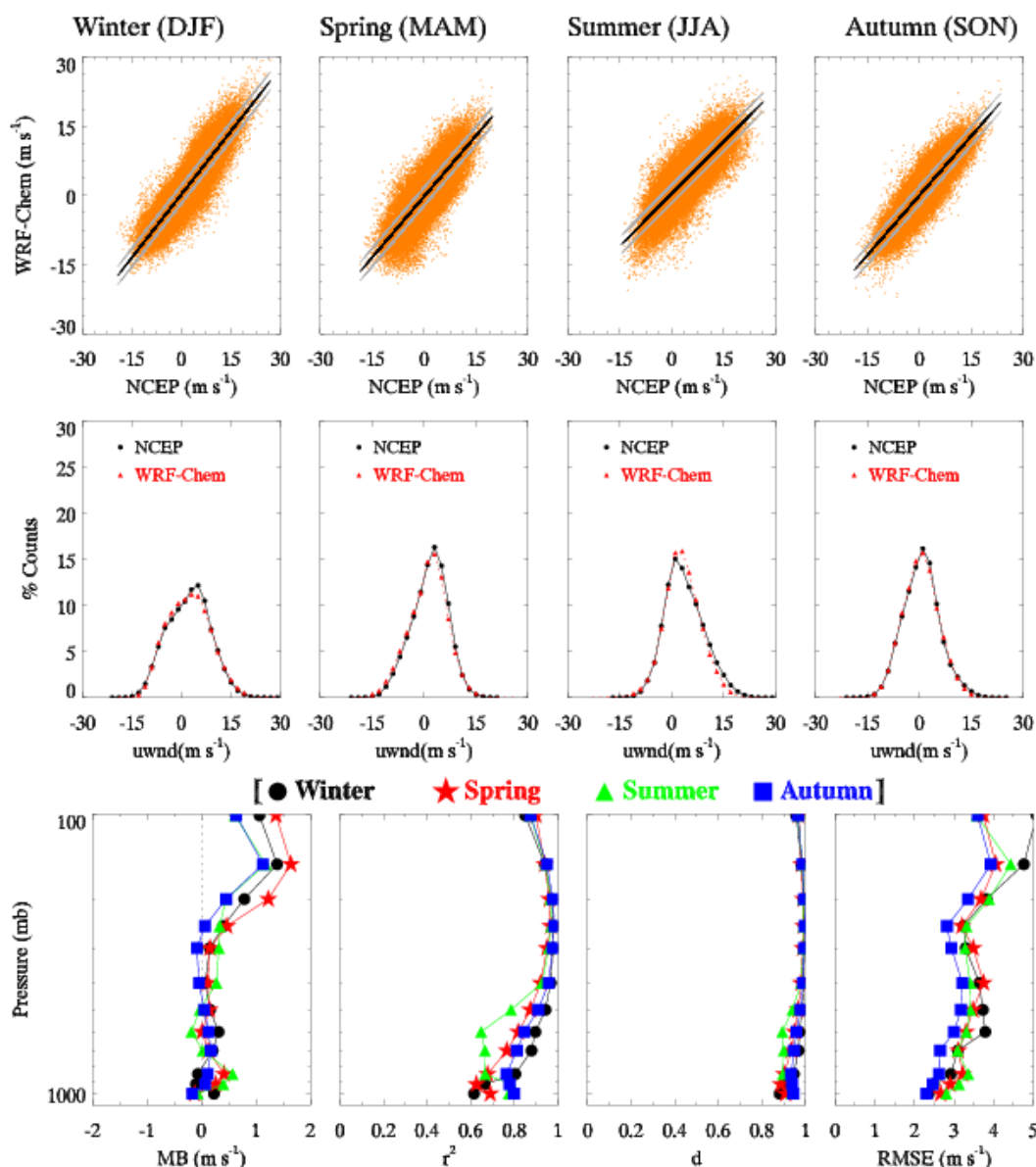


Figure 3-8: The scatter plots (top panel) and the frequency analyses (middle panel) of NCEP and model zonal wind component at 2 m s^{-1} interval for 700 hPa during the four seasons of the year 2008. The black lines in the scatter plots represent the linear fit to the data while the grey lines are the 95% confidence interval estimates in the fitted values. The vertical profiles (bottom panel) of MB, r^2 , d and RMSE for each season are also shown.

The r^2 and index of agreement for the zonal wind component (r^2 : 0.61-0.98; d : 0.88-0.99) at all pressure levels are estimated to be better than for the meridional wind component (r^2 : 0.38-0.94; d : 0.78-0.98) in all seasons. The RMSE in both the zonal and meridional wind components exhibit an increasing tendency with altitude and are estimated to be $2.3\text{-}5.1 \text{ m s}^{-1}$ and $2.2\text{-}3.9 \text{ m s}^{-1}$ respectively. However, the relative error in zonal wind component decrease

with altitude due to increase in wind speed at higher altitudes during all the seasons except during summer when relative error first increase up to 500 hPa and then decrease up to 100 hPa. Like temperature and water vapor, the RMSE in wind components are estimated to be mainly unsystematic.

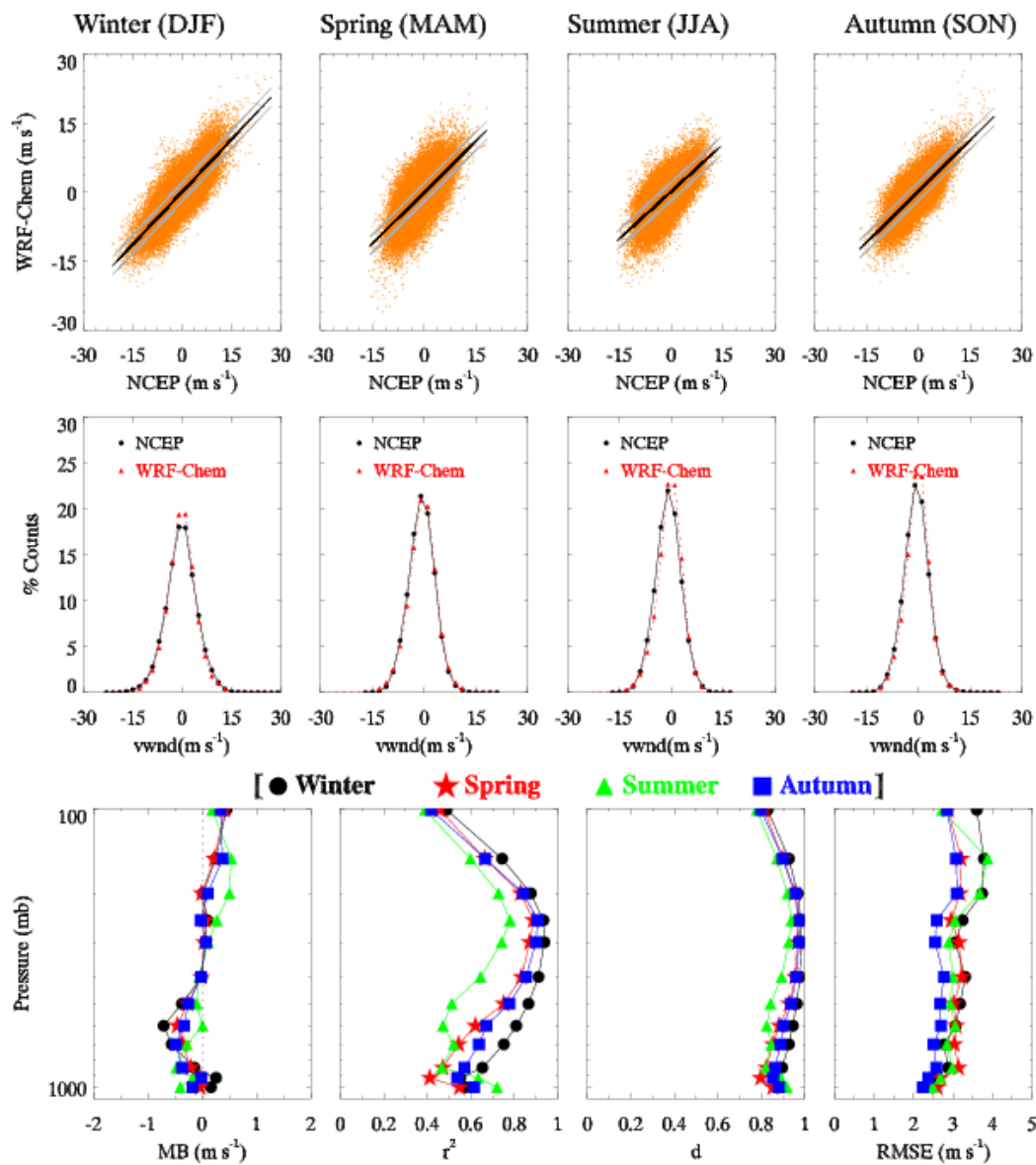


Figure 3-9: The scatter plots (top panel) and the frequency analyses (middle panel) of NCEP and model meridional wind component at 2 m s^{-1} interval for 700 hPa during the four seasons of the year 2008. The black lines in the scatter plots represent the linear fit to the data while the grey lines are the 95% confidence interval estimates in the fitted values. The vertical profiles (bottom panel) of MB, r^2 , d and RMSE for each season are also shown.

The benchmarks proposed for wind speed [Emery, 2001] suggest that index of agreement (d) should be greater than 0.6, mean bias (MB) should be less than $\pm 0.5 \text{ m s}^{-1}$ and root mean square error (RMSE) should be less than 2 m s^{-1} . The index of agreement for both components is well above the proposed benchmark. The mean bias in both the wind components below 300 hPa is well within the proposed benchmark limits but RMSE values are slightly higher than the benchmark values. The estimated mean bias ($< 0.6 \text{ m s}^{-1}$) in both wind components below 300 hPa can cause the transport of pollutants to be off by about 52 km in 24 hours which is greater than the grid spacing of the model used here. *de Meij et al.* [2009] found that ozone levels over the mountain areas near Po Valley in their chemistry transport model simulations driven by WRF meteorology are higher by 6-9 ppbv than those driven by MM5 meteorology and attributed these discrepancy to the difference of about 1 m s^{-1} between monthly mean wind speed of WRF and MM5. The overestimation of ozone concentrations due to larger wind speeds has also been reported over the subalpine mountain ranges [Minguzzi et al., 2005]. The impact of biases in zonal and meridional wind components along with those of temperature and water vapor on the simulations of tropospheric ozone, CO and NO_x will be assessed later in section 3.4.

3.3.3 TRMM Precipitation

The spatial distributions of precipitation observed by TRMM and simulated by the model along with the absolute difference (WRF-TRMM) are depicted in Figure 3-10. The seasonal cycle of the precipitation as seen by TRMM is successfully captured by the model. Both TRMM and the model show highest precipitation during summer and lowest during winter with some differences in the absolute magnitude and spatial distributions. In general, the difference between the model and TRMM rainfall values is within $\pm 10 \text{ mm day}^{-1}$ over much of the domain and during all the seasons except during summer, when the model overestimates the precipitation by more than 20 mm day^{-1} along the Himalayas, the coastline in eastern regions like Bangladesh, Burma and west coast of India.

Accurate simulations of summertime rainfall over the Indian region have been a challenging task due to its anomalous characteristics in tropical circulation. Different studies based on regional meteorological models (MM5 or WRF) show that summer monsoonal rainfall is not very well simulated by these regional models [e.g. *Ratnam and Kumar, 2005; Rakesh et al., 2009*]. Analysis of modeled precipitation showed that summer rainfall over India is dominated by convective precipitation and hence overestimation in the model could be due to

use of the Kain-Fritsch scheme in the model. *Rakesh et al.* [2009] used the same convective scheme (Kain-Fritsch) and also found that the WRF model overestimates the summertime rainfall over this region. The discrepancies between TRMM and the model can be attributed to the coarse model resolution (45 km), errors in the lateral boundary conditions, uncertainties associated with the parameterization of physical processes in the model and errors in the grid resolvable meteorological variables related to the precipitation (e.g. temperature, water vapor and heat fluxes).

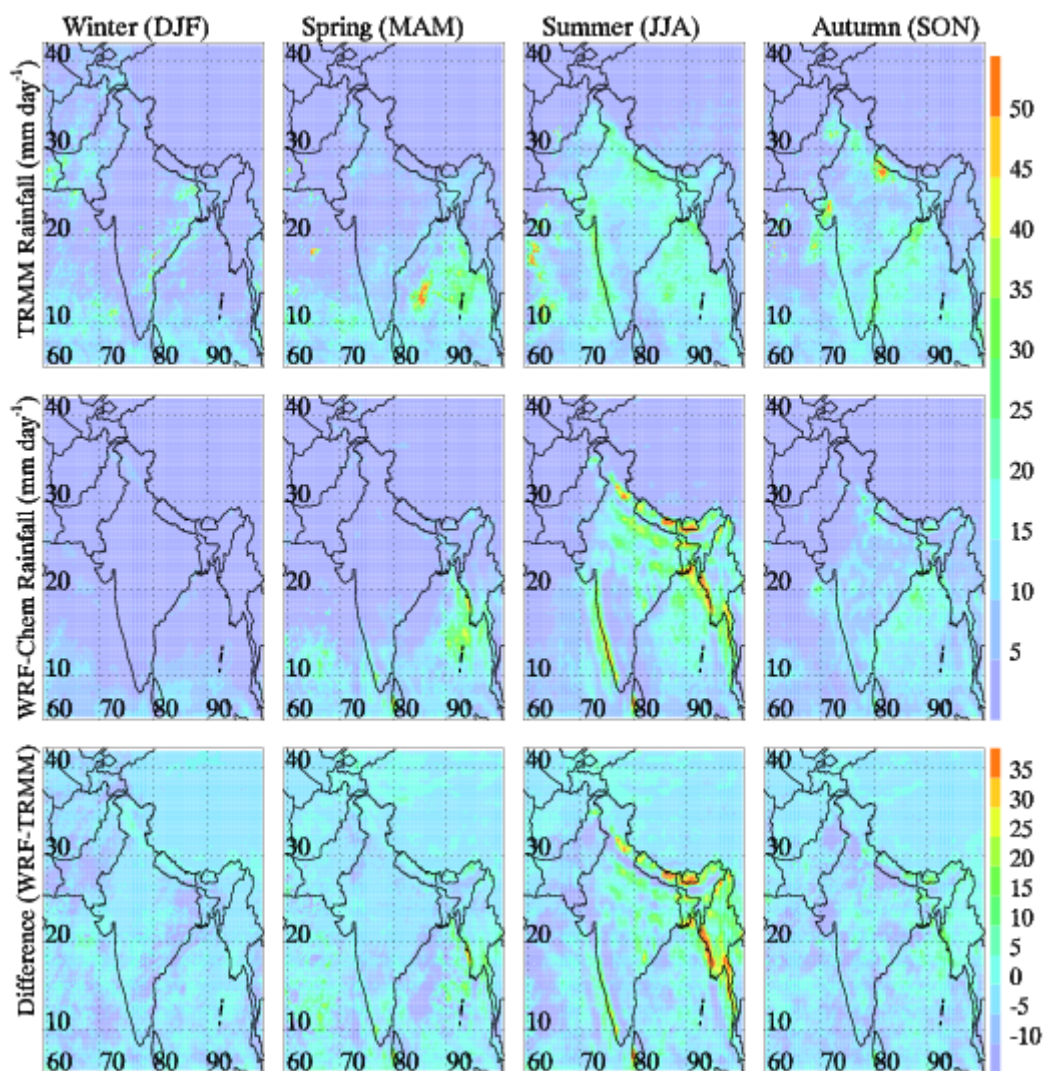


Figure 3-10: Spatial distribution of co-located TRMM (top panel) and WRF-Chem (second panel) total precipitation during the winter, spring, summer and autumn seasons of the year 2008. Difference (WRF-TRMM) in the total precipitation values are shown in the bottom panel.

Sensitivity simulations indicate that estimated biases in modeled temperature and water vapor can lead to errors of $\pm (1-8) \text{ mm day}^{-1}$ in modeled precipitation. Further, the lower accuracy

of TRMM retrievals in regions of sharp rainfall gradients, warm clouds and rapidly varying orography [Nair *et al.*, 2009] may also contribute to these differences. In order to quantify the domain-wide differences between TRMM and WRF precipitation, the hit rate statistics is calculated during each season at 11 rainfall threshold values (1, 5, 10, 15, 20, 25, 30, 35, 40, 45, 50; all values in mm/day) and is shown in Table 3-7.

Table 3-7: Hit rate statistics (probability of detection (POD), false alarm rate (FAR), frequency bias (FBI), Hansen-Kuipers Score (HKS) and odd ratio (ORT)) for WRF-Chem and TRMM daily precipitation data during winter, spring, summer and autumn at different threshold values.

Season		Threshold Precipitation (mm day ⁻¹)										
		1	5	10	15	20	25	30	35	40	45	50
POD	Winter	0.59	0.55	0.51	0.46	0.40	0.35	0.30	0.25	0.20	0.14	0.10
	Spring	0.62	0.55	0.49	0.44	0.40	0.36	0.32	0.29	0.25	0.22	0.18
	Summer	0.76	0.67	0.60	0.54	0.49	0.44	0.39	0.34	0.30	0.26	0.22
	Autumn	0.67	0.61	0.56	0.51	0.45	0.40	0.35	0.30	0.26	0.22	0.18
FAR	Winter	0.09	0.04	0.03	0.02	0.01	0.01	0.01	0.01	0.00	0.00	0.00
	Spring	0.15	0.09	0.06	0.05	0.04	0.03	0.02	0.02	0.01	0.01	0.01
	Summer	0.34	0.25	0.19	0.16	0.13	0.10	0.08	0.06	0.05	0.04	0.03
	Autumn	0.14	0.10	0.08	0.06	0.05	0.04	0.03	0.02	0.01	0.01	0.01
FBI	Winter	0.60	0.64	0.62	0.62	0.65	0.70	0.76	0.86	1.02	1.30	1.80
	Spring	0.72	0.65	0.60	0.57	0.56	0.55	0.56	0.58	0.62	0.67	0.73
	Summer	0.69	0.60	0.52	0.48	0.46	0.44	0.45	0.46	0.47	0.50	0.54
	Autumn	0.78	0.70	0.65	0.63	0.63	0.65	0.68	0.72	0.79	0.88	1.00
HKS	Winter	0.50	0.51	0.48	0.44	0.39	0.34	0.29	0.25	0.20	0.14	0.10
	Spring	0.48	0.46	0.43	0.39	0.36	0.33	0.30	0.27	0.24	0.21	0.18
	Summer	0.42	0.43	0.41	0.39	0.37	0.34	0.31	0.28	0.25	0.22	0.19
	Autumn	0.52	0.51	0.48	0.45	0.41	0.36	0.32	0.28	0.24	0.21	0.17
ORT	Winter	14.2	27.3	37.3	44.3	49.6	55.6	62.0	70.2	79.4	84.2	91.7
	Spring	9.6	12.5	14.6	16.2	18.1	20.4	22.7	25.3	28.2	31.4	34.9
	Summer	6.3	6.3	6.2	6.4	6.7	7.1	7.4	7.9	8.6	9.4	10.2
	Autumn	12.0	14.1	15.2	16.2	17.0	18.3	19.8	21.6	23.6	26.6	29.5

The evaluation at 11 threshold values provides the information about the model skill in simulating a range of precipitation events. The values of probability of detection (POD) and false alarm rate (FAR), which range from 0.1-0.76 and 0-0.34, respectively, are highest in summer and lowest in winter. However, the Hansen-Kuipers Score (HKS) and odds ratios (ORT) values, which range from 0.1-0.52 and 6.25-91.7, respectively, are highest in winter and lowest in summer. The frequency bias index (FBI) values, which range from 0.44-1.08, indicate that the model generally overestimates the domain-wide precipitation observed by the TRMM except for the precipitation events exceeding the threshold of 40 mm day⁻¹ in winter. Both POD and FAR show a decreasing tendency with increase in rainfall threshold but the ORT values indicate that the probability of detecting a rainfall event by the model above any rainfall threshold is greater than the false simulation of rainfall events. However, the simultaneous increase in FBI values and decrease in HKS score with increasing rainfall threshold indicate deterioration in the model skill for heavier precipitation events.

3.3.4 Radiosonde Observations – Temperature and Dew Point Temperature

Model simulated temperature and dew point temperature are compared with the 00 and 12 UTC radiosonde observations (RAOB) at 34 stations (Table 3-1; Figure 3-1) within the simulation domain. The seasonal variations of the RAOB and the model simulated temperature and dew point temperature at the surface, 700 hPa, 500 hPa and 300 hPa for Delhi (DEL), Bangalore (BAN), Thiruvananthapuram (THI) and Port-Blair (POR) are shown in Figure 3-11. DEL, BAN, THI and POR are selected to represent the low altitude, moderately high altitude, coastal and island sites respectively. In general, the seasonal variations of both the temperature and dew point temperature simulated by the model at all the pressure levels are in reasonably good agreement with the observations.

Some differences between model and observed values of the dew point temperature are seen at higher altitudes. The discrepancies for dew point temperature are consistent with the model-AIRS water vapor comparison for which an increase in RMSE is seen with altitude (Figure 3-6). Port Blair, an island site, shows some differences at surface levels as the model is not able to separate out island with the oceanic region; this will be discussed later in this section. Like AIRS retrievals, RAOB observations also show differences in the seasonal cycle amplitude for the sites located north and south of the 20°N latitude belt. The seasonal amplitudes at DEL are clearly larger than those at BAN, THI and POR and this difference is also very well replicated by the model. Figure 3-12 shows the vertical profiles of the

statistical metrics for the temperature and dew point temperature at all the sites belonging to the low altitude, moderately high altitude, coastal and island sites respectively. The correlation (r^2) is better for temperature for the case of low altitude and moderately high altitude sites below 300 hPa. The poorer correlation at the coastal and island sites appears to be largely due to the erroneous model representation of the underlying surface at these sites.

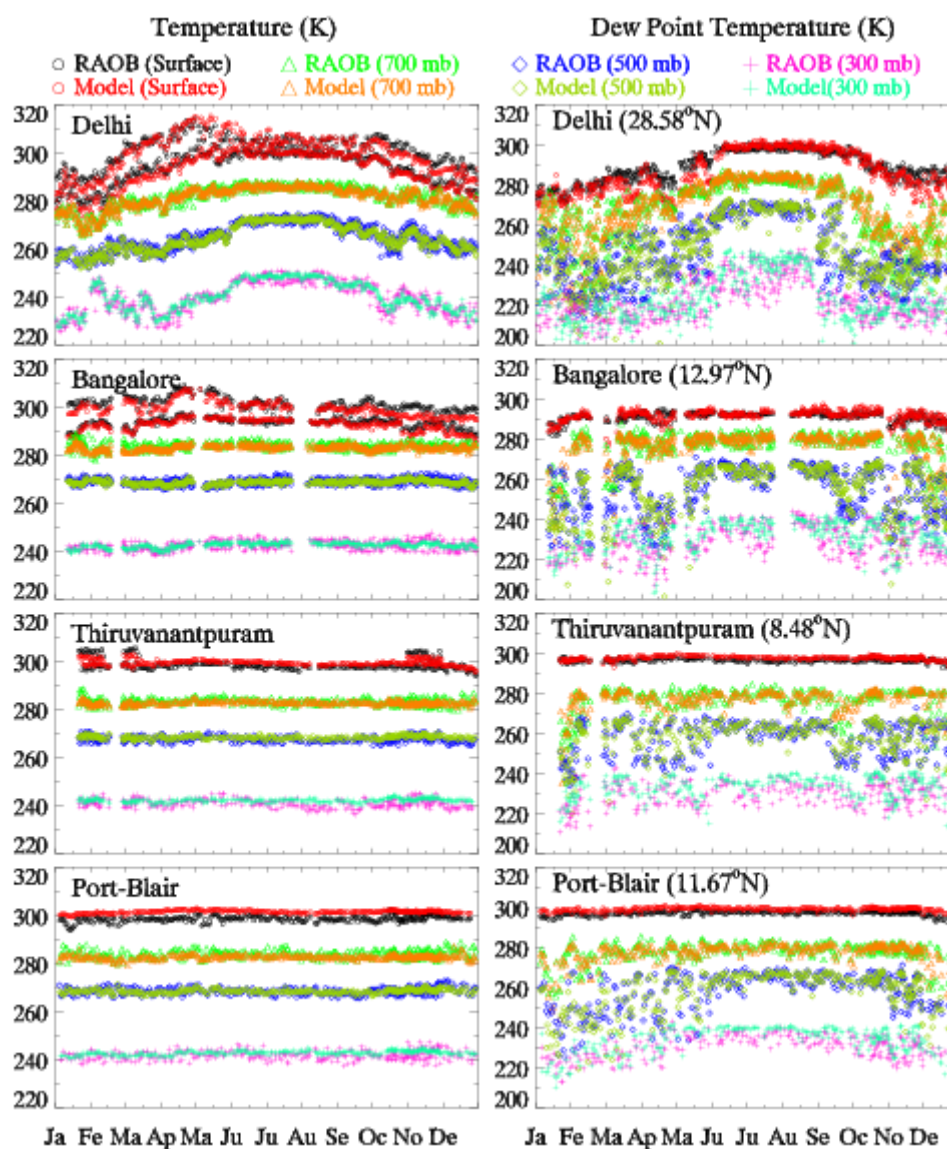


Figure 3-11: Seasonal variation of co-located observed and the model simulated temperature (left panels) and dew point temperature (right panels) at the surface, 700 hPa, 500 hPa and 300 hPa for Delhi (low altitude), Bangalore (moderately high altitude), Thiruvananthapuram (coastal) and Port-Blair (island) during 2008.

An examination of the land-use categories used by the model indicates that all three island sites (AMI, MIN and POR) and the six coastal sites (BOM, GOA, PAN, COC, THI and VIS)

are treated as “water bodies” by the model and the other four coastal sites (BHU, MAC, MAD and KAR) are treated as “Irrigated Cropland and Pasture”. The differences between the true and the model topography may also contribute to errors in the model simulated temperature. The actual altitudes of the site along with the altitude used by the model are shown in the Table 3-1. The difference in the true and the model topography is less than 250 m for all the sites and is less than 50 m for 26 out of the 34 sites considered here.

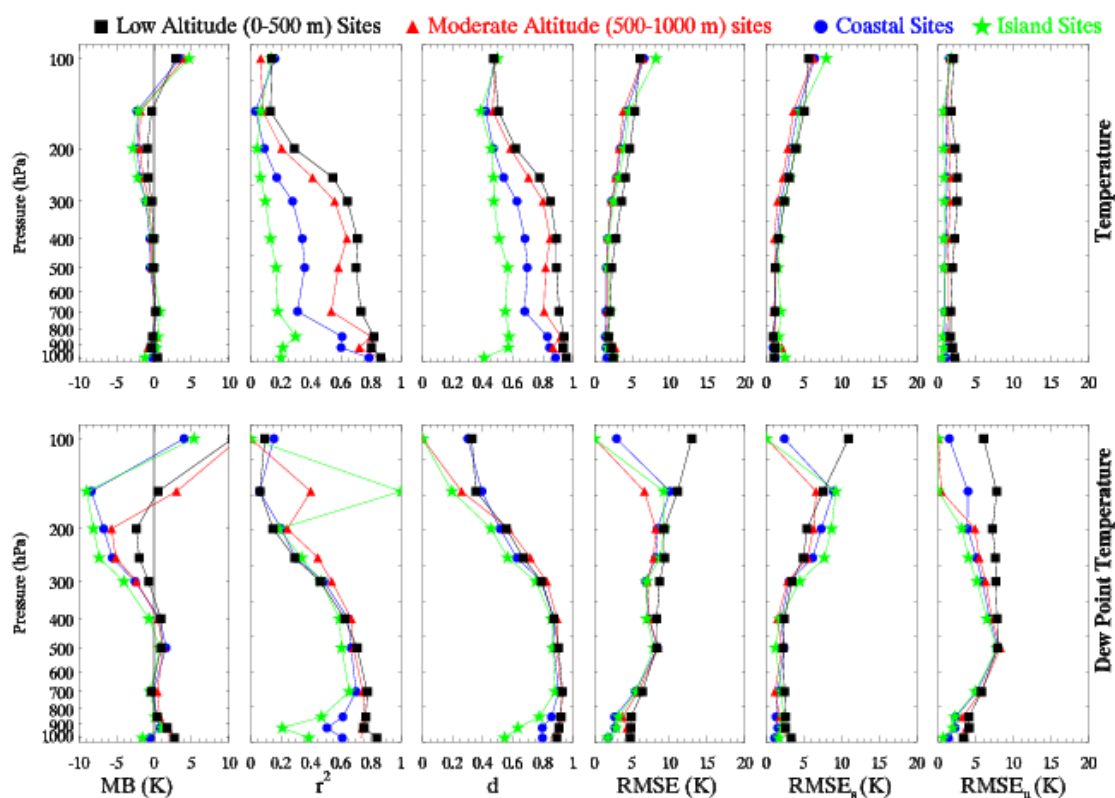


Figure 3-12: Vertical profiles of the statistical metrics for temperature (top panel) and dew point temperature (bottom panel) at all the sites belonging to low altitude, moderate altitude, coastal and island sites. Average profiles of the statistical metrics for each site category are also shown. The dotted lines represent the profiles for individual sites and solid lines connected by symbols represent the respective average profiles.

The MB, RMSE, $RMSE_s$ and $RMSE_u$ show a gradual increase in magnitude with altitude. For all the site categories, average values of MB, RMSE, $RMSE_s$ and $RMSE_u$ are lower for the temperature (0.2-7 K) compared to dew point temperature profiles (0.1-10 K). Systematic errors contribute more to RMSE between the model and in situ observations. Apart from the model, the errors in the radiosonde water vapor measurements due to reduced water vapor amount and slower response of the sensor to the ambient humidity at higher altitudes may also degrade the model-observation relationship particularly for the dew point temperature.

3.3.5 Tropopause Pressure (AIRS and Radiosonde)

The budget of trace species, in particular of ozone and water vapor, in the troposphere is affected through stratosphere-troposphere exchange processes and therefore evaluation of the model simulated tropopause pressure is also important. Since the model output does not contain the tropopause pressure, we derive it following the method of *Reichler et al.* [2003]. This method defines tropopause pressure as the lowest pressure level at which the lapse rate decreases to 2 K km^{-1} or less and the average lapse rate between this level and all higher levels within 2 km does not exceed 2 K km^{-1} . This method is reported to calculate the tropopause pressure with small errors of 10-20 hPa in the tropics and 30-40 hPa in the extratropics [*Reichler et al.*, 2003]. Here, the model simulated tropopause pressure is compared with that retrieved by AIRS and observed by the radiosonde (RAOB), both of which are estimated using the methodology of *Reichler et al.* [2003].

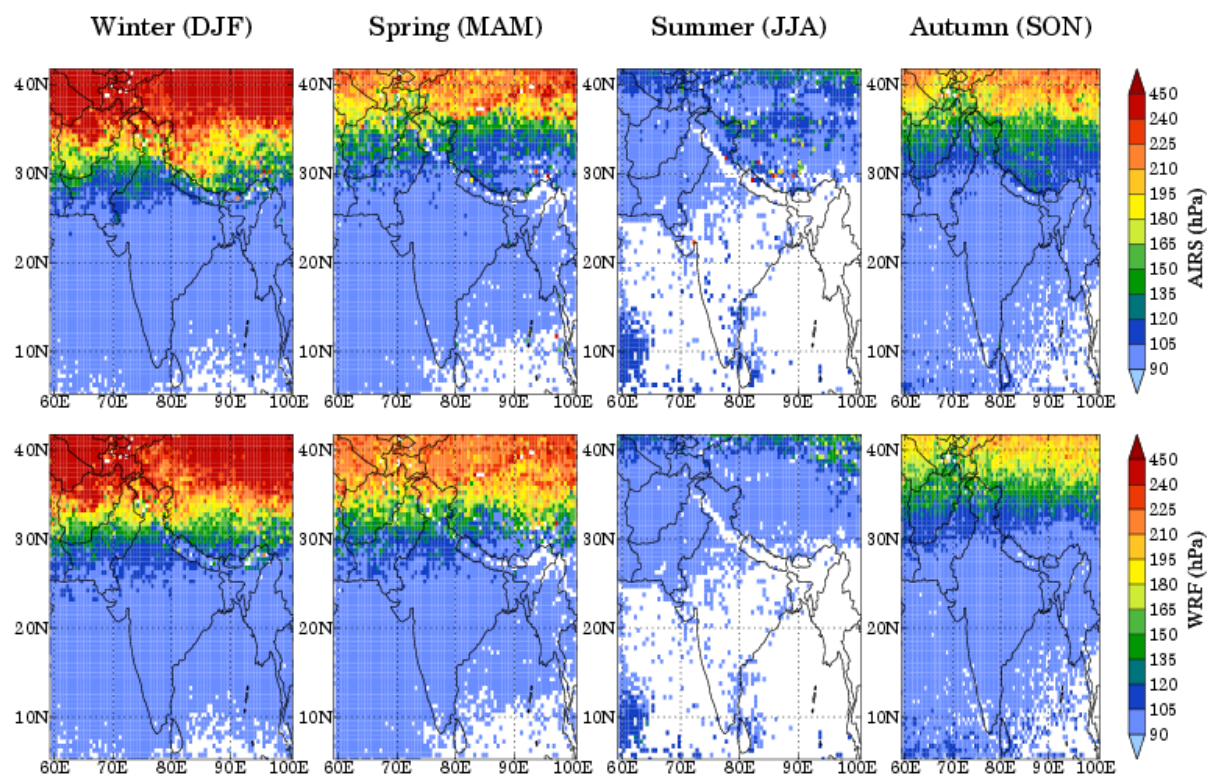


Figure 3-13: Spatial distribution of co-located AIRS retrieved (top panel) and model simulated (bottom panel) tropopause pressure during the winter, spring, summer and autumn seasons of the year 2008.

The spatial distributions of AIRS retrieved and model simulated tropopause pressure for winter, spring, summer and autumn are shown in Figure 3-13. The spatial distribution of

tropopause pressure as retrieved by AIRS is reasonably well simulated by the model during all seasons. The values of r^2 (> 0.6) and index of agreement (>0.9) between AIRS and model are high except during summer when there are fewer clear-sky observations and a smaller set of observations available. Both AIRS and model tropopause pressure show a distinct seasonal cycle with highest tropopause pressure in summer (90-100 hPa) and lowest in winter (120-270 hPa) over the regions located north of 30°N latitude belt. South of 30°N the seasonal amplitude is small (10-20 hPa). The latitudinal variation in tropopause pressure can be attributed to the seasonal variability in solar radiation at the sub-tropical latitudes. The differences between AIRS and the model tropopause pressure can be discerned over the topographically complex Himalayan region. The mean bias values in the model simulated tropopause pressure as compared to the AIRS retrievals are estimated as 1 hPa, -9 hPa, 2 hPa and 5 hPa for the four seasons, respectively and the corresponding RMSE values are 36, 36, 24 and 25 hPa, respectively. These differences over the Himalayan region could be attributed to the errors in the simulated temperature profiles associated with improper representation of surface topography in the model and the topography induced errors in the satellite retrievals.

Table 3-8: Annual average and standard deviation in co-located RAOB and WRF-Chem tropopause pressures for the four site categories defined in this study are shown along with mean bias and the root mean square error. All these statistical parameters are also shown for co-located AIRS and WRF-Chem tropopause pressure values. All the values are rounded off to their nearest integer values.

Site Category	WRF-Chem Vs RAOB				WRF-Chem Vs AIRS			
	Tropopause Pressure (hPa)				Tropopause Pressure (hPa)			
	RAOB	WRF-Chem	MB	RMSE	AIRS	WRF-Chem	MB	RMSE
Low Altitude	115 ± 14	101 ± 8	14	21	101±21	103±18	-2	22
Moderately High Altitude	115 ± 12	100 ± 2	15	19	98±4	99±2	-2	4
Coastal	118 ± 13	102 ± 2	16	21	100±18	101±2	-1	18
Island	120 ± 15	103 ± 2	17	23	99±2	102±2	-3	3

Apart from evaluation with AIRS retrievals, the errors in WRF-Chem simulated tropopause pressure are also quantified by comparing the model results with RAOB datasets. The annual

average values of the RAOB and the model estimated tropopause pressure values for the defined four site categories are shown in Table 3-8, which also shows the comparison of WRF-Chem and AIRS tropopause pressure for the four site categories. Mean WRF-Chem and AIRS tropopause pressure values are estimated by averaging the co-located data points over a $0.25^\circ \times 0.25^\circ$ box centered at the geographical location of a RAOB site. The annual average tropopause pressure values in WRF-Chem and AIRS are estimated to be around 98-103 hPa as compared to the RAOB values of 115-120 hPa. The MB and RMSE in the model estimated tropopause pressure values with respect to the corresponding RAOB values are estimated to be 14-17 hPa and 19-23 hPa respectively (Table 3-8) while the respective values resulting from comparison with AIRS are -1 to -3 hPa and 3-22 hPa respectively. By having an accurately placed tropopause, stratosphere-troposphere exchange processes should be reasonably represented. This is particularly important for the Himalayan region.

3.4 Sensitivity Simulations

The possible impacts of estimated errors in meteorological parameters on the simulations of chemical species concentrations were discussed qualitatively and individually for each parameter in the previous sections. This section presents the results from sensitivity simulations conducted to quantify the errors in chemistry simulations by combining the errors in meteorological parameters. The initial and boundary conditions for temperature, water vapor and wind components are modified by adding highest MB value, identified by comparing MB profiles of all the four seasons, of the respective meteorological parameter at each level between 1000 hPa and 100 hPa and 10-days runs are conducted during May and July (representing the months of dry and wet weather conditions). The MB profiles used for perturbation of meteorological parameters are shown in Table 3-9.

It is to be noted that emissions of trace gases and aerosols are not changed from the base model run values for these sensitivity runs. The percentage differences in model simulated tropospheric column ozone, CO and NO_x between sensitivity and base model runs are calculated for each grid point and are shown in Figure 3-14. In general, the percentage differences in tropospheric column ozone and CO are within $\pm 10\%$ while those in NO_x are as high as 25% for some of the grid points.

Table 3-9: Vertical profiles of mean bias in temperature, water vapor and wind components used to modify the initial and boundary conditions of these meteorological variables between 1000 and 100 hPa for sensitivity simulations. Note that mean bias profiles for water vapor are estimated only up to 300 hPa.

Pressure (hPa)	Temperature (K)	Water Vapor (%)	Zonal Wind (m s ⁻¹)	Meridional Wind (m s ⁻¹)
1000	1.4	-6.7	0.23	-0.40
925	-1.4	13.9	0.40	0.25
850	-0.4	-17.1	0.57	-0.47
700	-0.3	-16.8	0.20	-0.55
600	-0.8	-5.7	0.31	-0.70
500	-1.3	-14.3	0.15	-0.36
400	-0.8	-15.0	0.27	-0.05
300	-0.7	-32.0	0.32	0.11
250	-1.2	-	0.34	0.27
200	-1.2	-	1.22	0.51
150	-1.5	-	1.64	0.54
100	-1.8	-	1.37	0.44

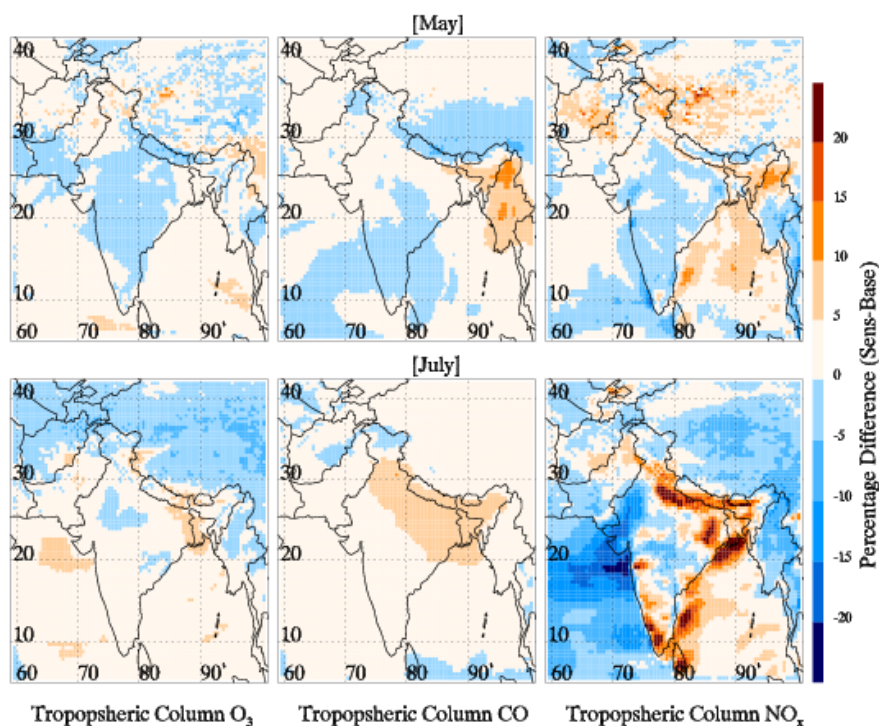


Figure 3-14: Spatial distributions of percentage differences in model simulated tropospheric column ozone, CO and NO_x between sensitivity and base model runs during May and July 2008.

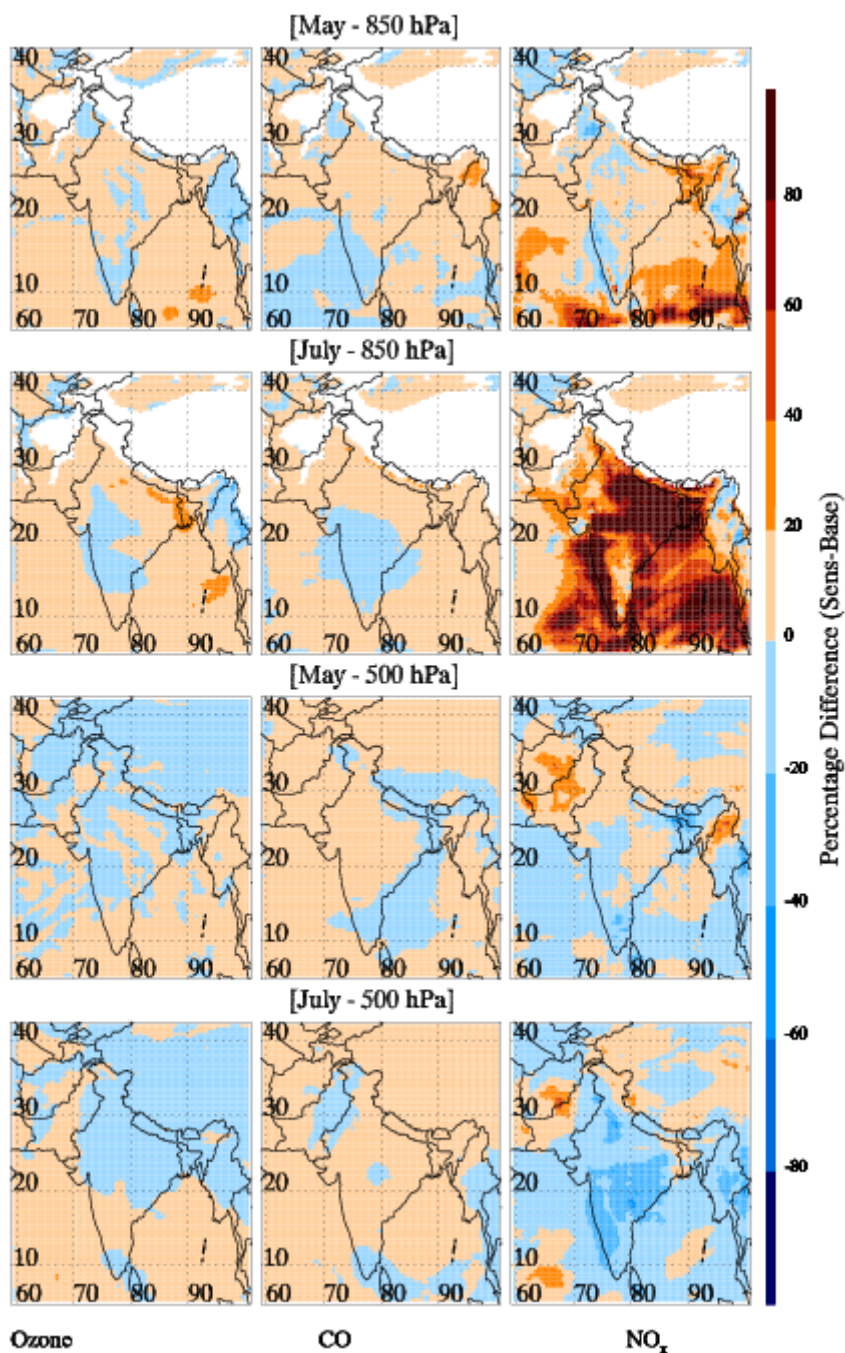


Figure 3-15: Spatial distributions of percentage differences in ozone, CO and NO_x at 850 and 500 hPa between sensitivity and base model runs during May and July 2008. White space in the top two panels indicates the regions of surface pressure lower than 850 hPa.

Largest differences in tropospheric column NO_x are seen over parts of Indo-Gangetic Plain, southern tip of India and along eastern Indian coast. Since these simulations do not include lightning-NO_x parametrization, therefore these differences cannot be attributed to lightning-NO_x process. In order to understand the reasons for larger differences in tropospheric NO_x

distributions, model simulated precipitation from sensitivity and base runs are analyzed along with spatial distributions of ozone, CO and NO_x at four different pressure levels (850 hPa, 700 hPa, 500 hPa and 300 hPa).

The spatial distributions of percentage differences in model simulated ozone, CO and NO_x at 850 and 500 hPa during May and July are shown in Figure 3-15. It is found that perturbations in meteorological parameters increase NO_x levels by more than 60-100% in the lower atmosphere and decrease them by 0-40% in the middle and upper troposphere. Similar enhancement in the lower atmosphere and decrease in middle-upper troposphere is also observed for model simulated nitric acid (HNO₃) and formaldehyde (HCHO) values. Analysis of modeled precipitation reveals that areas of enhanced NO_x, HNO₃ and HCHO levels are associated with reduced precipitation. The reduction in precipitation results in a longer HNO₃ lifetime allowing it to transform back to NO_x via photolysis. The percentage differences in ozone and CO at different pressure levels are estimated to be within $\pm 20\%$.

3.5 Summary

This chapter describes the evaluation of meteorological fields simulated by the Weather Research and Forecasting model coupled with Chemistry (WRF-Chem), set-up over the South Asian region, for the year 2008. The evaluation is carried out through comparison with a variety of datasets including radiosonde observations of temperature, dew point temperature and tropopause pressure, AIRS retrievals of temperature, water vapor and tropopause pressure, NCEP reanalysis zonal and meridional wind components and TRMM derived daily precipitation. The model results are co-located in both space and time with the quality-controlled observed data for proper comparison. The model successfully replicated the general features of the South Asian meteorology such as the seasonal changes in wind patterns along with the seasonal cycle of temperature, water vapor, precipitation and tropopause pressure. All these meteorological parameters showed a distinct seasonal cycle with highest values (altitude in case of tropopause pressure) in summer and lowest during winter.

The model-observation relationship and the errors in the model simulated parameters are quantified using different statistical metrics. The statistics obtained by this comparison indicate that the agreement between model and observations is better for temperature as compared to the other parameters. The model is biased cold near the surface in all the seasons

while it is biased warm aloft with MB and RMSE values within ± 2 K and 1-4 K, respectively. Both MB and RMSE in temperature are estimated to be higher at the surface and lower at upper levels. On average, the model is biased dry at 1000 hPa in winter and spring while it is biased wet at this level in summer and autumn with MB and RMSE values less than 20%. The mean bias and RMSE in water vapor at upper pressure levels range between 20-30% and 20-65% respectively. The model simulated winds show both an easterly and a northerly bias. RMSE in zonal and meridional wind components are estimated to be 2.3-5.1 m s^{-1} and 2.2-3.9 m s^{-1} respectively. MB and RMSE in wind components increase gradually with altitude. The spatial and temporal variability of rainfall events is also captured reasonably well by the model as indicated by higher odd ratio values (6-92). The frequency bias index values indicate that the model generally overestimates domain-wide precipitation except for some events exceeding 40 mm day^{-1} in winter.

The radiosonde observations are classified into low altitude, moderately high altitude, coastal and island sites. The seasonal variability of temperature and dew point temperature for these four categories is replicated well by the model. However, estimated statistical metrics indicate relatively better result for inland sites as compared to coastal and island sites. Analysis of the topography and land-cover used by the model suggest that erroneous representation of these surface characteristics possibly due in parts to the coarse model resolution (45 km) leads to a poorer correlation for these sites. The spatio-temporal variability of tropopause pressure is also simulated well by the model with mean bias and RMSE values less than 25 hPa.

The statistical metrics estimated for temperature, water vapor and wind components are also compared with a set of proposed benchmarks to assess the implications of errors in these parameters for chemistry simulations. In general, the errors in model simulated meteorological parameters are well within or comparable to the proposed benchmark values and comparison with other studies showed that the errors in these parameters should induce only small errors in chemistry simulations. The errors in simulations of tropospheric ozone, CO and NO_x due to biases in simulations of temperature, water vapor and wind components are estimated to be within \pm (10-25%). Overall, the model has good ability to simulate the spatio-temporal variabilities of meteorological parameters over this region and would be of sufficient quality for use in chemical transport modeling.

4. WRF-Chem: Chemistry Evaluation and Initial Results

The meteorological fields simulated by the WRF-Chem model over the South Asian domain were evaluated against a variety of observations in the previous chapter. It was shown that the model performs reasonably well in simulating the spatial and temporal variability of many key meteorological parameters such as temperature, water vapor, dew point temperature, zonal and meridional wind components, precipitation and tropopause pressure. This chapter presents the evaluation of the WRF-Chem simulated ozone, carbon monoxide and nitrogen dioxide against in situ (surface based and ozonesonde) and satellite based observations (TES, MOPITT and OMI). The satellite based measurements have proven to be useful for evaluating the chemical transport model in the recent years, particularly in the regions of limited ground-based observations as is the case here [e.g. *Pfister et al.*, 2004; *Herron-Thorpe et al.*, 2010; *Sheel et al.*, 2010]. Here, we have used the ozone retrievals from Tropospheric Emission Spectrometer (TES), CO retrievals from Measurements of Pollution in the Troposphere (MOPITT) and NO₂ retrievals from Ozone Monitoring Instrument (OMI). The chapter begins with a description of different observational datasets used for the model evaluation. The evaluation along with initial results is presented thereafter.

4.1 Datasets and Evaluation Methodology

4.1.1 Ground-based and Balloon-borne Observations

This study uses surface ozone observations reported from seven sites in India: Ahmedabad (23.0°N, 72.6°E, ~49 m amsl) [*Lal et al.*, 2000], Gadanki (13.5°N, 79.2°E, ~375 m amsl) [*Naja and Lal*, 2002], Mt. Abu (24.6°N, 72.7°E, ~1680 m amsl) [*Naja et al.*, 2003], Pune (11.7°N, 77.6°E, ~600 m amsl) [*Beig et al.*, 2007], Anantapur (14.7°N, 77.6°E, ~331 m amsl) [*Reddy et al.*, 2008], Nainital (29.4°N, 79.5°E, ~1958 m amsl) [*Kumar et al.*, 2010] and

Thumba (8.6°N, 77.0°E, ~2m amsl) [David and Nair, 2011]. The geographic locations of all these sites are shown in Figure 4-1 by white filled circles along with spatial distributions of anthropogenic CO, NO_x and NMVOC emissions, and population density.

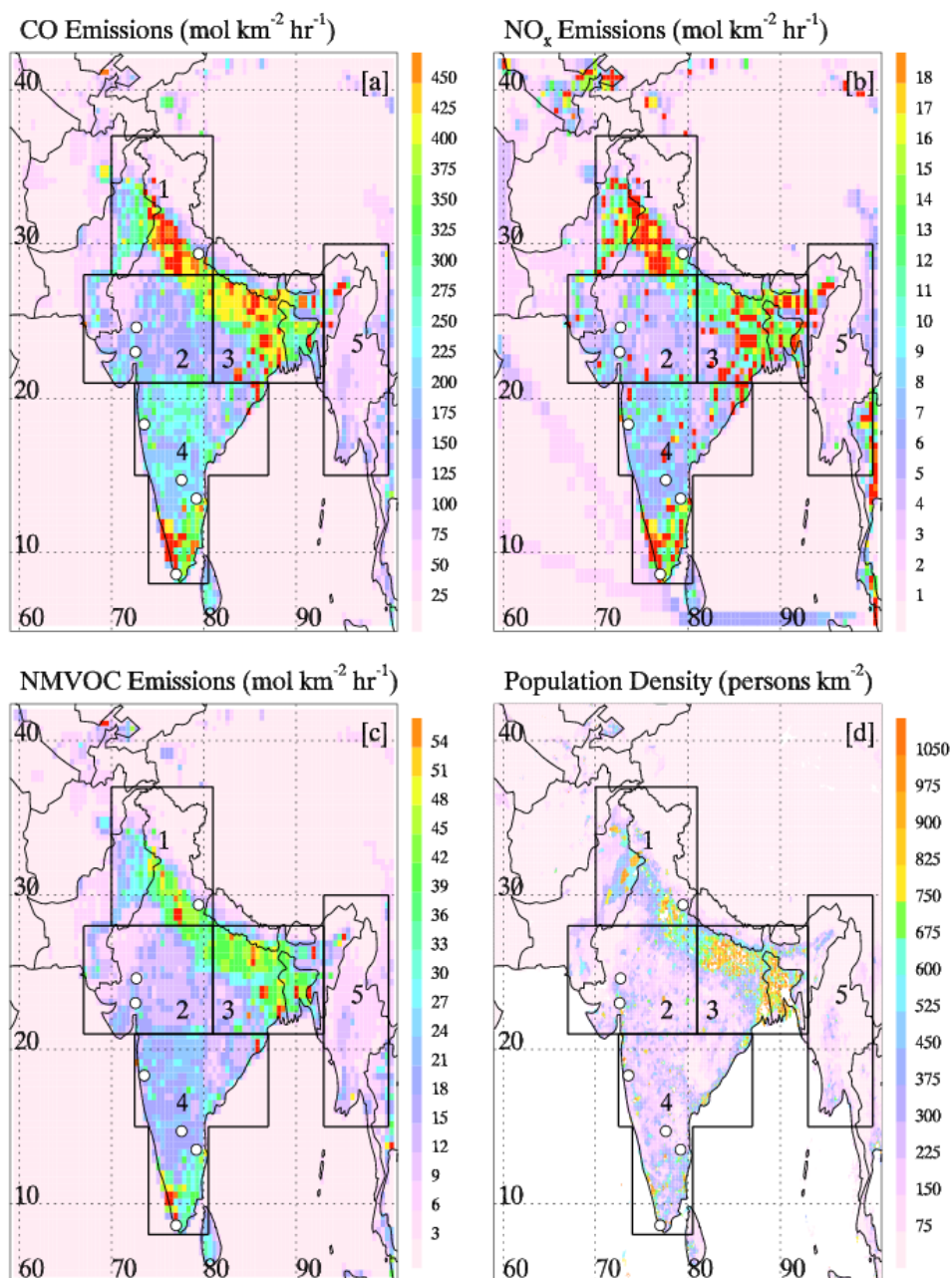


Figure 4-1: Spatial distributions of total anthropogenic (a) CO, (b) NO_x and (c) non-methane volatile organic compounds (NMVOC) emissions and (d) population density over the simulation domain. The emissions are representative of January. Regional classification of (1) North India, (2) West India, (3) East India, (4) South India and (5) Burma is also shown along with the locations of surface ozone observation sites (white filled circles) over the Indian region.

These sites are representative of different chemical environments ranging from urban (Ahmedabad), semi-urban (Pune) and rural (Anantapur and Gadanki) to coastal (Thumba) and high-altitude cleaner (Mt-Abu and Nainital) sites. These sites also cover nearly the entire latitudinal extent of India from about 8°N (Thumba) to about 30°N (Nainital). Surface ozone observations at these sites have been made using online ozone analyzers based on the well known technique of ultraviolet photometry, which is shown to have an absolute accuracy of about 5% [Kleinman *et al.*, 1994]. Additionally, surface measurements of CO and NO_x from Ahmedabad, Mt. Abu and Gadanki have also been used to evaluate the model simulations. CO observations were made either by analyzing the whole air samples with gas chromatography or by using online CO analyzers based on non-dispersive infrared spectroscopy, while NO_x measurements were made using online analyzers based on the chemiluminescence technique [e.g. Lal *et al.*, 2000; Naja and Lal, 2002; Naja *et al.*, 2003]. NO_x values reported in these observational studies could be higher than actual values due to use of Molybdenum convertors in the analyzers.

In addition to the surface observations, ozonesonde data at Delhi and Thumba have also been obtained for the period 2000-2009 from the World Ozone and Ultraviolet Radiation Data Center (WOUDC) (<http://woudc.org/>). Ozonesonde data from WOUDC have been used widely for evaluating satellite retrievals [e.g. Worden *et al.*, 2007; Nassar *et al.*, 2008] and model simulations [e.g. Emmons *et al.*, 2010] and to study long-term trends in tropospheric ozone [e.g. Logan, 1994; Cooper *et al.*, 2010]. The ozonesonde measurements over India are carried out by the Indian Meteorological Department (IMD) and are based on a modified electrochemical Brewer Bubbler ozone sensor [Shreedharan, 1968] for which the precision is estimated to be better than ±2% at the peak of the ozone layer [WMO, 1994]. These IMD ozonesondes have participated in the Jülich Ozone Sonde Intercomparison Experiment (JOSIE) held in 1996 [Harris *et al.*, 1998]. Ozonesonde data from these sites have also been used to study the long-term trends in tropospheric ozone over the Indian region [Saraf and Beig, 2004].

4.1.2 Satellite-borne Observations

This study uses Tropospheric Emission Spectrometer (TES) retrieved vertical profiles of ozone, Measurement of Pollution in the Troposphere (MOPITT) retrieved vertical profiles and total column of CO and Ozone Monitoring Instrument (OMI) retrieved tropospheric

column NO₂ abundances. TES aboard NASA's Earth Observing System (EOS)-Aura platform is an infrared Fourier transform spectrometer which measures the Earth's radiance in the 650-3050 cm⁻¹ (15.4-3.3 μm) spectral range with a ground footprint of about 5 km x 8 km in nadir mode [Beer *et al.*, 2001]. Aura operates at an altitude of about 705 km in sun-synchronous polar orbit with a local overpass time of about 1345 hours ± 15 min. The radiances measured by TES in the 995-1070 cm⁻¹ (10.1-9.3 μm) spectral range are used to retrieve atmospheric ozone concentrations [Bowman *et al.*, 2002; Worden *et al.*, 2004] using an optical estimation approach [Rodgers, 2000]. Here, Version 0004 Level 2 TES ozone retrievals from the nominal operational mode (global-survey mode) are used. In the clear sky conditions, TES nadir ozone profiles have approximately 4 degrees of freedom (DFS), two of which generally belong to the troposphere [Bowman *et al.*, 2002; Worden *et al.*, 2004]. The vertical resolution of TES nadir ozone profiles as estimated from averaging kernels and error covariances is typically 6-7 km in the troposphere [Worden *et al.*, 2004]. The comparison of TES nadir ozone profiles with ozonesonde measurements indicates a positive bias of 3-10 ppbv [Worden *et al.*, 2007; Nassar *et al.*, 2008].

MOPITT aboard the NASA EOS-Terra satellite, flying in a sun-synchronous orbit (local mean solar time of about 1030 in ascending node), is a gas filter radiometer and measures the thermal infrared radiation (near 4.7 μm) with a ground footprint of about 22 km x 22 km. These radiances are then used to retrieve CO mixing ratios profile and total column amounts [Deeter *et al.*, 2003a] using an optimal estimation method [Rodgers, 2000]. This study uses version 4.0 Level 2 MOPITT data products which provide CO mixing ratios at 10 pressure levels between the surface and 100 hPa with a difference of 100 hPa between the levels. The DFS of MOPITT CO retrievals is estimated to be more than 1 over the tropical and midlatitude regions [Deeter *et al.*, 2004]. MOPITT CO retrievals have been validated against aircraft CO measurements [Emmons *et al.*, 2004, 2007 and 2009] and are found to positively biased by about 20%.

The Ozone Monitoring Instrument (OMI) is also flying aboard NASA's EOS-Aura satellite and measures the radiation backscattered by the Earth's atmosphere and surface over the 0.27-0.5 μm wavelength range with a spatial resolution of about 13 km x 24 km at nadir in normal operational mode. The radiances measured by OMI are used for daily global retrievals of several trace species such as ozone, NO₂, BrO, SO₂, HCHO and aerosols. Here, we use the tropospheric column NO₂ datasets available from KNMI (Royal Netherlands Meteorological

Institute) because it provides access to the averaging kernel and a priori profiles that play a major role in comparing model results to satellite retrievals [e.g. *Emmons et al.*, 2004]. More details on the algorithm used to determine the tropospheric column NO₂ abundances at KNMI are given in *Bucsela et al.* [2006]. The comparison of OMI retrieved tropospheric column NO₂ amounts at KNMI with INTEX-B aircraft measurements indicate good correlation ($r^2 = 0.67$, slope = 0.99 ± 0.17) between two quantities with no significant biases [*Boersma et al.*, 2008]. OMI retrievals are found to correlate well ($r = 0.64$) with MAX-DOAS ground-based measurements [*Kramer et al.*, 2008]. However, a number of recent studies have suggested that KNMI OMI retrieval is biased positively, most likely with a magnitude of 0-30% irrespective of season [e.g. *Boersma et al.*, 2009a; *Zhou et al.*, 2009].

Level-2 tropospheric column NO₂ retrievals from Global Ozone Monitoring Experiment-2 (GOME-2) derived by KNMI are also used apart from OMI retrievals. Tropospheric column NO₂ retrievals from GOME-2 are retrieved using essentially the same approach as used for OMI although some differences exist due to the unique properties of two instruments [*Boersma et al.*, 2007]. The size of the GOME-2 viewing pixel (40 km x 80 km) is also different than OMI (13 km x 24 km). GOME-2 NO₂ retrievals have not been validated directly with in situ observations but are found to compare well with the validated SCIAMACHY retrievals [e.g. *Boersma et al.*, 2009a].

4.2 Evaluation Methodology

The model results are compared with ground-based observations by bi-linearly interpolating the model output to the geographical locations of these sites. Unlike in situ observations, satellite retrievals cannot be compared directly with the model output. This is because the retrievals of trace gases from radiances measured by the satellites depend on the relative sensitivity of the retrievals to different altitudes in the atmosphere and on the a priori information about the retrieved trace gas amounts. Thus, any modeled profile must account explicitly for a priori information and sensitivity of retrieved profiles to the true retrievals (as given by the averaging kernel) before its comparison with satellite retrieval.

A two step approach is employed here to compare model results directly with the satellite data. In the first step, best quality satellite retrievals are selected and the model output is co-located in both space and time with these best quality retrievals. In the second step, the spatially and temporally matched model results are transformed using the averaging kernel

and a priori profiles used in the satellite retrievals to obtain a model profile that a satellite instrument would measure for the modeled state of the atmosphere in the absence of other errors. These steps are discussed below.

4.2.1 Data Filtering and Model-Satellite Co-location

The best quality satellite retrievals are selected by using quality assurance flags and cloud cover information available with each satellite product. TES retrievals are screened for cloudy scenes and unphysical retrievals by selecting the retrievals corresponding to average cloud optical depth of less than 0.1, retrieval quality flag of 1 and O₃ C-cure quality flag of 1 [Osterman *et al.*, 2009]. This screening filtered out 55%, 69%, 81% and 67% of the total TES retrievals during winter (DJF), spring (MAM), summer (JJA) and autumn (SON) respectively. The influence of clouds on OMI retrievals is reduced by selecting pixels with cloud fraction less than 0.3 and unreliable retrievals are removed by selecting pixels with tropospheric column flag equal to 0 [Boersma *et al.*, 2009b]. The cloud screening criteria used here is same as is used for generating the level-2G cloud-screened tropospheric NO₂ product from OMI [Celarier, 2009]. The screening procedure removed 51%, 60%, 68% and 53% of total OMI retrievals during winter, spring, summer and autumn respectively. GOME-2 retrievals are also filtered by selecting pixels with cloud fractions less than 0.3 and tropospheric column flag equal to 0. Further, nighttime pixels from OMI and GOME-2 data are also removed from the analysis. The number of samples accepted for TES, OMI and GOME-2 is lowest during summer because of the prevalence of cloudy conditions over the simulation domain. Unlike TES and OMI, MOPITT retrievals are performed only for cloud-free pixels. MOPITT retrievals were screened for pixels with DFS value greater than or equal to 1. The DFS condition removed 21%, 11%, 14% and 17% of total MOPITT retrievals during winter, spring, summer and autumn respectively. The best quality retrievals are then co-located in space and time with model output using the method described in the previous chapter.

4.2.2 Averaging Kernels and a Priori Profiles

This section describes the procedures used for transforming modeled ozone, CO and NO₂ profiles for direct comparison with TES, MOPITT and OMI retrievals. The model data co-located with the best quality satellite retrievals is first mapped onto the pressure grids of the different sensors. The model top is located at 10 hPa while the TES pressure grid extends up to 0.1 hPa, therefore modeled ozone profiles above 10 hPa are approximated by appending

the TES a priori profile. The appended modeled profile is then interpolated to a fine level pressure grid (800 levels from 1260 hPa to 0.046 hPa) and then a mapping matrix is used to interpolate the fine level modeled profile to the 67 pressure level TES grid following *Worden et al.* [2007]. The TES averaging kernel A_{TES} and a priori constraint vector X_{apriori} are then applied to the WRF-Chem ozone profile X_{int} (which is now on TES pressure grid) to obtain the WRF-Chem ozone profile WRF-Chem (AK) through the following equation:

$$\text{WRF - Chem(AK)} = X_{\text{apriori}} + A_{\text{TES}} [X_{\text{int}} - X_{\text{apriori}}] \quad (4-1)$$

The WRF-Chem (AK) accounts for TES sensitivity and vertical resolution. A similar procedure is used to transform the modeled CO profiles using MOPITT averaging kernels and a priori profiles. However, a simple linear interpolation is used to interpolate the modeled profile on to the ten pressure level MOPITT grid from 1000 hPa to 100 hPa [*Deeter et al.*, 2003b].

The procedure for transforming the WRF-Chem simulated tropospheric column NO_2 abundances for comparison to OMI and GOME-2 retrievals is different from that used for TES and MOPITT. This procedure requires the user to calculate the tropospheric averaging kernels (A_{trop}) through the following equation:

$$A_{\text{trop}} = A \bullet \frac{\text{AMF}}{\text{AMF}_{\text{trop}}} \quad (4-2)$$

where A is the total column averaging kernel and AMF and AMF_{trop} are the air mass factors for the total columns and tropospheric columns, respectively. The tropospheric averaging kernels are then applied to the tropospheric vertical profiles of NO_2 simulated by WRF-Chem using the following equation:

$$Y_{\text{trop}} = A_{\text{trop}} \bullet X_{\text{trop}} \quad (4-3)$$

where Y_{trop} is the transformed model profile and X_{trop} is the tropospheric WRF-Chem NO_2 profile interpolated to the OMI/GOME-2 pressure grid. The tropopause pressure used for estimating tropospheric WRF-Chem profiles is taken from the OMI/GOME-2 data.

4.2.3 Statistical Metrics

Five statistical metrics namely index of agreement (d), root mean square error (RMSE), mean normalized gross error (MNGE), mean bias (MB) and mean normalized bias (MNB) are used to assess the model performance. These metrics were developed by *Yu et al.* [2005] and have been successfully used in several studies for evaluating the performance of regional air

quality models [e.g. *Zhang et al.*, 2006; *Han et al.*, 2009]. The index of agreement determines the model skill in simulating the variations around the observed mean and is defined as

$$d = 1 - \frac{N \cdot RMSE^2}{\sum_{i=1}^N (|O_i - \bar{O}| + |M_i - \bar{O}|)^2} \quad (4-4)$$

where the summations are performed over the total number of model-observations pair values (N) while O_i and M_i represent the i^{th} observed and modeled values respectively. The over bars over O and M indicate the average values in the observation and model respectively. The index of agreement is a dimensionless quantity and varies between 0 (no agreement between model and observations) and 1 (perfect agreement). The mean bias provides the information on the overestimation/underestimation of any variable by the model and is defined as

$$MB = \frac{1}{N} \sum_{i=1}^N (M_i - O_i) \quad (4-5)$$

MNB provides the information about the relative mean bias and is calculated as

$$MNB = \frac{1}{N} \sum_{i=1}^N \left(\frac{M_i - O_i}{O_i} \right) \times 100\% \quad (4-6)$$

The RMSE considers error compensation due to opposite sign differences and is calculated as

$$RMSE = \sqrt{\frac{\sum_{i=1}^N (M_i - O_i)^2}{N}} \quad (4-7)$$

Although RMSE encapsulates the average error produced by the model but it does not illuminate the sources or the types of errors. The MNGE represents the gross error in model simulations relative to the observations and is estimated as

$$MNGE = \frac{1}{N} \sum_{i=1}^N \left(\frac{|M_i - O_i|}{O_i} \right) \times 100\% \quad (4-8)$$

4.3 Comparison with Ground-based and Ozonesonde Observations

This section presents the comparison of WRF-Chem simulated ozone, CO and NO_x with ground-based and balloon-borne observations available over the Indian region. Since some of the ground-based observations are available for 1993-2000 while other data are representative of 2000-2010, published data are used here to demonstrate the model's skill in simulating the seasonal variations of these species. The monthly average modeled surface ozone is compared against ground-based observations (Figure 4-2) and it is seen that the seasonal variation in surface ozone over India is simulated reasonably well by the model.

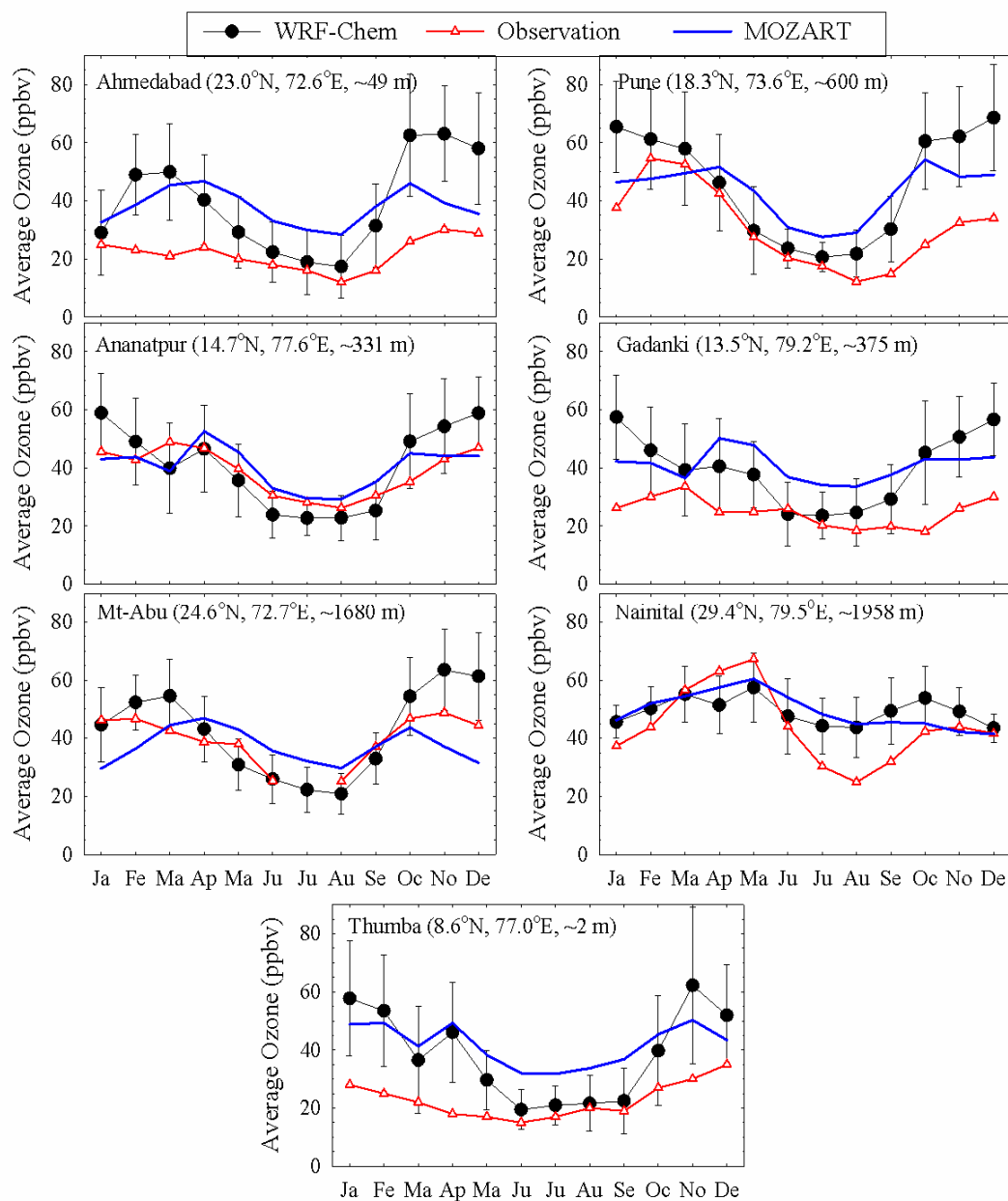


Figure 4-2: Comparison of the observed and WRF-Chem simulated seasonal variations in surface ozone at seven sites located within the Indian region. Note that, except for Nainital, the observations are not representative of the year 2008. These sites are representative of urban (Ahmedabad), semi-urban (Pune), rural (Anantapur and Gadanki), coastal (Thumba) and high-altitude cleaner (Mt-Abu and Nainital) chemical environments respectively. The standard deviations in monthly average ozone levels at these sites are generally 5-20 ppbv depending upon the season.

In general, surface ozone is lowest during summer and higher during other seasons. Ozone levels at all the sites except Nainital peak around late autumn to early spring while those at

Nainital are highest during April-May with a secondary peak during October-November. Surface ozone at Pune (in south west India) shows a clear maximum in late winter and early spring, while the two sites in western India (Ahmedabad and Mt Abu) show maximum ozone in late autumn and early winter. This indicates regional differences in the ozone seasonality over the Indian region. The regional differences in ozone seasonality will be explored further using TES retrievals in the next section.

Lower ozone levels observed over the Indian region during summer are in sharp contrast with the seasonal patterns observed typically in North America and Europe [e.g. Logan, 1985; Solberg *et al.*, 2008] but are similar to those observed over East Asia [e.g. Pochanart *et al.*, 2003; Wang *et al.*, 2006]. These lower summertime ozone levels over India [e.g. Lal *et al.*, 2000; Jain *et al.*, 2005; Roy *et al.*, 2008; Kumar *et al.*, 2010] can be attributed mainly to long-range transport of ozone-poor marine air-masses from the Arabian Sea, Indian Ocean and Bay of Bengal with some contributions from reduced photochemical production and wet scavenging of ozone precursors. WRF-Chem ozone levels show significant reduction during summertime at all the sites except at Nainital and it is seen that these reduced values are in good agreement with the observed values at these sites (Figure 4-2). An earlier study employing an offline regional model with comparable spatial resolution showed an overestimation of ozone levels during summer over India [Roy *et al.*, 2008].

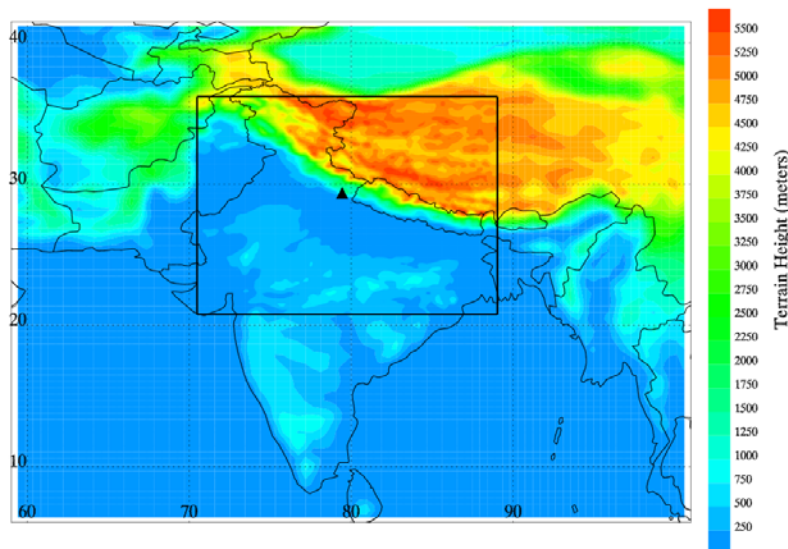


Figure 4-3: Parent and nested domain used in the sensitivity simulation. The location of Nainital is shown by a triangle.

Nainital is located in the Himalayan region, where topography is highly complex and the height of mountain-tops changes by about 2000 m over a distance of less than 50 km. Therefore, the model resolution of 45 km is unable to resolve the meteorological features induced by rapidly varying topography around Nainital. To assess the impact of the model resolution, we performed a nested domain run for 10 days during 10-20 July 2008. The selection of this period has been motivated by back-air trajectory analysis (not shown), which revealed consistent influence of marine air-masses at Nainital during this period. The nested domain covers the Northern Indian region with 121 x 115 grid points and has a spatial resolution of 15 km (Figure 4-3).

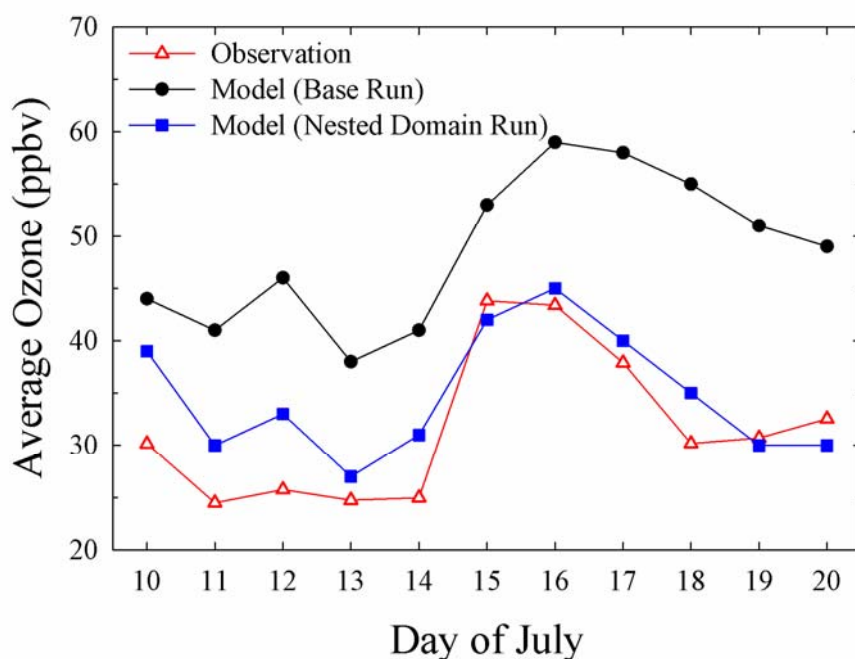


Figure 4-4: Day to day variations in surface ozone at Nainital during 10-20 July with output from base and nested domain model run.

The model simulated surface ozone from the nested domain is found to agree very well with surface ozone observations at Nainital (Figure 4-4) as mean bias reduced from 17 ppbv, in the base run, to 3 ppbv in the nested domain model run. This suggests that errors in surface ozone simulations over the central Himalayan region during summer/monsoon can be reduced by employing the model at a higher spatial resolution. However, longer simulations are required for lending more confidence to this finding. A high resolution annual simulation could not be performed for this study due to limited computational resources.

The seasonal variations of MOZART simulated surface ozone at these sites are also shown in Figure 4-2. Qualitatively, the ozone seasonality is reproduced well by MOZART at some sites but the performance of WRF-Chem is better than MOZART particularly at capturing the lower summertime ozone at all the sites and variations in surface ozone levels from September to December. This is likely due to the coarse horizontal resolution ($2.8^\circ \times 2.8^\circ$) of MOZART. At the global model resolution, the model has limited ability in simulating cloud cover and underestimation of cloud cover will enhance the photochemical ozone production. Transport and dilution errors will also impact the model ozone.

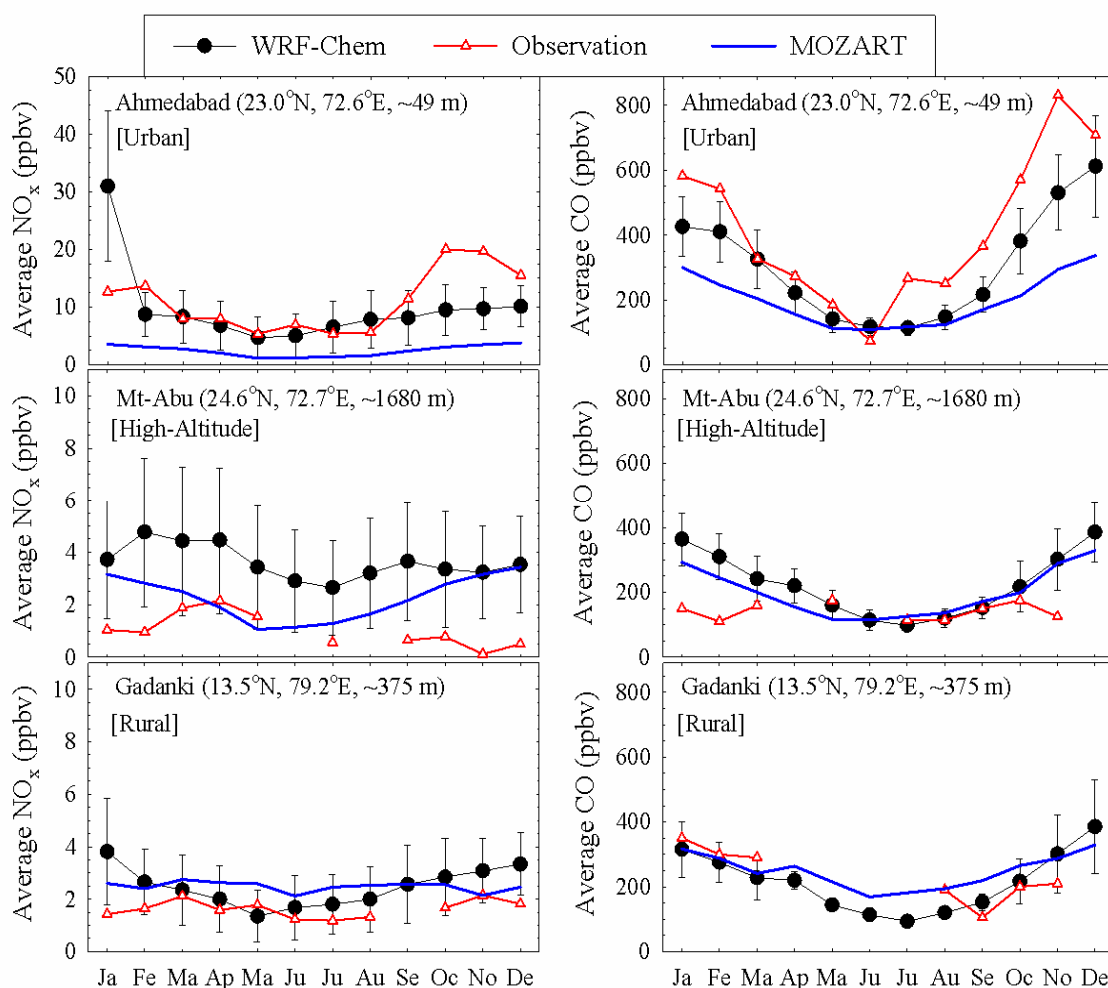


Figure 4-5: Comparison of the observed and WRF-Chem simulated seasonal variations in average surface NO_x (left panel) and CO (right panel) at three sites located within the Indian region. Note the scales vary among the sites and that the observations are not representative of the year 2008. The standard deviations in monthly average CO levels at these sites are generally 50-200 ppbv and those in NO_x levels are generally 1-6 ppbv.

The seasonal variations in near surface monthly average CO and NO_x observed at Ahmedabad, Mt. Abu and Gadanki are also compared to those simulated by WRF-Chem and MOZART (Figure 4-5). The seasonal variation of CO is reproduced well by the model for all three sites with highest values during late autumn - winter and lowest during summer/monsoon. NO_x values at Ahmedabad are unusually high in January and are due to significantly higher anthropogenic NO_x emissions over Ahmedabad in January (~120 mol km⁻² hr⁻¹) as compared to other months (20-30 mol km⁻² hr⁻¹). Discrepancies between the observed and modeled NO_x seasonalities are evident at all the sites. The reasons for larger discrepancies in the NO_x results will be discussed in more detail in section 4.4. The seasonal variations in MOZART CO and NO_x values are similar to WRF-Chem except for NO_x variations at Mt-Abu. Interestingly, MOZART CO values at Ahmedabad (urban site) are found to be lower than WRF-Chem values while they are similar to WRF-Chem at Mt. Abu (high altitude site) and Gadanki (rural site), which likely is due to the coarser resolution of MOZART-4. Previous studies [e.g. *Tie et al.*, 2010] showed that models at finer resolution capture more local features around urban emission sources, while coarser resolution models tend to dilute concentrations from localized emission sources.

In addition to the ground-based observations, the vertical distribution of the model simulated ozone at Delhi and Trivandrum is also compared with a ten year (2000-2009) climatology derived from ozonesonde observations. The comparison for winter, spring, summer and autumn is depicted in Figure 4-6. The total number of ozonesonde profiles used to obtain the climatology for Delhi and Trivandrum are 104 and 103, respectively. Both the ozonesonde and model data are averaged over 100 hPa pressure intervals. The vertical gradient as well as the seasonal variability of tropospheric ozone at both the sites is reproduced well by the model with average modeled values falling within one standard deviation of the climatological mean value below 200 hPa. However, the model underestimates the observed ozone values in the middle and upper troposphere in winter and slightly in spring over Delhi. MOZART ozone values also fall within one standard deviation (Figure 4-6) of the climatological mean value and show vertical gradient and seasonal variability similar to WRF-Chem.

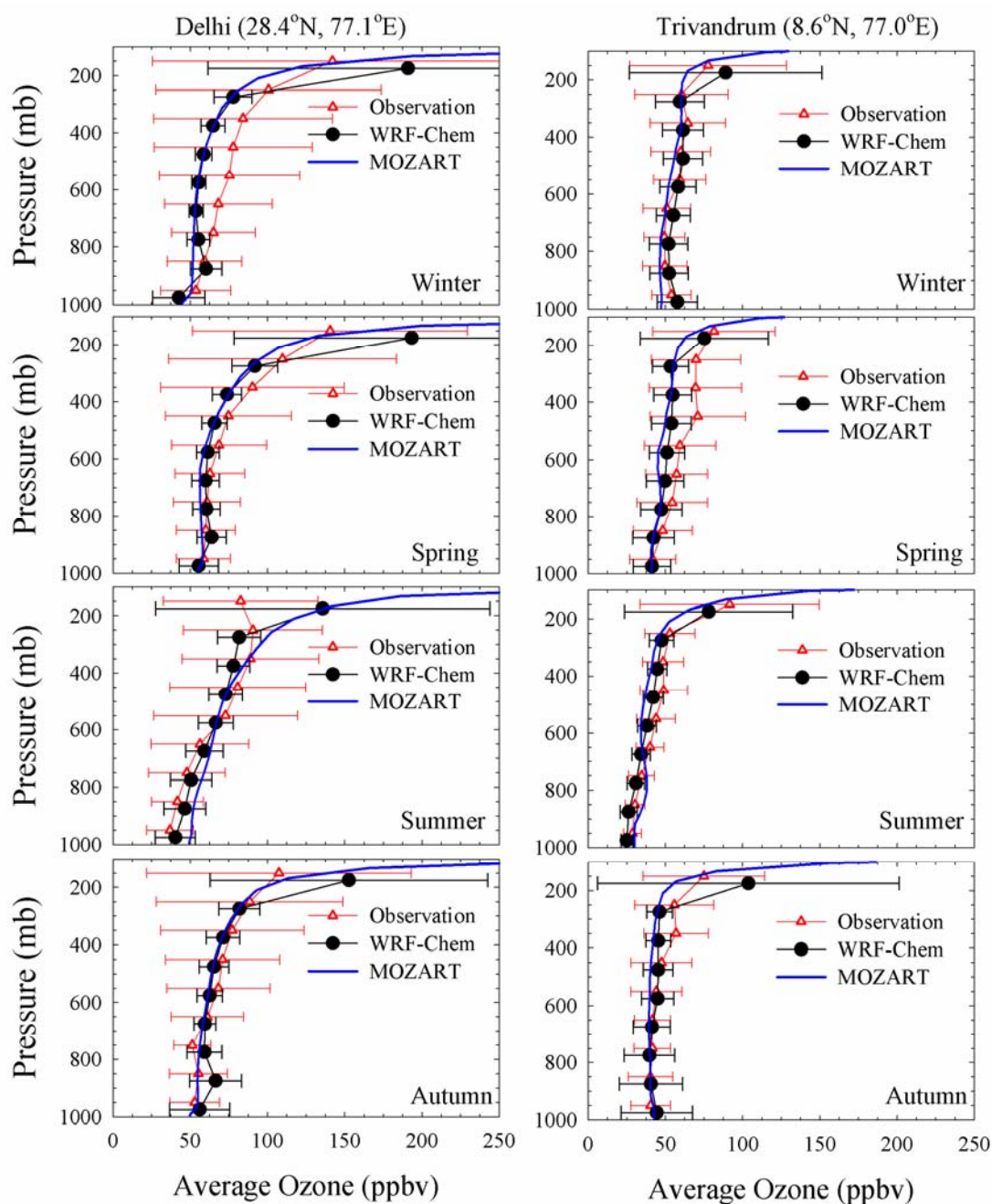


Figure 4-6: Comparison of the vertical profiles of ozone mixing ratios observed by ozonesondes and simulated by WRF-Chem at Delhi and Trivandrum. The observed profiles shown here are averages of all the ozonesonde measurements available during 2000-2009. Seasonally averaged MOZART ozone profiles for both sites are also shown to demonstrate the influence of boundary conditions.

4.4 Comparison with Space-borne Observations

The comparison of model simulated ozone, CO and NO_x against in situ observations presented in the previous section indicates that the model qualitatively reproduces the

observed features of lower tropospheric ozone and CO seasonality, but shows discrepancies in simulating NO_x seasonal variations. However, the model bias and errors were not quantified mainly due to differences in the time periods of observations and model simulations. Further, the comparison was limited to a few sites and thus information about the model performance over larger spatial scales was not obtained. In this section, satellite observations of ozone, CO and NO_2 are used to assess the model performance over the entire domain and to quantify the errors and biases in model simulations. The possible sources of uncertainties in the model simulations are also discussed.

4.4.1 Comparison with TES Ozone Retrievals

The vertical profiles of model simulated and TES retrieved ozone during winter (DJF), spring (MAM), summer (JJA) and autumn (SON) 2008 are shown in Figure 4-7. Both the model and TES values are averaged over 100 hPa pressure intervals. Similar to the comparison with ozonesonde observations, the vertical gradients and the seasonal variability of TES retrieved ozone profiles are reproduced well by the model. The model generally agrees well with TES retrievals below 300 hPa, but overestimates TES ozone above 300 hPa.

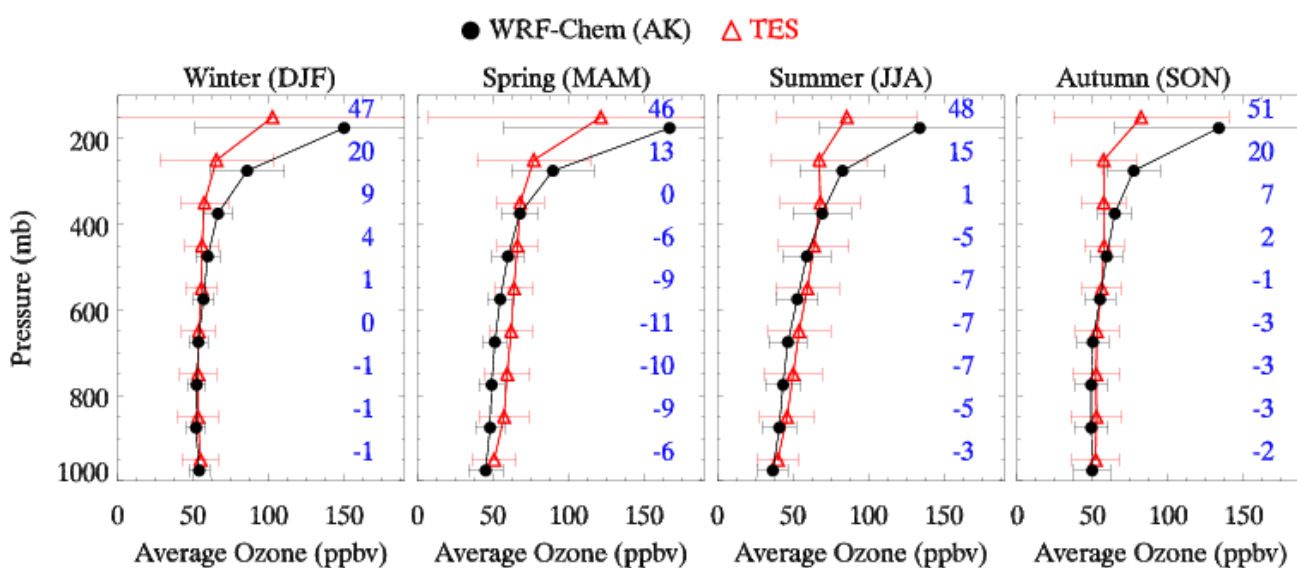


Figure 4-7: Comparison of the vertical profiles of ozone mixing ratios retrieved by TES and simulated by WRF-Chem during winter, spring, summer and autumn 2008. WRF-Chem profiles are transformed using TES averaging kernel and a priori profile before this comparison. The vertical profiles are obtained using co-located WRF-Chem and TES data. Numbers on the right in each panel give the difference in ozone mixing ratios between WRF-Chem and TES ($\text{WRF-Chem} - \text{TES}$).

The absolute difference between average modeled and TES retrieved values below 300 hPa is less than 12 ppbv during all the seasons, which is comparable to the positive bias of 3-12 ppbv reported in TES retrievals against ozonesonde observations [e.g. Nassar *et al.*, 2008]. The difference between WRF-Chem and TES values increases to 10-50 ppbv above 300 hPa. Larger differences between WRF-Chem and TES in the upper troposphere could be due to errors in ozone inflow from domain boundaries as comparison of TES retrievals with MOZART output within $\pm 10^\circ$ longitudinal and latitudinal bands around the domain boundaries revealed that MOZART ozone levels are higher by 10-70 ppbv than TES retrievals above 300 hPa.

Table 4-1: Seasonal variation in Index of Agreement (*d*), Mean Bias (MB), Mean Normalized Bias (MNB), Root Mean Square Error (RMSE) and Mean Normalized Gross Error (MNGE) computed using the co-located WRF-Chem and TES ozone values (year 2008) in the lower troposphere (Surface – 500 hPa). The total number of data points (*N*) used in the calculation is also listed.

Month	<i>d</i>	MB ¹	MNB ²	RMSE ¹	MNGE ²	N
Jan	0.64	0	3	10	14	4103
Feb	0.65	-1	1	10	15	4020
Mar	0.76	-5	-6	12	16	2919
Apr	0.75	-10	-15	15	18	3007
May	0.68	-11	-16	16	20	2351
Jun	0.76	-10	-14	17	18	1111
Jul	0.81	-7	-8	14	17	1412
Aug	0.90	-3	-1	11	17	2082
Sep	0.88	-3	-2	10	16	3068
Oct	0.83	-2	-1	10	14	3575
Nov	0.75	-2	0	11	15	2668
Dec	0.67	-1	2	10	15	3134

¹ Unit: ppbv

² Unit: %

The monthly statistical analysis of TES retrieved and model simulated lower tropospheric (surface to 500 hPa) ozone is shown in Table 4-1. The upper limit of 500 hPa, used in the

comparison, is similar to that used in validation studies of TES ozone retrievals [Worden *et al.*, 2007; Nassar *et al.*, 2008] and ensures that TES retrievals have sufficient sensitivity in the comparison region. Worden *et al.* [2007] showed that TES averaging kernel rows for pressure values between the surface and 500 hPa peak around 600-700 hPa indicating that TES has good sensitivity in this region. The index of agreement between model and TES varies between 0.64 and 0.9 during different months, which indicate good model performance in simulating the observed variation around the TES retrieved mean value. The model systematically underestimates the TES retrievals leading MB values ranging from 0 to -11 ppbv during all the months. The MB is smallest from August to February (-1 to -3 ppbv). MNB, RMSE and MNGE also show similar temporal variations and the estimated range is 0 to -16%, 10-17 ppbv and 14% to 20% respectively. Larger differences during spring and early summer could be indicative of additional ozone precursor sources (e.g. biomass burning) and processes during this period.

TES retrievals are also used to examine the regional variability in the lower tropospheric ozone over the Indian region and to investigate whether the model is capable of capturing the spatio-temporal heterogeneity. In this context, the seasonal variation of model simulated lower tropospheric (surface to 500 hPa) ozone is compared with the co-located TES retrievals over four geographical regions of India: North India (28°N-37°N, 70°E-81°E), West India (21°N-28°N, 67°E-81°E), East India (21°N-28°N, 81°E-93°E) and South India (15°N-21°N, 72.5°E-87°E and 8°N-15°N, 74°E-80.5°E) (Figure 4-1). The seasonal variation is also examined for the geographical region of Burma, including some part of East India (15°N-30°N, 93°E-100°E) that is characterized by lower anthropogenic emissions and very high fire activity especially during winter and spring. The comparison over Burma is intended to provide better insight into the model's response to emissions from biomass burning. Seasonal variations of model simulated and TES retrieved lower tropospheric ozone values over these five regions are shown in Figure 4-8.

The seasonal variations in TES retrievals are captured well by the model except in spring, when modeled ozone levels are somewhat lower. Regional differences in seasonality are also evident from Figure 4-8. Except for North India, ozone is lowest during summer-monsoon season, which as previously mentioned, is associated mainly with long range transport of ozone poor marine air masses, prevalence of cloudy conditions and extensive rainfall due to monsoonal circulation. For North India we find highest ozone during spring-summer and

lowest values during winter. The spring to summer decrease in ozone values is observed during June over South India and Burma, while in July over West and East India.

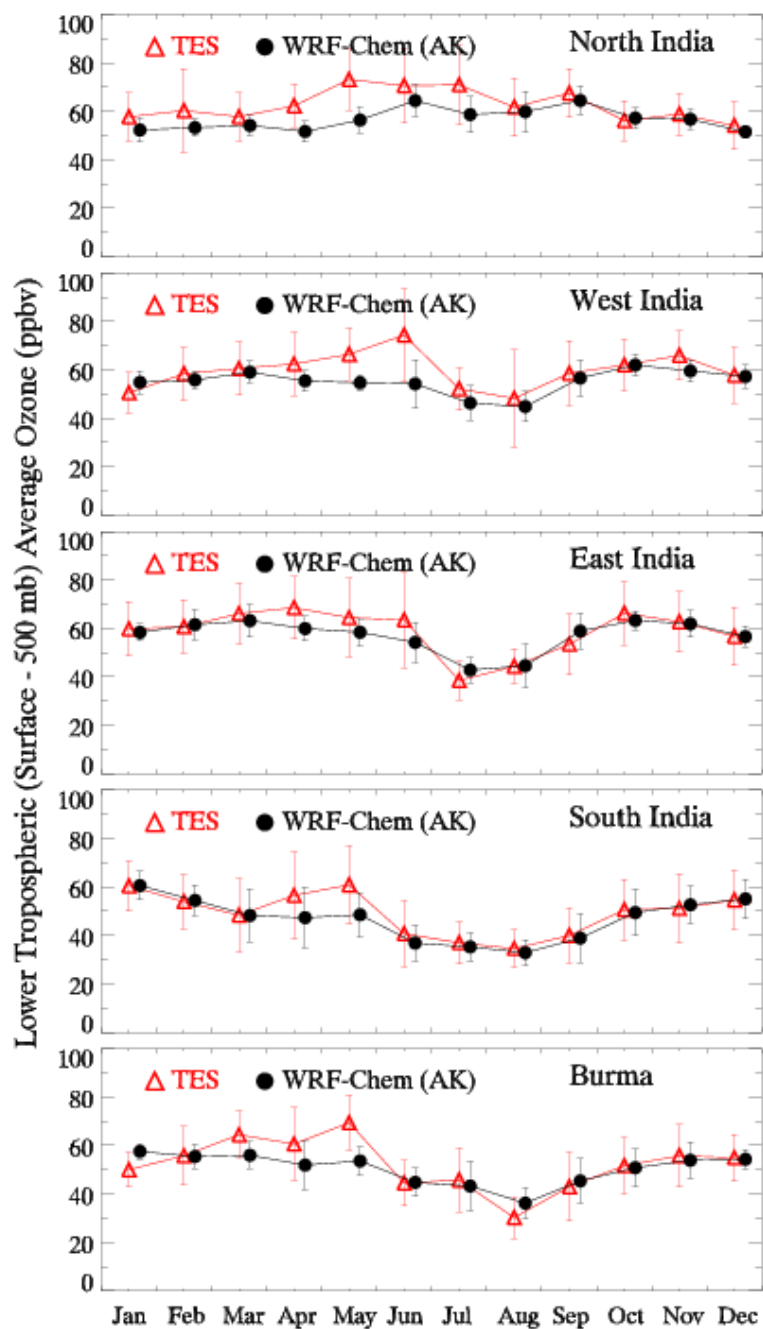


Figure 4-8: Seasonal variations in WRF-Chem simulated and TES retrieved ozone in the lower troposphere (surface-500 hPa) over the five regions defined in Figure 4-1.

To understand the regional differences in ozone seasonality over these regions, model simulated 2 m height water vapor mixing ratios and surface-reaching daytime (0730-1730 IST; IST is 5.5 hours ahead of GMT) solar radiation are analyzed. The water vapor mixing

ratios are found to be highest during summer/monsoon over all the regions but their values are significantly smaller over North India ($2\text{-}11\text{ g kg}^{-1}$) than those over other regions ($4\text{-}21\text{ g kg}^{-1}$) (Figure 4-9a). Like ozone, the seasonal variations in solar radiation over North India are also different from the other regions with highest values in spring-summer (Figure 4-9b).

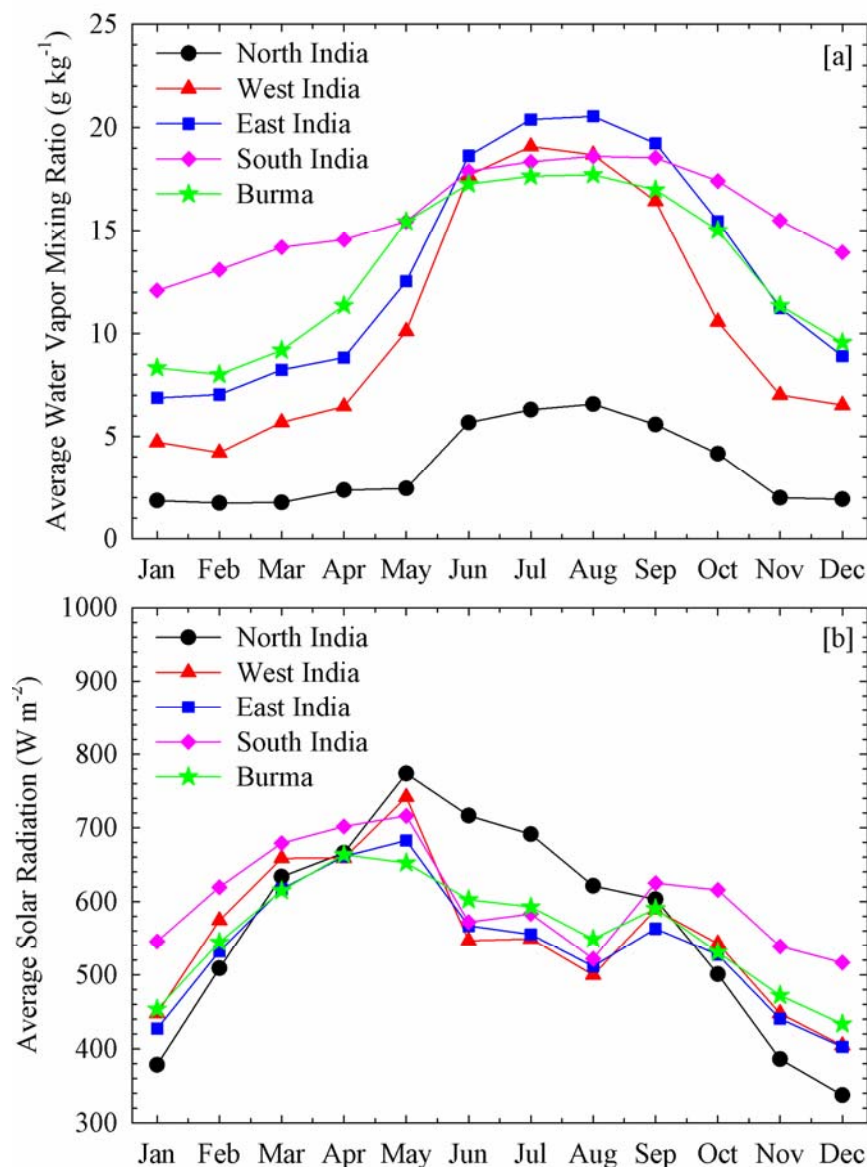


Figure 4-9: Variations in monthly average [a] 2m water vapor mixing ratios and [b] surface reaching daytime (0730-1730 IST) solar radiation over North India, West India, East India, South India and Burma regions.

This suggests that regional differences in ozone seasonality over India are associated with temporal differences in the start of the monsoon and the arrival of pristine marine air masses to the respective regions. Such latitudinal differences in transition from spring maximum to

summer minimum have also been reported over East Asia and associated with the spatially varying influence of Asian monsoon [e.g. *He et al.*, 2008; *Lin et al.*, 2009].

Another notable regional difference is observed during the transition from autumn to winter season. TES ozone over South India continues to increase from summer through autumn to winter while ozone over other regions increases from summer to autumn and decreases or becomes steady during winter. This is due to the availability of higher solar radiation over South India as compared to other regions during winter (Figure 4-9b). The differences between TES and WRF-Chem are largest during spring and particularly over North India. The poor agreement between the model and TES over North India is likely associated with improper representation of surface properties and errors in meteorological simulations due to complex topography over this region. The errors in model simulated ozone during spring could also result, in part, due to underestimation of CO and NO_x by the model (likely due to underestimation of CO and NO_x emissions by biomass burning) as shown in subsequent sections.

4.4.2 Comparison with MOPITT CO Retrievals

The spatial distributions of model simulated and MOPITT retrieved seasonal mean total column CO during winter, spring, summer and autumn of the year 2008 are shown in Figure 4-10. Both model and MOPITT data are averaged over a 0.25° x 0.25° grid. The MOPITT retrieved total column CO values are mostly representative of the free tropospheric CO, which is the region where MOPITT retrievals have highest sensitivity. The spatial variability as well as the seasonal variation of the MOPITT retrieved total column CO is reproduced well by the model. In general, both the model and MOPITT are highest during winter, decrease during spring, attain minimum levels during summer and increase again during autumn.

The percentage difference between model and MOPITT relative to MOPITT retrieved total column CO abundances is also shown in Figure 4-10. The model is generally within ± 20% of MOPITT, but mostly underestimates MOPITT during spring and overestimates MOPITT during other seasons. The monthly variation of different statistical metrics calculated using the co-located WRF-Chem and MOPITT retrievals is shown in Table 4-2.

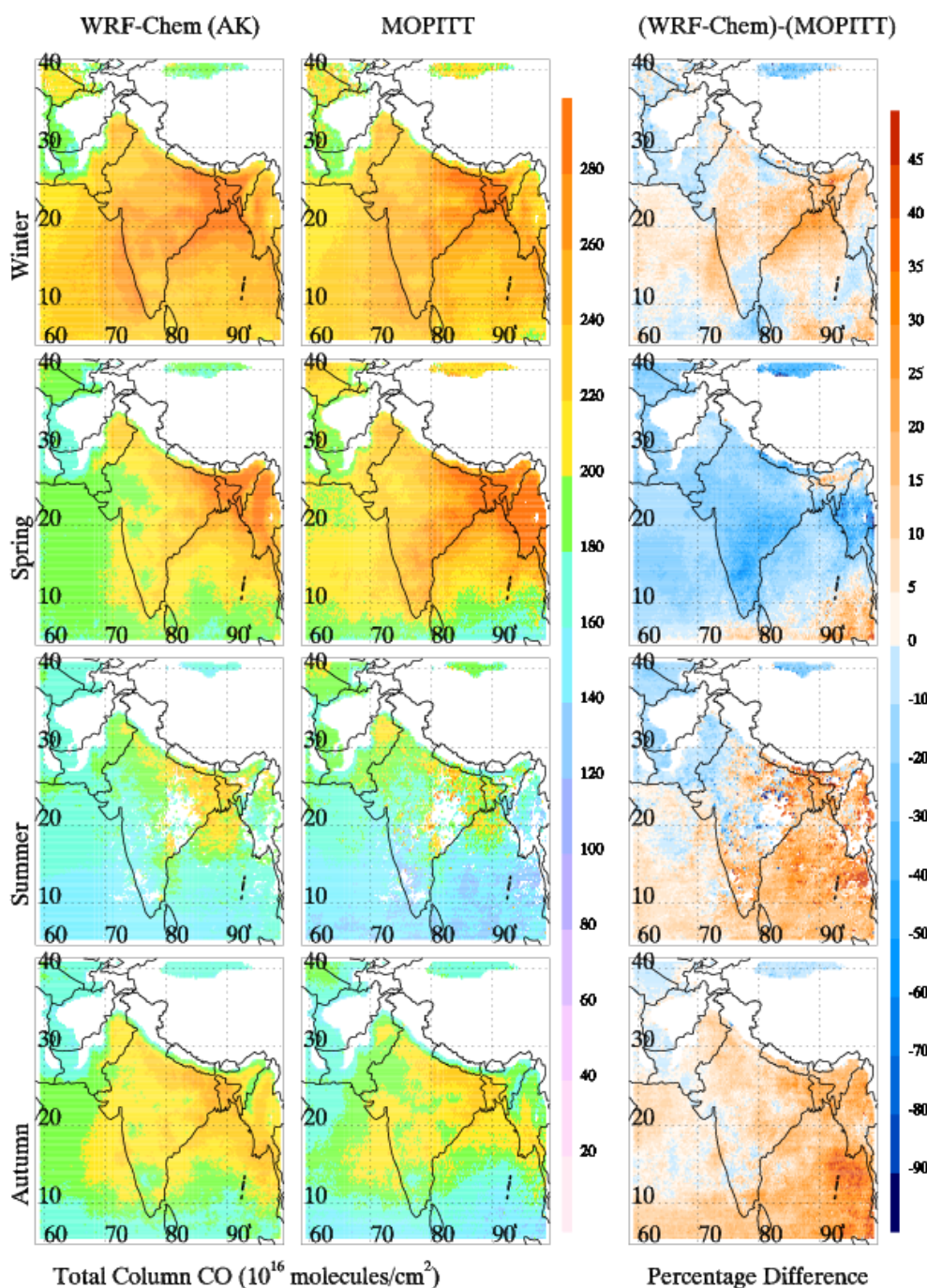


Figure 4-10: Spatial distributions of WRF-Chem simulated and MOPITT retrieved total column CO during winter (DJF), spring (MAM), summer (JJA) and autumn (SON) 2008. Note that WRF-Chem profiles are smoothed with MOPITT averaging kernel before comparison.

The index of agreement varies between 0.63 and 0.84 indicating that the model performs generally well in simulating the variations around the MOPITT mean. The model systematically underestimates MOPITT retrievals from February to July with MB ranging

from $-0.33 \bullet 10^{17}$ to $-2.21 \bullet 10^{17}$ molecules cm^{-2} and overestimates MOPITT during August-January with MB ranging from $0.05 \bullet 10^{17}$ to $1.32 \bullet 10^{17}$ molecules cm^{-2} . The mean bias is highest during spring (high fire activity season). MNB, RMSE and MNGE also show similar seasonal variability and are estimated to be about 7 to -9.3%, $2.38 \bullet 10^{17}$ to $3.45 \bullet 10^{17}$ molecules cm^{-2} and 8% to 11%, respectively.

Table 4-2: Seasonal variation in Index of Agreement (d), Mean Bias (MB), Mean Normalized Bias (MNB), Root Mean Square Error (RMSE) and Mean Normalized Gross Error (MNGE) computed using the co-located WRF-Chem and MOPITT retrieved total CO column values. The total number of data points (N) used in the calculation is also listed.

Month	D	MB ¹	MNB ²	RMSE ¹	MNGE ²	N
Jan	0.74	1.18	-5.0	2.58	8.1	146900
Feb	0.83	-1.13	-4.2	2.71	7.9	116336
Mar	0.84	-1.77	-6.4	3.45	10.2	179429
Apr	0.75	-2.21	-8.8	3.66	11.4	189166
May	0.74	-2.02	-9.3	2.86	10.5	140377
Jun	0.67	-0.78	-2.8	2.65	9.6	51872
Jul	0.63	-0.33	-0.1	2.41	9.1	47443
Aug	0.71	0.05	1.8	2.17	8.9	64440
Sep	0.69	0.68	5.2	2.22	10.2	117444
Oct	0.75	1.10	6.9	2.41	10.5	166349
Nov	0.82	1.08	5.7	2.38	9.0	190242
Dec	0.78	1.32	6.0	2.71	9.0	152983

¹Unit: $\times 10^{17}$ molecules cm^{-2}

²Unit: %

The relationship between WRF-Chem and MOPITT retrieved total column CO is further portrayed in terms of scatter plot analysis in Figure 4-11. Data over India and Burma are represented by red triangles and green squares respectively while data over the other regions are shown as grey filled circles. The correlation coefficients (r) for these regions are estimated to be 0.43 to 0.91 during all the seasons. The agreement between WRF-Chem and MOPITT is better during winter and autumn as compared to spring and summer. Lowest r values during summer could in part be associated with a fewer number of samples due to wide-spread cloud cover associated with monsoonal circulation over this region and also due

to larger errors in meteorological parameters during summer. WRF-Chem and MOPITT column CO over the entire domain are generally distributed between the $y=0.5x$ and $y=2x$ lines. However, MOPITT CO retrievals for both Burma and India are mostly overestimated by WRF-Chem during all the seasons except during spring when they are underestimated.

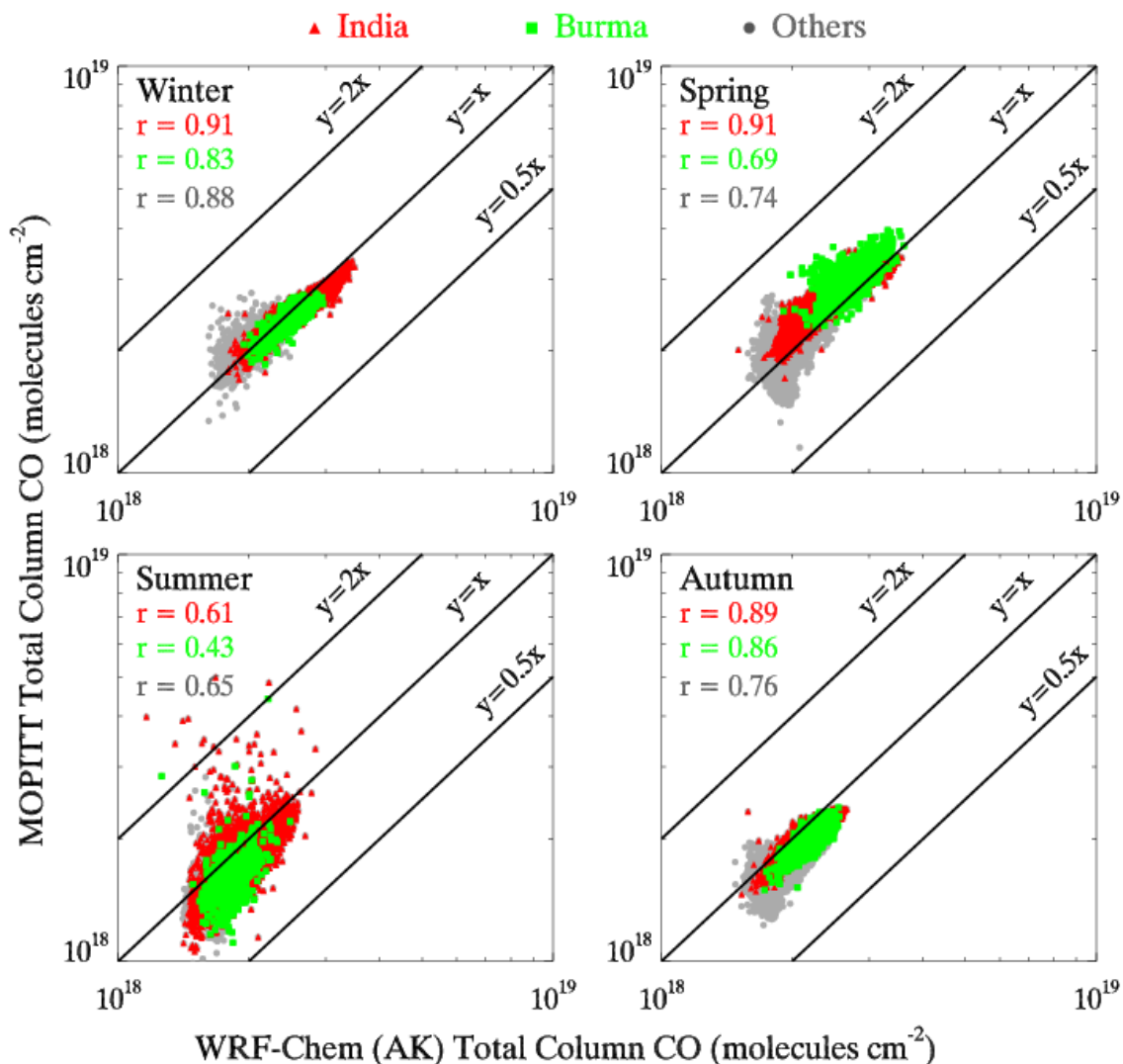


Figure 4-11: Scatter plot between seasonally averaged WRF-Chem simulated and MOPITT retrieved total column CO during winter, spring, summer and autumn of the year 2008. Others correspond to the areas not covered by regions 1-5 shown in Figure 4-1. The correlation coefficients for each region are also shown.

Since biomass burning constitutes the major fraction of total CO emissions over Burma, it is suggested that CO emissions from biomass burning could be slightly underestimated. In addition, the absence of plume-rise parameterization in the present model simulations can also contribute to underestimation over the biomass burning regions. A sensitivity study

showed that inclusion of plume-rise parameterization during April can increase tropospheric column CO by 10-50% over biomass burning regions. The overestimation of MOPITT CO retrievals during other seasons (characterized by low fire activity) indicates slight overestimation of anthropogenic emissions over this region.

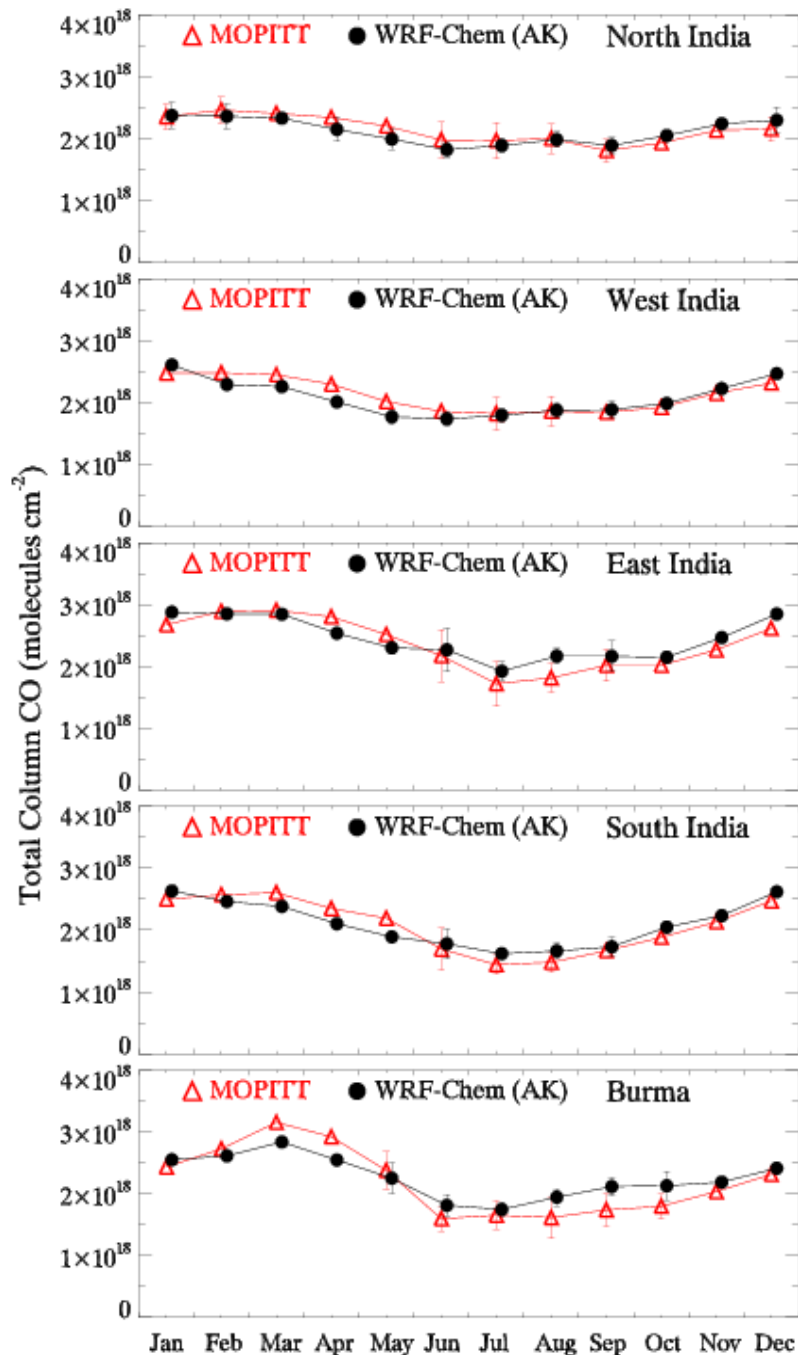


Figure 4-12: Seasonal variations in WRF-Chem simulated and MOPITT retrieved CO total column over the five regions defined in Figure 4-1.

The seasonal variations in the model simulated and the MOPITT retrieved total column CO abundances over the defined five regions agree well as shown in Figure 4-12. The seasonal variation in both the model simulated and MOPITT retrieved total column CO over Burma are much different from the Indian regions. Total column CO over Burma is highest during March-April while those over the Indian regions are highest during winter. The March-April maximum in CO over Burma is associated with intense high biomass burning activity during these months. Biomass burning activity over India is also highest during spring but biomass burning does not increase total column CO values significantly because CO emissions from biomass burning over the defined four Indian regions are estimated to be lower than the corresponding anthropogenic CO emissions by 2-32% while those over Burma are estimated to be higher than the anthropogenic CO emissions by 3-31%.

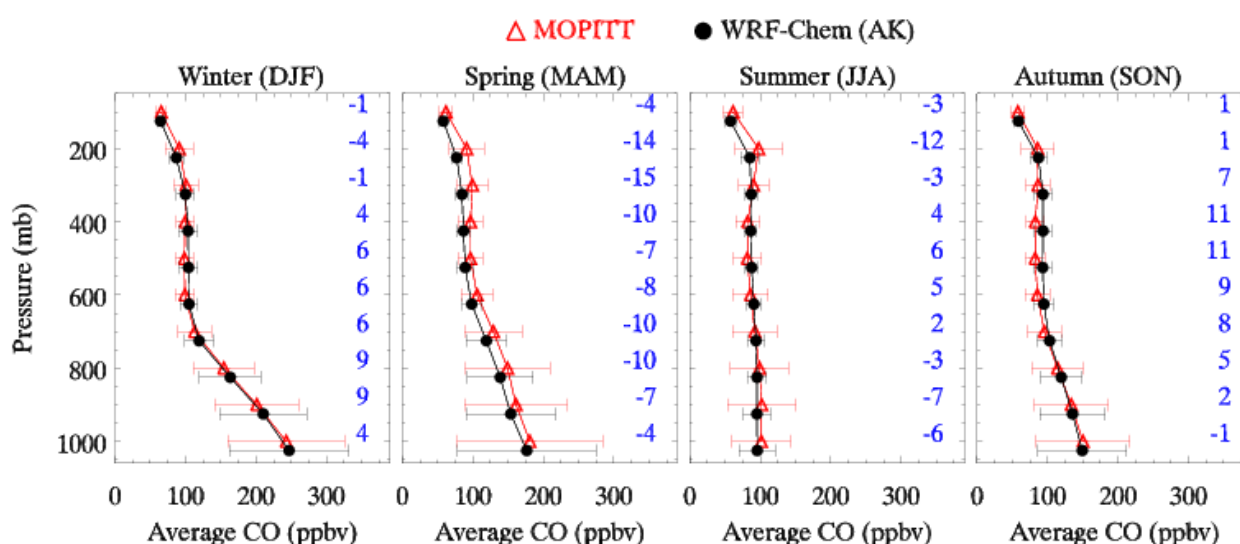


Figure 4-13: Comparison of the vertical profiles of CO mixing ratios retrieved by MOPITT and simulated by WRF-Chem during the winter, spring, summer and autumn seasons 2008. WRF-Chem profiles are transformed using MOPITT averaging kernel and a priori profile before this comparison. The vertical profiles are obtained using co-located WRF-Chem and MOPITT data. The difference between WRF-Chem simulated and MOPITT retrieved average CO value (ppbv) is also shown for each level.

In addition to the total CO column, the model simulated vertical distributions of CO are also compared to MOPITT retrievals for different seasons (Figure 4-13). The vertical gradient of MOPITT CO retrievals is captured well by the model during all the seasons with differences in the order of -15 ppb to 12 ppbv. These values are comparable to the bias (< 20 ppbv) reported in MOPITT retrievals against in situ aircraft measurements [Emmons *et al.*, 2004].

4.4.3 Comparison with OMI NO₂ Retrievals

The spatial distributions of the model simulated and OMI retrieved seasonal mean tropospheric column NO₂ during winter, spring, summer and autumn 2008 are shown in Figure 4-14. Both model and OMI data are averaged over a 0.25° x 0.25° grid.

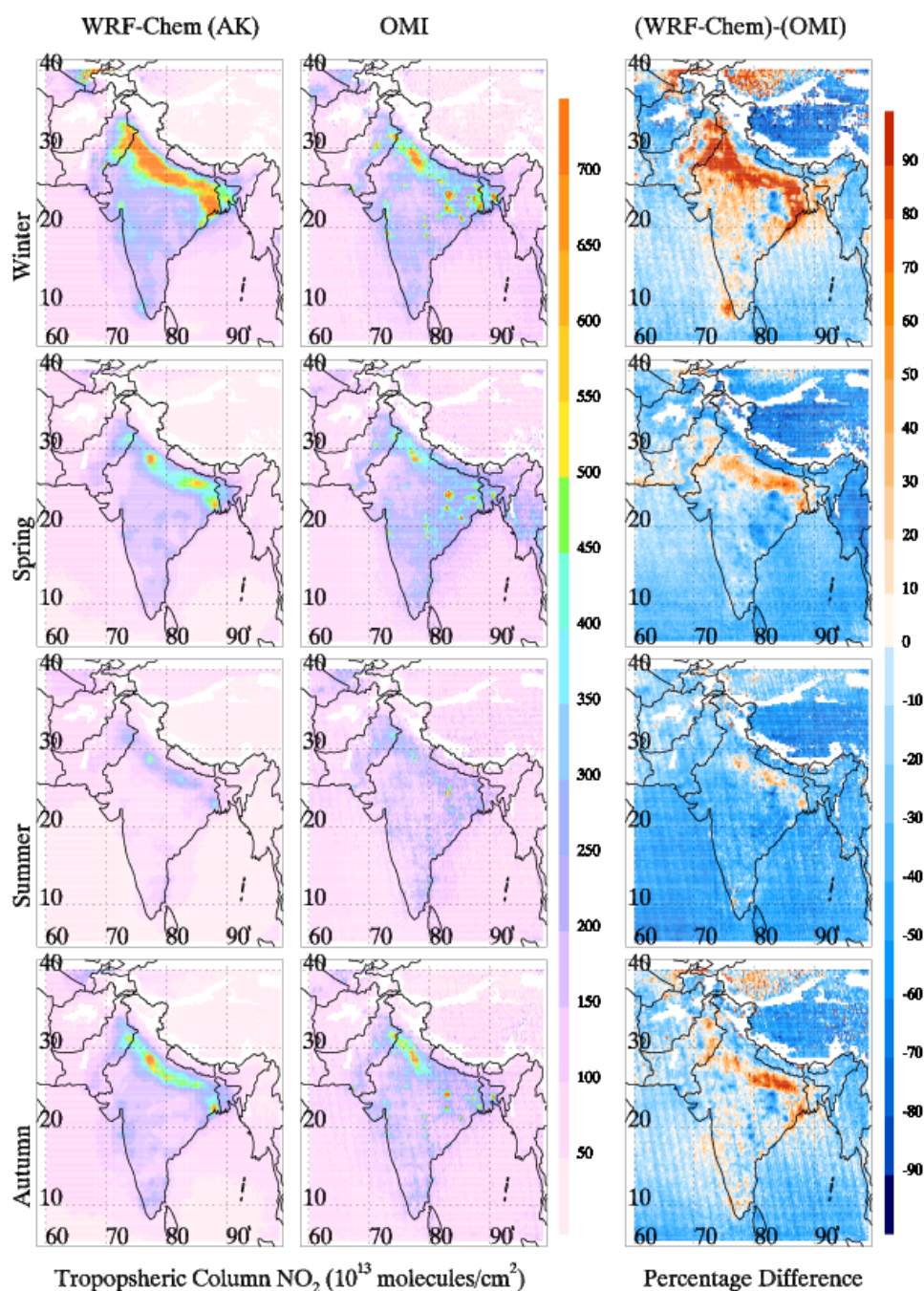


Figure 4-14: Spatial distributions of WRF-Chem simulated and OMI retrieved tropospheric column NO₂ during winter (DJF), spring (MAM), summer (JJA) and autumn (SON) 2008. Note that WRF-Chem profiles are smoothed with OMI averaging kernel before comparison.

Like OMI, the model shows highest tropospheric column NO₂ abundances over the Indo-Gangetic Plain region during all the seasons. The percentage differences between WRF-Chem and OMI relative to OMI tropospheric column NO₂ (Figure 4-14) show that the model tends to overestimate OMI retrievals by 10-50% over the Indo-Gangetic Plain region with differences as high as 90% during winter. Percentage difference values over rest of the model domain are -50% to 10% during all the seasons. The model generally underestimates OMI retrievals during spring and summer, and also over low NO_x emission regions during winter and autumn. The monthly statistical analysis of co-located WRF-Chem and OMI tropospheric column NO₂ abundances are listed in Table 4-3.

Table 4-3: Seasonal variation in Index of Agreement (*d*), Mean Bias (*MB*), Mean Normalized Bias (*MNB*), Root Mean Square Error (*RMSE*) and Mean Normalized Gross Error (*MNGE*) computed using the co-located WRF-Chem and OMI tropospheric column NO₂ values. The total number of data points (*N*) used in the calculation is also listed.

Month	<i>d</i>	MB ¹	MNB ²	RMSE ¹	MNGE ²	N
Jan	0.61	0.29	271.0	2.36	308.0	271339
Feb	0.68	0.04	273.6	1.53	313.6	237513
Mar	0.66	-0.30	201.9	1.41	255.7	278571
Apr	0.66	-0.33	248.5	1.27	302.6	303453
May	0.71	-0.49	122.8	1.21	184.7	296121
Jun	0.64	-0.49	117.0	0.95	189.3	193869
Jul	0.61	-0.41	141.6	0.77	212.3	194030
Aug	0.61	-0.36	171.7	0.74	238.3	177826
Sep	0.66	-0.32	139.7	0.80	200.3	181364
Oct	0.71	-0.16	268.7	1.04	313.4	250336
Nov	0.73	-0.03	357.5	1.49	395.5	244510
Dec	0.72	0.06	314.8	1.83	351.4	235815

¹ Unit: x 10¹⁵ molecules cm⁻²

² Unit: %

The index of agreement between model and OMI (0.61-0.73) are smaller than those calculated from the comparison with TES and MOPITT indicating relatively poor model performance in simulating the NO₂ variability compared to CO and O₃ variability. The

estimated MB ranges from $-0.03 \bullet 10^{15}$ to $0.29 \bullet 10^{15}$ molecules cm^{-2} and MNB varies between about 117% and 357% over the simulation domain. RMSE is estimated as $0.74 \bullet 10^{15}$ to $2.36 \bullet 10^{15}$ molecules cm^{-2} and MNGE as 184% to 395%.

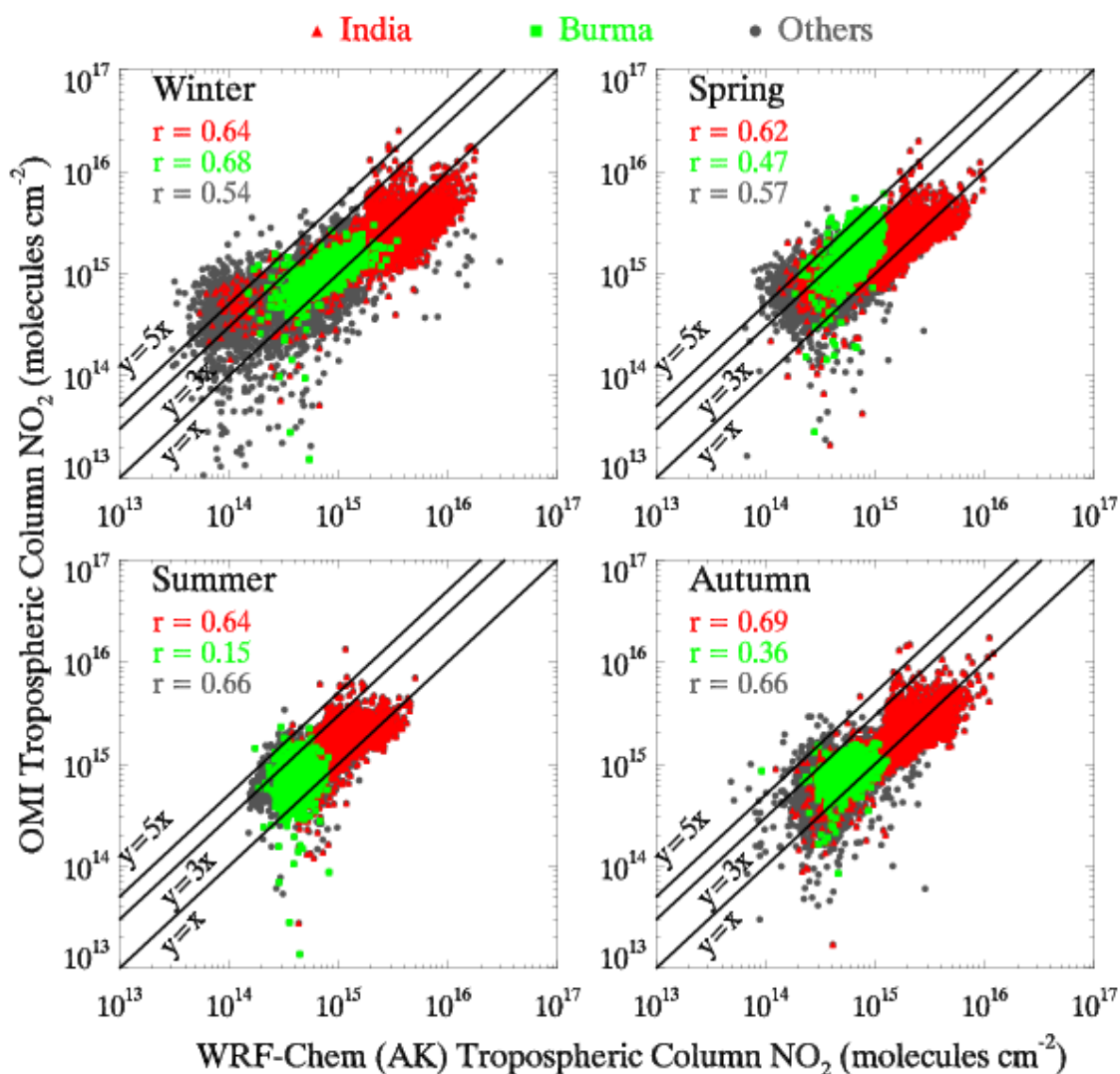


Figure 4-15: Scatter plot between seasonally averaged WRF-Chem simulated and OMI retrieved tropospheric column NO_2 during winter, spring, summer and autumn 2008. Others correspond to the areas not covered by regions 1-5 shown in Figure 4-1. The correlation coefficients for each region are also shown.

The discrepancies between WRF-Chem and OMI are further illustrated by means of scatter plots in Figure 4-15. The scatter plot analysis confirms the systematic underestimation of OMI retrievals by WRF-Chem over most of the domain during all the seasons except over some regions during winter. Retrieved and modeled tropospheric column NO_2 abundances over India are generally distributed between the $y=3x$ lines, i.e., the agreement is within a

factor of 3. Over Burma, better agreement is found during winter and autumn ($y=3x$), while during spring and summer we find differences larger than a factor 5. The correlation coefficients over these regions are estimated to be 0.36 to 0.69 during all the seasons except over Burma during summer (0.15). The poor agreement between model and OMI during summer over Burma could be related to very low levels ($< 1 \bullet 10^{15}$ mol cm⁻²) of tropospheric column NO₂ over this region. These low levels are comparable to the retrieval error of 0.5-1.0•10¹⁵ mol cm⁻² reported for OMI tropospheric column NO₂ [Boersma *et al.*, 2007]. Burma is significantly influenced by biomass burning activities during spring (Figure 4-16) and larger model-OMI discrepancies in this region could be due to underestimation of NO_x emissions from fires.

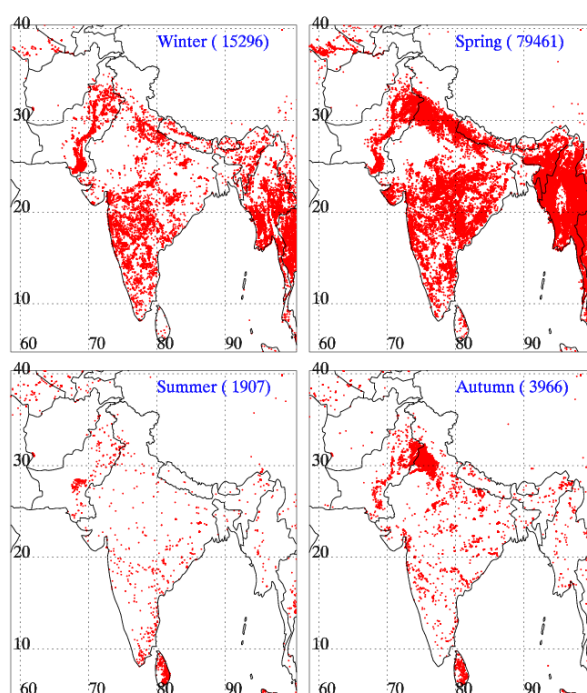


Figure 4-16: Spatial distribution of the MODIS derived fire locations over the model domain during winter (DJF), spring (MAM), summer (JJA) and autumn (SON) of the year 2008. These fire locations are used in FINN for estimating the biomass burning emissions. Numbers in the parenthesis denote total fire counts in each season.

Like Burma, the model also underestimates OMI retrievals over other regions influenced by the fires during spring such as Indian regions due south of 25°N, Indus Plain in western Pakistan (Figures 4-14 and 4-16). The uncertainties in datasets of fuel load, emission factors, combustion efficiency and burned area are the likely contributors to errors in biomass burning emission inventories and these errors must be reduced to improve the model

performance in regions influenced by intense biomass burning activity. The absence of plume rise parameterization in the present simulations could also contribute to these discrepancies over Burma and other biomass burning regions. A sensitivity analysis conducted by including plume rise parameterization during April showed that this parameterization can increase the tropospheric column NO_2 by more than 100% over Burma and by 10-50% over biomass burning regions in India.

The model also underestimates OMI retrievals over the model domain during seasons of low fire activity (summer and autumn) and this indicates that also the anthropogenic NO_x emissions are underestimated over the South Asian region. The errors in anthropogenic emission estimates arise mainly due to uncertainties in basic energy consumption, emission factors and socio-economic datasets used for constructing emission inventory. In addition to the uncertainties in anthropogenic emission estimates, the use of year 2006 anthropogenic emissions in the present model simulations (year 2008) may also explain some of the discrepancies. Analysis of historical data (1980-2003) from the Regional Emission Inventory for Asia (REAS) shows that Indian NO_x emissions have increased by about 177% ($\sim 7.7\%$ per year) from 1980 to 2003 [Ohara *et al.*, 2007]. Tropospheric column NO_2 abundances have also shown positive trend over India from 1996 to 2006 [Ghude *et al.*, 2008].

To examine the impact of the reported increase in anthropogenic emissions from 2006 to 2008, a 10-day sensitivity model run is performed during July with NO_x emissions increased by 15%. July correspond to the months of low anthropogenic NO_x emissions. The sensitivity run shows that increasing the emissions by the reported growth rate increase the model simulated tropospheric column NO_2 amounts over inland by 5-15% during July. Tropospheric column NO_2 amount over the oceanic regions increases by less than 10%. The largest increase in tropospheric column NO_2 abundances is seen over the Indo-Gangetic Plain region. While adjusting the emissions for temporal trends, does increase the model values, it only accounts for a small part of the differences to OMI retrievals. These results suggest the need for substantial improvements in the anthropogenic NO_x emission inventories in order to accurately simulate the NO_x distribution over South Asia. Some other important sources that can possibly lead to discrepancies are NO_x emissions from microbial activity and lightning, uncertainties in seasonal variations of emissions, and absence of diurnal and vertical profiles of anthropogenic emissions. The MEGAN soil NO_x emissions are estimated to be uncertain and these uncertainties could add to model-observation discrepancy especially in rural Indian

regions during summer where heavy precipitation events are shown to induce strong pulses of NO_x amounting to a total of $23\text{--}28 \text{ ng N m}^{-2} \text{ s}^{-1}$ [Ghude *et al.*, 2010]. Lightning NO_x emissions were not included in the simulations but are suggested to contribute very little to NO_x emissions over the Indian region [Ghude *et al.*, 2010].

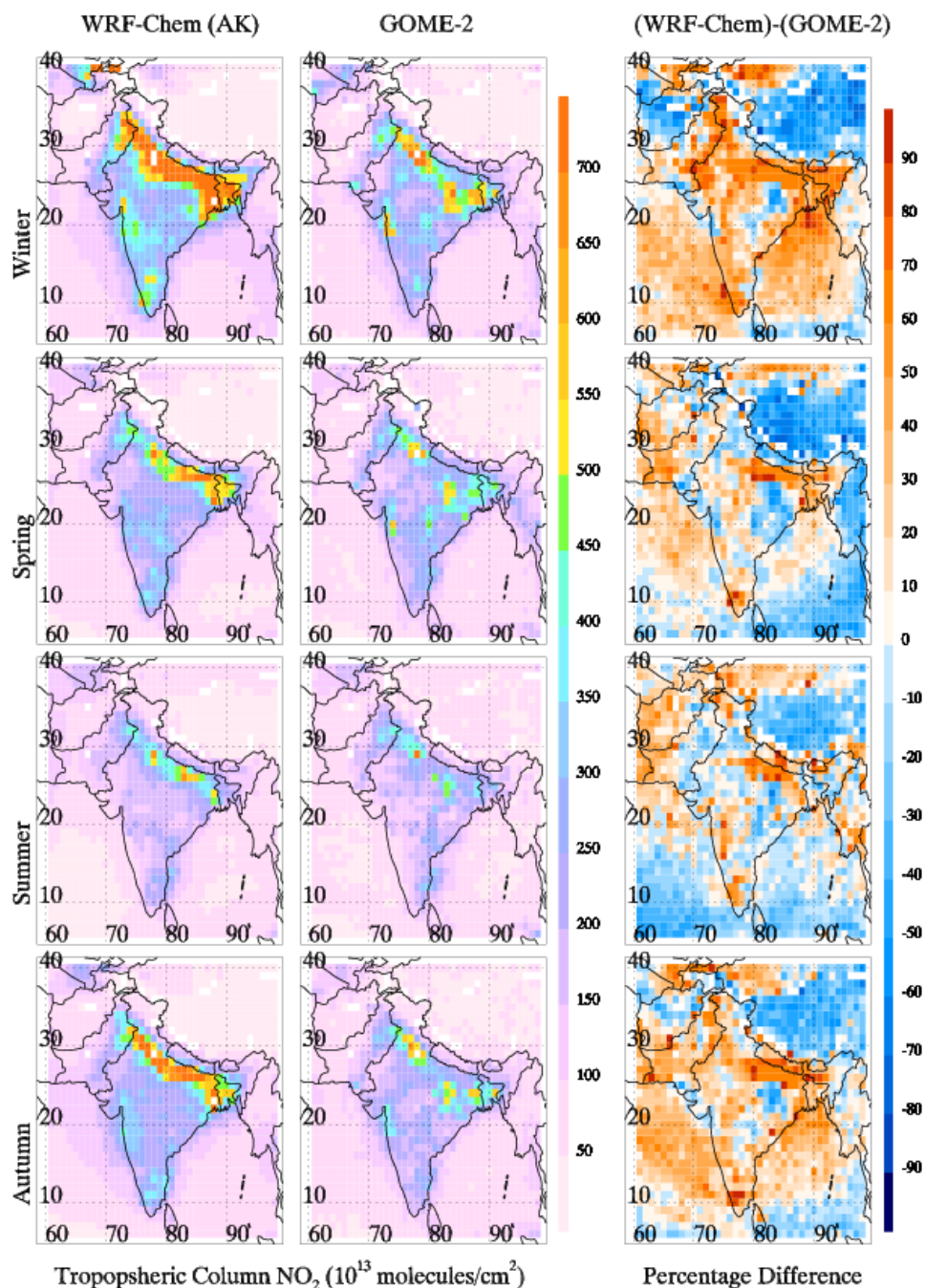


Figure 4-17: Spatial distributions of WRF-Chem simulated and GOME-2 retrieved tropospheric column NO_2 during winter (DJF), spring (MAM), summer (JJA) and autumn (SON) 2008. Note that WRF-Chem profiles are smoothed with GOME-2 averaging kernel before comparison.

To confirm the reality of these large uncertainties in NO_x simulations, the model simulated tropospheric NO_2 is also compared with GOME-2 retrievals. The spatial distributions of model simulated and GOME-2 retrieved tropospheric column NO_2 abundances during the four seasons of 2008 are shown in Figure 4-17 along with percentage difference between WRF-Chem and GOME-2 relative to GOME-2 retrievals. GOME-2 retrievals and modeled values are averaged over $1^\circ \times 1^\circ$ grid considering larger size (40 km x 80 km) of GOME-2 viewing pixel. Like OMI and WRF-Chem, GOME-2 also shows highest tropospheric NO_2 values over the Indo-Gangetic plain during all the seasons. Similar to OMI retrievals, the model also overestimates the GOME-2 retrievals over the Indo-Gangetic Plain region by 10-50% and generally underestimates them during spring and summer except for a few grid boxes. The model significantly underestimates GOME-2 retrievals over Burma and other biomass burning regions during spring by -10 to -50% and over the regions of low NO_x emissions. In contrast to OMI retrievals, the model overestimates the GOME-2 retrievals over parts of Arabian Sea and Bay of Bengal where tropospheric column NO_2 abundances are low ($< 1 \bullet 10^{15}$ molecules cm^{-2}). However, it should be noted that GOME-2 values over these regions are comparable to the error of $0.5\text{-}1.0 \times 10^{15}$ molecules cm^{-2} reported for GOME retrievals.

The seasonal variations in tropospheric NO_2 simulated by WRF-Chem over the defined five regions are compared with co-located OMI and GOME-2 retrievals in Figure 4-18. Both OMI and GOME-2 tropospheric NO_2 columns show a general increase from winter to spring over all regions, decrease during summer/monsoon season and increase again during autumn. Model simulated NO_2 values show a systematic increase during autumn but fails to show springtime higher levels. Highest OMI NO_2 values over India are observed in May while over Burma in March. The seasonal variations in OMI and GOME-2 tropospheric column NO_2 are found to agree well with the seasonal variability of fire counts (not shown) in the respective regions. The largest discrepancies during spring again point to uncertainties in the biomass burning emission estimates apart from the uncertainties in anthropogenic emission estimates. Interestingly, WRF-Chem values are closer to OMI retrievals than GOME-2 but similar variations in both the WRF-Chem datasets (co-located with OMI and GOME-2) indicate that differences estimated between model and satellite retrievals and the inferences drawn about the NO_x emissions from these differences may be real.

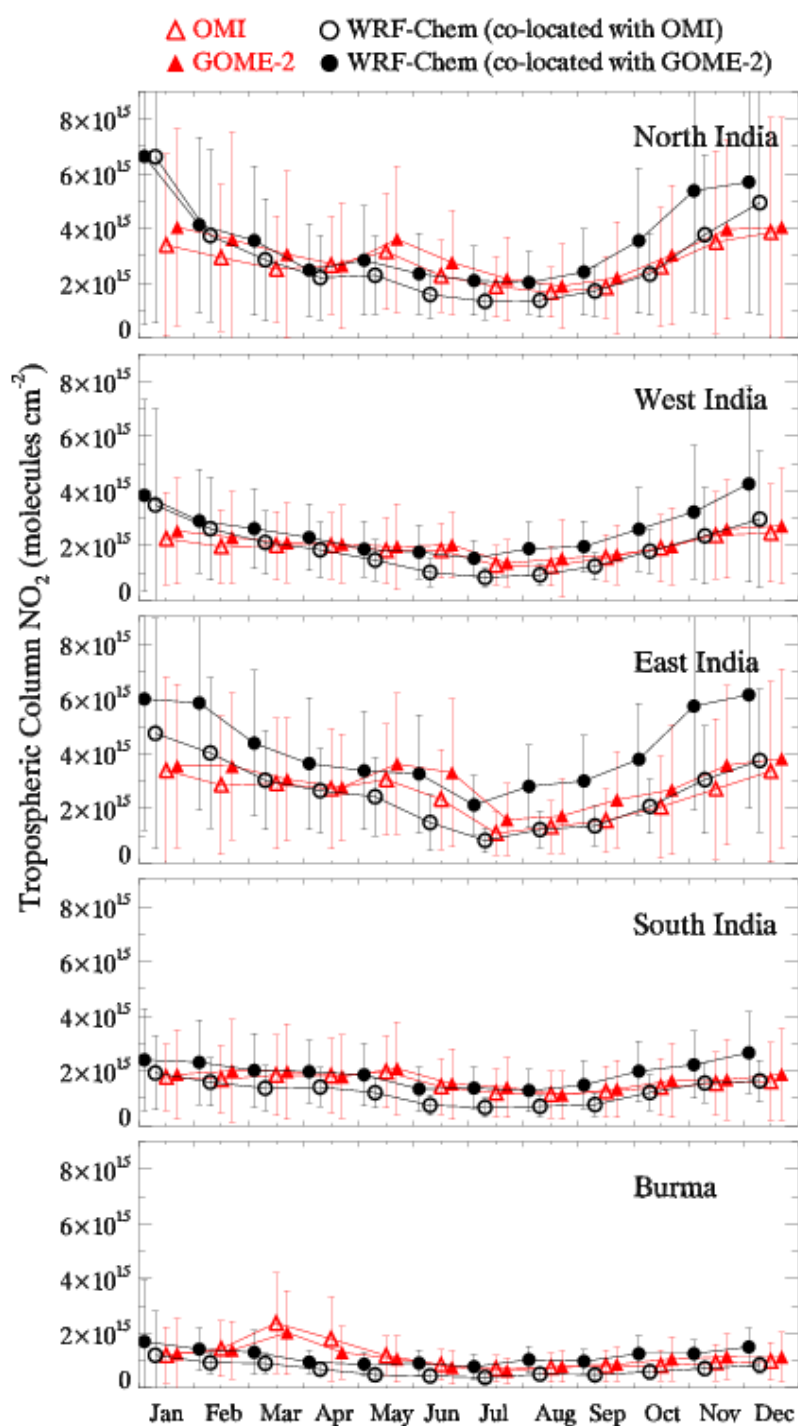


Figure 4-18: Seasonal variations in WRF-Chem simulated, OMI and GOME-2 retrieved tropospheric column NO_2 values over the regions defined in Figure 4-1.

The evaluation results confirm that the model is capable of reproducing many of the observed patterns and overall captures the seasonal variation in surface ozone and CO across the Indian region. The evaluation against TES and MOPITT satellite retrievals also lends confidence to

the model's ability in simulating general seasonal patterns of lower tropospheric ozone and total column CO. Regional differences in the seasonal variations of ozone, CO and NO₂ are also reproduced by the model. While there are weaknesses in the model performance, e.g. in representing the magnitude and seasonality of NO₂ columns, the evaluation results give confidence that the model provides meaningful information to examine the spatio-temporal distribution of surface ozone over India.

4.5 Analysis of Modeled Surface Ozone

The spatial distributions of model simulated monthly mean surface ozone during January, April, August and October (representing winter, spring, summer and autumn) over South Asia along with 10 m wind vectors are depicted in Figure 4-19. During January, ozone levels are highest (> 55 ppbv) over central and eastern parts of India, the Arabian Sea along the coast and the northern Bay of Bengal. Interestingly, ozone values along the coasts during January are higher than those over land. This indicates en-route additional photochemical ozone production in offshore continental polluted air due to strong tropical solar radiation and effects of marine boundary layer. The marine boundary layer suppresses the loss of pollutants associated with ventilation and dry deposition due to its shallower and less turbulent nature. In addition, subsidence of ozone rich free tropospheric air during night-time could also increase ozone levels into the marine boundary layer. Higher ozone levels simulated over these oceanic regions are consistent with the observations made during INDOEX [e.g. *Lal and Lawrence, 2001; Stehr et al., 2002*] and other ship cruises [e.g. *Naja et al., 2004; Srivastava et al., 2011*]. A small region of ozone values less than 16 ppbv is also discerned over northern India during January, which is likely due to lower solar radiation and titration of ozone by higher NO_x levels as indicated by analysis of modeled solar radiation and NO_x values and also higher anthropogenic NO_x emissions in this region (Figure 4-1). Ozone values over Tibetan Plateau are also higher (45-65 ppbv) than those over the adjacent Northern Indian IGP areas.

Moving to spring, modeled ozone remains high in Eastern India and increases in Northern parts of India, but the high ozone concentrations in Southern India and along the coast disappear. This is associated with changes in wind patterns from offshore to onshore, which transports cleaner marine air-masses to the inland regions. It should be mentioned, that ozone values during spring may be underestimated due to underestimation of CO and NO_x

concentrations by the model (section 4.4). Lowest ozone values are simulated for August with average surface ozone not exceeding 40 ppbv over most of India.

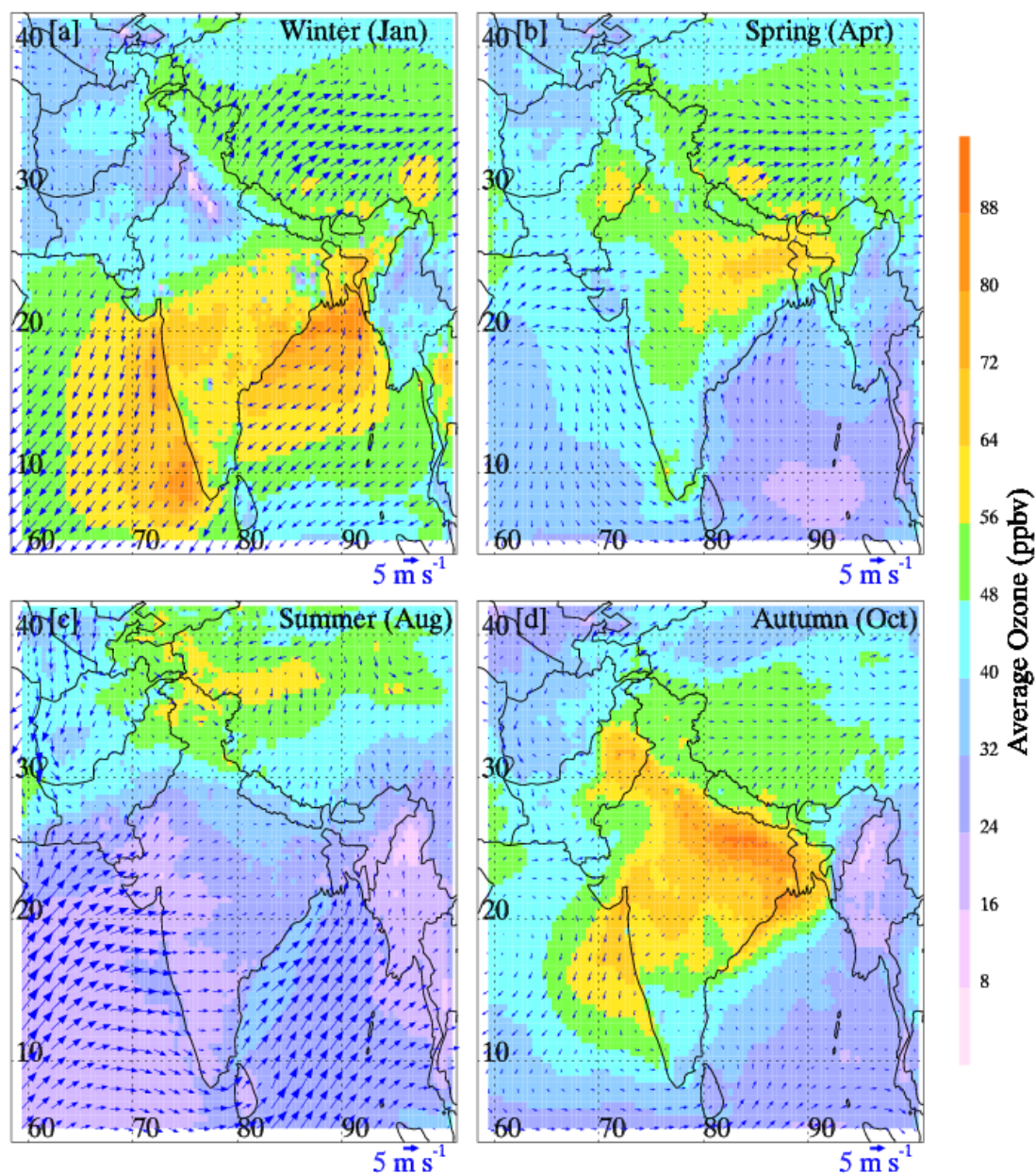


Figure 4-19: Spatial distribution of WRF-Chem simulated surface ozone during January, April, August and October of the year 2008. Monthly mean 10 m wind vectors are also shown.

The levels of ozone precursors are also found to be low during August (Figures 4-12 and 4-18). The strong inflow of marine air-masses into the Indian region leads to the development of cloudy and rainy conditions which, in turn, reduces the solar radiation and suppresses photochemical ozone production during August. Lower levels of ozone precursors may be

associated with washout (HNO_3) and vertical transport (CO) to higher altitudes induced by deep convection [e.g. *Fu et al.*, 2006; *Park et al.*, 2007]. The marine air-masses do not influence the regions north of 30°N and thus higher ozone values (> 55 ppbv) are still seen in those regions and over Tibetan Plateau.

During October, modeled ozone again increases over nearly the entire Indian region and over the entire Indo-Gangetic Plain (IGP) and central India reach the seasonal peak. Highest ozone mixing ratios (70-80 ppbv) are seen over the eastern part of the IGP. This increase is associated with an increase in solar radiation and ozone precursors concentrations associated with a change in wind patterns from onshore to offshore. Like January, the offshore transport of pollutants leads to higher ozone mixing ratios along the coastal regions.

To gain further insights into the spatial and temporal variability of surface ozone, the ozone net production (ONP) due to photochemistry is estimated for daytime (1130-1530 LT) over the model domain. ONP is calculated as the difference between gross ozone formation (P (O_3)) and loss (L (O_3)) rates given by the following equations:

$$P [\text{O}_3] = k_1[\text{HO}_2][\text{NO}] + \sum_i k_{2i}[\text{RO}_2]_i [\text{NO}]\phi_i \quad (4-9)$$

$$L (\text{O}_3) = k_3[\text{O}(^1\text{D})][\text{H}_2\text{O}] + k_4[\text{OH}][\text{O}_3] + k_5[\text{HO}_2][\text{O}_3] \quad (4-10)$$

where k_1 - k_5 represent the rate coefficients of the HO_2+NO , RO_2+NO , $\text{O}(^1\text{D})+\text{H}_2\text{O}$, $\text{OH}+\text{O}_3$ and HO_2+O_3 reactions and ϕ is the yield of NO_2 from RO_2+NO reaction. The spatial distributions of average daytime ONP during January, April, August and October over the model domain are depicted in Figure 4-20. In general, ONP values are positive over land and negative over the oceanic and parts of the Himalayan regions during all seasons. Positive ONP values arise due to dominance of ozone production from the combination of higher levels of ozone precursors and strong daytime solar radiation. Positive ONP values are also discerned along the coast in January and October indicating net daytime ozone production in the continental outflow even over oceanic regions. ONP values remain between 0 and -1 ppbv hr^{-1} during daytime over the cleaner environments.

During January, ONP values are highest over central-eastern and coastal regions of India with magnitudes of 2-5 ppbv hr^{-1} and are within 0-2 ppbv hr^{-1} over other parts of India and Burma. Positive ONP values with magnitudes less than 2 ppbv hr^{-1} are also observed over the regions of the Arabian Sea and the Bay of Bengal experiencing outflow of continental air. Positive

ONP values over these oceanic regions disappear during April due to the reversal in wind patterns. ONP values show an increase of about 1 ppbv hr^{-1} over northern parts of IGP and slight decrease over central India during April.

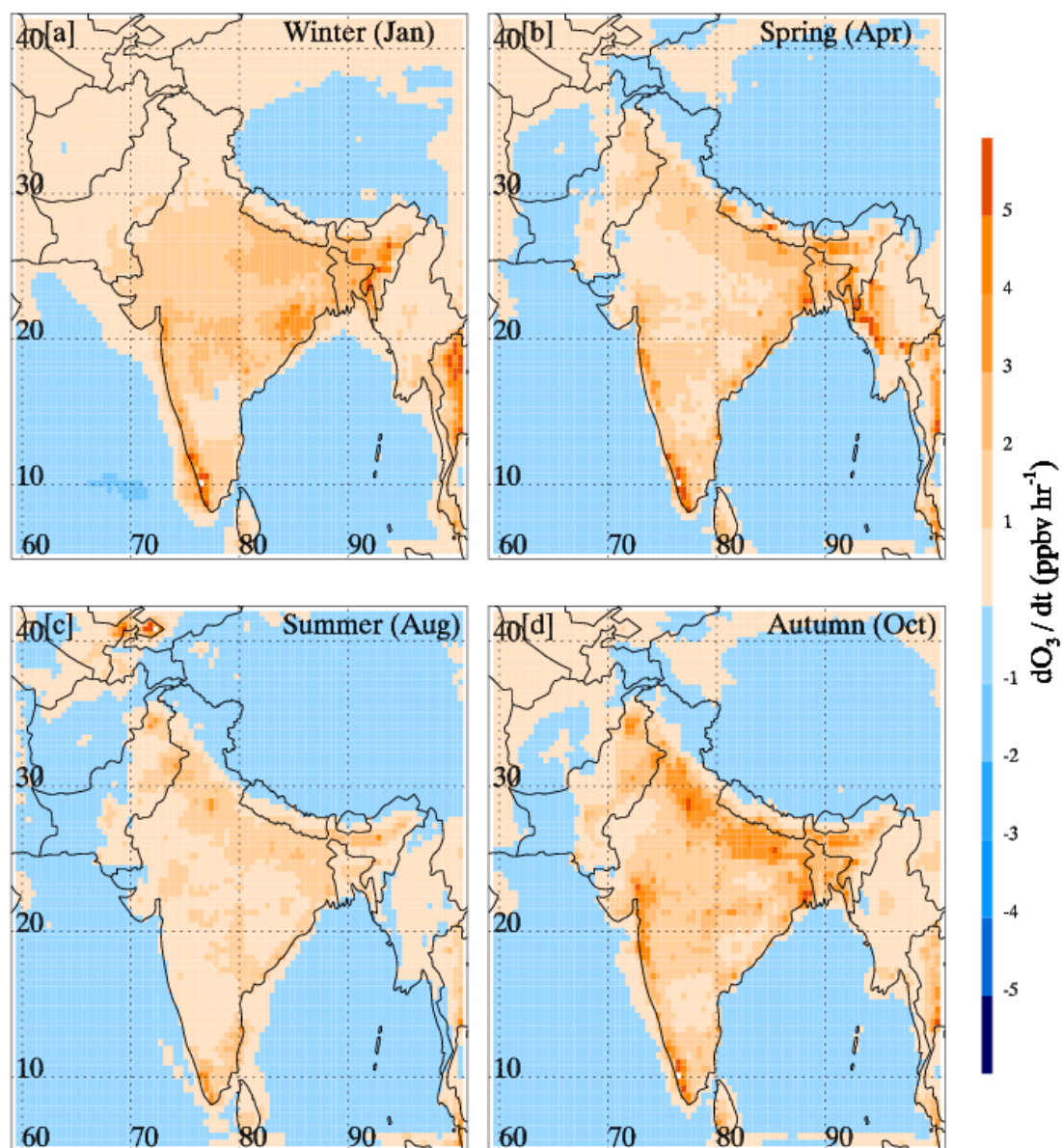


Figure 4-20: Spatial distributions of WRF-Chem simulated daytime (1130-1530 LT) ozone net production during January, April, August and October 2008.

Lowest ONP values are estimated in August with magnitudes less than about 2 ppbv hr^{-1} over most of India. The low ONP values again indicate suppression of photochemical activity during August (monsoon season). In October, ONP values increase by a factor of 2-3 over the entire Indian region relative to August due to increased solar radiation and reversed wind patterns. Daytime ONP values during October reach up to $4\text{-}5 \text{ ppbv hr}^{-1}$ over the IGP region.

Net daytime ozone production in the outflow regions over the Arabian Sea are also seen during October. These results clearly indicate that the spatial and seasonal patterns of surface ozone over South Asia are determined by photochemical net ozone production and closely linked to the varying influence of marine air-masses associated with monsoonal circulation.

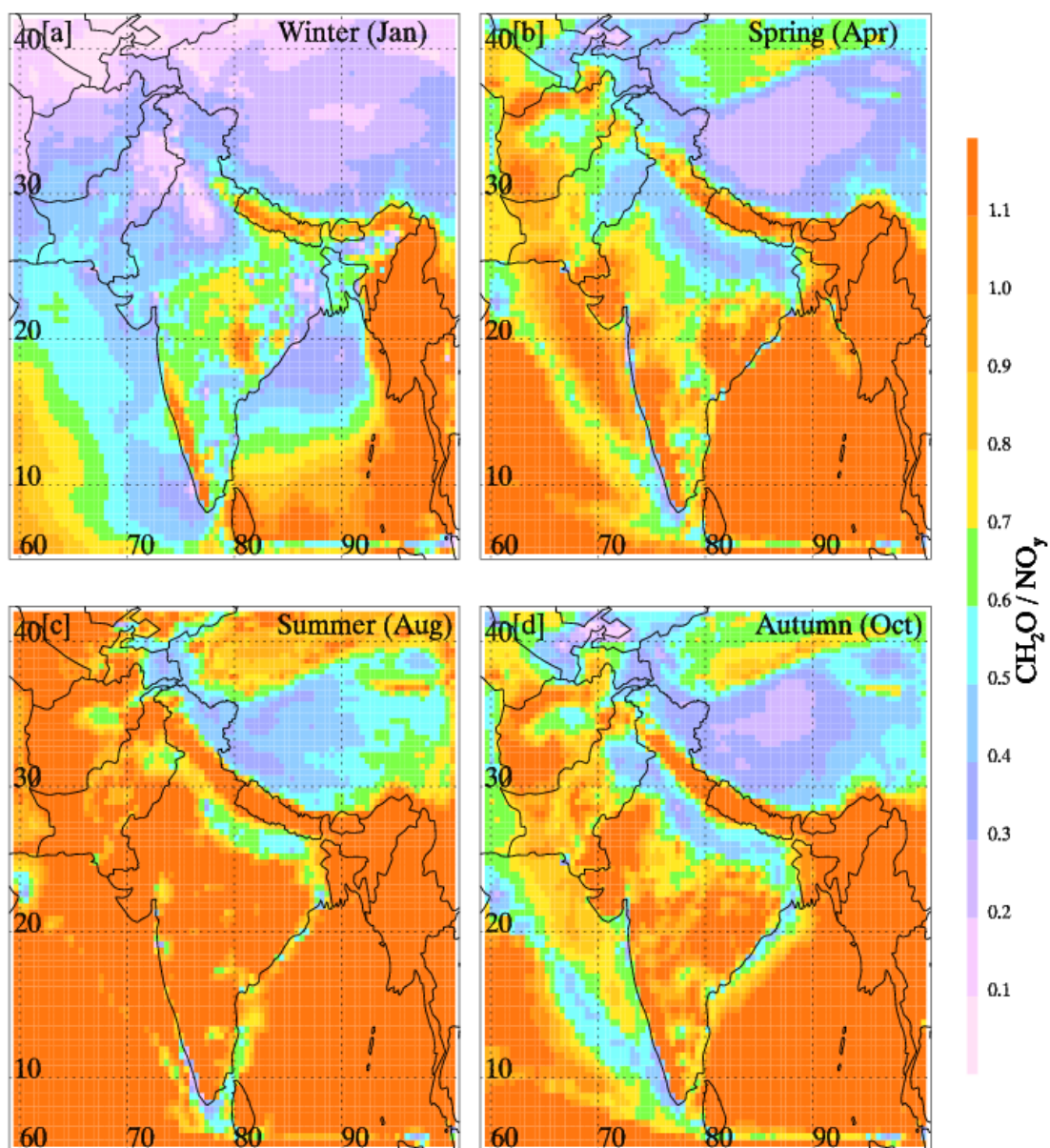


Figure 4-21: Spatial distributions of WRF-Chem simulated afternoon (1130-1430 LT) CH_2O to NO_y ratio during January, April, August and October of the year 2008.

The model results are further used to examine the relative importance of NO_x and NMHCs in ozone production over South Asia. *Sillman* [1995] showed that model simulated afternoon ratios of CH_2O to NO_y , H_2O_2 to HNO_3 and O_3 to $(\text{NO}_y - \text{NO}_x)$ are very useful indicators of the

ozone production regime. The critical values of the ratios $\text{CH}_2\text{O}/\text{NO}_y$, $\text{H}_2\text{O}_2/\text{HNO}_3$ and $\text{O}_3/(\text{NO}_y-\text{NO}_x)$ separating the two ozone production regimes, are suggested to be 0.28, 0.4 and 7 respectively with lower values indicating a VOC-limited regime while higher values correspond to a NO_x -sensitive regime [Sillman, 1995]. $\text{CH}_2\text{O}/\text{NO}_y$ has been successfully used to distinguish ozone production regimes over the urban areas of Shanghai [Geng *et al.*, 2007] and Mexico [Tie *et al.*, 2007].

The spatial distributions of the simulated monthly average afternoon (1130-1430 LT) CH_2O to NO_y ratio during January, April, August and October 2008 are shown in Figure 4-21. The ratio is less than 0.28 over some parts of the IGP during winter indicating hydrocarbon limited ozone production regime over this region. The rest of the Indian region appears to be NO_x -limited throughout the year. Interestingly, the ratio is seen to be lower over the shipping routes in the Arabian Sea and Indian Ocean reflecting the critical role of shipping NO_x emissions in ozone production over the cleaner marine regions. The $\text{H}_2\text{O}_2/\text{HNO}_3$ ratio (not shown) is estimated to be less than 0.4 only in a few grid cells over the IGP region during October and the $\text{O}_3/(\text{NO}_y-\text{NO}_x)$ (not shown) is estimated to be greater than 7 over the region for all seasons. These results confirm the dominance of a NO_x -limited ozone production regime over India. NO_x -limited ozone production over South Asia might be associated with the fact that emissions in this region are influenced largely by incomplete combustion process, particularly by biofuel burning, and thus have higher NMHC to NO_x emission ratio as compared to other regions of the Northern Hemisphere [Lawrence and Lelieveld, 2010]. Earlier, it was also shown using observed ozone-CO and ozone- NO_x correlation over some of the sites that the emissions of ozone precursors and thus ozone levels are largely determined by incomplete combustion process [Naja and Lal, 2002; Naja *et al.*, 2003]. The sensitivity runs performed by increasing NO_x emissions over the model domain by 15% and 30% did not alter the ozone production regime much except for some regions in Northern India where ozone production regime changed from NO_x -limited to NMHC-limited. The decrease in CH_2O to NO_y ratios is, however, observed over the whole domain with the increase in NO_x emissions.

4.6 Summary

This chapter presents the evaluation of model simulated ozone, carbon monoxide and nitrogen oxides are compared with co-located ground-based, balloon-borne and space-borne observations. Ground-based observations include surface ozone from seven sites and CO and

NO_x observations from three sites, while balloon-borne observations are available from two sites in the Indian region. Space-borne observations include retrievals of ozone from TES, nitrogen dioxide from OMI and GOME-2, and carbon monoxide from MOPITT. The errors and biases in model simulation are quantified through a set of statistical metrics.

The evaluation results indicate that the model has a good ability of simulating the seasonal variations of surface ozone and CO over the Indian region but shows some differences for NO_x seasonality particularly during spring. The vertical distribution of ozone is also simulated well by the model. The index of agreement, between model simulations and satellite retrievals from TES, OMI and MOPITT, is estimated to be 0.47 - 0.9 indicating that model is capable of reproducing the overall spatial and temporal variability of ozone, CO and NO₂. However, bias analysis indicates that TES retrieved lower tropospheric ozone values are underpredicted by the model during all seasons. OMI tropospheric column NO₂ retrievals are also generally underestimated except over the Indo-Gangetic Plain region. MOPITT total column CO retrievals are underpredicted during February-July while they are overestimated during other months. The largest difference between model and observations are seen during spring, which is also the season of intense biomass burning activity and is related to uncertainties in the emissions and the treatment of biomass burning sources. Large discrepancies between model and OMI tropospheric column NO₂ abundances for seasons other than spring also point towards large uncertainties in anthropogenic NO_x emission estimates. A sensitivity simulation employing plume rise parameterization showed significant enhancement in tropospheric CO and NO_x over biomass burning regions.

Chemical and meteorological model fields are used to understand the spatio-temporal variability of surface ozone and the analysis clearly indicates regional differences in the seasonality of surface ozone over South Asia. The inland regions show net ozone production (0 to 5 ppbv hr⁻¹) while the cleaner marine and mountainous regions show net ozone destruction (0 to -2 ppbv hr⁻¹) during daytime. Net ozone production (0-2 ppbv hr⁻¹) is also seen over the marine regions experiencing outflow from the South Asian region. Highest net ozone production rates are seen over the Indo-Gangetic Plain (IGP) region and some cities located along the coastal regions of India. Ozone production over South Asia is estimated to be limited mostly by NO_x except for some regions over the Indo-Gangetic Plain region during winter.

5. Tracer-based analysis of Wintertime CO

The evaluation results presented in the previous chapter showed that WRF-Chem model has good ability in simulating tropospheric CO over South Asia. Here, this chapter is aimed at understanding the different processes controlling wintertime tropospheric CO distribution in South Asia. Carbon monoxide (CO) is of great importance in the troposphere due to its important implications on air quality, atmospheric chemistry and global climate. Higher levels of CO in the boundary layer can lead to serious health problems [e.g. *Raub and Benignus*, 2002]. CO affects the oxidizing capacity of the atmosphere by removing troposphere's primary oxidant hydroxyl (OH) radical [*Warneck*, 2000] and influencing tropospheric ozone budget [*Logan et al.*, 1981; *Levy II et al.*, 1997]. CO can contribute to climate change indirectly by affecting the concentrations of key greenhouse gases such as methane and ozone [e.g. *Wigley et al.*, 2002]. CO with a mean tropospheric lifetime of about 2 months is also a useful tracer for tracking the transport of continental polluted air masses [e.g. *Pfister et al.*, 2004; *Yashiro et al.*, 2009]. Therefore, it is important to understand different processes controlling the distribution and variability of CO in the troposphere.

In the above perspective, numerous efforts have been made to measure CO in different chemical environments from multiple platforms including ground, aircraft and satellite based instruments [e.g. *Novelli et al.*, 1992; *Drummond and Mand*, 1996; *Beer et al.*, 2001; *Allen et al.*, 2004]. These observations have been integrated with chemical transport models to understand the spatio-temporal variability and budget of CO in the troposphere [e.g. *Granier et al.*, 1999; *de Latt et al.*, 2001; *Pfister et al.*, 2004]. However, such studies have been sparse over the South Asian region where anthropogenic CO emissions have been increasing fast ($\sim 2.3\%$ year⁻¹) during the past 2-3 decades [*Ohara et al.*, 2007] and have characteristics

different from those in other parts of the world due to their disproportionately large contribution from biofuel and biomass burning [Lawrence and Lelieveld, 2010].

Surface CO measurements over South Asia are extremely sparse and are available only over a few sites in western [Lal et al., 2000; Naja et al., 2003; Beig et al., 2007], southern [Naja and Lal, 2002, Kumar et al., 2008] and northern [Aneja et al., 2001] parts of India. Few short-term campaign mode observations of surface CO are also available over the adjoining oceanic regions of the Arabian Sea and Bay of Bengal [e.g. Lelieveld et al., 2001; Lal et al., 2007; David et al., 2011]. Observations of the CO vertical distributions are not available over South Asia. Due to scarcity of observations, the uses of satellite observations together with models are highly essential. The aforementioned observations despite of their scarcity provide important information on CO seasonality and show that CO levels in this region are highest during winter. Different ground and satellite based observations show that levels of other trace gases such as ozone, NO_x and NMHCs [e.g. Lal et al., 2000; Ghude et al., 2008; Sahu and Lal, 2006; Kar et al., 2010] and aerosols [Tripathi et al., 2005; Di Girolamo et al., 2004] are also higher during winter over this region. Further, the observations over the marine regions suggest that pollutants from inland South Asian regions can be transported to the cleaner oceanic regions during winter. For these reasons, the present study aims at conducting budget analysis of wintertime tropospheric CO and studying the role of regional meteorology in distributing CO over the South Asian region.

The budget of CO in the troposphere is controlled by a combination of physical and chemical processes including emissions, deposition, transport and photochemistry. CO is emitted by both natural and anthropogenic sources but global total CO emissions are dominated by the latter [e.g. Granier et al., 2000; Horowitz et al., 2003]. The individual contributions of different processes to the CO budget have been determined in several studies by including CO tracers into global and regional models [e.g. Granier et al., 1999; Lamarque and Hess, 2003; Pfister et al., 2004, 2010; Huang et al., 2010]. This concept has also been used to quantify the contribution of different emission sources to total CO over the Indian Ocean during the Indian Ocean Experiment (INDOEX) [de Laat et al., 2001]. More recently, this concept has been successfully implemented in the Weather Research and Forecasting Model with Chemistry (WRF-Chem) to study the CO budget over the USA [Pfister et al., 2011; Boynard et al., 2012]. This study employs the WRF-Chem model to study wintertime CO budget and variability over South Asia by including CO tracers into the model. The chapter

begins with a description of the WRF-Chem model and different CO tracers in Section 5.1. Section 5.2 illustrates the ability of the model to reproduce the spatial and vertical structure of wintertime tropospheric CO through comparison with Measurement of Pollution in the Troposphere (MOPIIT) retrievals. The analysis of the tropospheric CO budget and role of regional meteorology in distributing CO over South Asia is discussed in Section 5.3 and results are summarized in Section 5.4.

5.1 The Model description

The simulations for this chapter are conducted using version 3.3.1 of the WRF-Chem model instead of the version 3.1.1 used for earlier chapters. However, various schemes used for the parameterization of atmospheric processes into the model are same as described in chapter 2 except the gas phase chemistry and inclusion of plume-rise parameterization [Freitas *et al.*, 2007]. The gas-phase chemistry for this chapter is based on Regional Acid Deposition Model (RADM2) which includes 63 gas-phase species, 21 photolysis and 136 gas-phase reactions [Stockwell *et al.*, 1990]. The effects of aerosols have also not been considered into these simulations. The spatial distribution of wintertime average anthropogenic CO emissions over the model domain is shown in Figure 5-1. Anthropogenic CO emissions are highest over the Indo-Gangetic Plain (IGP) region and around some megacities (Ahmedabad, Bombay and Thiruvananthapuram) in western and southern India. CO anthropogenic emissions summed over the model domain during winter are estimated to be 28740 Gg CO and include contributions from residential (41%), industrial (30%), transportation (28%) and power plants (1%) sectors. Biomass burning is a small contribution during wintertime and total biomass burning CO emissions over the model domain for the considered time period are estimated to be 2471 Gg.

This study includes 11 model CO tracers to keep the track of CO originating from different sources and geographical regions. CO tracers are synthetic tracers added as individual species to the simulation with each tracer representing CO molecules from different sources. These tracers also undergo same transport, loss and chemical processes as the total simulated CO. Here, we include tracers for CO emitted from regional anthropogenic (CO-ANT), biogenic (CO-BIO) and biomass burning (CO-BB) sources, CO produced photochemically within the domain from regional emissions of non-methane hydrocarbons (CO-CHEM) and CO inflow from lateral domain boundaries (CO-BC). In addition to these five tracers, the anthropogenic emissions from five different geographical regions within the domain, namely northern India (NI), western India (WI), eastern India (EI), southern India (SI) and Burma (BUR) are tagged

separately. These regions represent the largest surface emitters of anthropogenic pollution (including CO) within the model domain and are shown in Figure 5-1. Anthropogenic emissions of CO from outside these five regions are also tagged separately and are classified as others (OTH). Regional anthropogenic CO tracers are defined as CO-ANI, CO-AOTH etc. Each tagged CO undergoes the same chemical processes as the standard CO species and is deposited at the surface with the same deposition velocity.

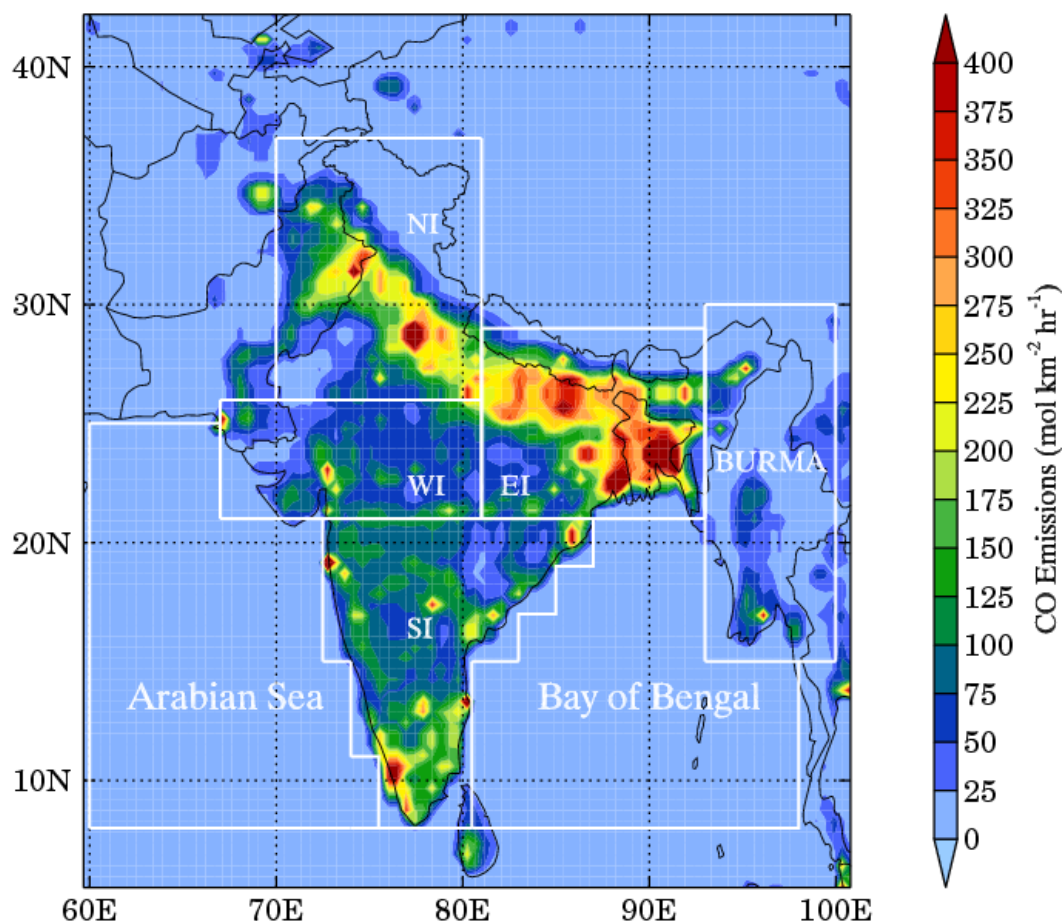


Figure 5-1: Spatial Distribution of wintertime (DJF) average anthropogenic CO emissions over the model domain. Regional classification of different geographical regions along with Arabian Sea and Bay of Bengal is also shown. NI, WI, EI and SI represent northern, western, eastern, and southern India respectively.

The model simulation starts on 01 Dec 2007 0000 UTC with a time step of 180 seconds and results are output every hour. The percentage difference between instantaneous total CO and sum of CO tracers ($CO_{\text{trac}} = CO\text{-ANT} + CO\text{-BIO} + CO\text{-BB} + CO\text{-CHEM} + CO\text{-BC}$) at the surface after 10, 20 and 31 days are shown in Figure 5-2. The sum of all tracers approaches

total CO values after 20 days and CO_{trac} is within $\pm 10\%$ of total CO at the surface. The tracers are well spun up after 31 days with differences of less than $\pm 2\%$ over the domain and remains within $\pm 2\%$ throughout the simulation. In order to avoid the effects due to spin-up, the analysis of model results is limited to the period from 1 January to 29 February 2008.

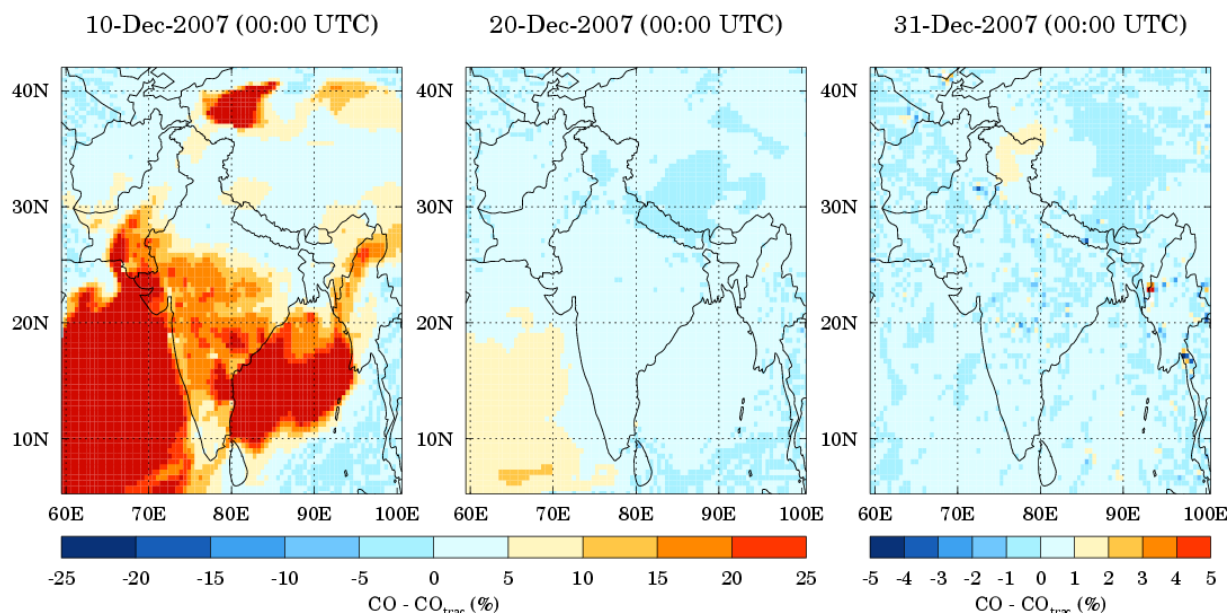


Figure 5-2: Spatial distribution of the percentage difference between total CO and sum of CO tracers ($CO_{trac} = CO-ANT + CO-BIO + CO-BB + CO-CHEM + CO-BC$) at the surface on 10, 20 and 31 Dec 2007 at 00:00 UTC. The model simulation starts at 01 Dec 2007 at 00:00 UTC.

5.2 Model Evaluation

The Measurements of Pollution in the Troposphere (MOPITT) version 4.0 Level 2 retrievals of total column and vertical profiles of CO mixing ratios [Deeter *et al.*, 2010] are used here for evaluating the model performance. MOPITT retrievals provide CO mixing ratios at 10 pressure levels between the surface and 100 hPa with a spacing of 100 hPa. The MOPITT retrieval algorithm uses thermal infrared radiation (near 4.7 μm) measurements in conjunction with a maximum a posteriori (MAP) optimal estimation approach [Deeter *et al.*, 2003; Rodgers, 2000]. MOPITT V4 retrievals have been extensively validated against observations from different chemical environments and are shown to have a bias of less than $\pm 10\%$ at all levels [Emmons *et al.*, 2009; Deeter *et al.*, 2010]. Here, we use only daytime MOPITT retrievals with degrees of freedom for signal (DFS) greater than 1 because daytime retrievals have better information content than nighttime data [Deeter *et al.*, 2010]. For comparison of model output and MOPITT, the model profile is first interpolated to the time

and location of the selected MOPITT retrievals and the interpolated model profile is then transformed by applying the averaging kernel and a priori profile associated with the corresponding MOPITT retrieval following *Emmons et al.* [2009]. The transformed profile is denoted as WRF-Chem (AK) and represents the model profile which MOPITT would measure in absence of other errors. The spatial distributions of MOPITT and WRF-Chem (AK) total column CO averaged from 1 January to 29 February 2008 along with the percentage difference are shown in Figure 5-3. Both MOPITT and model show similar spatial distributions with highest CO values in the regions of highest anthropogenic CO emissions (eastern India and Bangladesh; Figure 5-1).

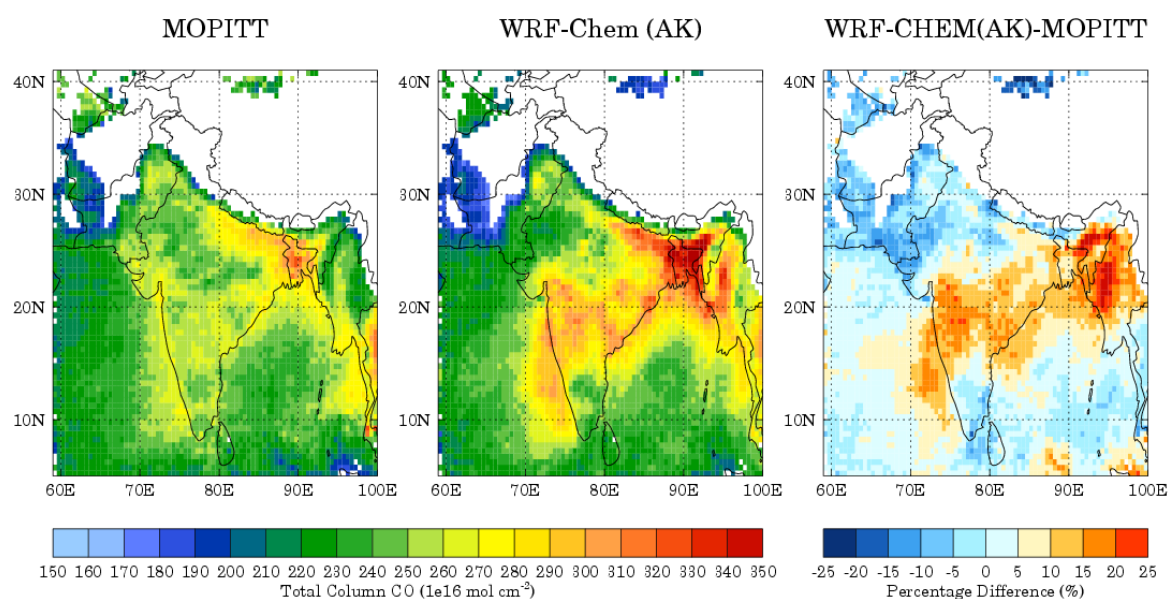


Figure 5-3: Spatial Distribution of average CO total column retrieved from MOPITT and the corresponding WRF-Chem (AK) column (simulated column convolved with MOPITT averaging kernel) during Jan-Feb 2008. Percentage difference between model and MOPITT is also shown. The comparison includes only MOPITT daytime retrievals with DFS more than 1. The white space indicates regions without valid data.

Higher CO column amounts are also seen over southern India, Burma and coastal regions of the Arabian Sea and Bay of Bengal. The MOPITT and WRF-Chem (AK) total column CO averaged over the entire domain during January-February 2008 is estimated as $2.4 \pm 0.2 \cdot 10^{18}$ and $2.5 \pm 0.3 \cdot 10^{18}$ molecules cm⁻² respectively with a mean bias of $9.1 \pm 19.5 \cdot 10^{16}$ molecules cm⁻² ($4 \pm 8\%$) and a correlation coefficient of 0.82. The percentage difference plot indicates that the model underestimates MOPITT CO total column over northern, western and some parts of southern India, while it overestimates satellite retrieved CO over other regions.

However, the percentage difference is within $\pm 20\%$ except over Burma and north-eastern states of India where the differences reach up to about 25%.

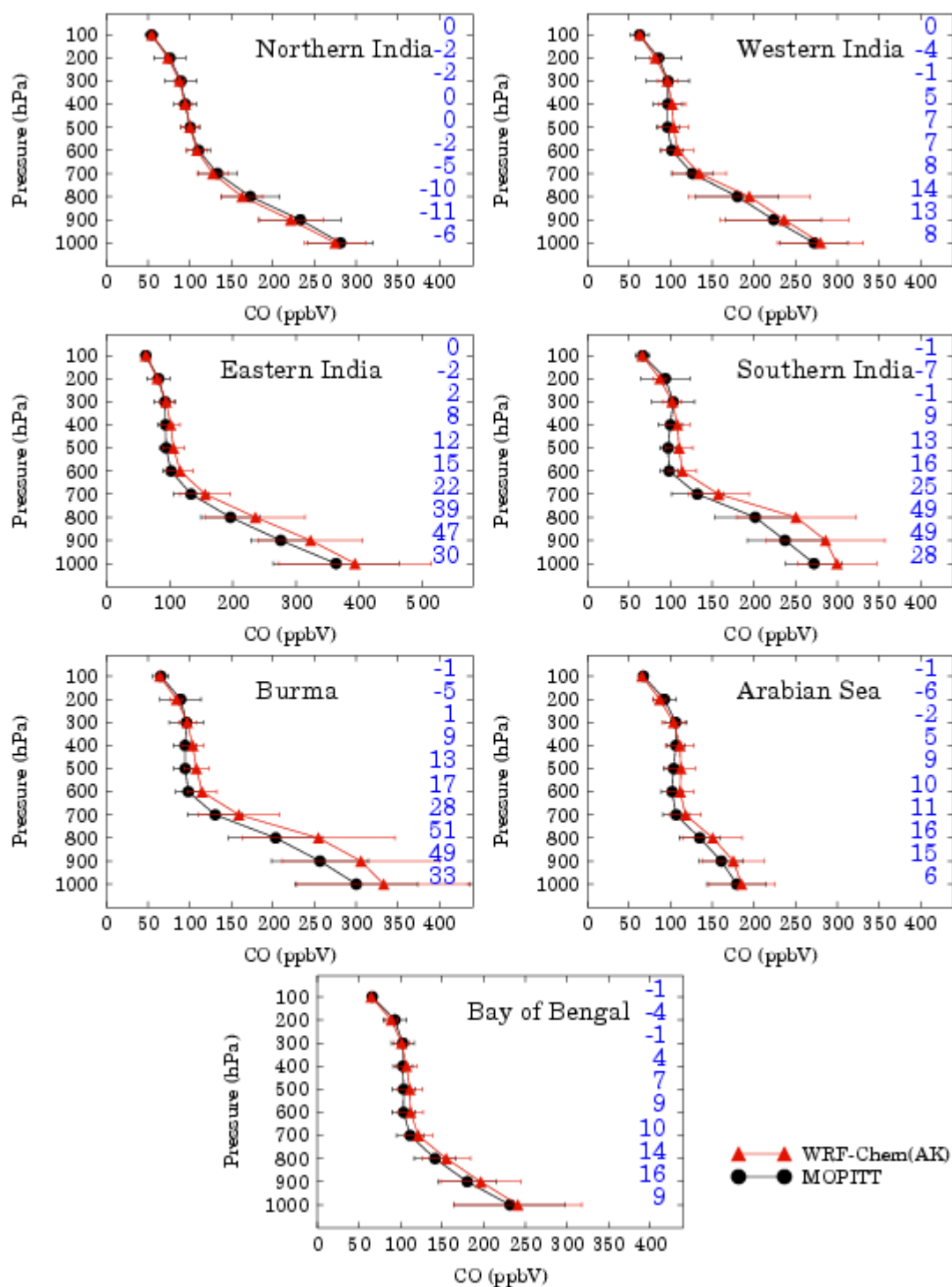


Figure 5-4: Vertical profiles of average CO retrieved from MOPITT and the corresponding WRF-Chem (AK) profiles during Jan-Feb 2008 over seven geographical regions defined in Figure 5-1. The horizontal bars represent standard deviation in the mean values. Absolute difference between model and MOPITT for each level is also shown along right Y-axis.

The MOPITT retrieved vertical profiles of CO are compared with corresponding WRF-Chem (AK) profiles in Figure 5-4 over seven geographical regions defined in Figure 5-1. The northern, western, eastern and southern India represents regions of varying anthropogenic emission strength. Burma represents a region of lower anthropogenic and high biomass burning emissions and the Arabian Sea and Bay of Bengal represent clean marine regions with negligible emissions. The vertical distributions and gradients of CO mixing ratios are reproduced fairly well by the model over all the regions and the average model and MOPITT profiles are within one standard deviation at all pressure levels. Both model and MOPITT show that CO mixing ratios below 700 hPa are significantly higher than those above 700 hPa. The absolute difference between model and MOPITT varies significantly from region to region. Largest differences are seen over eastern India, southern India and Burma where mean bias reaches up to 50 ppbV at some levels in the lowermost troposphere. This indicates that overestimation of MOPITT total column CO (Figure 5-3) by the model over these regions is mainly due to positive biases in the lowermost troposphere and could be associated with uncertainties in model emission estimates. Errors in model transport and chemistry along with uncertainty in satellite retrievals could also contribute to this discrepancy. The mean bias at all levels over other regions is generally within ± 20 ppbV.

5.3 Spatial Distribution of CO

The spatial distributions of total CO mixing ratios and relative contributions from different source terms (CO-ANT, CO-BB, CO-CHEM, CO-BIO and CO-BC) at the surface and in the free troposphere (FT) averaged during January-February 2008 are depicted in Figures 5-5 and 5-6 respectively. Average CO mixing ratios in the FT are estimated by normalizing the FT CO column by the corresponding FT air column. The FT columns are obtained by integrating CO and air density from top of planetary boundary layer (PBL) to tropopause altitude estimated using the thermal tropopause definition [Reichler *et al.*, 2003]. The average tropopause and PBL heights during January-February 2008 along with surface altitude are shown in Figure 5-7 to help the interpretation. The average tropopause height is 16-17 km over regions south of 25°N and decreases sharply to about 10-11 km from 25°N to 40°N. The average PBL height is 200-600 m over most of the Indian region but shows strong diurnal variability with daytime height reaching up to about 1000-3000 m and nighttime height remaining below 200 m. The average PBL height over the oceanic regions is 400-900 m with little spatial and diurnal variability.

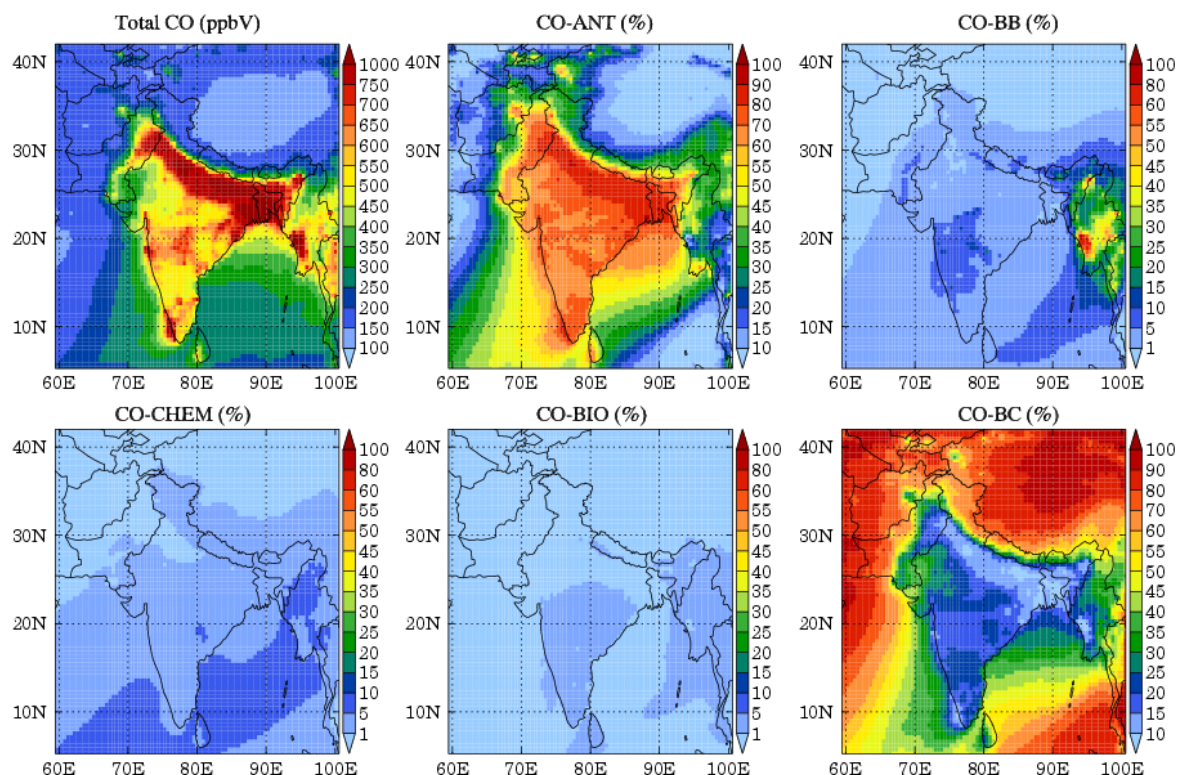


Figure 5-5: Spatial distributions of average total CO mixing ratios (ppbV) and relative contributions of CO-ANT (%), CO-BB (%), CO-CHEM (%), CO-BIO (%) and CO-BC (%) to total CO at the surface during January-February 2008. Note the variation in color scales among the graphs.

CO mixing ratios at the surface exhibit large spatial variability and are highest (> 600 ppbV) over the entire Indo-Gangetic Plain (IGP) region, parts of central India, southern tip of India and southern parts of Burma. The CO-ANT distribution shows that higher CO mixing ratios over the Indian region are to a larger degree due to anthropogenic emissions. Anthropogenic CO accounts for more than 60% of total CO at the surface over India except for the high altitude Himalayan regions in North India. Interestingly, CO-ANT also contributes significantly (30-70%) to the total CO over the Arabian Sea and Bay of Bengal, where anthropogenic emissions are negligible (Figure 5-1). Elevated CO mixing ratios over Burma are due to biomass burning as evident from the CO-BB distribution. CO-BB contributes to 10-80% to surface CO over Burma while CO-ANT contributes 10-40%. CO-BB also contributes 5-10% to surface CO over southern India. The contributions of CO-CHEM and CO-BIO to total CO are generally less than 10% over the model domain. However, there is a clear signature of en-route photochemical production of CO over the oceanic regions in the plumes originating from Burma and India. The distribution of CO-BC shows that pollution

inflow generally contributes less than 40% of the total surface CO over India and Burma. The CO-BC accounts for more than 60% of the total CO over the Himalayan region including Tibetan Plateau. The distributions of total CO and all the tracers in the PBL (not shown) are also found to be similar to those at the surface.

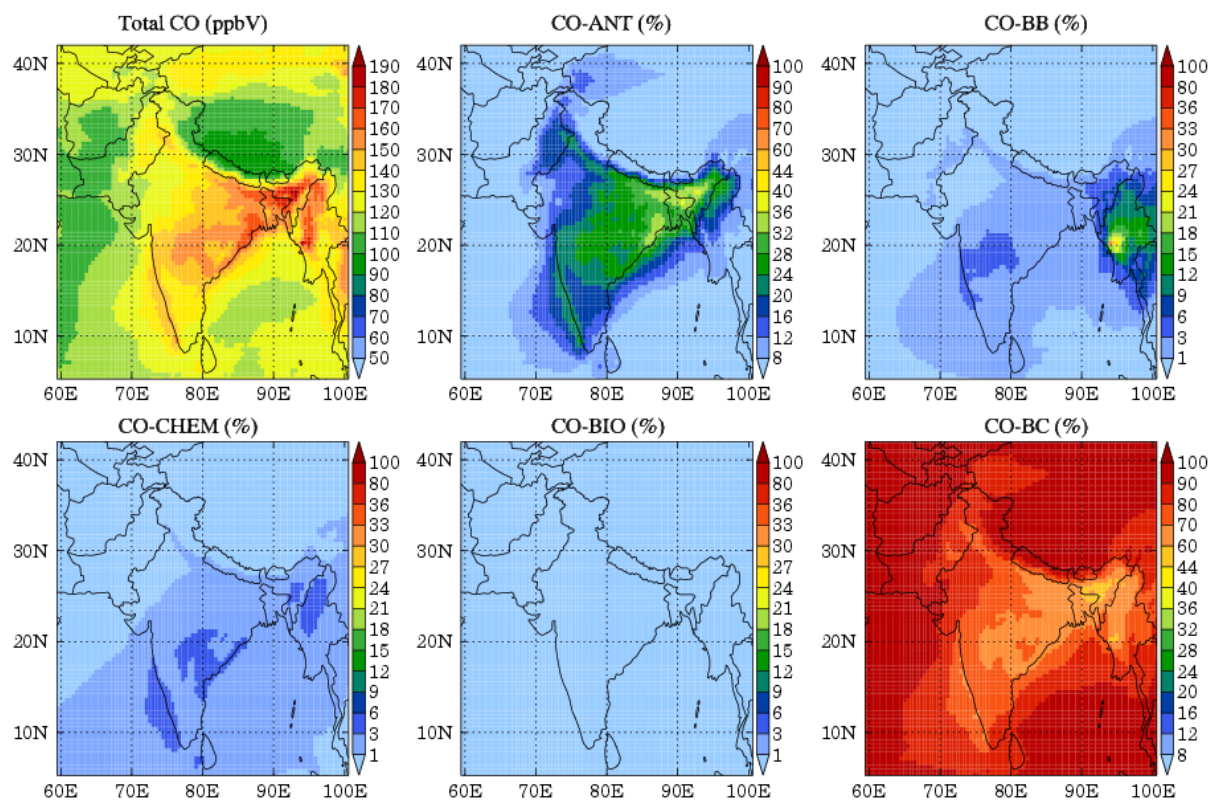


Figure 5-6: Spatial distributions of average total CO mixing ratios (ppbV) and relative contributions of CO-ANT (%), CO-BB (%), CO-CHEM (%), CO-BIO (%) and CO-BC (%) to total CO in the free troposphere (average CO amount between top of PBL and tropopause altitude) during January-February 2008. Note the variation in color scales among the graphs.

Average CO mixing ratios in the FT exhibit small spatial variability and range from 90 up to 200 ppbV with highest values over the eastern Indo-Gangetic Plain (IGP) region, central India and Burma. The main contributor to FT CO is from inflow (>40%) as evident from CO-BC distribution. CO-ANT and CO-BB distributions show that anthropogenic and biomass burning emissions at the surface can be transported to the free troposphere in the vicinity of strong sources. These distributions also show that higher CO levels over eastern IGP and central India are due to the addition of anthropogenic CO (24-36%) to the CO inflow, while those over Burma are due to the addition of CO emitted from biomass burning (12-24%). The contribution from CO-Chem is less than 6% and is higher over the regions close to biomass

burning sources reflecting the vertical transport of CO precursors in fire plumes. The CO-BIO distribution highlights that biogenic emissions do not influence FT strongly and contribute less than 1%.

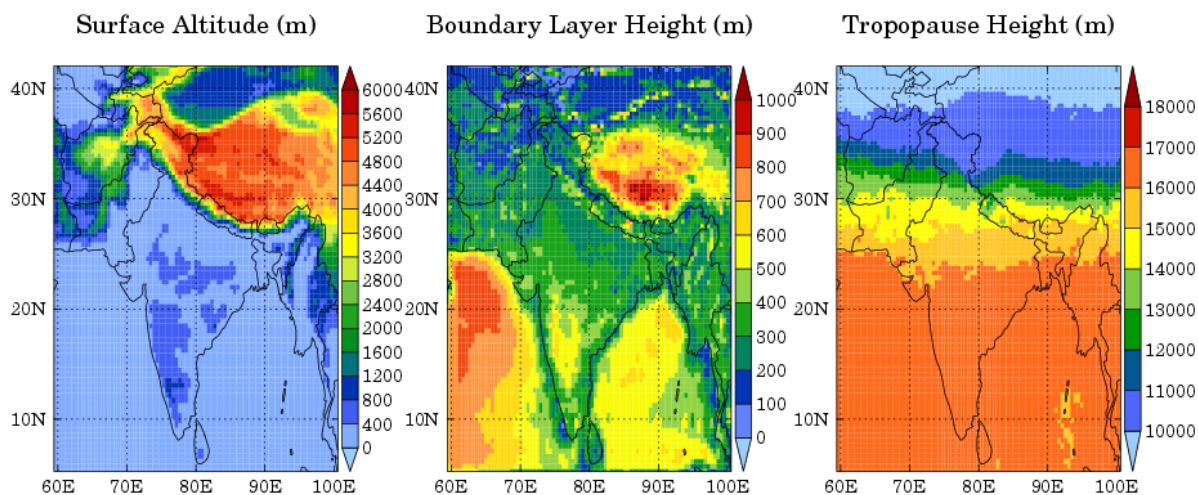


Figure 5-7: Spatial distribution of surface altitude, average boundary layer height and average tropopause height over the model domain during January-February 2008.

5.4 Vertical Distribution of CO

The time series of the vertical distributions of total CO and different CO tracers averaged over East India and Bay of Bengal from 1 January to 29 February 2008 are depicted in Figures 5-8 and 5-9 respectively. East India and Bay of Bengal represent different chemical environments over the model domain with the former a continental region with highest anthropogenic CO emissions and the latter a marine region with negligible anthropogenic CO emissions (Figure 5-1). The time series of PBL height averaged over both the regions is also shown in each plot. The modeled PBL height over East India varies from ~87 m during nighttime to ~1750 m during daytime reflecting rapid response of land masses to diurnal heating cycle while it remains nearly constant over the Bay of Bengal.

CO mixing ratios shows a sharp vertical gradient over East India with significantly higher values in the PBL (250-500 ppbV) than in the FT (100-300 ppbV). The mixing ratios of total CO, CO-ANT, CO-BB and CO-BIO in the PBL show a strong diurnal cycle (not shown) with higher values during nighttime and lower values during daytime. Note that anthropogenic emissions in the model do not have a diurnal cycle and so these diurnal variations are largely due to trapping of CO molecules in the nighttime shallow boundary layer and substantial mixing into a larger volume during daytime. CO-Chem shows a moderate diurnal cycle and

no diurnal variation is seen in CO-BC. Similar variations in total CO and all the CO tracers are seen over northern, western and southern India, and Burma.

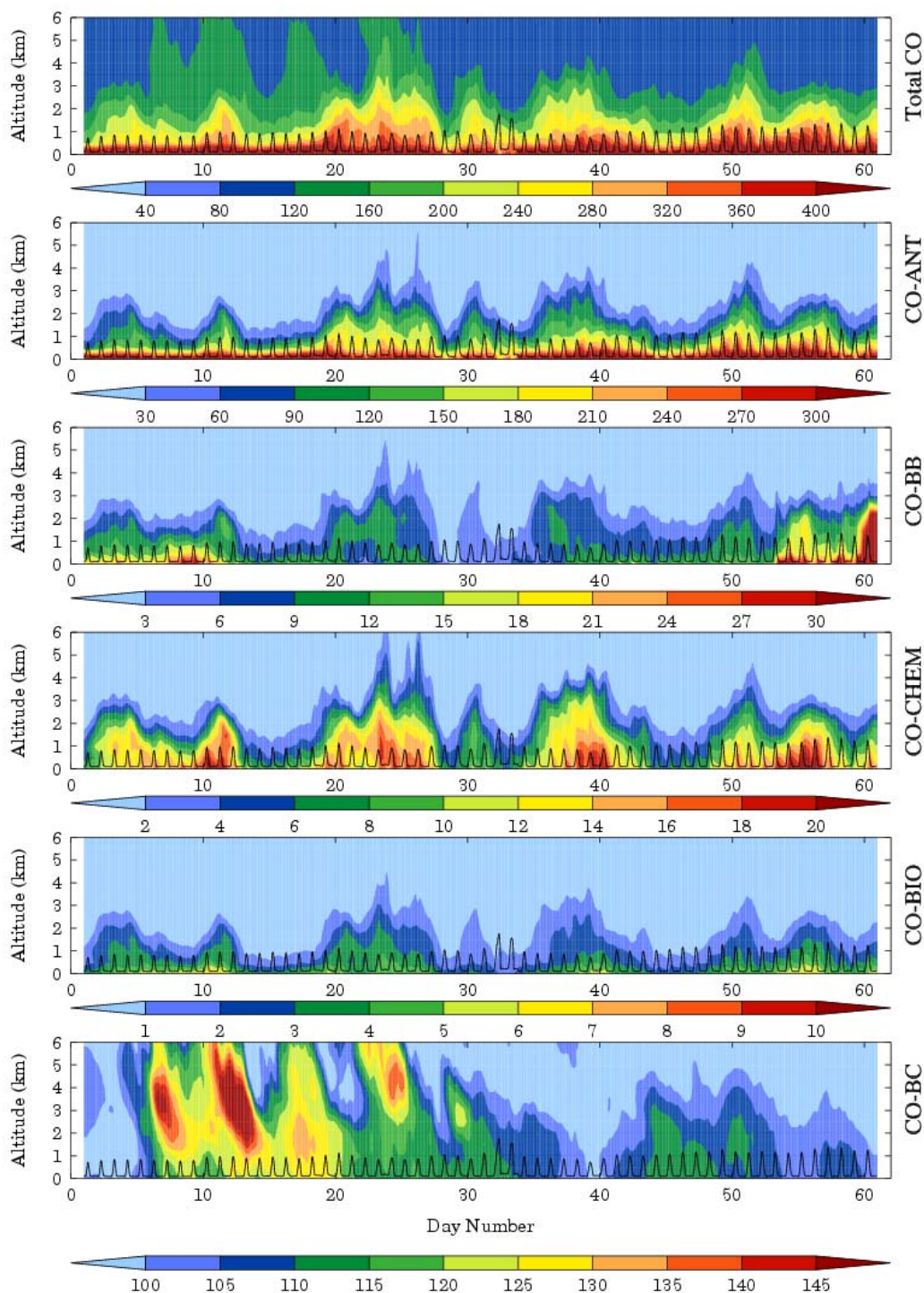


Figure 5-8: Vertical distribution of total CO and different CO tracers averaged over eastern India from 1 January to 29 February 2008. Note that eastern India is the region of highest anthropogenic emissions in the model domain and all values are in ppbV. Time series of PBL height averaged over eastern India is also shown by solid black lines.

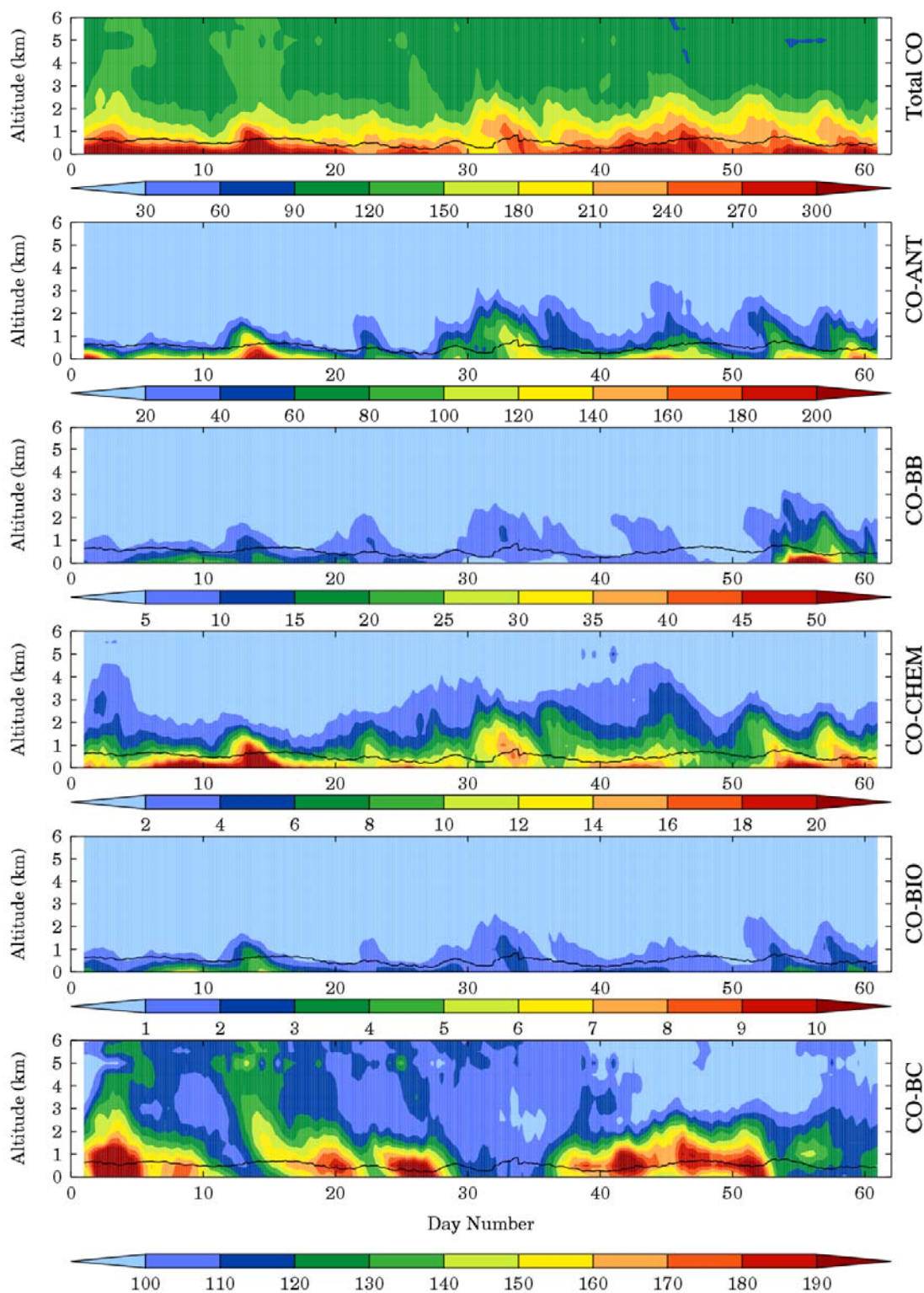


Figure 5-9: Vertical distribution of total CO and different CO tracers averaged over Bay of Bengal from 1 January to 29 February 2008. All values are shown in ppbV. Time series of PBL height averaged over Bay of Bengal is also shown by solid black lines.

The vertical distributions of CO-ANT, CO-BB and CO-BIO also show that regional emissions are generally constrained within lowest 3 km of the atmosphere over all the regions

except for CO-BB over Burma during late February when this region experience intense biomass burning activity and CO plumes (> 100 ppbV) from fires reach up to 5 km (not shown). The vertical distribution of total CO mixing ratios over Bay of Bengal is similar to those observed over land regions with higher values in the PBL (180-400 ppbV) and lower values in the FT (90-250 ppbV), but the gradient is smaller and there is no clear signal of a diurnal variation in CO. This is interesting since the emissions over Bay of Bengal are negligible and thus indicates the transport of CO from the surrounding land regions to the oceanic regions during winter. Higher values of CO-ANT, CO-BB and CO-BIO distributions in the PBL indicate that transport of pollutants generally occur within the PBL. The en-route photochemical production also adds 10-20 ppbV to CO in the PBL over Bay of Bengal as evident from CO-CHEM distribution. CO-BC distribution shows that pollution inflow also enhances CO in both the PBL and in the FT frequently by more than 150 ppbV. This is likely due to anthropogenic and biomass burning emissions in Southeast Asia which are included in the MOZART-4 simulations that supply boundary conditions to WRF-Chem.

5.5 CO Budget Analysis

This section presents the budget analysis of CO at the surface, in the PBL and FT for the entire domain and the regions defined in Figure 5-1. CO mixing ratios from different source terms averaged at the surface, in the PBL and FT over the entire domain during January-February 2008 are shown in Figure 5-10. Average total CO mixing ratios at the surface are estimated as 318 ± 290 ppbV out of which 155 ± 241 ppbV ($34 \pm 27\%$) are provided by anthropogenic sources (CO-ANT), 133 ± 49 ppbV ($60 \pm 30\%$) by pollution inflow (CO-BC), 18 ± 140 ppbV ($3 \pm 7\%$) by biomass burning (CO-BB), 9 ± 11 ppbV ($2 \pm 2\%$) by chemistry (CO-CHEM) and 3 ± 4 ($1 \pm 1\%$) by biogenic sources (CO-BIO). Average total CO mixing ratios in the PBL (277 ± 207 ppbV) and the contributions from different sources are found to be similar to those at the surface and are estimated as 119 ± 176 ppbV ($30 \pm 25\%$) for CO-ANT, 133 ± 48 ppbV ($63 \pm 29\%$) for CO-BC, 14 ± 85 ppbV ($3 \pm 7\%$) for CO-BB, 8 ± 11 ppbV ($3 \pm 3\%$) for CO-CHEM and 2 ± 3 ppbV ($1 \pm 1\%$) for CO-BIO. Average total CO mixing ratios in the FT (124 ± 27 ppbV) are much lower than those at the surface and in the PBL, and are mainly influenced by pollution inflow as indicated by a higher average contribution of 108 ± 14 ppbV ($89 \pm 13\%$) from CO-BC. The average mixing ratios for other CO tracers in the FT are estimated as 12 ± 19 ppbV ($8 \pm 11\%$) for CO-ANT, 2 ± 8 ppbV ($1 \pm 3\%$) for CO-BB, 2 ± 2 ppbV ($1 \pm 1\%$) for CO-CHEM and 0.3 ± 0.4 ppbV ($0.2 \pm 0.3\%$) for CO-BIO.

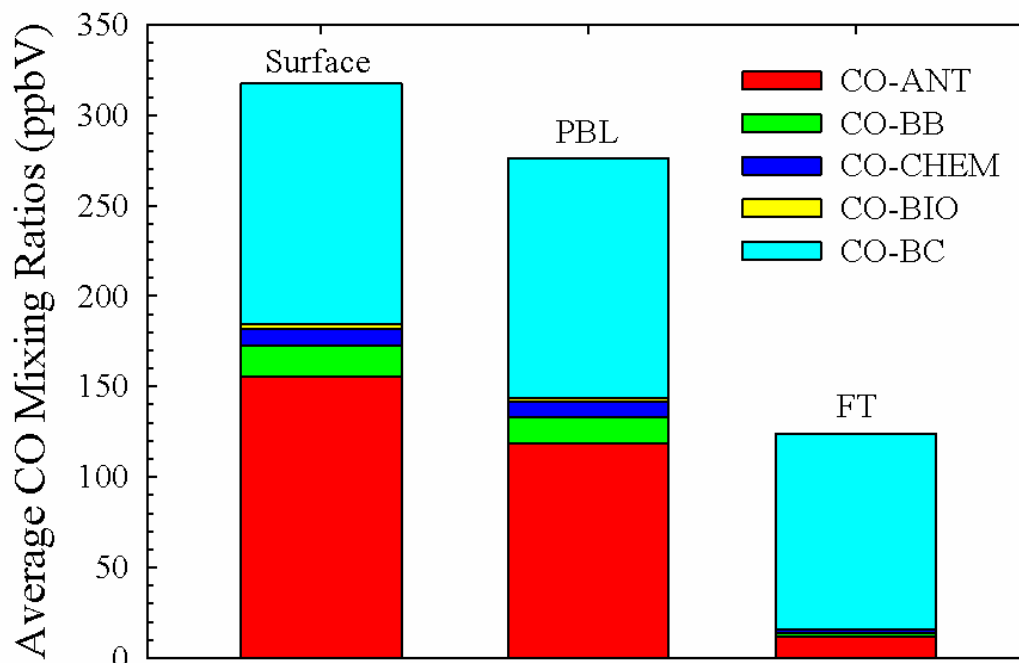


Figure 5-10: CO mixing ratios averaged at the surface, in the PBL and in the FT over the entire model domain during January-February 2008.

The budget of CO is also analyzed for the seven geographical regions defined in Figure 5-1. The mixing ratios of total CO and different CO tracers averaged at the surface over these regions are depicted in Table 5-1 along with relative contribution of each tracer to total CO mixing ratios. Average total CO mixing ratios at the surface ranges from 400 to 724 ppbV over the land regions with highest values over eastern India. More than 65% of the total surface CO over the Indian regions comes from anthropogenic sources and pollution inflow (CO-BC) contribution ranges from 17% to 31% with absolute mixing ratios between 110 and 120 ppbV. The contribution of other sources remains less than 5% over the Indian region. Over Burma, biomass burning (24%) also emerges as an important source in addition to anthropogenic sources (36%) and pollution inflow (33%). Average total surface CO mixing ratios over the Arabian Sea (233 ± 71 ppbV) and the Bay of Bengal (317 ± 54 ppbV) are significantly lower than those over the land regions but are mainly due to anthropogenic sources (37-40%) and pollution inflow (49-57%). The statistics for total CO and different tracers in the PBL is found to be similar to that estimated for the surface. In the FT, average total CO mixing ratios ranges from 120 to 143 ppbV over different regions with more than 75% of CO provided by pollution inflow and 10-21% by anthropogenic sources.

Table 5-1: Mixing ratios of total CO and different CO tracers averaged at the surface during January-February 2008 over the seven geographical regions defined in Figure 5-1. The percentage contribution of each tracer to total CO mixing ratio is also given in parentheses. All numbers are rounded-off to the nearest whole number value.

Region	Total CO ^a	CO-ANT ^a	CO-BB ^a	CO-CHEM ^a	CO-BIO ^a	CO-BC ^a
Northern India	400±96	270±95 (65 ± 9)	7±5 (2 ± 1)	4±2 (1 ± 1)	2±1 (-)	118±7 (31 ± 9)
Western India	473±123	326±122 (67 ± 9)	15±8 (3 ± 2)	10±5 (2 ± 1)	5±2 (1 ± 0)	117±7 (27 ± 8)
Eastern India	724±182	571±176 (78 ± 6)	21±19 (3 ± 2)	14±5 (2 ± 1)	7±2 (1 ± 0)	111±7 (17 ± 5)
Southern India	554±145	387±136 (68 ± 7)	26±14 (5 ± 2)	20±5 (4 ± 1)	8±2 (1 ± 0)	112±10 (22 ± 6)
Burma	463±162	159±46 (36 ± 11)	133±153 (24 ± 16)	21±5 (5 ± 1)	9±2 (2 ± 1)	140±29 (33 ± 10)
Arabian Sea	233±71	99±63 (37 ± 15)	6±5 (2 ± 1)	9±6 (3 ± 1)	1±1 (-)	117±8 (57 ± 18)
Bay of Bengal	317±54	132±42 (40 ± 15)	17±17 (5 ± 5)	17±5 (5 ± 1)	3±1 (1 ± 0)	148±30 (49 ± 11)

^aMean ± 1 sigma.

Here, it should be noted that higher surface CO values over the Bay of Bengal than the Arabian Sea are consistent with previous observations of different trace species in these oceanic regions [e.g. *Naja et al.*, 2004; *Lal et al.*, 2007; *Kedia and Ramachandran*, 2008; *Nair et al.*, 2008; *Srivastava et al.*, 2011]. The analysis of different tracers shows that the contribution of CO-ANT, CO-BB, CO-CHEM and CO-BC to total CO over Bay of Bengal are higher than those over Arabian Sea. This suggests that the Bay of Bengal is more strongly affected by the regional sources and en-route photochemistry than the Arabian Sea. Higher CO-BC values are likely due to transport from Southeast Asia as evident from Figure 5-5.

5.6 Regional Meteorology and surface CO distribution

The results presented in the previous section showed that the CO budget at the surface and in the PBL over South Asian region is mostly controlled by anthropogenic sources and pollution inflow. In this Section, we assess the relative importance of local anthropogenic sources and transport of anthropogenic CO from other regions for the defined geographical regions. The

spatial distributions of CO emitted from anthropogenic sources in northern India (CO-ANI), western India (CO-AWI), eastern India (CO-AEI), southern India (CO-ASI), Burma (CO-ABUR) and other regions (CO-OTH) averaged at the surface during January-February 2008 along with averaged 10 m wind vectors are shown in Figure 5-11. The wind patterns indicate that the low level circulation is favourable for transport of pollutants from northern to southern parts of the model domain. The winds from North India blow in two channels: one consisting of north-westerly along the Indo-Gangetic Plain region and the other one consisting of north-easterly winds blowing towards west India. The winds entering the Bay of Bengal from East India change to north-easterly and become nearly easterlies as they approach South India. The winds entering the northern Arabian Sea are northerly and change to north-easterly as they progress towards the south.

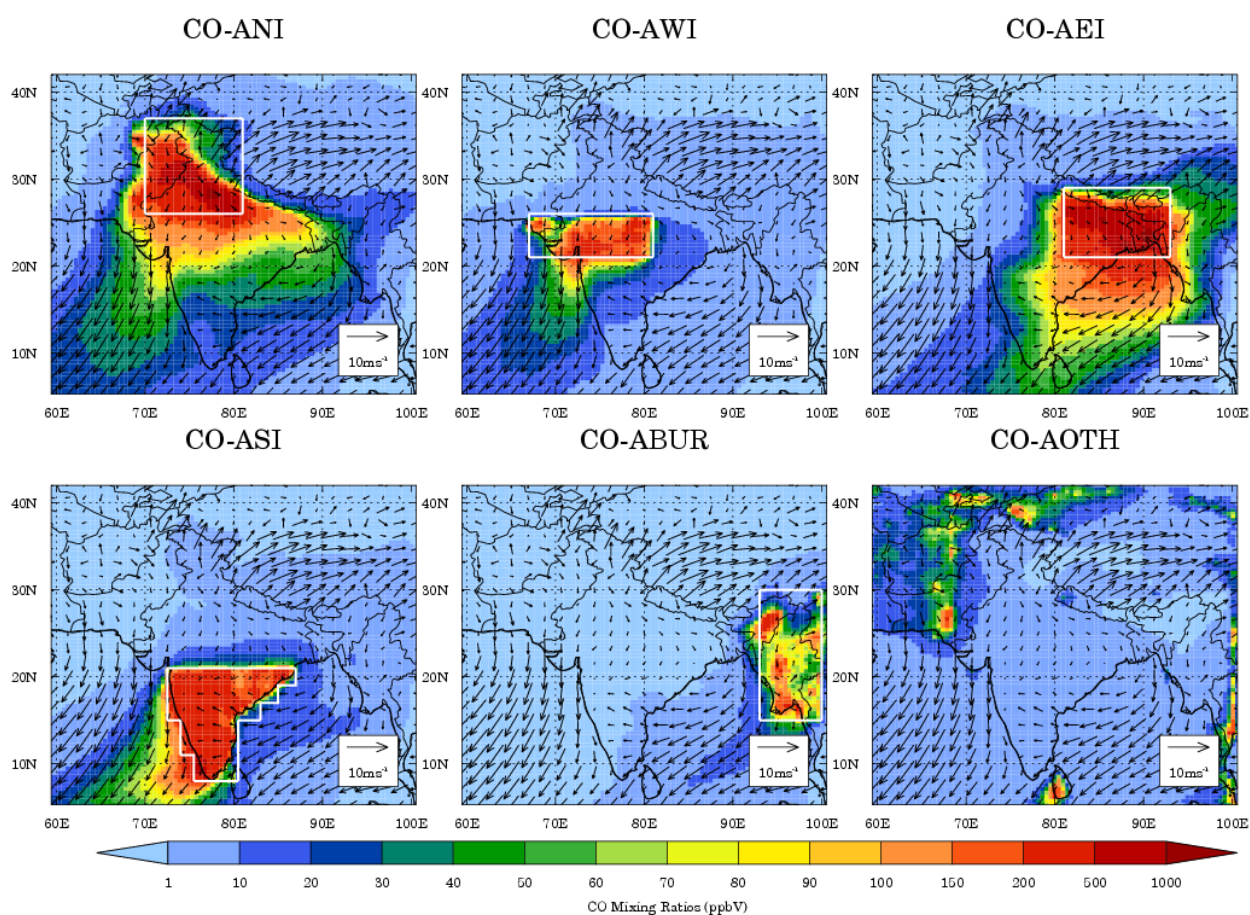


Figure 5-11: Spatial distributions of surface CO emitted from anthropogenic sources in northern (CO-ANI), western (CO-AWI), eastern (CO-AEI), and southern (CO-ASI) India, Burma (CO-ABUR) and other regions (CO-OTH) averaged at the surface during January-February 2008. Averaged 10 m wind vectors are also shown to portray regional low level circulation. The white box shows the geographical boundaries of the respective regions.

The CO-ANI distribution shows that anthropogenic emissions from northern India can influence surface CO over most parts of the domain with a contribution of more than 50 ppbV over eastern and western India, the Arabian Sea and northern Bay of Bengal. The impacts of anthropogenic emissions from western India (CO-AWI) are strongest over the Arabian Sea. Eastern Indian anthropogenic emissions (CO-AEI) contribute significantly to surface CO over the Bay of Bengal, Burma and southern India. Anthropogenic emissions from southern India (CO-ASI) are the major contributor to total anthropogenic CO over southern Arabian Sea and those from Burma (CO-ABUR) can contribute 10-20 ppbV over the Bay of Bengal. Anthropogenic emissions from other regions (CO-AOTH) contribute less than 20 ppbv to surface CO over all the Indian regions, Burma and oceanic regions. Similar spatial distributions are seen for all these tracers in the PBL.

Table 5-2: *Mixing ratios of total anthropogenic CO and different anthropogenic regional CO tracers averaged at the surface during January-February 2008 over the seven geographical regions defined in Figure 5-1. The percentage contribution of each tracer to total anthropogenic CO mixing ratio is also given in parentheses. All numbers are rounded-off to the nearest whole number value.*

Region	CO-ANT ^a	CO-ANI ^a	CO-AWI ^a	CO-AEI ^a	CO-ASI ^a	CO-ABUR ^a	CO-AOTH ^a
Northern India	270±95	249±90 (92±7)	3±5 (1±2)	10±13 (4±5)	1±4 (-)	-	7±2 (3 ± 1)
Western India	326±122	136±54 (43 ± 12)	142±71 (42 ± 13)	30±25 (9 ± 7)	10±14 (3 ± 3)	-	8±3 (3 ± 1)
Eastern India	571±176	68±31 (13 ± 7)	8±5 (2 ± 1)	476±173 (82 ± 7)	11±9 (2 ± 2)	6±5 (1 ± 1)	2±0 (-)
Southern India	387±136	38±13 (11 ± 3)	25±9 (6 ± 2)	76±36 (22 ± 9)	245±111 (59 ± 11)	1±1 (-)	2±1 (1 ± 0)
Burma	159±46	12±6 (8 ± 4)	4±3 (2 ± 2)	54±32 (33 ± 14)	7±7 (4 ± 4)	78±31 (51 ± 19)	3±1 (2 ± 1)
Arabian Sea	99±63	32±21 (36 ± 14)	23±15 (27 ± 7)	8±9 (6 ± 5)	30±28 (22 ± 14)	-	5±2 (9 ± 7)
Bay of Bengal	132±42	19±9 (14 ± 6)	5±4 (4 ± 2)	85±32 (62 ± 9)	9±8 (7 ± 6)	10±8 (9 ± 6)	4±2 (4 ± 4)

^aMean ± 1 sigma.

The mixing ratios of total anthropogenic CO and different anthropogenic CO tracers averaged at the surface over the defined seven regions are shown in Table 5-2 along with relative contribution of each tracer to total anthropogenic CO mixing ratios. It is estimated that 92% of the total anthropogenic CO over northern India (270 ppbV) originates from the local sources. Interestingly, the contribution of northern Indian sources (43%) to total anthropogenic CO over western India (326 ppbV) is as important as that from local sources (42%). Most of the anthropogenic CO over eastern India (571 ppbV) comes from local (82%) and northern Indian sources (13%) while that over southern India (387 ppbV) comes from local (59%), eastern (22%) and northern Indian sources (11%). Eastern Indian anthropogenic emissions also contribute 33% to total anthropogenic CO over Burma (159 ppbV) where local sources contribute 51%. The major sources for total anthropogenic CO over the Bay of Bengal (132 ppbV) are eastern India (62%) and northern India (14%) with contributions of less than 10% from the remaining regions. In contrast, total anthropogenic CO over the Arabian Sea (99 ppbV) is determined mainly by northern (36%), western (27%) and southern Indian (22%) sources. These results show that regional meteorology plays an important role in distributing the regional emissions and thus controlling surface CO variability over the South Asian region.

5.7 Summary

The Weather Research and Forecasting Model with Chemistry (WRF-Chem) has been used to conduct a budget analysis of tropospheric CO distribution in South Asia during January-February 2008. A total of eleven CO tracers were included in the model with five of them keeping track of CO originating from emissions sources (anthropogenic, biogenic and biomass burning), photochemistry and pollution inflow, and the other six tracking CO emitted from anthropogenic sources located in different geographical regions of the domain. The model performance is evaluated by comparing the model output with CO retrievals from the Measurements of Pollution in the Troposphere (MOPITT) instrument. The spatial distribution of MOPITT total column CO and the vertical distribution of CO mixing ratios over different geographical regions of South Asia are fairly well reproduced by the model. However, the model generally overestimates MOPITT retrievals in the lower troposphere.

The CO budget is analyzed at the surface, in the planetary boundary layer (PBL) and free troposphere (FT). CO mixing ratios at the surface, in the PBL and the FT averaged over the entire domain are estimated to be 318 ppbV, 277 ppbV and 124 ppbV respectively during

January-February 2008. CO at the surface and in the PBL exhibit large spatial variability and is controlled largely by pollution inflow and anthropogenic sources, while CO in FT shows little spatial variability and is controlled mainly by pollution inflow. Average CO mixing ratios from anthropogenic sources and pollution inflow are estimated to be 155 ppbV and 133 ppbV respectively at the surface, and 12 ppbV and 108 ppbV respectively in the free troposphere. Biomass burning sources contribute significantly (10-80%) to total CO concentration at the surface and in the PBL of Burma. Average mixing ratios of other tracers are less than 20 ppbV over the model domain. The vertical distributions of CO tracers for anthropogenic, biogenic and biomass burning sources indicate that regional emissions are generally constrained within the lowest 3 km of the atmosphere except over Burma where fire plumes reach altitudes as high as 5 km.

The analysis of low level circulation along with regional anthropogenic CO emission tracers showed that, apart from local sources, transport of anthropogenic emissions from other regions can also enhance surface CO in a given region by 10-100 ppbV. The contribution of anthropogenic emissions to total surface CO is also found to be significant over the oceanic regions of the Arabian Sea (37%) and the Bay of Bengal (40%). The major source regions contributing to anthropogenic CO over the Arabian Sea are found in northern, western and southern India while those for the Bay of Bengal are located in eastern and northern India. Anthropogenic emissions from northern India also affect surface CO over eastern and western India while those from eastern India also affect surface CO over southern India and Burma.

6. Conclusions and Future Scope

The anthropogenic emissions of several key trace gases and aerosols have been increasing dramatically over Asian region due to rapid growth in economy, industries, transportation and urbanization. These rising emissions not only affect the air quality and climate of Asia but also of other continents. Some efforts have been made to understand the regional and global implications of Asian emissions by integrating observations from intensive field campaigns (e.g. PEM West-A, PEM-West B, TRACE-P and CARE-Beijing etc.) and satellite-based instruments with chemical transport modeling. However, such efforts focused mainly on the East Asian region and are limited (INDOEX) over South Asia where increasing pollution is suggested to have important implications for crops, vegetation and freshwater resources. South Asian anthropogenic emissions are also suggested to have characteristics different from much of the Northern Hemisphere because a large fraction of these emissions comes from biomass and bio-fuel burning. Consequently, the chemical processes over this region may also differ from what is known for other regions on the globe. In addition, the strong tropical solar radiation and higher water vapor amount lead to very high photochemical activity over this region.

In view of the above, ground-based measurements of both ozone and aerosols were initiated over the inland as well as the oceanic regions of South Asia in the 1990s. However, these measurements provide information for selected species only and have limited spatial coverage. Additionally, the observational time series are not long enough for understanding the climatic impacts of trace species in this region. Due to the scarcity of in situ observations, the use of satellite observations along with chemistry transport models is essential for improving our understanding of distribution and variability of trace species over this region. The available modeling studies indicate significant discrepancies between modeled and observed values of ozone and related gases and a lack of understanding of the relevant processes. In light of the above conditions, this dissertation focused on setting-up the Weather

Research and Forecasting – Chemistry (WRF-Chem) model over the South Asian region. The evaluated configuration is used to examine distribution of surface ozone and analyze wintertime CO distribution over South Asia. The model domain is set-up to cover the South Asian region from 5°N to 40°N and 60°E to 100°E. The anthropogenic emissions for the simulation domain are prepared by inserting an Asian emission inventory prepared for INTEX-B mission in the global RETRO emission inventory. The initial and boundary conditions for the meteorological fields are taken from FNL datasets while those for the chemical fields are taken from the results of MOZART-4. The results from this study are presented in chapters 3 to 5 and are summarized in this chapter

6.1 Conclusions

The meteorological fields simulated by the WRF-Chem model are evaluated against radiosonde observations, NCEP reanalysis fields and retrievals from AIRS and TRMM in chapter 3. The evaluated variables include temperature, water vapor, dew point temperature, zonal and meridional wind components, precipitation and tropopause pressure. The model data is co-located in space and time with quality controlled observations. The main results from chapter 3 are:

- The general features of South Asian meteorology such as seasonal changes in wind patterns along with the seasonal cycle of temperature, water vapor, precipitation and tropopause pressure are successfully reproduced by the model. Different statistical metrics estimated from model-observation comparison indicate that the agreement between model and observations is better for temperature as compared to the other parameters.
- The mean bias (MB) and root mean square error (RMSE) in all meteorological parameters show an increasing tendency with altitude. The model is biased cold near the surface in all the seasons while it is biased warm aloft. On average, the model is biased dry at 1000 hPa in winter and spring while it is biased wet at this level in summer and autumn. The model simulated winds show both an easterly and a northerly bias. The spatial and temporal variability of rainfall events is also captured reasonably well by the model. The frequency bias index values indicate that the model generally overestimates domain-wide precipitation except for some events exceeding 40 mm day⁻¹ in winter.

- The seasonal variability of temperature and dew point temperature at 34 stations located within the Indian region replicated well by the model. However, estimated statistical metrics indicate relatively better result for inland sites as compared to coastal and island sites. Analysis of the topography and land-cover used by the model suggest that erroneous representation of these surface characteristics possibly due in parts to the coarse model resolution (45 km) leads to a poorer correlation for these sites. The spatio-temporal variability of tropopause pressure is also simulated well by the model.
- The comparison of statistical metrics with a set of proposed benchmarks revealed that errors in model simulated meteorological parameters are well within or comparable to the proposed benchmark values and errors in these parameters should induce only small errors in chemistry simulations. The biases in simulations of temperature, water vapor and wind components can introduce errors of \pm (10-25%) in simulations of tropospheric ozone, CO and NO_x. In summary, the model has good ability to simulate the spatio-temporal variabilities of meteorological parameters over this region and modeled meteorology is of sufficient quality for use in chemical transport modeling.

The model simulated ozone, carbon monoxide and nitrogen oxides are compared with co-located ground-based, balloon-borne and space-borne observations in chapter 4. Ground-based observations include surface ozone from seven sites and CO and NO_x observations from three sites, while balloon-borne observations of ozone are available from two sites in the Indian region. Space-borne observations include retrievals of ozone from TES, nitrogen dioxide from OMI and GOME, and carbon monoxide from MOPITT. The main results from chapter 4 are:

- The model has good ability of simulating the seasonal variations of surface ozone and CO over the Indian region but shows some differences for NO_x seasonality particularly during spring. The vertical distribution of ozone and CO is also simulated well by the model. The index of agreement between model and satellite retrievals is estimated to be 0.47 - 0.9 indicating that model is capable of reproducing the overall spatial and temporal variability of ozone, CO and NO₂.
- Bias analysis indicates that the model underestimates TES retrieved lower tropospheric ozone values. The model also underestimates OMI retrieved tropospheric column NO₂ values except during winter. MOPITT total column CO retrievals are

underpredicted during February-July while they are overestimated during other months. The discrepancies between the model and observations indicate large uncertainties in anthropogenic and biomass burning emissions estimates, particularly for NO_x . The absence of plume rise parameterization could also contribute to model-observation discrepancy.

- Chemical and meteorological model fields are used to understand the spatio-temporal variability of surface ozone and the analysis clearly indicates regional differences in the seasonality of surface ozone over South Asia. The inland regions show net ozone production (0 to 5 ppbv hr^{-1}) while the cleaner marine and mountainous regions show net ozone destruction (0 to -2 ppbv hr^{-1}) during daytime. Net ozone production (0-2 ppbv hr^{-1}) is also seen over the marine regions experiencing outflow from the South Asian region. Highest net ozone production rates are seen over the Indo-Gangetic Plain (IGP) region and some cities located along the coastal regions of India. Ozone production over South Asia is estimated to be limited mostly by NO_x except for some regions over the Indo-Gangetic Plain region during winter.

The WRF-Chem model is used to conduct a budget analysis of tropospheric CO distribution over South Asia during January-February 2008. A total of eleven CO tracers are included in the model with five of them keeping track of CO originating from emissions sources (anthropogenic, biogenic and biomass burning), photochemistry and pollution inflow, and other six tracking CO emitted from anthropogenic sources located in different geographical regions of the domain. The main results from chapter 5 are:

- The spatial distribution of MOPITT total column CO and the vertical distribution of CO mixing ratios over different geographical regions of South Asia are reproduced fairly well by the model. However, the model generally overestimates MOPITT retrievals in the lower troposphere.
- The CO budget is analyzed at the surface, in the planetary boundary layer (PBL) and free troposphere (FT) during January-February 2008. CO at the surface and in the PBL show large spatial variability and is controlled largely by pollution inflow and anthropogenic sources while CO in the FT show little spatial variability and is controlled mainly by pollution inflow. Biomass burning sources contribute significantly (10-80%) to total CO at the surface and in the PBL only over Burma. The vertical distributions of CO tracers for anthropogenic, biogenic and biomass

burning sources indicate that regional emissions are generally constrained within lowest 3 km except over Burma where fire plumes reach as high as 5 km.

- Intra-regional transport of CO is also estimated to be an important source of surface CO over different geographical regions in addition to local sources. The contribution of anthropogenic emissions to total surface CO is also found to be significant over the oceanic regions of Arabian Sea (37%) and Bay of Bengal (40%). The major source regions contributing to anthropogenic CO over Arabian Sea are found to be North, West and South India while those for Bay of Bengal are East India and North India.

6.2 Future Scope

This work set up a fully coupled online regional chemical transport model known as Weather Research and Forecasting Model with Chemistry (WRF-Chem) over South Asia and lends confidence to the use of WRF-Chem for analyzing the spatial and temporal variability in trace gases over India. A number of interesting prospects that can be investigated as a continuation of this research work are as follows:

- ✓ The observations of ozone and related gases are highly limited over the South Asian region and this scarcity inhibits thorough evaluation of regional/global models and space-borne observations. Therefore, it is imperative to conduct co-located measurements of ozone and precursors including intermediate radical species with sufficient spatial and temporal coverage over this region. In addition, these observations will provide information on the chemical characteristics of pollutants in this region and can be integrated with the WRF-Chem model for understanding regional distribution of ozone and related species.
- ✓ Large uncertainties in the existing emission inventories might lead to significant errors in tropospheric ozone simulations over South Asia which in turn will pose a major limitation to the regional air quality management. Therefore, it is highly essential to improve the emission estimates to study the response of ozone to increasing anthropogenic emissions and reduce the uncertainties in simulation of ozone concentration in this region. The WRF-Chem model can be used as a forward model in conjunction with satellite-observations to improve the emission estimates over this region.
- ✓ Regional meteorology is seen to play an important role in controlling the distribution of

wintertime CO over South Asia. The WRF-Chem model in tagged tracer mode can be used to examine how the changes in regional meteorology can affect the distribution of CO and other trace species over this region. These simulations will also provide useful insight into the impact of pollution inflow on seasonal variability of trace species over this region.

- ✓ The WRF-Chem model can also be used to examine the relative contributions of anthropogenic, biomass burning and biogenic emission sources to the budget of different trace species. Such budget studies will provide guidance for defining the air pollution mitigation policies in this region.

In addition to the issues stated above, other important issues such as the estimation of impacts of South Asian pollutants on the radiation and water budgets, transport patterns and the enroute physical and chemical transformation processes in the South Asian outflow can be addressed by integrating the WRF-Chem model with in situ and space-borne observations. Detailed and focused modeling work together with an increased number of observations will enable a better understanding of tropospheric chemistry and current and future air quality over South Asia, which is presently lacking.

References

- Ackermann, I. J., H. Hass, M. Memmesheimer, A. Ebel, F. S. Binkowski and U. Shankar (1998), Modal aerosol dynamics model for Europe: development and first applications, *Atmos. Environ.*, *32* (17), 2981-2999.
- Adler, R. F., et al. (2000), Tropical Rainfall Distributions Determined using TRMM Combined with Other Satellite and Rain Guage Information, *J. Appl. Meteorol.*, *39*, 2007-2023.
- Agrawal, M. (2003), Air pollution impact on vegetation in India, in: *Air pollution impacts on crop and forests: a global assessment*, Imperial College Press, London, UK, 165-187.
- Akimoto, H. (2003), Global air quality and pollution, *Science*, *302*, 1716-1719, doi: 10.1126/science.1092666.
- Allen, D., K. Pickering, and M. Fox-Rabinovitz (2004), Evaluation of pollutant outflow and CO sources during TRACE-P using model-calculated, aircraft-based, and Measurements of Pollution in the Troposphere (MOPITT)-derived CO concentrations, *J. Geophys. Res.*, *109*, D15S03, doi: 10.1029/2003JD004259.
- Aneja, V. P., A. Agarwal, P. A. Roelle, S. B. Phillips, Q. Tong, N. Watkins, and R. Yablonsky (2001), Measurements and analysis of criteria pollutants in New Delhi, India, *Environ. Int.*, *27*, 35-42.
- Asnani, G. C. (2005), Climatology of the tropics, in *Tropical Meteorology*, vol. 1, pp. 100-204, G.C. Asnani, Pune, India.
- Aumann, H. H., Chahine, M. T., Gautier, C., Goldberg, M. D., Kalnay, E., McMillin, L. M., Revercomb, H., Rosenkranz, P. W., Smith, W. L., Staelin, D. H., Strow, L. L., and Susskind, J. (2003), AIRS/AMSU/HSB on the Aqua mission: Design, science objectives, data products, and processing systems, *IEEE Trans. Geosci. Remote Sens.*, *41*(2), 253-264.
- Bao, J.-W., Michelson, S. A., McKeen, S. A., and Grell, G. A. (2005), Meteorological evaluation of a weather-chemistry forecasting model using observations from the TEXAS AQS 2000 field experiment, *J. Geophys. Res.*, *110*, D21105, doi: 10.1029/2004JD005024.
- Beer, R., T. A. Glavich, and D. M. Rider (2001), Tropospheric Emission Spectrometer for the Earth Observing System Aura satellite, *Appl. Opt.*, *40*, 2356-2367.
- Beig, G. and G. P. Brasseur (2006), Influence of anthropogenic emissions on tropospheric ozone and its precursors over the Indian tropical region during a monsoon, *Geophys. Res. Lett.*, *33*, L07808, doi: 10.1029/2005GL024949.
- Beig, G. and K. Ali (2006), Behavior of boundary layer ozone and its precursors over a great alluvial plain of the world: Indo-Gangetic Plains, *Geophys. Res. Lett.*, *33*, L24813, doi: 10.1029/2006GL028352.
- Beig, G., S. Gunthe, and D. B. Jadhav (2007), Simultaneous measurements of ozone and its precursors on a diurnal scale at a semi urban site in India, *J. Atmos. Chem.*, *57*, 239-253, doi: 10.1007/s10874-007-9068-8.
- Beljaars, A. C. M., (1994), The parameterization of surface fluxes in large-scale models under free convection, *Quart. J. Roy. Meteor. Soc.*, *121*, 255-270.

References

- Binkowski, F. S. and U. Shankar (1995), The regional particulate matter model, 1. Model description and preliminary results, *J. Geophys. Res.*, *100*, 26191-26209.
- Boersma, K. F., Dirksen, R. J., Veefkind, J. P., Eskes, H. J., and van der A, R. J. (2009b), *Dutch OMI NO₂ (DOMINO) data product, HE5 data file user manual*, available at http://www.temis.nl/docs/OMI_NO2_HE5_1.0.2.pdf.
- Boersma, K. F., Eskes, H. J., Veefkind, J. P., Brinksma, E. J., van der A, R. J., Sneep, M., van den Oord, G. H. J., Levelt, P. F., Stammes, P., Gleason, J. F., and Bucsela, E. J. (2007), Near-real time retrieval of tropospheric NO₂ from OMI, *Atmos. Chem. Phys.*, *7*, 2103-2118.
- Boersma, K. F., Jacob, D. J., Bucsela, E. J., Perring, A. E., Dirksen, R., van der A, R. J., Yantosca, R. M., Park, R. J., Wenig, M. O., Bertram, T. H., and Cohen, R. C. (2008), Validation of OMI tropospheric NO₂ observations during INTEX-B and application to constrain NO_x emissions over the eastern United States and Mexico, *Atmos. Environ.*, *42*, 4480-4497.
- Boersma, K. F., Jacob, D. J., Trainic, M., Rudich, Y., DeSmedt, I., Dirksen, R., and Eskes, H. J. (2009a), Validation of urban NO₂ concentrations and their diurnal and seasonal variations observed from the SCIAMACHY and OMI sensors using in situ surface measurements in Israeli cities, *Atmos. Chem. Phys.*, *9*, 3867-3879.
- Bowman, K. W., Steck, T., Worden, H. M., Worden, J., Clough, S., and Rodgers, C. (2002), Capturing time and vertical variability of tropospheric ozone: A study using TES nadir retrievals, *J. Geophys. Res.*, *107* (D23), 4723, doi: 10.1029/2002JD002150.
- Boynard, A., G. G. Pfister and D. P. Edwards (2012), Boundary layer versus free tropospheric CO budget and variability over the United States during summertime, *J. Geophys. Res.*, *117*, D04306, doi: 10.1029/20011JD016416.
- Bucsela, E. J., Celarier, E. A., Wenig, M. O., Gleason, J. F., Veefkind, J. P., Boersma, K. F., and Brinksma, E. J. (2006), Algorithm for NO₂ vertical column retrieval from the ozone monitoring instrument, *IEEE T. Geosci. Remote*, *44* (4), 1245-1258.
- Celarier, E. A., and Retscher, C. (2009), *OMNO2e Data product Readme File, Document Revision 1.2, NASA Goddard Space Flight Center*, available at http://toms.gsfc.nasa.gov/omi/no2/OMNO2e_DP_Readme.pdf.
- Chang, H.-I., Niyogi, D., Kumar, A., Kishitawal, C. M., Dudhia, J., Chen, F., Mohanty, U. C., and Shepherd, M. (2009), Possible relation between land surface feedback and post-landfall structure of monsoon depressions, *Geophys. Res. Lett.*, *36*, L15826, doi: 10.1029/2009GL037781.
- Chou, M.-D. and M. J. Suarez (1994), An efficient thermal infrared radiation parametrization for use in general circulation models, *NASA Tech. Memo. 104606*, *3*, 85 pp.
- Collins, W. D., et al. (2001), Simulating aerosols using a chemical transport model with assimilation of satellite aerosol retrievals: Methodology for INDOEX, *J. Geophys. Res.*, *106*, 7313-7336.
- Collins, W. D., et al. (2002), Simulation of aerosol distributions and radiative forcing for INDOEX: Regional climate impacts, *J. Geophys. Res.*, *107*, 8028, doi: 10.1029/2000JD000032.
- Cooper, O. R., Parrish, D. D., Stohl, A., Trainer, M., Nédélec, P., Thouret, V., Cammas, J. P., Oltmans, S. J., Johnson, B. J., Tarasick, D., Leblanc, T., McDermid, I. S., Jaffe, D.,

References

- Gao, R., Stith, J., Ryerson, T., Aikin, K., Campos, T., Weinheimer, A., and Avery, M. A. (2010), Increasing springtime ozone mixing ratios in the free troposphere over western North America, *Nature*, *463*, 344-348.
- Courant, R., K. Friedrichs and H. Lewy (1928), Über die partiellen Differenzgleichungen der mathematischen Physik. *Math. Ann.* 100, 32–74.
- Dalvi, M., G. Beig, U. Patil, A. Kaginalkar, C. Sharma and A. P. Mitra (2006), A GIS based methodology for gridding large scale emission inventories: Application to carbon-monoxide emissions over Indian region, *Atmos. Environ.*, *40*, 2995-3007.
- David, L. M., and Nair, P. R. (2011), Diurnal and seasonal variability of surface ozone and NO_x at a tropical coastal site: Association with mesoscale and synoptic meteorological conditions, *J. Geophys. Res.*, *116*, D10303, doi: 10.1029/2010JD015076.
- David, L. M., I. A. Girach, and P. R. Nair (2011), Distribution of ozone and its precursors over Bay of Bengal during winter 2009: role of meteorology, *Ann. Geophys.*, *29*, 1613-1627, doi: 10.5194/angeo-29-1613-2011.
- de Latt, A., J. Lelieveld, G. Roelofs, R. Dickerson and J. Lobert (2001), Source analysis of carbon monoxide pollution during INDOEX 1999, *J. Geophys. Res.*, *106*, D22, doi: 10.1029/2000JD900679.
- de Meij, A., Gzella, A., Thunis, P., Cuvelier, C., Bessagnet, B., Vinuesa, J. F., Menut, L. (2009), The impact of MM5 and WRF meteorology over complex terrain on CHIMERE model calculations, *Atmos. Chem. Phys.*, *9*, 6611-6632.
- Deb, S. K., T. P. Srivastava and C. M. Kishtawal (2008), The WRF model performance for the simulation of heavy precipitation events over Ahmedabad during August 2006, *J. Earth. Syst. Sci.*, *117* (5), pp. 589-602.
- Decesari, S., Facchini, M. C., Carbone, C., Giulianelli, L., Rinaldi, M., Finessi, E., Fuzzi, S., Marinoni, A., Cristofanelli, P., Duchi, R., Bonasoni, P., Vuillermoz, E., Cozic, J., Jaffrezo, J. L., and Laj, P. (2010), Chemical composition of PM₁₀ and PM₁ at the high-altitude Himalayan station Nepal Climate Observatory-Pyramid (NCO-P) (5079 m a.s.l.), *Atmos. Chem. Phys.*, *10*, 4583-4596.
- Deeter, M. N. (2003b), *MOPITT (Measurements of Pollution in the Troposphere), Validated Version 4 Product User's Guide*, MOPITT Algorithm Development Team, Atmospheric Chemistry Division, National Center for Atmospheric Research, Boulder, 18-19 pp.
- Deeter, M. N., Emmons, L. K., Edwards, D. P., Gille, J. C., Drummond, J. R. (2004), Vertical resolution and information content of CO profiles retrieved by MOPITT, *Geophys. Res. Lett.*, *31*, L15112, doi: 10.1029/2004GL020235.
- Deeter, M. N., Emmons, L. K., Francis, G. L., Edwards, D. P., Gille, J. C., Warner, J. X., Khatatov, B., Ziskin, D., Lamarque, J.-F., Ho, S.-P., Yudin, V., Attié, J.-L., Packman, D., Chen, J., Mao, D., Drummond, J. R. (2003a), Operational carbon monoxide retrieval algorithm and selected results for the MOPITT instrument, *J. Geophys. Res.*, *108* (D14), 4399, doi: 10.1029/2002JD003186.
- Deeter, M. N., et al. (2010), The MOPITT version 4 CO product: Algorithm enhancements, validation, and long-term stability, *J. Geophys. Res.*, *115*, D07306, doi: 10.1029/2009JD013005.

References

- Di Girolamo, L., et al. (2004), Analysis of Multi-angle Imaging Spectro-Radiometer (MISR) aerosol optical depths over greater India during winter 2001-2004, *Geophys. Res. Lett.*, *31*, L23115, doi: 10.1029/2004GL021273.
- Divakarla, M. G., Barnet, C. D., Goldberg, M. D., McMillin, L. M., Maddy, E., Wolf, W., Zhou, L., and Liu, X. (2006), Validation of Atmospheric Infrared Sounder temperature and water vapor retrievals with matched radiosonde measurements and forecast, *J. Geophys. Res.*, *111*, D09S15, doi: 10.1029/2005JD006116.
- Drummond, J. R., and G. S. Mand (1996), The Measurement of Pollution in the Troposphere (MOPITT) Instrument: Overall performance and calibration requirements, *J. Atmos. Oceanic Technol.*, *13*, 314-320.
- Dutta, S. K. and V. S. Prasad (2010), Assessment of WRF-VAR assimilation for a cyclonic storm – Nisha, *Current Science.*, *99*(1), 86-91.
- Emery, C. A. (2001), *Enhanced meteorological modeling and performance evaluation for two Texas ozone episodes*, Prepared for the Texas Natural Resource Conservation Commission, by ENVIRON International Corporation.
- Emmons, L. K., D. P. Edwards, M. N. Deeter, J. C. Gille, T. Campos, P. Nédélec, P. Novelli, and G. Sachse (2009), Measurements of Pollution in the Troposphere (MOPITT) validation through 2006, *Atmos. Chem. Phys.*, *9*, 1795-1803, doi: 10.5194/acp-9-1795-2009.
- Emmons, L. K., Deeter, M. N., Gille, J. C., Edwards, D. P., Attié, J.-L., Warner, J., Ziskin, D., Francis, G., Khattatov, B., Yudin, V., Lamarque, J.-F., Ho, S.-P., Mao, D., Chen, J. S., Drummond, J., Novelli, P., Sachse, G., Coffey, M. T., Hannigan, J. W., Gerbig, C., Kawakami, S., Kondo, Y., Takegawa, N., Schlager, H., Baehr, J., and Ziereis, H. (2004), Validation of Measurements of Pollution in the Troposphere (MOPITT) CO retrievals with aircraft in situ profiles, *J. Geophys. Res.*, *109*, D03309, doi: 10.1029/2003JD004101.
- Emmons, L. K., Pfister, G. G., Edwards, D. P., Gille, J. C., Sachse, G., Blake, D., Wofsy, S., Gerbig, C., Matross, D., and Nédélec, P. (2007), Measurements of Pollution in the Troposphere (MOPITT) validation exercises during summer 2004 field campaigns over North America, *J. Geophys. Res.*, *112*, D12S02, doi: 10.1029/2006JD007833.
- Emmons, L. K., Walters, S., Hess, P. G., Lamarque, J.-F., Pfister, G. G., Fillmore, D., Granier, C., Guenther, A., Kinnison, D., Laepple, T., Orlando, J., Tie, X., Tyndall, G., Wiedinmyer, C., Baughcum, S., L., Kloster, S. (2010), Description and evaluation of the Model for Ozone and Related chemical Tracers, version 4 (MOZART-4), *Geosci. Model Dev.*, *3*, 43-67.
- Engardt, M. (2008), Modelling of near-surface ozone over South Asia, *Journal of Atmospheric Chemistry*, *59*, 61-80, doi: 10.1007/s10874-008-9096-z.
- Erisman, J. W., A. van Paul and P. Wyers (1994), Parameterization of surface resistance for the quantification of atmospheric deposition of acidifying pollutants and ozone, *Atmos. Environ.*, *28*, 2595-2607.
- Forster, P., V. Ramaswamy, P. Artaxo, T. Berntsen, R. Betts, D.W. Fahey, J. Haywood, J. Lean, D.C. Lowe, G. Myhre, J. Nganga, R. Prinn, G. Raga, M. Schulz and R. Van Dorland (2007), Changes in Atmospheric Constituents and in Radiative Forcing. In: *Climate Change 2007: The Physical Science Basis. Contribution of Working Group I*

References

- to the Fourth Assessment Report of the Intergovernmental Panel on Climate Change [Solomon, S., D. Qin, M. Manning, Z. Chen, M. Marquis, K.B. Averyt, M. Tignor and H.L. Miller (eds.)]. Cambridge University Press, Cambridge, United Kingdom and New York, NY, USA.
- Freitas, S. R., K. M. Longo, R. Chatfield, R. Latham, M. A. S. Silva Dias, M. O. Andreae, E. Prins, J. C. Santos, R. Gielow, and J. A. Carvalho Jr. (2007), Including the sub-grid scale plume rise of vegetation fires in low resolution atmospheric transport models, *Atmos. Chem. Phys.*, *7*, 3385-3398, doi: 10.5194/acp-7-3385-2007.
- Fu, R., Hu, Y., Wright, J. S., Jiang, J. H., Dickinson, R. E., Chen, M., Filipiak, M., Read, W. G., Waters, J. W., Wu, D. L. (2006), Short circuit of water vapor and polluted air to the global stratosphere by convective transport over the Tibetan Plateau, *Proc. Natl. Acad. Sci. U. S. A.*, *103*, 5664-5669.
- Geng, F., Zhao, C., Tang, X., Lu, G., and Tie, X. (2007), Analysis of ozone and VOCs measured in Shanghai: A case study, *Atmos. Environ.*, *41*, 989-1001.
- Gettelman, A., Weinstock, E. M., Fetzer, E. J., Irion, F. W., Eldering, A., Richard, E. C., Rosenlof, K. H., Thompson, T. L., Pittman, C., Webster, R., and Herman, R. L. (2004), Validation of Aqua satellite data in the upper troposphere and lower stratosphere with in situ aircraft measurements, *Geophys. Res. Lett.*, *31*, L22107, doi: 10.1029/2004GL020730.
- Ghude S. D., S. Fadnavis, G. Beig, S. D. Polade, and R. J. van der A (2008), Detection of surface emission hot spots, trends, and seasonal cycle from satellite-retrieved NO₂ over India, *J. Geophys. Res.*, *113*, D20305, doi: 10.1029/2007JD009615.
- Ghude, S. D., Lal, D. M., Beig, G., van der A, R., and Sable, D. (2010), Rain-Induced Soil NO_x Emissions from India During the Onset of the Summer Monsoon: A Satellite Perspective, *J. Geophys. Res.*, *115*, D16304, doi: 10.1029/2009JD013367.
- Giglio, L., I. Csiszar and C. O. Justice (2006), Global distributions and seasonality of active fires as observed with the Terra and Aqua Moderate Resolution Imaging Spectroradiometer (MODIS), *J. Geophys. Res.*, *111*, G02016, doi: 10.1029/2005JG000142.
- Govindankutty, M. et al. (2008), The impact of Assimilation of MODIS Observations Using WRF-VAR for the Prediction of a Monsoon Depression During September 2006, *The Open Atmospheric Science Journal*, *2*, 68-78.
- Granier, C., G. Petron, J. -F. Mueller, and G. Brasseur (2000), The impact of natural and anthropogenic hydrocarbons on the tropospheric budget of carbon monoxide, *Atmos. Environ.*, *34*, 5255-5270.
- Granier, C., J. F. Mueller, G. Petron and G. Brasseur (1999), A three dimensional study of the global CO budget, *Chemosphere Global Change Sci.*, *1*, 255-261, doi: 10.1016/S1465-9972(99)00007-0.
- Grell, G. A., S. E. Peckham, R. Schmitz, S. A. Mckeen, G. Frost, W. C. Skamarock, and B. Eder (2005), Fully coupled online chemistry within the WRF model, *Atmos. Environ.*, *39*, 6957-6975, doi: 10.106/j.atmosenv.2005.04.027.
- Guenther, A., T. Karl, P. Harley, C. Wiedinmyer, P. I. Palmer, and C. Geron (2006), Estimates of global terrestrial isoprene emissions using MEGAN (Model of Emissions

References

- of Gases and Aerosols from Nature), *Atmos. Chem. Phys.*, *6*, 3181-3210, doi: 10.5194/acp-6-3181-2006.
- Han, K. M., Song, C. H., Ahn, H. J., Park, R. S., Woo, J. H., Lee, C. K., Richter, A., Burrows, J. P., Kim, J. Y., and Hong, J. H. (2009), Investigation of NO_x emissions and NO_x-related chemistry in East Asia using CMAQ-predicted and GOME-derived NO₂ columns, *Atmos. Chem. Phys.*, *9*, 1017-1036, 2009.
- Hansen, M., R. DeFries, J. R. Townshend, M. Carroll, C. Dimiceli, R. Sohlberg (2003), 500 m MODIS Vegetation Continuous Fields, *The Global Land Cover Facility, College Park, Maryland*.
- Harris, N., Hudson, R. and Phillips, C. (1998), *Assessment of Trends in the Vertical Distribution of ozone*, SPARC Report No. 1, WMO Ozone Research and Monitoring Project Report No. 43.
- Hashiguchi, N. O., Yamanaka, M. D., Ogino, S.-Y., Shiotani, M., and Sribimawati, T. (2006), Seasonal and interannual variations of temperature in the tropical tropopause layer (TTL) over Indonesia based on operational rawinsonde data during 1992-1999, *J. Geophys. Res.*, *111*, D15110, doi: 10.1029/2005JD006501.
- He, Y. J., Uno, I. Z., Wang, F., Pochanart, P., Li, J., and Akimoto, H. (2008), Significant impact of the East Asian monsoon on ozone seasonal behavior in the boundary layer of Eastern China and the west Pacific region, *Atmos. Chem. Phys.*, *8*, 7543-7555.
- Hegde, P., Pant, P., Naja, M., Dumka, U. C., Sagar, R. (2007), South Asian dust episode in June 2006: Aerosol observations in the central Himalayas, *Geophys. Res. Lett.*, *34*, L23802, doi: 10.1029/2007GL030692.
- Herron-Thorpe, F. L., Lamb, B. K., Mount, G. H., and Vaughan, J. K. (2010), Evaluation of a regional air quality forecast model for tropospheric NO₂ columns using the OMI/Aura satellite tropospheric NO₂ product, *Atmos. Chem. Phys.*, *10*, 8839-8854.
- Horowitz, L. W., et al. (2003), A global simulation of tropospheric ozone and related tracers: Description and evaluation of MOZART, version 2, *J. Geophys. Res.*, *108*(D24), 4784, doi: 10.1029/2002JD002853.
- Hu, X.-M., Gammon, J. W. N.-, and Zhang, F. (2010), Evaluation of Three Planetary Boundary Layer Schemes in the WRF model, *J. Appl. Meteor.*, *49*, 1831-1844.
- Huang, M., et al. (2010), Impacts of transported background ozone on California air quality during the ARCTAS-CARB period: A multi-scale modeling study, *Atmos. Chem. Phys.*, *10*, 6947-6968, doi: 10.5194/acp-10-6947-2010.
- Ito, A. and J. E. Penner (2004), Global estimates of biomass burning emissions based on satellite imagery for the year 2000, *J. Geophys. Res.*, *109*, D14S05.
- Jain, S. L., Arya, B. C., Kumar, A., Ghude, S. D., and Kulkarni, P. S. (2005), Observational study of surface ozone at New Delhi, India, *Int. J. Remt. Sens.*, *26* (16), 3515-3524.
- Janjic, Z. I. (1994), The step-mountain eta coordinate model: further developments of the convection, viscous sublayer and turbulence closure scheme, *Mon. Wea. Rev.*, *122*, 927-945.
- Janjic, Z. I. (1996), The surface layer in the NCEP Eta Model, *Eleventh Conference on Numerical Weather Prediction*, Norfolk, VA, 19-23 August, Amer. Meteor. Soc., Boston, Boston, MA, 354-355.

References

- Janjic, Z. I., (2002), Nonsingular Implementation of the Mellor-Yamada Level 2.5 Scheme in the NCEP Meso model, *NCEP Office Note*, 437, 61.
- Jones, A., D. L. Roberts and A. Slingo (1994), A climate model study of indirect radiative forcing by anthropogenic sulphate aerosols, *Nature*, 370, 450-453.
- Kain, J. S., (2004), The Kain-Fritsch convective parameterization: An update, *J. Appl. Meteor.*, 43, 170-181.
- Kalnay, E., Kanamitsu, M., Kistler, R., Collins, W., Deaven, D., Gandin, L., Iredell, M., Saha, S., White, G., Woollen, J., Zhu, Y., Chelliah, M., Ebisuzaki, W., Higgins, W., Janowiak, J., Mo, K. C., Ropelewski, C., Wang, J., Leetmaa, A., Reynolds, R., Jene, R., and Joseph, D. (1996), The NCEP/NCAR 40-year reanalysis project, *Bull. Am. Meteorol. Soc.*, 77 (3), 437-471.
- Kar, J., M. N. Deeter, J. Fishman, Z. Liu, A. Omar, J. K. Creilson, C. R. Trepte, M. A. Vaughan, and D. M. Winker (2010), Wintertime pollution over the Eastern Indo-Gangetic Plains as observed from MOPITT, CALIPSO and tropospheric ozone residual data, *Atmos. Chem. Phys.*, 10, 12273-12283, doi: 10.5194/acp-10-12273-2010.
- Kedia, S., and S. Ramachandran (2008), Features of aerosol optical depths over the Bay of Bengal and the Arabian Sea during premonsoon season: Variabilities and anthropogenic influence, *J. Geophys. Res.*, 113, D11201, doi: 10.1029/2007JD009070.
- Kistler, R., Kalnay, E., Collins, W., Saha, S., White, G., Woollen, J., Chelliah, M., Ebisuzaki, W., Kanamitsu, M., Kousky, V., van den Dool, H., Roy, J., and Fiorino, M. (2001), The NCEP-NCAR 50-year Reanalysis: Monthly means CD-ROM and documentation, *Bull. Am. Meteorol. Soc.*, 82 (2), 247-267, 2001.
- Kleinman, L., Lee, Y.-N., Springston, S. R., Nunnermacker, L., Zhou, A., Brown, R., Hallock, K., Klotz, P., Leahy, D., Lee, J. H., Newman, L. (1994), Ozone formation at a rural site in the southern United States, *J. Geophys. Res.*, 99, 3469-3482.
- Kramer, L. J., Leigh, R., Remedios, J. J., and Monks, P. S. (2008), Comparison of OMI and ground-based in situ and MAX-DOAS measurements of tropospheric nitrogen dioxide in an urban area, *J. Geophys. Res.*, 113, D16S39, doi: 10.1029/2007JD009168.
- Kulmala, M., Lakkonen, A. and Pirjola, L. (1998), Parameterization for sulphuric acid/water nucleation rates, *J. Geophys. Res.*, 103, 830-8307.
- Kumar, G. M., S. Sampath V. S. Jeena, and R. Anjali (2008), Carbon Monoxide Pollution Levels at Environmentally Different Sites, *J. Ind. Geophys. Union*, 12, 1, 31-40.
- Kumar, R., Naja, M., Venkataramani, S., and Wild, O. (2010), Variations in surface ozone at Nainital, a high altitude site in the Central Himalayas, *J. Geophys. Res.*, 115, D16302, doi: 10.1029/2009JD013715.
- Kunhikrishnan, T. et al. (2004), Analysis of tropospheric NO_x over Asia using the model of atmospheric transport and chemistry (MATCH-MPIC) and GOME-satellite observations, *Atmos. Environ.*, 38, 581-596.
- Kunhikrishnan, T., Lawrence, M. G., von Kuhlmann, R., Wenig, M. O., Asman, W. A. H., Richter, A., and Burrows J. P. (2006), Regional NO_x emission strength for the Indian

References

- subcontinent and the impact of emissions from India and neighboring countries on regional O₃ chemistry, *J. Geophys. Res.*, *111*, D15301, doi: 10.1029/2005JD006036.
- Lal, S., and Lawrence, M. G. (2001), Elevated mixing ratios of surface ozone over the Arabian Sea, *Geophys. Res. Lett.*, *28*, 1487-1490.
- Lal, S., L. K. Sahu, and S. Venkataramani (2007), Impact of transport from the surrounding continental regions on the distributions of ozone and related gases over the Bay of Bengal during February 2003, *J. Geophys. Res.*, *112*, D14302, doi: 10.1029/2006JD008023.
- Lal, S., M. Naja, and B. H. Subbaraya (2000), Seasonal variations in surface ozone and its precursors over an urban site in India, *Atmos. Environ.*, *34*, 2713-2724, doi: 10.1016/S1352-2310(99)00510-5.
- Lal, S., Naja, M., and Jayaraman, A. (1998), Ozone in the marine boundary layer over the tropical Indian Ocean, *J. Geophys. Res.*, *103* (D15), 18907-18917.
- Lamarque, J. -F., and P. G. Hess (2003), Model analysis of the temporal and geographical origin of the CO distribution during the TOPSE campaign, *J. Geophys. Res.*, *108*(D4), 8354, doi: 10.1029/2002JD002077.
- Laprise, R. (1992), The Euler Equations of motion with hydrostatic pressure as independent variable, *Mon. Wea. Rev.*, *120*, 197-207.
- Latifovic, R., Z. Zhu, J. Cihlar, J. Beaubien and R. Fraser (2003), *The land cover map for north America in the year 2000*, GLC2000 Database, European Commission Joint Research Centre, <http://gvm.jrc.it/glc2000/>.
- Lau, W. K. M. and K. M. Kim (2010), Fingerprinting the impacts of aerosols on long-term trends of the Indian summer monsoon region rainfall, *Geophys. Res. Lett.*, *37*, L16705, doi: 10.1029/2010GL043255.
- Lawrence, M. G., and J. Lelieveld (2010), Atmospheric pollutant outflow from southern Asia: a review, *Atmos. Chem. Phys.*, *10*, 11017-11096, doi: 10.5194/acp-10-11017-2010.
- Lawrence, M. G., Rasch, P. J., von Kuhlmann, R., Williams, J., Fischer, H., de Reus, M., Lelieveld, J., Crutzen, P. J., Schultz, M., Stier, P., Huntrieser, H., Heland, J., Stohl, A., Forster, C., Elbern, H., Jakobs, H., and , Dickerson, R. R. (2003), Global chemical weather forecasts for field campaign planning: predictions and observations of large-scale features during MINOS, CONTRACE, and INDOEX, *Atmos. Chem. Phys.*, *3*, 267-289.
- Lelieveld, J., Crutzen, P. J., Ramanathan, V., Andreae, M. O., Brenninkmeijer, C. A. M., Campos, T., Cass, G. R., Dickerson, R. R., Fischer, H., de Gouw, J. A., Hansel, A., Jefferson, A., Kley, D., de Laat, A. T. J., Lal, S., Lawrence, M. G., Lobert, J. M., Mayol-Bracero, O. L., Mitra, A. P., Novakov, T., Oltmans, S. J., Prather, K. A., Reiner, T. A., Rodhe, H., Scheeren, H. A., Sikka, D., and Williams, J. (2001), The Indian Ocean Experiment: Widespread Air Pollution From South and Southeast Asia, *Science*, *291*, 1031-1036.
- Levy II, H., P. S. Kasibhatla, W. J. Moxim, A. A. Klonecki, A. L. Hirsch, S. J. Oltmans and W. L. Chameides (1997), Global impact of human activity on tropospheric ozone, *Geophys. Res. Lett.*, *24*, 791-794.

References

- Lin, M., Holloway, T., Oki, T., Streets, D. G., and Richter A. (2009), Multi-scale model analysis of boundary layer ozone over East Asia, *Atmos. Chem. Phys.*, *9*, 3277-3301.
- Logan, J. (1994), Trends in the vertical distribution of ozone: an analysis of ozonesonde data, *J. Geophys. Res.*, *99*, 25553-25585.
- Logan, J. A. (1985), Tropospheric ozone: Seasonal behavior, trend and anthropogenic influences, *J. Geophys. Res.*, *90* (D6), 10463-10482.
- Logan, J. A., M. J. Prather, S. C. Wofsy and M. B. McElroy (1981), Tropospheric Chemistry: A global perspective, *J. Geophys. Res.*, *86*, 7210-7254, doi: 10.1029/JC086iC08p07210.
- Marcq, S., Laj, P., Roger, J. C., Villani, P., Sellegri, K., Bonasoni, P., Marinoni, A., Cristofanelli, P., Verza, G. P., and Bergin, M. (2010), Aerosol optical properties and radiative forcing in the high Himalaya based on measurements at Nepal Climate Observatory-Pyramid site (5079 m a.s.l.), *Atmos. Chem. Phys.*, *10*, 5859-5872.
- Mellor, G. L. and T. Yamada (1982), Development of a turbulence closure model for geophysical fluid problems, *Rev. Geophys. Space Phys.*, *20*, 851-875.
- Middleton, P., W. R. Stockwell and W. P. L. Carter (1990), Aggregation and analysis of volatile organic compound emissions for regional modeling, *Atmos. Environ.*, *24A*, 1107-1133.
- Minguzzi, E., Bedogni, M., Carnevale, C., Pirovano, G. (2005), Sensitivity of CTM simulations to meteorological input, *Int. J. Environ. Pollut.*, *24*, 36-50.
- Minvielle, F., et al. (2004a), Modeling the transport of aerosols during INDOEX 1999 and comparison with experimental data-1: Carbonaceous aerosol distributions, *Atmos. Environ.*, *38*, 1811-1822.
- Minvielle, F., et al. (2004b), Modeling the transport of aerosols during INDOEX 1999 and comparison with experimental data-1: Continental aerosols and their optical depth, *Atmos. Environ.*, *38*, 1823-1837.
- Mittal, M. L., Peter G. Hess, S.L. Jain, B.C. Arya, and C. Sharma (2007) , Surface ozone in the Indian region, *Atmos. Environ.*, *41*, 6572-6584.
- Mlawer, E. J. et al. (1997), Radiative transfer for inhomogenous atmosphere: RRTM, a validated correlated-k model for the long-wave, *J. Geophys. Res.*, *102* (D14), 16663-16682.
- Monin, A. S. and A. M. Obukhov (1954), Basic laws of turbulent mixing in the surface layer of the atmosphere, *Contrib. Geophys. Inst. Acad. Sci., USSR*, *151*, 163-187 (in Russian).
- Moorthy, K. K., Satheesh, S. K., Babu, S. S. and Dutt, C. B. S. (2008), Integrated Campaign for Aerosols, gases and Radiation Budget (ICARB): An overview, *J. Earth Syst. Sci.*, *117*, 243-262.
- Moorthy, K. K., Satheesh, S. K., Babu, S. S., and Saha, A. (2005), Wintertime spatial characteristics of boundary layer aerosols over peninsular India, *J. Geophys. Res.*, *110*, D08207, doi: 10.1029/2004JD005520.
- Nair, S., Srinivasan, G., and Nemani, R. (2009), Evaluation of Multi-Satellite TRMM Derived Rainfall Estimates over a Western State of India, *J. Meteorol. Soc. Japan*, *87* (6), 927-939, doi: 10.2152/jmsj.87.927.

References

- Nair, V. S., S. S. Babu, and K. K. Moorthy (2008), Spatial distribution and spectral characteristics of aerosol single scattering albedo over the Bay of Bengal inferred from shipborne measurements, *Geophys. Res. Lett.*, *35*, L10806, doi: 10.1029/2008GL033687.
- Naja M., and S. Lal (2002), Surface ozone and precursors gases at Gadanki (13.5°N, 79.2°E), tropical rural site in India, *J. Geophys. Res.*, *107*(D14), 4197, doi: 10.1029/2001JD002477.
- Naja, M., Chand, D., Sahu, L. and Lal, S. (2004), Trace gases over marine regions around India, *Indian J. Mar. Sci.*, *33*, 95-106.
- Naja, M., S. Lal, and D. Chand (2003), Diurnal and seasonal variabilities in surface ozone at a high-altitude site Mt. Abu (24.6°N, 72.7°E, 1680 m asl) in India, *Atmos. Environ.*, *37*, 4205-4215, doi: 10.1016/S1352-2310(03)00565-X.
- Nassar, R., Logan, J. A., Worden, H., Megretskaia, I. A., Bowman, K. W., Osterman, G. B., Thompson, A. M., Tarasik, D. W., Austin, S., Claude, H., Dubey, M. K., Hocking, W. K., Johnson, B. J., Joseph, E., Merrill, J., Morris, G. A., Newchurch, M., Oltmans, S. J., Posny, F., Schmidlin, F. J., Voemel, H., Whiteman, D. N., and Witte, J. C. (2008), Validation of Tropospheric Emission Spectrometer (TES) nadir ozone profiles using ozonesonde measurements, *J. Geophys. Res.*, *113*, D15S17, doi: 10.1029/2007JD008819.
- Nenes, A., Pilinis, C., and Pandis, S. N. (1998), ISOROPIA: a new thermodynamic model for inorganic multicomponent atmospheric aerosols, *Aquatic Geochemistry*, *4*, 123-152.
- Niranjan, K., V. Sreekanth, B. L. Madhavan and K. Krishna Moorthy (2006), Wintertime aerosol characteristics at a north Indian site Kharagpur in the Indo-Gangetic plains located at the outflow region into Bay of Bengal, *J. Geophys. Res.*, *111*, D24209, doi: 10.1029/2006JD007635.
- Novelli, P. C., L. P. Steele, and P. P. Tans (1992), Mixing Ratios of Carbon Monoxide in the Troposphere, *J. Geophys. Res.*, *97*, D18, 731-750, doi: 10.1029/92JD02010.
- Odum, J. et al. (1996), Gas/particle partitioning and secondary organic aerosol yields, *Environ. Sci. Technol.*, *30*, 2580-2585.
- Ohara, T., H. Akimoto, J. Kurokawa, N. Horri, K. Yamaji, X. Yan and T. Hayasaka (2007) An Asian emission inventory of anthropogenic emission sources for the period 1980-2020, *Atmos. Chem. Phys.*, *7*, 4419-4444, doi: 10.5194/acp-7-4419-2007.
- Olsen, T. E., Fishbein, E., Hearty, T., Lee, S.-Y., Irion, F. W., Kahn, B., Manning, E., Blaisdell, J., Susskind, J., Iredell, L., Barnet, C., Maddy, E., Rosenkranz, P., McMillan, W. W., Machado, S. D., and Knuteson, R. (2007), *AIRS Version 5 Release Level 2 Standard Product Quickstart*, available at <http://airs.jpl.nasa.gov/>.
- Osterman, G. (Ed.), Bowman, K., Eldering, A., Fisher, B., Herman, R., Jacob, D., Jourdain, L., Kuawik, S., Luo, M., Monarrez, R., Paradise, S., Payne, V., Poosti, S., Richards, N., Rider, D., Shephard, D., Vilttotter, F., Worden, H., Worden, J., Yun, H., and Zhang, L. (2009), *TES Level 2 Data User Guide, v4.0*, JPL D-38042, 20 May 2009, available at <http://tes.jpl.nasa.gov/documents/>.
- Park, M., W. J. Randel, A. Gettelman, S. T. Massie and J. H. Jiang (2007), Transport above the Asian summer monsoon anticyclone inferred from Aura Microwave Limb Sounder tracers, *J. Geophys. Res.*, *112*, D16309, doi: 10.1029/2006JD008294.

References

- Pfister, G. G., et al. (2010), Variability of springtime transpacific pollution transport during 2000-2006: the INTEX-B mission in the context of previous years, *Atmos. Chem. & Phys.*, *10*, 1345-1359.
- Pfister, G. G., J. Avise, C. Wiedinmyer, D. P. Edwards, L. K. Emmons, G. D. Diskin, J. Podolske, and A. Wisthaler (2011), CO source contribution analysis for California during ARCTAS-CARB, *Atmos. Chem. Phys.*, *11*, 7515-7532, doi: 10.5194/acp-11-7515-2011.
- Pfister, G., G. Pétron, L. K. Emmons, J. C. Gile, D. P. Edwards, J.-F. Lamarque, J.-L. Attie, C. Granier, and P. C. Novelli (2004), Evaluation of CO simulations and the analysis of the CO budget for Europe, *J. Geophys. Res.*, *109*, D19304, doi: 10.1029/2004JD004691.
- Pleim, J. E., A. Venkatram, R. Yamartino (1984), ADOM/TADAP Model Development Program, *The Dry Deposition Module*, *4*, Ont. Min. of the Environment, Canada.
- Pochanart, P., Akimoto, H., Kajii, Y., and Sukasem, P. (2003), Regional background ozone and carbon monoxide variations in remote Siberia/East Asia, *J. Geophys. Res.*, *108* (D1), 4028, doi: 10.1029/2001JD001412.
- Rajeevan, M., Kesarkar, A., Thampi, S. B., Rao, T. N., Radhakrishna, B., Rajasekhar, M. (2010), Sensitivity of WRF cloud microphysics to simulations of a severe thunderstorm event over Southeast India, *Ann. Geophys.*, *28*, 603-619.
- Rakesh, V., R. Singh and P. C. Joshi (2009), Intercomparison of the performance of MM5/WRF with and without satellite data assimilation in short-range forecast applications over the Indian region. *Meteorol. Atmos. Phys.*, *105*, 133-155, doi: 10.1007/s00703-009-0038-3.
- Ramachandran, S. and T. A. Rajesh (2007), Black carbon aerosol mass concentrations over Ahmedabad, an urban location in western India: Comparison with urban sites in Asia, Europe, Canada and the United States, *J. Geophys. Res.*, *112*, D06211, doi: 10.1029/2006JD007488.
- Ramanathan, V., P. J. Crutzen, J. T. Kiehl and D. Rosenfeld (2001), Aerosols, climate and the hydrological cycle, *Science*, *292*, 2119-2124.
- Rao, V., Chapa, S., and Cavalcanti, I. (1998), Moisture budget in the tropics and the Walker circulation, *J. Geophys. Res.*, *103*, D12, doi: 10.1029/98JD00943.
- Rasch, P. J., W. D. Collins and B. E. Eaton (2001), Understanding the Indian Ocean Experiment (INDOEX) aerosol distribution with an aerosol assimilation, *J. Geophys. Res.*, *106*, 7337-7355.
- Ratnam, V. J., and Kumar, K. K. (2005), Sensitivity of the simulated monsoon of 1987 and 1988 to convective parameterization schemes in MM5, *J. Clim.*, *18*, 2724-2743.
- Raub, J. A. and V. A. Benignus (2002), Carbon Monoxide and the Nervous System, *Neuroscience and Biobehavioral Reviews*, *26* (8), 925-940.
- Reddy, M. S., et al. (2004), General circulation model estimates of aerosol transport and radiative forcing during the Indian Ocean Experiment, *J. Geophys. Res.*, *109*, D16205, doi: 10.1029/2004JD004557.
- Reddy, R. R., Rama Gopal, K., Reddy, L. S. S., Narasimhulu, K., Kumar, K. R., Ahammed, Y. N., Reddy, C. V. K. (2008), Measurements of surface ozone at semi-arid site Anantapur (14.62°N, 77.65°E, 331 m asl) in India, *J. Atmos. Chem.*, *59*, 47-59.

References

- Reichler, T., Dameris, M., and Sausen, R. (2003), Determining the tropopause height from gridded data, *Geophys. Res. Lett.*, *30* (20), 2042, doi: 10.1029/2003GL018240.
- Reiner, T., et al. (2001), Chemical characterization of pollution layers over the tropical Indian Ocean: Signatures of emissions from biomass and fossil fuel burning, *J. Geophys. Res.*, *106* (D22), 28497-28510.
- Remsburg, E., Bhatt, P., and Miles, T. (1992), A Comparison of Nimbus 7 Limb Infrared Monitor of the Stratosphere and Radiosonde Temperatures in the Lower Stratosphere Pole ward of 60 N, *J. Geophys. Res.*, *97*, D12, doi: 10.1029/92JD01012.
- Richter, A., J. P. Burrows, H. Nüss, C. Granier, and U. Niemeier (2005), Increase in tropospheric nitrogen dioxide over China observed from space, *Nature*, *437*, 129-132, doi: 10.1038/nature04092.
- Rodgers, C. D. (2000), *Inverse Methods for Atmospheric Sounding, Theory and Practice*, World Sci, River Edge, N. J.
- Routray, A., et al. (2010), Simulation of heavy rainfall events over Indian monsoon region using WRF-3DVAR data assimilation system, *Meteorol. Atmos. Phys.*, *106*, 107-125, doi: 10.1007/s00703-009-0054-3.
- Roy, S., G. Beig and D. Jacob (2008), Seasonal distribution of ozone and its precursors over the tropical Indian region using regional chemistry-transport model, *J. Geophys. Res.*, *113*, D21307, doi: 10.1029/2007JD009712.
- Ruggaber, A., R. Dulgi, T. Nakajima (1994), Modeling of radiation quantities and photolysis frequencies in the troposphere, *J. Atmos. Chem.*, *18*, 171-210.
- Sagar, R., B. Kumar, U. C. Dumka, K. Krishna Moorthy, and P. Pant (2004), Characteristics of aerosol optical depths over Manora Peak: A high altitude station in the central Himalayas, *J. Geophys. Res.*, *109*, D06207 doi: 10.1029/2003JD003954.
- Sahu, L. K. and S. Lal (2006), Distributions of C2-C5 NMHCs and related trace gases at a tropical urban site in India, *Atmos. Environ.*, *40* (5), 880-891.
- Saraf, N., G. Beig and M. Schultz (2003), Tropospheric distribution of ozone and precursors over the tropical Indian Ocean, *J. Geophys. Res.*, *108*, 4636, doi: 10.1029/2003JD003521.
- Saraf, N., and Beig, G. (2004), Long-term trends in tropospheric ozone over the Indian tropical region, *Geophys. Res. Lett.*, *31* (L05101), doi: 10.1029/2003GL018516.
- Satheesh, S. K., Moorthy, K. K., Babu, S. S., Vinoj, V., Nair, V. S., Beegum, S. N., Dutt, C. B. S., Alappattu, D. P., and Kunhikrishnan, P. K. (2009), Vertical structure and horizontal gradients of aerosol extinction coefficients over coastal India inferred from airborne lidar measurements during the Integrated Campaign for Aerosol, Gases and Radiation Budget (ICARB) field campaign, *J. Geophys. Res.*, *114*, D05204, doi: 10.1029/2008JD011033.
- Saxena, P., A. B. Hudischewskyj, C. Seigneur, J. H. Seinfeld (1986), A comparative study of equilibrium approaches to the chemical characterization of secondary aerosols, *Atmos. Environ.*, *20*, 1471-1483.
- Schell, B., I. J. Ackermann, H. Hass, F. S. Binkowski and A. Ebel (2001), Modeling the formation of secondary organic aerosol within a comprehensive air quality model system, *J. Geophys. Res.*, *106* (D22), 28275-28293.

References

- Schwartz, B., and Govett, M. (1992), A Hydrostatically Consistent North American Radiosonde Data base at the forecast System Laboratory, 1946- Present, *NOAA Tech. Memorandum, ERL, FSL-4*, Boulder, Colorado.
- Sheel, V., Lal, S., Richter, A., Burrows, J. P. (2010), Comparison of satellite observed tropospheric NO₂ over India with model simulations, *Atmos. Environ.*, *44*, 3314-3321.
- Shreedharan, C. R. (1968), An Indian electrochemical ozonesonde, *J. Phys. E. Sci. Instrum. Sr.*, *2*, 995-997.
- Sillman, S. (1995), The use of NO_y, H₂O₂ and HNO₃ as indicators for ozone-NO_x-hydrocarbon sensitivity in urban locations, *J. Geophys. Res.*, *100 (D7)*, 14175-14188.
- Skamarock, W. C., J. B. Klemp, J. Dudhia, D. O. Gill, D. M. Barker, M. Duda, X.-Y. Huang, W. Wang, and J. G. Powers (2008), A description of the Advanced Research WRF version 3, *NCAR Tech. Note NCAR/TN-475+STR*, 125 pp., Natl. Cent. For Atmos. Res., Boulder, Colo.
- Slinn, S. A. and W. G. N. Slinn (1980), Prediction for particle deposition on natural waters, *Atmos. Environ.*, *14*, 1013-1016.
- Solberg, S., Hov, Ø, Søvde, A., Isaksen, I. S. A., Coddeville, P., De Backer, H., Forster, C., Orsolini, Y., Uhse, K. (2008), European surface ozone in extreme summer 2003, *J. Geophys. Res.*, *113*, D07307, doi: 10.1029/2007JD009098.
- Srivastava, S., S. Lal, S. Venkataramani, S. Gupta, and Y. B. Acharya (2011), Vertical distribution of ozone in the lower troposphere over the Bay of Bengal and the Arabian Sea during ICARB-2006: Effects of continental outflow, *J. Geophys. Res.*, *116*, D13301, doi: 10.1029/2010JD015298.
- Stauffer, D. R. and N. L. Seaman (1994), Multiscale four-dimensional data assimilation, *J. Appl. Meteor.*, *33*, 416-434.
- Stehr, J. W., Ball, W. P., Dickerson, R. R., Doddridge, B. G., Piety, C. A., and Johnson, J. E. (2002), Latitudinal gradients in O₃ and CO during INDOEX 1999, *J. Geophys. Res.*, *107*, 8015, doi: 10.1029/2001JD000446.
- Stephenson, D. B. (2000), Use of the "odd ratios" for diagnosing forecast skill, *Wea. Forecasting.*, *15*, 221-232.
- Stockwell, R. W., F. Kirchner, M. Kuhn and S. Seefeld (1997), A new mechanism for regional atmospheric chemistry modeling, *J. Geophys. Res.*, *102 (D22)*, 25847-25879.
- Stockwell, W. R., P. Middleton, J. S. Chang, and X. Tang (1990), The second Generation Regional Acid Deposition Model Chemical Mechanism for Regional Air Quality Modeling, *J. Geophys. Res.*, *95(D10)*, 16343-16367, doi: 10.1029/JD095iD10p16343.
- Tanimoto, H, T. Ohara, and I. Uno (2009), Asian anthropogenic emissions and decadal trends in springtime tropospheric ozone over Japan: 1998-2007, *Geophys. Res. Lett.*, *36*, L23802, doi; 10.1029/2009GL041382.
- Thompson, G., R. M. Rasmussen and K. Manning (2004), Explicit forecasts of winter precipitation using an improved bulk microphysics scheme. Part I: Description and sensitivity analysis, *Mon. Wea. Rev.*, *132*, 519-542.
- Tie, X., Brasseur, G. and Ying, Z. (2010), Impact of model resolution on chemical ozone formation in Mexico City: application of the WRF-Chem model, *Atmos. Chem. Phys.*, *10*, 8983-8995.

References

- Tie, X., Madronich, S., Li, G., Ying, Z., Zhang, R., Garcia, A., Lee-Taylor, J., and Liu, Y. (2007), Characterization of chemical oxidants in Mexico City: A regional chemical dynamical model (WRF-CHEM) study, *Atmos. Environ.*, *41*, 1989-2008.
- Tripathi, S. N., S. Dey, V. Tare, and S. K. Satheesh (2005), Aerosol black carbon radiative forcing at an industrial city in Northern India, *Geophys. Res. Lett.*, *32*, L08802, doi: 10.1029/2005GL022515.
- Vieno, M., Dore, A. J., Stevenson, D. S., Doherty, R., Heal, M. R., Reis, S., Hallsworth, S., Tarrason, L., Wind, P., Fowler, D., Simpson, D., and Sutton, M. A. (2010), Modelling surface ozone during the heat-wave in the UK, *Atmos. Chem. Phys.*, *10*, 7963-7978.
- Wang, T. J., Lam, K. S., Xie, M., Wang, X. M., Carmichael, G., Li, Y. S. (2006), Integrated studies of a photochemical smog episode in Hong Kong and regional transport in the Pearl River Delta of China, *Tellus B*, *58* (1), 31-40.
- Warneck, P. (2000), *Chemistry of the Natural Atmosphere*, 927 pp., Academic, San Diego, California.
- Wesley, M. L. (1989), Parameterization of surface resistance to gaseous dry deposition in regional numerical model, *Atmos. Environ.*, *16*, 1293-1304.
- Whitby, E. R., P. H. McMurry, U. Shankar and F. S. Binkowski (1991), Modal aerosol dynamics modeling, *Rep. 600/3-91/020*, *Atmospheric Research and Exposure Assessment Laboratory*, US Environmental Protection Agency, Research Triangle Park, NC, 1991 (Available as NTIS PB91-1617291 from National Technical Information Service, Springfield, VA).
- Wiedinmyer, C. et al. (2006), Estimating emissions from fires in North America for Air Quality Modeling. *Atmos. Environ.*, *40*, 3419-3432.
- Wiedinmyer, C., S. K. Akagi, R. J. Yokelson, L. K. Emmons, J. A. Al-Saadi, J. J. Orlando, and A. J. Soja (2011), The Fire Inventory from NCAR (FINN): A high resolution global model to estimate the emissions from open burning, *Geosci. Model Dev.*, *4*, 625-641, doi: 10.5194/gmd-4-625-2011.
- Wigley, T. M. L., S. J. Smith, and M. J. Prather (2002), Radiative forcing due to reactive gas emissions, *J. Clim.*, *15* (18), 2690-2696, doi: 10.1175/1520-0442(2002)015<2690:RFDTRG>2.0.CO;2
- Wild, O., X. Zhu, and M. J. Prather (2000), Accurate simulation of in- and below cloud photolysis in tropospheric chemical models, *J. Atmos. Chem.*, *37*, 245-282.
- Willmott, C. J. (1981), On the validation of models, *Phys. Geogr.*, *2*, 184-194.
- WMO (World Meteorological Organization) (1994), Third WMO inter-comparison of the ozonesonde used in the Global Ozone Observing System (Canada, 13-24 May, 1991), *Global Atmospheric Watch, Rep.*, *27*, Geneva, Switzerland.
- Worden, H. M., Logan, J. A., Worden, J. R., Beer, R., Bowman, K., Clough, S. A., Eldering, A., Fisher, B. M., Gunson, M. R., Herman, R. L., Kulawik, S. S., Lampel, M. C., Luo, M., Megretskaia, I. A., Osterman, G. B., and Shephard, M. W. (2007), Comparison of Tropospheric Emission Spectrometer (TES) ozone profiles to ozonesondes: Methods and Initial Results, *J. Geophys. Res.*, *112*, D03309, doi: 10.1029/2006JD007258.
- Worden, J., Kulawik, S. S., Shephard, M. W., Clough, S. A., Worden, H., Bowman, K., and Goldman, A. (2004), Predicted errors of Tropospheric Emission Spectrometer nadir

References

- retrievals from spectral window selection, *J. Geophys. Res.*, *109*, D09308, doi: 10.1029/2004JD004522.
- Yashiro, H., S. Sugawara, K. Sudo, S. Akoi, and T. Nakazawa (2009), Temporal and spatial variations of carbon monoxide over the western part of the Pacific Ocean, *J. Geophys. Res.*, *114*, D08305, doi: 10.1029/2008JD010876.
- Yasunari, T. J., et al. (2010), Estimated impact of black carbon deposition during pre-monsoon season from Nepal Climate Observatory – Pyramid data and snow albedo changes over Himalayan glaciers, *Atmos. Chem. & Phys.*, *10*, 6603-6615.
- Yu, S., Eder, B., Dennis, R., Chu, S.-H., and Schwartz, S. (2005), On the development of new metrics for the evaluation of air quality models, *Atmos. Sci. Lett.*, *7*, 26-34.
- Zhang, M., Uno, I. Zhang, R., Han, Z., Wang, Z., and Pu, Y. (2006), Evaluation of the Models-3 Community Multi-Scale Air Quality (CMAQ) modeling system with observations obtained during the TRACE-P experiment: Comparison of ozone and its related species, *Atmos. Environ.*, *40*, 4874-4882.
- Zhang, Q., Streets, D. G., Carmichael, G. R., He, K. B., Huo, H., Kannari, A., Klimont, Z., Park, I. S., Reddy, S., Fu, J. S., Chen, D., Duan, L., Lei, Y., Wang, L. T., Yao, Z. L. (2009), Asian emissions in 2006 for the NASA INTEX-B mission, *Atmos. Chem. Phys.*, *9*, 5131-5153.
- Zhou, Y. Brunner, D., Boersma, K. F. Dirksen, R. and P. Wang (2009), An improved tropospheric NO₂ retrieval for satellite observations in the vicinity of mountain terrain, *Atmos. Meas. Tech.*, *2*, 401-416.
- Zilitinkevich, S. S., (1995), Non-local turbulent transport: pollution dispersion aspects of coherent structure of convective flows, *Air Pollution III- Volume I. Air Pollution Theory and Simulations*, Eds. H. Power, N. Moussiopoulos and C. A. Brebbia, Computational Mechanics Publications, Southampton, Boston, 53-60.

